

HEMIBIQUINONES: THE THEORY, SYNTHESIS, AND EXPERIMENTAL VALIDATION
OF AN ASYMMETRIC D—A BIPHENYL SYSTEM

by
JOSEPH E. MEANY

STEPHEN A. WOSKI, COMMITTEE CHAIR
ROBERT M. METZGER
SHANE C. STREET
GREGORY J. SZULCZEWSKI
PATRICK E. LECLAIR

A DISSERTATION

Submitted in partial fulfillment of the requirements
for the degree of Doctor of Philosophy
in the Department of Chemistry
in the Graduate School of
The University of Alabama

TUSCALOOSA, ALABAMA

2016

Copyright Joseph Edward Meany 2016
ALL RIGHTS RESERVED

ABSTRACT

In order to elucidate the governing characteristics behind asymmetric current flow in molecules (molecular rectification), it is important to establish size limitations for the electron transfer processes which make rectification possible. Here I present the rational design and synthesis of a molecular template which has been tested for its rectification properties, alongside important derivatives.

The molecular template in question, hemibiquinone (HBQ), is an asymmetric biphenyl derivative composed of a dimethoxybenzene ring covalently bonded to a benzoquinone (2,5-cyclohexadiene-1,4-dione) ring. It contains a 2-position group allowing the molecule to self-assemble. Early recognition that the molecule already possessed electroactive donor (dimethoxybenzene) and acceptor (benzoquinone) sections led the author to hypothesize that the torsion angle between the rings of biphenyl sufficiently isolates orbitals to be the requisite tunnel barrier necessary for unimolecular rectification. Spectroscopic and electrochemical data are presented to validate predictions made by Density Functional Theory calculations. A monolayer of the molecule sandwiched between gold is found to rectify with a forward/reverse current ratio approaching 200 at 2.5 V.

This result demonstrates that larger, saturated carbon bridges are not necessary components in the design of a molecular diode. Any way of breaking conjugation in the system will suffice. Beyond establishing a lower size limit for D- σ -A rectifiers, this work also lays the foundation to experimentally test how properties such as polarity, torsion angle, end-group effects and HOMO-LUMO gap energy affect the rectification efficiency for a given structure.

DEDICATION

This dissertation is dedicated to the awesome family and friends who have coached me, pressed me, and encouraged me to do my best.

Also, to my teachers and professors, who always put up with me asking those questions that no other kid would. Denise Junge, Jerry Jasinski, Richard Blatchly, Mike Cullinane, Frederick Wolf, Robert Shalit, Ted Miller, Keith Goodale, and Julia Imbarrato all deserve special recognition for their roles in my early scientific development.

LIST OF ABBREVIATIONS AND SYMBOLS

°	degree
3D	three-dimensional
A	acceptor
A	ampere
Å	angstrom
Ac	acetyl
AC	alternating current
AFM	atomic force microscopy
AR	Arieh Aviram and Mark Ratner
Ar	aromatic
Au ^{TS}	template-stripped gold
B	bridge
B3LYP	Becke, three-parameter, Lee-Yang-Parr

CAN	cerium ammonium nitrate
CAS	cerium ammonium sulfate
cm	centimeter
CMOS	complimentary metal-oxide semiconductors
CV	cyclic voltammogram
D	Debye
D	donor
DC	direct current
DCNQI	dicyanoquinoimine
DFT	density functional theory
DGDZVP	Density Gaussian Double-Zeta-Split-Valence + Polarization
E	energy
${}^1E_{1/2}^O$	half-wave oxidation potential
${}^1E_{1/2}^R$	first half-wave reduction potential
${}^2E_{1/2}^R$	second half-wave reduction potential
E_f	Fermi energy
EGaIn	eutectic gallium-indium amalgam

E_{HOMO}	HOMO eigenvalue
EI	electron ionization
E_{LUMO}	LUMO eigenvalue
E_{max}	maximum potential
eV	electron volt
Fc	ferrocene
FMO	frontier molecular orbital
g	grams
GAANN	Graduate Assistance in Areas of National Need
GCE	glassy carbon electrode
h	hours
\hbar	reduced Planck's constant
HBQ	hemibiquinone
HOMO	highest occupied molecular orbital
HRMS	high-resolution mass spectrometry
I	electrical current
IBM	International Business Machines Corporation

ICT	intramolecular charge-transfer
IEEE	Institute of Electrical and Electronics Engineers
IPES	inverse photoelectron spectroscopy
isoNC	isonitrile
<i>IV</i>	current-voltage
k	Boltzmann constant
K	Kelvin
kcal	kilocalorie
LB	Langmuir-Blodgett
LUMO	lowest unoccupied molecular orbital
m	electron mass
M	molarity
Me	methyl
MHz	megahertz
mL	milliliter
mM	millimolar
mm	millimeter

mmol	millimole
MO	molecular orbital
mol	mole
MPSH	molecular projected self-consistent Hamiltonian
mV	millivolt
n	negatively-doped silicon
n	nonbonding orbital
NEGF	non-equilibrium Green's function
nm	nanometer
NMR	nuclear magnetic resonance
OPT+FREQ	optimization and frequency
p	positively-doped silicon
Ph	phenyl
Py	pyridyl
R	general chemical group
R	resistance
RR	rectification ratio

RT	room temperature
s	second
SCE	saturated calomel electrode
STM	scanning tunneling microscope
STS	scanning tunneling spectroscopy
T	temperature
TCNQ	tetracyanoquinodimethane
UPS	ultraviolet photoelectron spectroscopy
UV-Vis	ultraviolet-visible
V	voltage
V	volt
$v(t)$	time-dependent voltage
V_0	initial voltage
VdW	Van der Waals
$v_R(t)$	$v(t)$ -dependent resistance
XPS	x-ray photoelectron spectroscopy
XRD	x-ray diffraction

Δ	chemical shift
ΔE_{rot}	energy of rotation
E	molar extinction coefficient
H	hapticity
Θ	angle
λ_{max}	wavelength of maximum absorption
μL	microliter
π	pi-bonding orbital
π^*	pi-antibonding orbital
σ	sigma bond
ϕ	work function

ACKNOWLEDGEMENTS

I have the distinct honor of giving thanks to all of the people who have made this work possible, especially to my advisor Dr. Stephen Woski and to my dissertation committee Professors Robert Metzger, Shane Street, Gregory Szulczewski, and Patrick Leclair. Through my time at The University of Alabama, they have provided me with curious and exciting conversation, wisdom, and insight. I would also like to thank my collaborator and co-graduate student, Marcus Johnson for making the measurements proving the hypothesis.

I would also like to thank the various faculty and graduate students who let me use their instruments or trained me on techniques which helped move this dissertation. Thanks go to Professor David Dixon and Dr. Edward Garner for their instruction on Density Functional Theory and Gaussian09. Thanks go to Professor Robin Rogers and Dr. Steven Kelley for providing x-ray diffraction measurements of any crystals I was able to grow. Steven and I had many engaging conversations about solid-state interactions. Additional thanks to Professor Elizabeth Papish and Dr. Deidra Gerlach for gathering extra crystal data. Thanks go to Professor Shanlin Pan, Dr. Caleb Hill and Nelly Kaneza for their instruction on cyclic voltammetry methods. Thanks goes to Professor Patrick Frantom for the use of his UV-Vis spectrometer.

Additional thanks must be extended to Professors Shane Street and John Vincent who were my Department of Education Graduate Assistance in Areas of National Need (GAANN) Fellowship advisors and helped begin to make *The Crimson Alchemist* what it is today.

I would like to thank the people who made Tuscaloosa livable including Bo Hicks, Elliot Roberts, and the rest of the Druid City Brewing Co. crew.

And finally, I have to thank my minions: Kindle, Brice-with-an-I, Lynda, Olivia, Neil, Steven, Katie, and Tabitha.

CONTENTS

ABSTRACT.....	ii
DEDICATION.....	iii
LIST OF ABBREVIATIONS AND SYMBOLS.....	iv
ACKNOWLEDGEMENTS.....	xi
LIST OF TABLES.....	xiv
LIST OF FIGURES.....	xv
CHAPTER 1 INTRODUCTION AND THEORY.....	1
CHAPTER 2 DESIGN AND THEORY.....	33
CHAPTER 3 SYNTHESIS.....	77
CHAPTER 4 SOLUTION AND CRYSTAL CHARACTERIZATION OF HBQS.....	120
CHAPTER 5 MONOLAYER ASSEMBLY AND ANALYSIS.....	174
CHAPTER 6 CONCLUSIONS AND FUTURE DIRECTIONS.....	200
REFERENCES.....	221
APPENDICES.....	234

LIST OF TABLES

Table 2.1 Calculated molecular and electronic properties for the HBQ series.	52
Table 2.2 The HOMO (left) and LUMO (right) of the parent HBQ backbone through various torsion angles.	57
Table 2.3 Calculated FMO levels by DFT	63
Table 2.4 Torsion angles and dipole moments of acetylated HBQ molecules	70
Table 2.5 FMO eigenvalues and HOMO-LUMO gap values of acetylated HBQ molecules.....	72
Table 2.6 Comparative DFT values of the FMOs for the donor, acceptor, and combined HBQ.	75
Table 4.1 Absorbance details of 2,5-dibromobenzoquinone and 2,5-dibromo-1,4- dimethoxybenzene.	124
Table 4.2 Absorbance details of various HBQ derivatives.....	129
Table 4.3 Peak Potentials (V vs. SCE)	140
Table 4.4 Peak Potentials (V vs. SCE)	142
Table 4.5 Orbital Potentials (vs. SCE).....	152
Table 6.1 DFT minimization of compounds in Figure 6.1	207

LIST OF FIGURES

Figure 1.1 The original Moore graph.	6
Figure 1.2 Schematic of a diode's <i>pn</i> junction.	9
Figure 1.3 Schematic of diode behaviors.	10
Figure 1.4 Schematic of energy levels within a D— σ —A device between two electrodes.	17
Figure 1.5 Electron transfer in the circuit under forward bias.	18
Figure 1.6 Electron transfer in the circuit under reverse bias.	19
Figure 1.7 Schematic of D and A placement within a junction.	21
Figure 1.8 Schematic representation of hexadecylquinolinium tricyanoquinodimethanide in a LB junction between two gold electrodes.....	22
Figure 1.9 Schematic of the HOMO and LUMO orbital energy shifting with respect to circuit bias.	24
Figure 1.10 Schematic of the molecular orbital distribution from AR.	30
Figure 1.11 Example of FMO spatial separation in a Ratner molecular diode.	31
Figure 2.1 A subset of the molecules tested in Venkatamaran <i>et al.</i>	39
Figure 2.2 Conductance values with respect to torsion angle.	40
Figure 2.3 Molecule calculated within Van Dyck and Ratner.	48

Figure 2.4 Orbital eigenvalue evolution adapted from Van Dyck and Ratner.	16
Figure 2.5 Detail of total calculated DFT molecular energy of HBQ versus torsion angle θ	51
Figure 2.6 The HOMO (left) and LUMO (right) of the AR molecule at optimized geometry.	56
Figure 2.7 Molecular orbital energy with respect to the torsion angle.	61
Figure 2.8 Example visualization of HBQ torsion angle calculation with corresponding dipole vector.	65
Figure 2.9 Dipole dependence on torsion angle.	66
Figure 2.10 Acetylated HBQ HOMO (left) and LUMO (right)	69
Figure 2.11 Monomer FMOs	74
Figure 2.12 Calculated relative energy gaps of the donor and acceptor portion of the molecules	76
Figure 3.1 The “hemiquinone” in AR as inspiration for the hemibiquinone backbone.....	80
Figure 3.2 Visualization of the FMO for BrHBQBr	81
Figure 3.3 Crystal structure data for 4.	117
Figure 3.4 Crystal structure data for 4, packing along <i>a</i> direction.	118
Figure 3.5 Crystal structure data for 10	119
Figure 3.6 Crystal structure data for 10, packing along <i>a</i> direction	120

Figure 4.1 Absorption spectrum of 2,5-dibromo-1,4-dimethoxybenzene (blue) compared with 2,5-dibromobenzoquinone (red)	125
Figure 4.2 Calculated energy gaps of the donor and acceptor portions of the molecules	126
Figure 4.3 Comparison of UV-Vis absorption spectra of BrHBQBr (red) and 2,5- dibromo-1,4-dimethoxybenzene (blue)	128
Figure 4.4 Comparison of UV-Vis absorption spectra of BrHBQBr (red) and BrHBQ(CN) ₂ (green)	132
Figure 4.5 Comparison UV-Vis absorption spectra of BrHBQBr (red) and BrHBQNH ₂ (blue).	133
Figure 4.6 Comparison UV-Vis absorption spectra of BrHBQ(CN) ₂ (green) and BrHBQH ₂ (CN) ₂ (black)	134
Figure 4.7 Comparison UV-Vis absorption spectra of BrHBQ(CN) ₂ in solution (blue) vs. as a monolayer supported on a glass slide (red).	135
Figure 4.8 Comparison of CVs of 2,5-dibromo-1,4-dimethoxybenzene (blue) and 2,5- dibromo-1,4-benzoquinone	137
Figure 4.9 CV of 2-bromo-1,4-dimethoxybenzene	138
Figure 4.10 CV of 2,5-dibromo-1,4-hydroquinone..	139
Figure 4.11 CV of BrHBQBr	143
Figure 4.12 CV of BrHBQ(Br) ₂	146
Figure 4.13 CV of BrHBQ(CN) ₂	147
Figure 4.14 CV of BrHBQNH ₂	149

Figure 4.15 Crystal structure of BrHBQBr viewed down the <i>a</i> crystallographic axis.	156
Figure 4.16 Crystal structure of BrHBQH ₂ (CN) ₂ viewed down the <i>c</i> crystallographic axis.	160
Figure 4.17 Crystal structure of BrHBQ(CN) ₂ viewed down the <i>b</i> crystallographic axis.	164
Figure 4.18 Crystal structure of BrHBQ(CN) ₂ viewed down the <i>b</i> crystallographic axis.	168
Figure 4.19 Crystal structure of BrHBQN ₃ viewed along the <i>b</i> crystallographic axis.	171
Figure 4.20 Crystal structure of biquinone BrDQBr depicted down the <i>b</i> crystallographic axis	173
Figure 5.1 Diagram of molecules self-assembled on flat template-stripped gold.	178
Figure 5.2 Schematic of the BrHBQ(CN) ₂ monolayer with EGaIn top contact.	181
Figure 5.3 Representative <i>IV</i> curve with EGaIn top contact.	182
Figure 5.4 Schematic of the BrHBQH ₂ (CN) ₂ monolayer with EGaIn top contact	184
Figure 5.5 Representative <i>IV</i> curve for BrHBQH ₂ (CN) ₂ with an EGaIn top contact	185
Figure 5.6 Schematic of the monolayer with Cold Au top contact	187
Figure 5.7 Representative <i>IV</i> curve with “Cold Au EGaIn” top contact.	188
Figure 5.8 Schematic of the monolayer with Pt/Ir STM top contact.	190
Figure 5.9 Representative <i>IV</i> curve with STM Pt/Ir top contact.	191
Figure 5.10 Representative RR trace for EGaIn BrHBQ(CN) ₂ Au ^{TS} sandwich.	194

Figure 5.11 Representative RR trace for EGaIn Au BrHBQ(CN) ₂ Au ^{TS} sandwich.	196
Figure 5.12 Representative RR trace for Pt/Ir BrHBQ(CN) ₂ Au ^{TS} sandwich.	199
Figure 6.1 TCNQ derivative of HBQ (left), the four configurational isomers of DCNQI-derived HBQ	212
Figure 6.2 Symmetric binding groups on the molecule lead to random order under self-assembly.	213
Figure 6.3 Structure and labeling of an azide functional group (adapted from Cenini).	216
Figure 6.4 An η^1 -bonded azide (left) and an η^3 -bonded azide (right).	217
Figure 6.5 An η^1 -bonded nitrene.	218

CHAPTER 1
INTRODUCTION

Section 1.1 Motivation

Section 1.1.1 Shrinking Computers

The twentieth century ushered in the greatest rate of change in technology since the development of agriculture. After the development of the transistor in the 1940s,¹ the daily impact of computing devices on an average consumer has grown exponentially. Over time, humanity's mastery over the flow of electricity in a circuit has evolved from simple incandescent lightbulbs and telephones in the late 19th century to the complex structures within our modern computing systems.

The field of Molecular Electronics entails the use of molecules to create functional devices. The advent for Molecular Electronics came about as researchers turned their attention towards miniaturizing the components of automatic computing machines. Cuevas and Scheer² note in their history that the Air Force was a major early player in supporting electronics research on an ever decreasing scale. At a meeting between the Air Force and top researchers in the early microelectronics industry, Colonel C. H. Lewis articulated the early goal of molecular electronics:

“We should synthesize, that is, tailor materials with predetermined electronic characteristics... We could design and create materials to perform desired functions... We call

this more exact process of constructing materials with predetermined electrical characteristics Molecular Electronics.”³

Molecular electronics and other derivative fields of nanotechnology were discussed conceptually in the middle of the twentieth century beginning with Richard Feynman’s^{2,4} popular lecture *Plenty of Room at the Bottom*, and developed over time into a fruitful area of interdisciplinary research. Building functional structures up from smaller pieces rather than “hewing” them from larger blocks is how scientists would deliver on their promise. Exploiting atoms and small molecules to mimic or replicate the function of bulk material properties has tremendous potential to deliver new ways to use electricity. As Feynman⁴ famously noted, this is not so straightforward as a concept. The importance of certain forces and effects change over the scale of sizes involved shrinking from the macroscale to the nanoscale.

Science Fiction and Futurist authors were quick to use the genres’ plentiful imaginations to popularize all sorts of exotic futures for the human race. Nanoscale versions of the self-replicating von Neumann probes (cellular automata) as nanobots or “nanites” pervade grey-goo type apocalypse scenarios, where they consume matter uncontrollably, as that matter is converted into even more nanites. These miniaturized robots come complete with manipulators, propulsion, some sort of read-write memory, and communication technology. They have been imagined in areas as widespread as space travel, medicine, and synthetic biology.⁵ Perhaps not so surprisingly, these machines are inspired by the behaviors of real biological macromolecules such as proteins⁶ or in more complex systems as viruses.

The complexity of bringing molecular electronics forward as a reality is neatly described in Choi and Mody’s³ “The Long History of Molecular Electronics.” Therein they describe the early

marketing of molecular scale circuitry from Westinghouse to the United States Air Force. The dominant idea in this first era of three (as coined by Choi and Mody³) was to create small, lightweight, and reliable electronic circuits for use in next-generation aircraft to remain competitive during the Space Race era. Between 1958 and 1963, lots of flowery language on the promise of molecular electronics was published by Westinghouse, but by 1963 the relationship had soured and focus returned to developing silicon semiconductor-based integrated circuits.³ Molecular electronics, as a descriptive term, fell out of vogue and into relative obscurity. This period of relative disinterest is the second of the three eras.³

Section 1.1.2 Moore's Law

As automated computing gained a foothold and IBM sought to create competitive computers, Gordon Moore^{7,8} published a paper in 1965, establishing a trend which would outlive its original prediction by an additional fifty years. This trend, eponymously dubbed “Moore's Law,” outlines that the density of semiconductor transistors on a chip would double every two years (Figure 1.1). Though the originally conservative estimate predicted the trend to continue for only ten years, scientists at IBM recently revealed a *commercial* chip with transistors only 7 nm long.⁹ Currently, computers and circuits have been made from doped silicon and complimentary metal-oxide semiconductors (CMOS) as a part of their circuit structure. These CMOS chips are made from the chemical etching and photolithography of semiconductor substrates. Since large bulk starting materials are required to create the finer operational structures, molecular electronics advocates term this type of fabrication the “top-down” method in contrast to the (idealized) atom-by-atom fabrication from the “bottom-up.” It took another decade from Moore's original prediction for a carbon-based circuit to be proposed, launching the modern era of molecular electronics.

Section 1.1.3 Application to Broader Electrical Circuitry

While Moore's Law was originally explicitly stated for transistor density on a microchip, it is a natural development of the research and application that other components of a microcircuit are able to shrink as well. This has required research into new materials and fabrication methods, particularly with regard to carbon-based materials over silicon and CMOS materials.

In 1974, Arieh Aviram and Mark Ratner¹⁰ (AR) published a theoretical framework that set Feynman's "bottom-up" approach in motion. They detailed a way that synthetic chemical principles could be used to specifically design a carbon-based molecule having particular electronic properties, and thus controlling the flow of electrons in a circuit to do useful work. This paper demonstrated the way a current of electrons (I) could flow more readily through a molecular circuit when a bias voltage (V) is applied in one direction than in the opposite direction. Current asymmetry of this type (as illustrated in Figure 2) is called rectifying behavior. Despite the publication of this paper, Molecular Electronics had yet to enter its third era of productivity until 1988,³ after the development of the scanning tunneling microscope (STM).

Section 1.1.4 Modern Molecular Electronics

It took until 1997 for researchers to finally confirm single molecule conduction^{11,12} and molecular rectification.¹³ Reed *et al.*^{11,12} at Yale measured conductance through a single molecule of benzenedithiol in a mechanically controlled break-junction, and Robert Metzger¹³⁻¹⁵ at The University of Alabama synthesized and reported the characteristics for hexadecylquinolinium tricyanoquinodimethanide. Now, forty years after AR inspired the field of molecular electronics, researchers have been able to create such exotic devices as molecular

wires, molecular diodes, organic field-effect transistors, and organic solar cells, among many others.¹⁶

Choi and Mody's³ history of Molecular Electronics is an apt summary of the field from its inception through the 1990s. Subsequent review articles and books summarize the field from 2000 onward.^{2,16-20} As computational chemistry has gained complexity in its ability to model electronic interactions of a molecule— particularly under non-equilibrium conditions— models of molecular systems have been available to assist in the anticipation or interpretation of integrated circuits involving organic molecules.²¹⁻²³

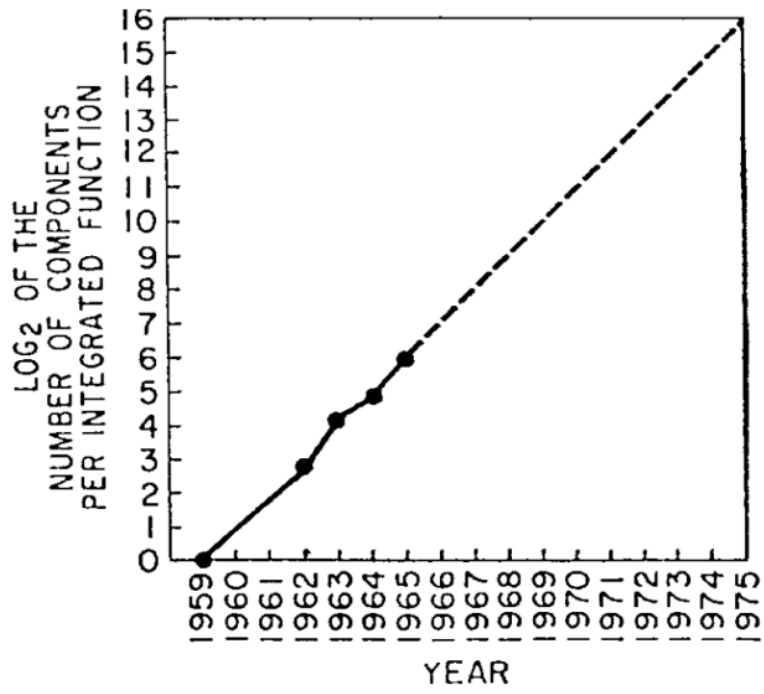


Figure 1.1. The original Moore graph.⁷ © 1965 and 2006, IEEE

As discussed in more detail in Chapter 2, derivatives of biphenyl have generated interest in studies involving conduction through single molecules. Of particular importance to this dissertation are the studies performed by Venkataraman *et al.*^{12,24-26} as well as Miskchenko *et al.*,²⁷⁻²⁹ on the conclusion that symmetrically substituted biphenyl derivatives vary their conductance as a function of $\cos^2\theta$ where θ is the angle between the rings. This is due to the fact that the rings of the biphenyl molecules lose conjugation with one another as they are twisted out of plane. A break in conjugation, as will be explained in Section 1.2.3 is crucial to the electrical operation of a molecule as a diode analogue.

Section 1.2 Diode Function

Section 1.2.1 Doping, *p* and *n* Junctions

Conduction asymmetry at a given voltage is the functional definition of a diode, and an assembly of diode(s) together into a device are called a rectifier.³⁰ Rectifiers are used to convert alternating current (AC) into direct current (DC). Traditional semiconductor diodes use doped silicon to achieve their function, with a sandwiched *pn* junction. The *p*-doped side is made up from Group 3 elements (Al, Ge, etc.) within the silicon structure, which leaves it electron-poor compared to the pure silicon crystal. Likewise, the *n*-doped side is made up of silicon that has been doped with Group 5 elements (P, As, etc.), which leaves it electron-rich compared to pure Si. When these *p* and *n* pieces are brought together, a thin insulating layer forms from the excess electrons in *n* cancelling out holes in *p*. This thin layer is called the depletion zone. It is through the elimination (conduction) or growth (insulation) of the depletion region that determines the exact *IV* characteristics of a silicon diode. A schematic of the *pn* junction is illustrated in Figure 1.2, showing the depletion zone between the *p* and *n* sections.

Section 1.2.2 Ideal, Real, and Molecular Diode Behavior

In a silicon diode, the ideal behavior appears in Figure 1.3 (left). In forward current, there is perfect conduction (resistance $R = 0 \Omega$) and in reverse there is no conduction at all ($R = \infty \Omega$). In a real diode (Figure 1.3, middle), there is negligible current until the diode's turn-on voltage is reached. At this point, current proceeds to flow. If a high enough voltage is applied in the reverse direction, a breakdown of the crystal will occur within the diode and current will begin to flow freely at this great overpotential.

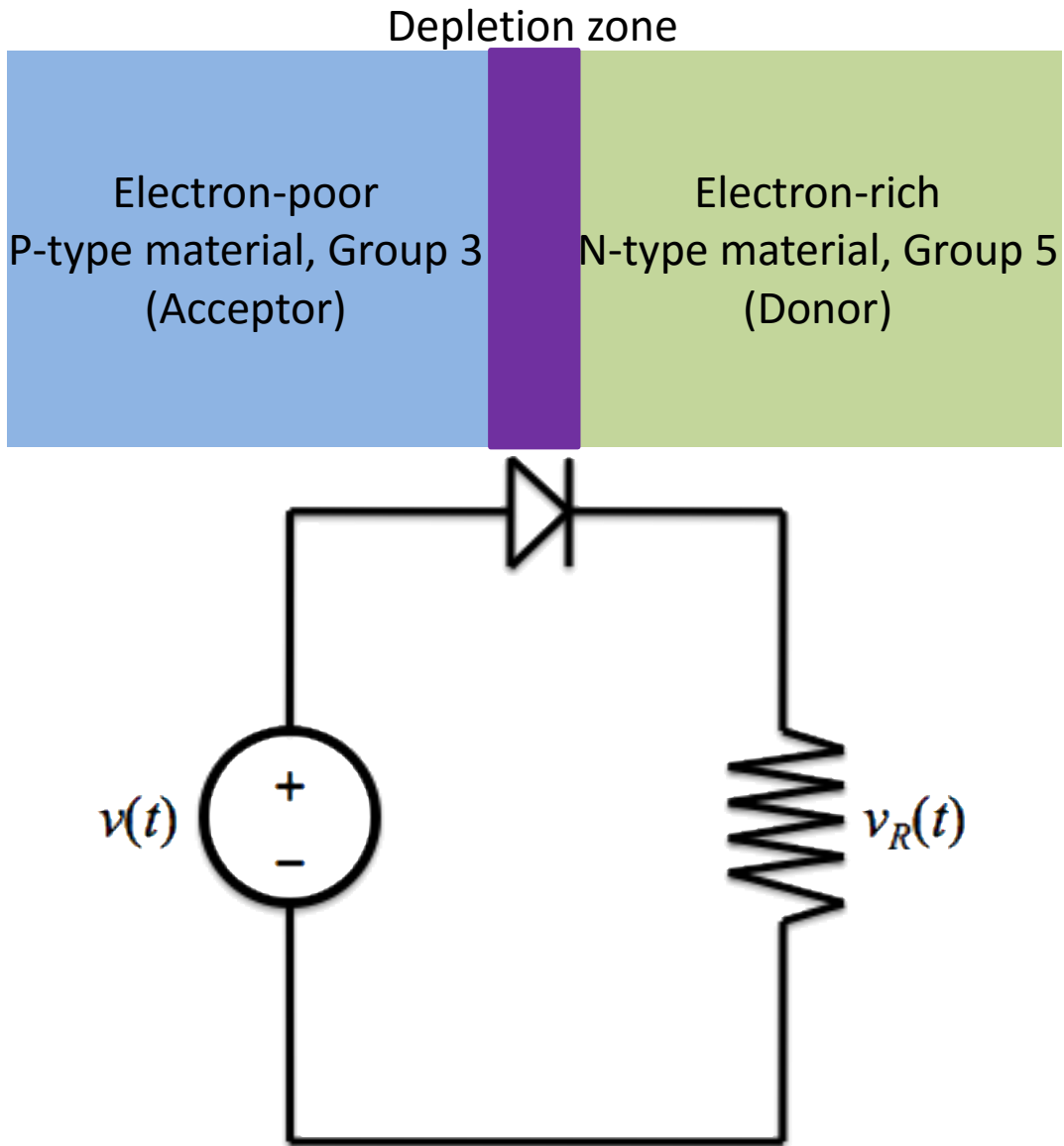


Figure 1.2. (Top) Schematic of a diode's *pn* junction. Charge carriers at the interface flow into one another, and the depletion zone (purple) is the insulating “bridge” between the two pieces. (Bottom) Schematic of a diode in a circuit. Current flow follows the direction of the diode arrow, by electronic convention.

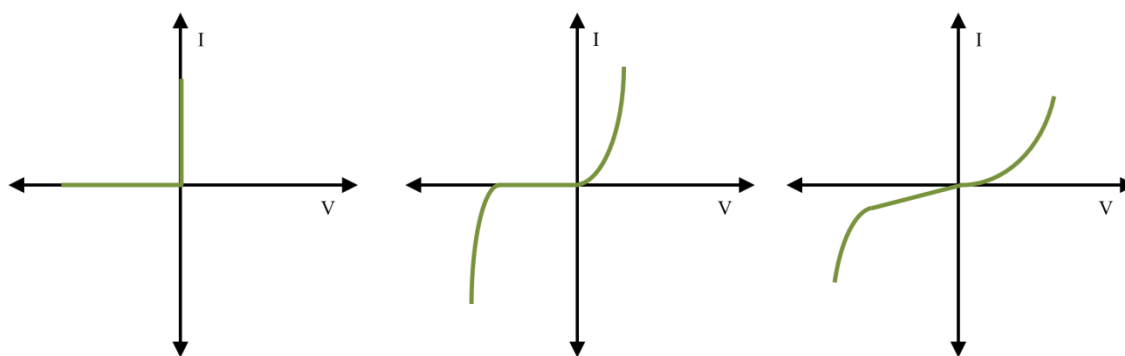


Figure 1.3. Schematic of diode behaviors. I represents current (Amperes) with respect to an applied bias voltage (V)
 (Left) Schematic representation of an ideal diode. (Middle) Schematic representation of a real diode. (Right)
 Schematic representation of an ideal molecular diode.

Section 1.2.3 Molecular Diode Structure

In Figure 1.4, an example three-sectioned molecule is arranged between two metal electrodes. One section, D (green), is electron rich and the eigenvalues of the orbitals associated with this section are at a relatively high-energy, when compared to the orbitals associated with A. Its purpose in the device is to donate electrons to the anode when the circuit is put under bias. A is electron poor (blue), and the eigenvalues of these orbitals are lower in absolute energy with respect to D. Its purpose is to accept electrons from the cathode when the circuit is put under bias. The third section within the hypothetical molecule is an insulating saturated-carbon bridge which acts as a tunneling barrier, as illustrated in Figure 4. Up to this point, I draw a clear analogy to a typical silicon diode: A is the *p*-doped semiconductor, D is the *n*-doped semiconductor, and the bridge is the depletion zone.

In rectifiers measured up to this point, the molecules were generally designed with an explicit saturated carbon bridge separating two electroactive portions. This break in conjugation interrupts electrons from moving across the molecule unimpeded. Introducing this saturated bridge creates a tunneling barrier that localizes molecular orbitals on either side of said barrier. This means the energetic difference of the distal frontier molecular orbitals (FMOs) on either side of the barrier will determine which applied bias will allow an electron to undergo resonant electron transfer.

Localizing the FMOs of the molecule is a critical component in controlling electron flow through the junction. This allows for controlled, stepwise transfer of electrons down an energy gradient strongly directed by the bias between the metals electrodes. This gradient involves

electrons being injected into a local LUMO and removed from a local HOMO. Full details of the conduction mechanisms are elucidated in Section 1.3.

Section 1.2.4 Rectification Ratio

Since the path length of conduction through a single molecule is so small (1–15 nm)¹⁶ with respect to bulk material properties ($>10^3$ nm), one needs to keep in mind that quantum tunneling currents will remain a factor in the device (Figure 1.3, right, negative bias). The probability of tunneling with respect to linear distance decays with respect to $(\hbar^2/2m(V_0 - E))^{1/2}$ where \hbar is the reduced Planck's constant, m is the mass of an electron, V_0 is the height of the tunneling barrier, and E is the energy of the electron in the system. Between two similar electrodes with nothing in between them, $V_0 = \phi$, the work function of the metal. However, in a system where a molecule is placed between two similar electrodes, V_0 is reduced because the FMOs become available for conduction at some energy $E < \phi$. This means that significant (non-negligible) current may be able to make its way across the junction that is not a part of the forward-bias high current (hopping) regime. Thus, there will be some non-negligible current flow in both directions, and it is up to the project designers to balance the research questions with practical considerations. Within the field of molecular electronics, the ratio of forward current at a particular voltage V to reverse current at a given voltage is called the rectification ratio (RR).

$$\text{RR} = \frac{I(V)}{-I(-V)}$$

In 1988 Aviram reported having assembled a device originally believed to rectify,³¹ but the paper was later retracted, citing STM tip anomalies.³² The molecule was similar in design concept to the one he proposed in 1974 (Scheme 1.1, left), as it had an electron-rich

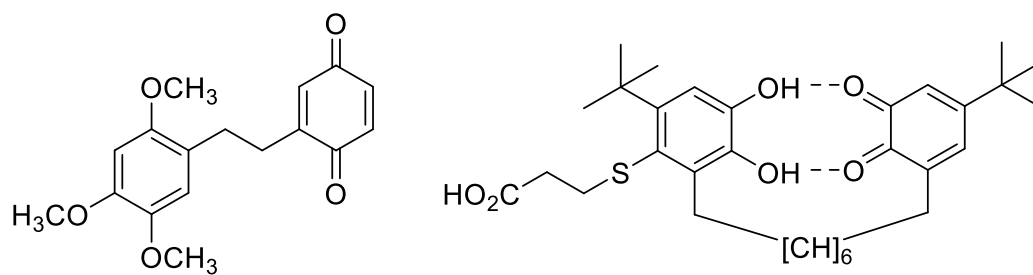
hydroquinone ring bonded through an *n*-octane chain to an electron-poor *ortho*-quinone (Scheme 1.1, right). The mercaptopropionic acid on the hydroquinone ring is used to self-assemble onto a gold surface for STM probing, a feature that the 1974 molecule lacked. The octane chain gave this molecule enough flexibility such that the rings could hydrogen-bond but still be electronically isolated from one another.

Section 1.3 Rectification Mechanisms

There are three main mechanisms by which electrons are able to asymmetrically conduct through molecules, and measuring rectification to determine the mechanism of electron flow is not a routine procedure.^{33,34} The dominant mechanisms are unimolecular rectification, as described by AR; asymmetric rectification, as described by a differential in electron tunneling probabilities; and Schottky rectification, as described by charge buildup due to potential energy barriers in the junction.³⁵

These mechanisms must be taken into account when a particular molecule is destined to assemble within the junction. This project focuses on creating a diode which conducts by the “unimolecular” mechanism, as proposed by AR in 1974.¹⁰ The concepts underlying the unimolecular rectification mechanism are summarized in Figures 1.4–1.6.

Scheme 1.1. (Left) Aviram-Ratner 1974 molecule.¹⁰ (right) Aviram *et al.* 1988 molecule.^{31,32}



Section 1.3.1 Unimolecular Rectification

In an open circuit for an ideal AR molecule, two equivalent electrodes with the same work function sandwich a molecule of interest (Figure 1.4). In the first step of forward electron transfer within an AR-type unimolecular rectifier under bias, a $D^+—\sigma—A^-$ zwitterion forms from low bias oxidation of the donor D and (simultaneous) reduction of the acceptor A (Figure 1.5). Subsequently the electron on A will tunnel across the molecule and eliminate the zwitterion. Since the HOMO is localized on D, and the LUMO localized on A, this elimination may also be described as a relaxation of the molecule back to its ground state.

This transfer of electrons from the cathode to A, from D to the anode, and intramolecular elimination happens across three low-bias tunneling events (electron hopping) where the electron ideally has a high probability for transmission. The tunneling barrier width for crossing from the cathode to A, and from D to the anode, is assumed to be thin with respect to the molecule/system in the AR mechanism when compared to the distance between D and A as separated by the insulating bridge (Figure 1.4). Therefore, according to AR, the limiting step in the current would be the rate of intramolecular electron transfer. In a real system, the barrier dimensions will be entirely dependent on the molecule being tested as well as its coupling to the electrodes.

Strong coupling decreases the barrier thickness to an effective minimum of 0 Å for electrophores which fully hybridize with the surface, whereas weak coupling would increase the barrier width to the geometric maximum distance from the electrode. See the section on Asymmetric Rectification below for a broader discussion.

The forward bias conduction of electricity occurs with much less resistance than conduction in the reverse direction. If the bias were to be reversed within the circuit in Figure 1.4, a much

larger bias must be placed on the system for the cathode to come into resonance with the D LUMO, while at the same time the anode comes into resonance with the HOMO of A (Figure 1.6). The reverse bias zwitterion, $D^- - \sigma - A^+$ is supposed to lie several eV beyond the turn-on voltage for the forward bias regime.¹⁸

In an ideal case, this disparity would lead to a high current hopping through the molecule under forward bias, while negligible (or at least greatly decreased) current tunneling in the opposite direction. In traditional semiconductor diodes, this reverse-bias conduction is called the leakage current. Meanwhile, there are two other mechanisms to take into consideration for the conduction of current through a molecule.

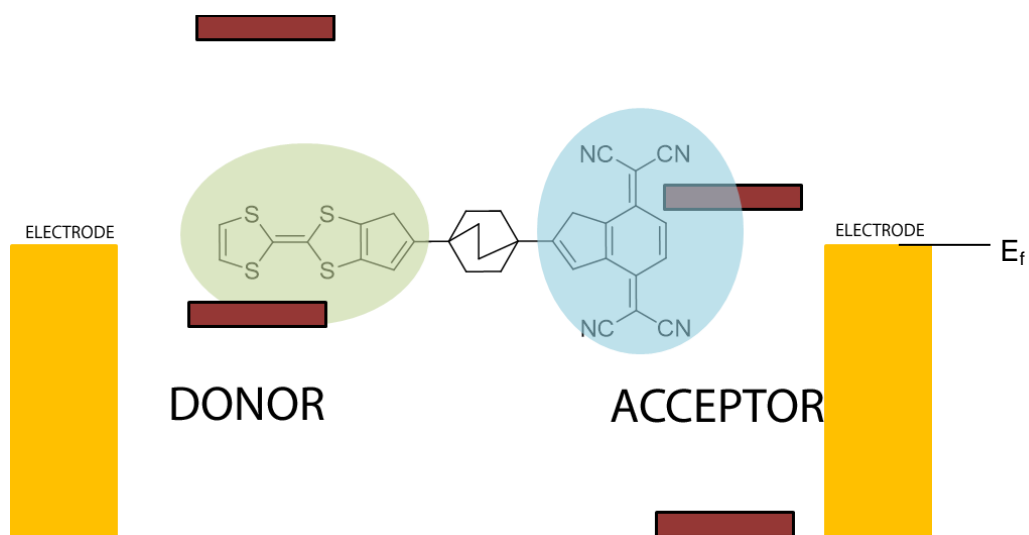


Figure 1.4. Schematic of energy levels within a D— σ —A device between two electrodes. Yellow blocks represent electron energies in the electrodes. A molecule containing an electron-rich donor and an electron-poor acceptor is suspended between two metal electrodes at zero bias, whose Fermi Level (E_f) lies between the HOMO and LUMO of the molecule.

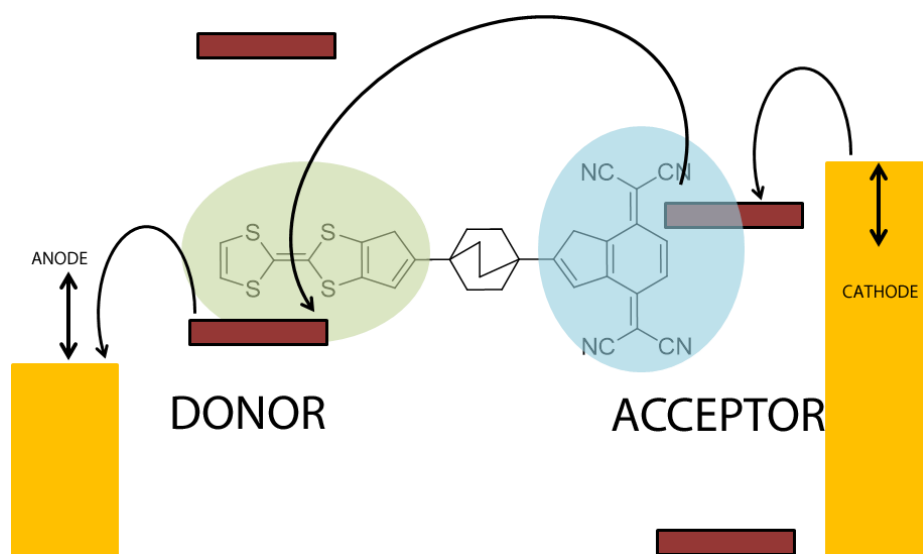


Figure 1.5. Electron transfer in the circuit under forward bias. Yellow blocks represent electron energies in the electrodes. Between the FMOs and the electrodes as well as between the FMOs themselves, a tunneling barrier isolates the orbitals. Arrows are not representative of energy trajectories.

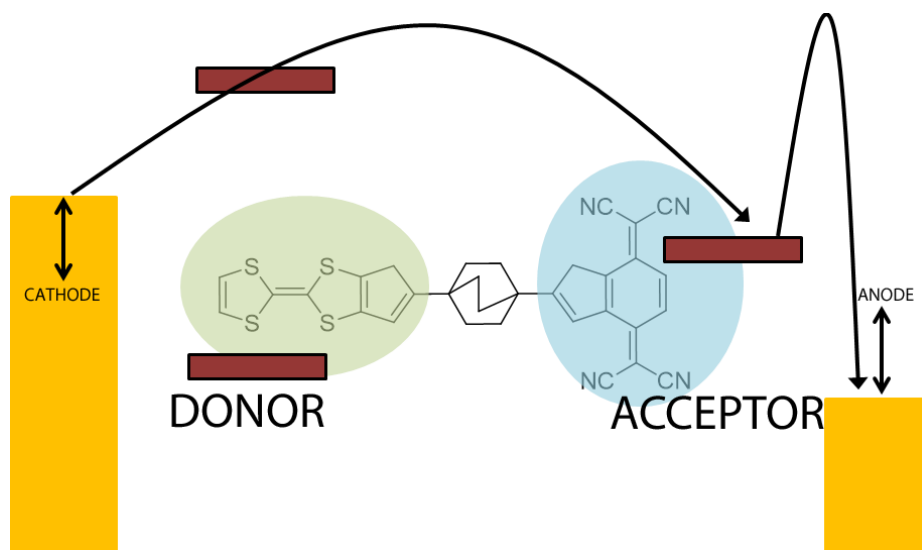


Figure 1.6. Electron transfer in the circuit under reverse bias. Yellow blocks represent electron energies in the electrodes. A low tunneling current is possible when the cathode reaches the LUMO level. Arrows are not representative of energy trajectories.

Section 1.3.2 Asymmetric Rectification

Asymmetric rectification is a size-dependent design factor within a molecular junction. In Figures 1.4–1.6, I outlined a molecule whose coupling strength with the metal is assumed to be low between both electrodes, and the tunneling probability is equal between both electrodes as well. If the distance from the electrode to the electrophore is dissimilar, or if orbital hybridization occurs, then the monolayer's ability as a whole to transfer electrons is dissimilar as well.^{13,35} When molecules are strongly coupled to the electrode, raising the Fermi energy of a metal electrode will lift the energy of an orbital nearby. Alternatively, lowering the Fermi energy will drop the energy of a nearby orbital. The degree to which an orbital's energy will be affected by this raising/lowering of Fermi energy by an electrode is related to how far away the orbital is from the electrode.¹⁸

Figures 1.7 and 1.8 illustrates this concept, where the molecule may be situated symmetrically in the junction (top), D may be situated closer to an electrode than A (middle), or vice versa (bottom). When a bias is placed on the system, the energy of the molecular orbitals will change with them (Figure 1.9).^{15,18,36} Assuming equivalent coupling strength on both ends of the molecule, the tendency of the orbital eigenvalues to raise or lower is going to be very dependent on the shape of the molecule within the junction and the distance of the molecule's electroactive orbitals from the electrode (Figure 1.8).^{18,37} This leads to rectification because the energy perturbations will bring orbitals into resonance across the molecule at different V in the positive and negative direction. When orbitals come into resonance with one another, a drastic increase in conduction is observed.³⁸⁻⁴¹

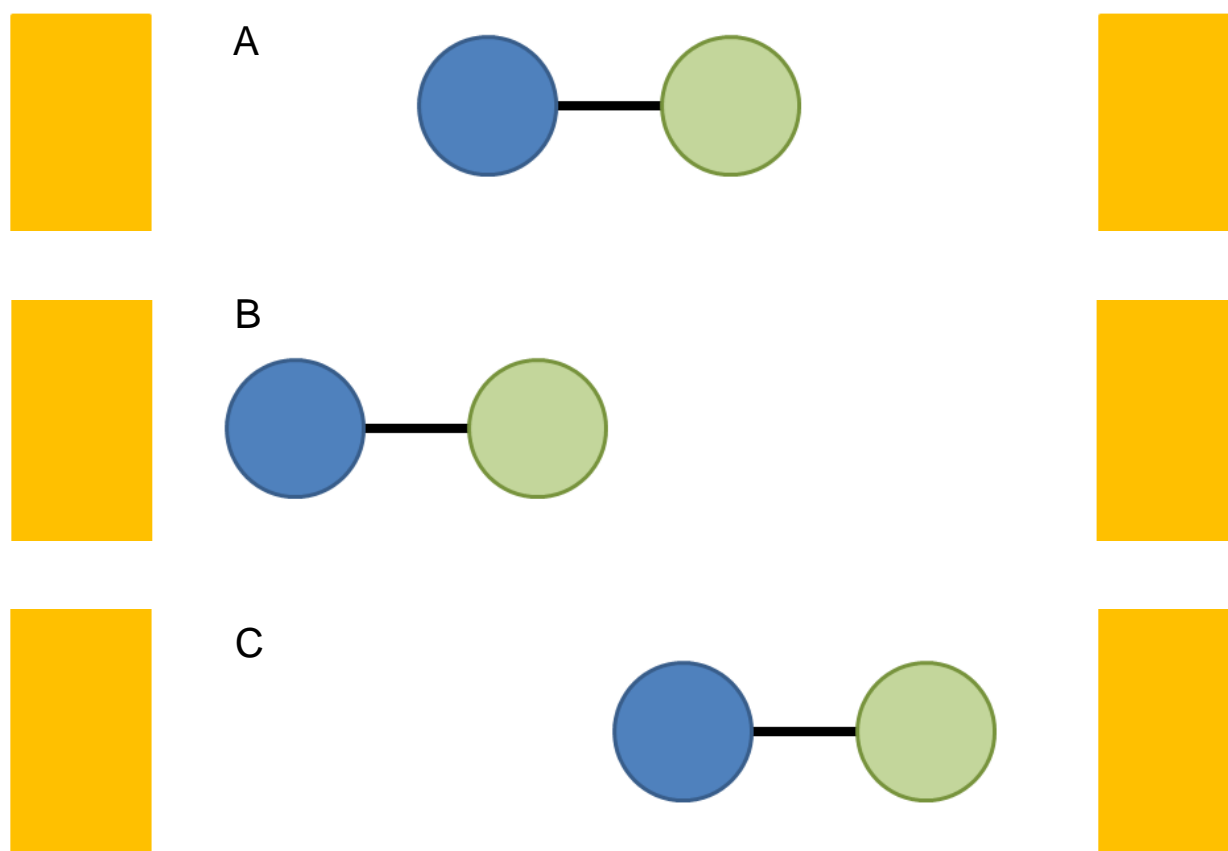


Figure 1.7. Schematic of D and A placement within a junction. Yellow blocks are electrode surfaces. (A) A molecule's electrophores are spaced evenly from the electrodes. Orbital energy perturbation will be equal. (B) Donor is closer to the electrode. Orbital energy perturbation will be greater on D. (C) Acceptor is closer to the electrode. Orbital energy perturbation will be greater on A.

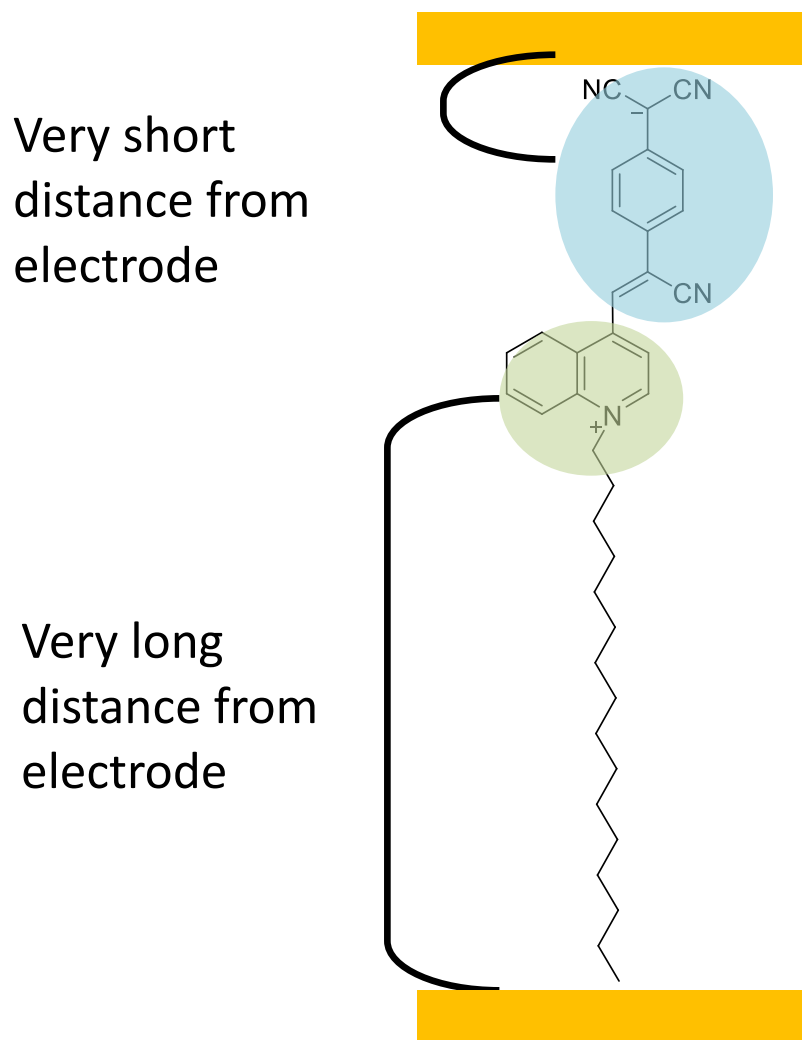


Figure 1.8. Schematic representation of hexadecylquinolinium tricyanoquinodimethanide in a LB junction between two gold electrodes. Asymmetric electron transfer rate is partially due to asymmetric change in the orbital energies as bias on the electrodes changes.

Section 1.3.3 Schottky Rectification

The third mechanism by which electrons can asymmetrically conduct is Schottky rectification, or a Schottky contact.⁴² In a traditional Schottky diode, silicon itself forms a joint contact to a metal, which acts as the *p*-type carrier. There is a potential energy barrier for the charge carriers to cross at the metal-molecule junction in one direction. In a molecular junction, this leads to partial charge exchange in the device, as represented in Figure 1.9 by the downward curve from the HOMO. The barrier height can be calculated experimentally from the extrapolation of $\log(I)$ vs. V , where the linear portion of the curve is extended to $V = 0$ V.⁴³ Due to the rate difference in an electron's ability to transfer within the cathode—molecule—anode system when these potential energy differences exist, they can cause molecules even without the prototypical D— σ —A system to rectify.⁴⁴

Section 1.3.4 Asymmetric Polarization

Diodes which function under this idea of polarization at the metal-molecule interface are still of both theoretical^{45,46} and experimental⁴⁷⁻⁵¹ interest. The local molecule—metal polarization is not the only factor governing a possible rectification. Asymmetric electrodes made from different materials (a bulk effect like a traditional diode) can create Schottky-type rectification, due to the metal's different work functions. This mismatch can lead to misleading measurements, though, since rectification would not be an inherent property of the molecule but rather a property of the device. It is important to take into consideration these asymmetric and Schottky effects when designing or analyzing a molecular diode.

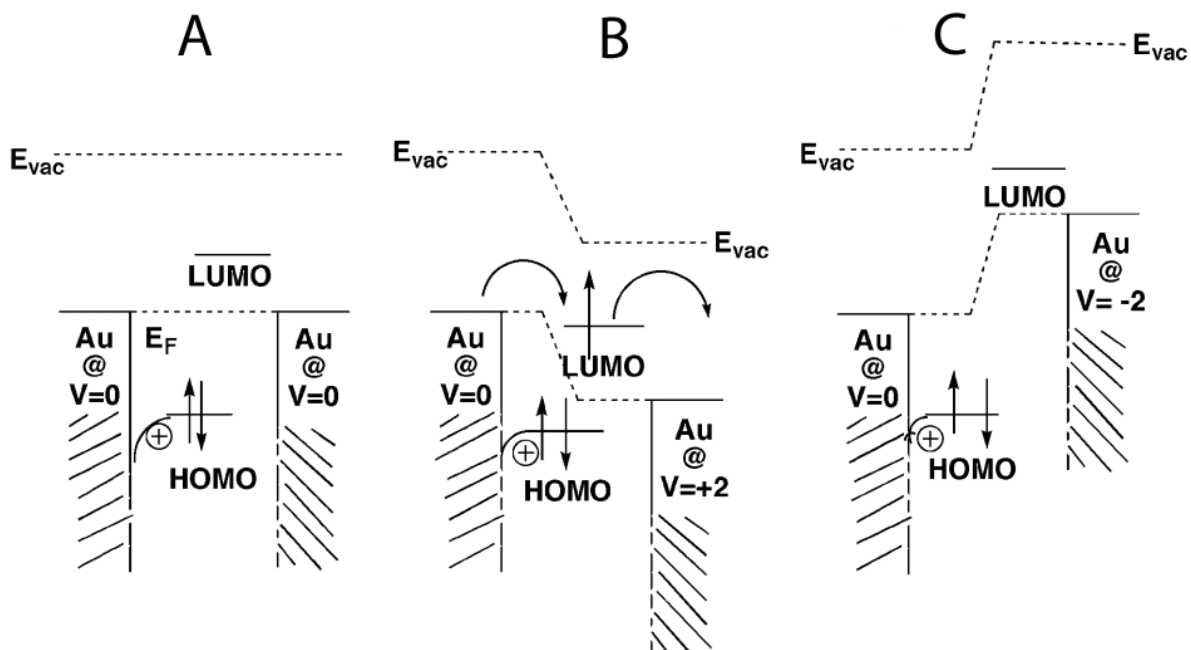


Figure 1.9. Schematic of the HOMO and LUMO orbital energy shifting with respect to circuit bias. From Metzger.¹⁸ The (+) symbol on the HOMO signifies some e^- density bending into the metal in a Schottky-like contact. (A) No bias is on the system. (B) +2 V bias is placed on the system, and an electron is injected into the LUMO, which then tunnels to the positive electrode. (C) A -2 V bias is placed on the system. Due to movement of the orbitals in energy, no conduction is possible. © 2008 RSC

Recently, Venkataraman and coworkers⁴⁸ experimentally demonstrated rectification through symmetric molecules. In the paper they measure the conductance for a series of symmetric molecules (bipyridine, alkyl dithiols, etc.) via a mechanically controlled break junction in different solvent environments. They found that nonpolar solvent environments led to symmetric tunneling through the junction, and that polar solvents led to temporary enhanced conduction in a preferential direction. They concluded rectification occurred because an electric double-layer formed from polar solvent arrangement, which was absent for nonpolar solvents. This solvent polarization under an electric field induces a temporary asymmetry within the junction. The authors do not present any scan-rate dependence of the conduction, the scan rate is 40 V(s⁻¹). It would be interesting to see a similar study done with the scan-rate tuning, to see how the RR changes at higher and lower scan rates.

Section 1.4 Experimental Considerations Behind the Hemibiquinones

Section 1.4.1 Monolayer Construction

These considerations lead to the first decision to make- what test methods are available to the research team? For example, is the project focused on contacting truly a single molecule? Is an ensemble of molecules acceptable? Note that “unimolecular rectification” and “single-molecule rectification” are two separate and distinct concepts. Unimolecular rectification refers to the first rectification mechanism outlined in Section 1.3.1, and single-molecule rectification refers to current asymmetry measured through only one molecule at a time. In the Woski and Metzger collaboration, we focused on molecular ensembles as our testbed method. Single-molecule methods exist and are reviewed thoroughly by Kiguchi,¹² Li,²⁹ as well as Cuevas and Sheer.³³

If a device is to be assembled using Langmuir-Blodgett (LB) deposition, then the molecule must have discernible amphiphilicity.¹⁸ In other words, the hydrophilic head must be only on the order of a few angstroms thick in order to interact with the topmost layers of water molecules but maintain a relatively large (10s of angstroms) hydrophobic tail for LB monolayers to reliably form. This design consideration for LB monolayers would then force a hypothetical diode candidate to be highly asymmetrically coupled to the electrodes, unless post-deposition functionalization occurs. Most of the molecules in a recent survey by Metzger¹⁶ share one property: long alkyl chains.

The other primary method is self-assembly. Self-assembly requires that the hypothetical molecule contain a group which will more strongly interact with a surface than any other group. This group is called an anchor group¹² or “alligator clip.”²⁰ Certain atoms or moieties are better at bonding to an electrode surface than others.^{52,53} Thiols and thioacetates are the most common choice of an anchor group, but nitriles, isocyanides, amines and carboxylic acids have also been investigated.¹² Early works on self-assembled monolayers through conductive molecules were dominated by James Tour and Mark Reed. Research into the effect of oligomer length on conduction through substituted oligo(phenylene-ethynylene)s (OPEs) earned that class of molecules the nickname “Tour Wires”.²⁰

The anchor group allows a molecule to be deposited on the chosen substrate directly from solution into a monolayer with a controlled degree of selectivity. Should a molecule not possess this anchor group, selectivity is lost, and monolayer formation is uncontrolled. Aryl groups and quinones, when not specifically synthesized with the appropriate alligator clips will lie flat on the surface.⁵⁴ This is true of any weakly interacting group such as halogens or alkyl groups. There is greater flexibility in monolayer design when dealing with self-assembled monolayers. One is not

limited to highly asymmetric molecules across the long molecular axis. Molecular design is limited (for the most part) only by the necessary design constraint that one end of the molecule *must* attach preferentially to the chosen electrode. After the molecule has been deposited on the surface, additional functionalization may occur to achieve the desired chemical structure. Post-assembly functionalization is important if anchor group effects are not a part of the research question; asymmetric electrode coupling has been shown to have a convoluting effect on the conduction mechanism through the molecule.⁵⁵

For most of the work tabulated in Metzger's 2015 review, the electrode of choice has been bulk gold; silicon, silver, and aluminum are also included in this list.^{16,56} That said, design considerations in this dissertation will focus only on groups that bind to gold, with only tangential mention to other substrates in the chapter that deals with future work.

Section 1.4.2 Frontier Molecular Orbital Separation

As a natural consequence of the *pn* junction analogy, molecules that are to rectify via the unimolecular mechanism need to have electron-rich and electron-poor regions separated in space by a bridge. As a result of these requirements, the FMOs should also be physically separated in space. D should have a HOMO and LUMO of energy that is similar to an isolated donor molecule, and A should have the same for an isolated acceptor molecule.

In the original AR proposal, we can see this illustrated as part of their Figure 3 (Figure 1.10, below).¹⁰ The HOMO (C) and LUMO (B) of the molecule are separated on either side of a tunneling barrier whereby a forward bias will inject an electron into (B) and remove one from (C). The electron-rich donor has molecular orbitals situated higher in energy than the acceptor, and the orbitals maintain (within this schematic) an alternating pattern across the barrier. If this

is indeed the case, then higher-bias scans need to take into account the energy levels of at least 4 separate orbitals (HOMO-1, HOMO, LUMO, LUMO+1).

Ratner⁴⁵ has continued this work forward, publishing a paper in which he uses density functional theory (DFT) calculations to demonstrate that anchor group choice is enough to induce an asymmetry within an otherwise symmetric molecule (Figure 1.11). The electron-donating thiol group was distinct enough from the electron-withdrawing nitrile, localizing the FMOs on opposite sides of a butane tunneling barrier. From this calculation, Ratner⁴⁵ was able to calculate a maximum rectification ratio of 150 in this system.

Molecular projected self-consistent Hamiltonian (MPSH) calculations discussed in the next chapter take into account the evolution of the molecular orbitals under bias, and are used in predictions for possible rectifier systems.^{39,40,46} While the MPSH calculations take into account the change in energy, the calculations do not take into account the polarization/distribution of the orbitals with respect to bias.

Section 1.4.3 Minimization of Other Rectification Effects

Taking into consideration the competition between the unimolecular, asymmetric, and Schottky rectification mechanisms; investigative questions must be decided upon early on in a project. Synthetic targets must be chosen by understanding something about how the molecule will form a junction, perhaps how its orbital energies will align with the electrode of choice. This is most easily accomplished using data generated by DFT calculations.

Once that step is complete, decisions can be made to determine particular targets and reduce the variety within a class of molecules. Particular attention must be paid to the coupling strength

of the electrophores to the electrodes, as explained in Section 1.3. Depending on the system, anchor group choice will affect both the molecular orbital energy and molecular geometry within the junction.

From this, testing the synthesized molecules in a junction will lead to data about how well current flows through the molecule, and checks to test a variety of molecules will give clues as to the nature of this conduction. However, the molecule within a junction should have a) equally spaced anchor groups from each electrode, b) a HOMO and LUMO within the available testing bias, c) a D— σ —A linear transfer, and d) consistent geometry on a monolayer surface.

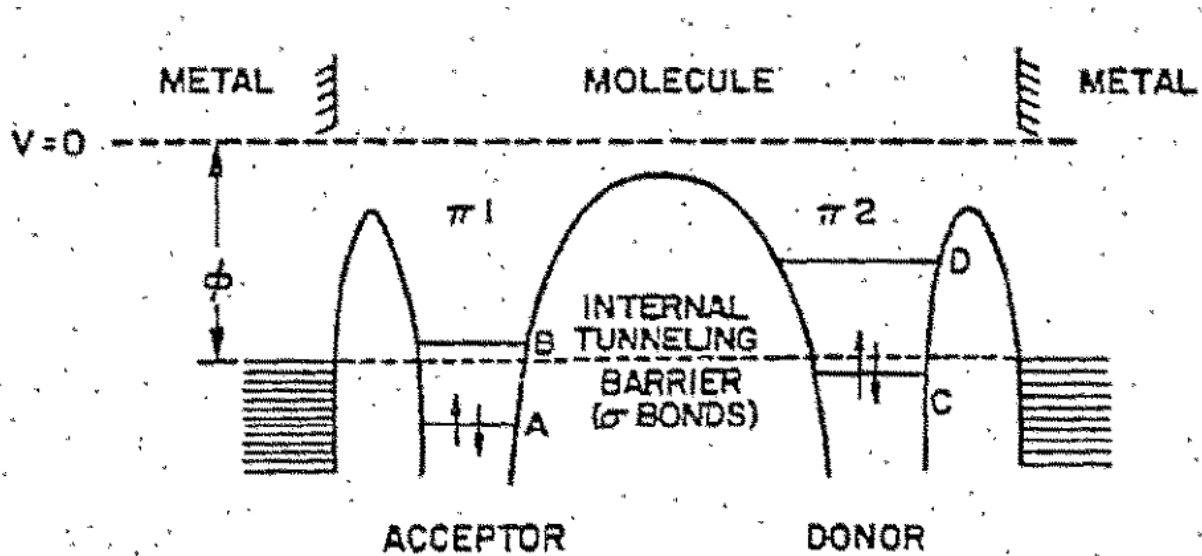


Figure 1.10. Schematic of the molecular orbital distribution from AR.¹⁰ © 1974 North-Holland Publishing Company.

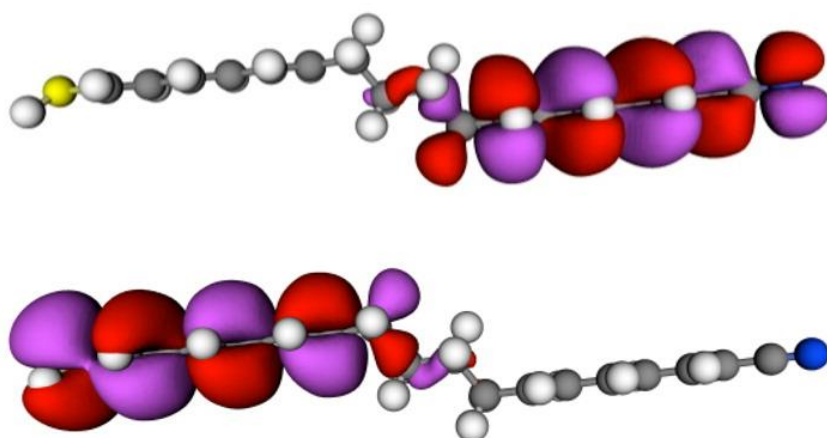
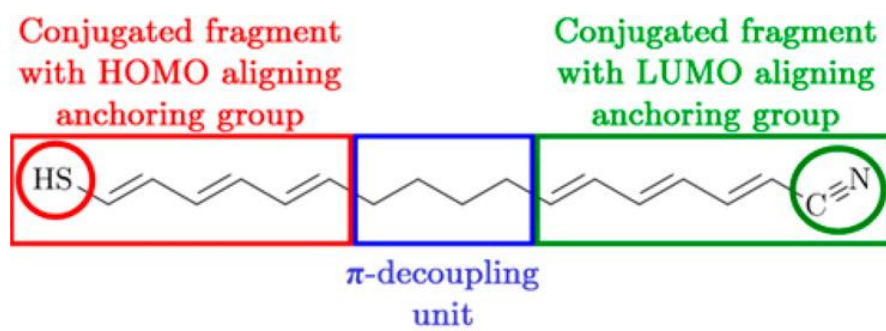


Figure 1.11. Example of FMO spatial separation in a Van Dyck and Ratner⁴⁵ molecular diode. The HOMO (bottom) and LUMO (top) do not share strong overlap and the excited state would follow the $D^+ - \sigma - A^-$ zwitterionic state. © 2015 American Chemical Society

All of the previously stated design considerations, in addition to specific knowledge about the compound in question, must be taken into account when looking to develop a new molecular rectifier. The goal of this dissertation was to design, synthesize, and analyze a new molecular system in order to determine whether the torsion angle between a phenyl ring donor and quinone ring acceptor can act as the insulating bridge. A molecularly rigid molecule that self-assembles via two nitrile contacts to the gold surface was synthesized, deposited on gold, and the conduction traces show evidence of rectification. These molecules are based off of a backbone of 2-bromo-5-(4'-bromo-2',5'-dimethoxyphenyl)cyclohexa-2,5-diene-1,4-dione, or hemibiquinone (HBQ) for short.

Several other HBQ derivatives were also synthesized on the way to creating a functional device, and experimental validation of their predicted properties is presented. Estimates of the HOMO and LUMO levels are presented in solution, as determined by cyclic voltammetry and compared to isolated donor and acceptor molecules. HOMO–LUMO gap values are determined in solution by UV–Vis spectroscopy, and correlated as well to the donor and acceptor components. Commentary on the tuning of the specific energetics for the HBQ molecules as a function of the 4-quinoid anchor group is presented, discussing the electron-donating and electron-withdrawing character of each substituent. Crystal structures of appropriate molecules are presented.

CHAPTER 2

DESIGN AND THEORY

The focus of this work rests on the suitability of biphenyl-based molecules as molecular rectifiers. The crux of this issue involves whether the twist between the aromatic rings can act as an insulating bridge component in a D— σ —A device. Knowledge about the geometry of the molecules and the distribution of their molecular orbitals underpin the understanding of why these diodes do or do not work. Especially important is knowledge about the torsion angle between the ring planes, as this is the defining electronic barrier in our system. As excess thermal energy through joule heating is a contributing factor within actual systems, commercial operational devices will need to consider torsional energy barriers and phonon interactions with conduction efficiency, but that is a discussion beyond the scope of this project.

Discussed in detail within the previous chapter, information about where the frontier molecular orbitals (FMOs) lie in both space and energy is necessary in order to predict and interpret results obtained from experiment. The relative potential energies of these molecular orbitals are tied into the optical and electronic properties of the molecules, which affect both the spectral characteristics as well the electrochemical behavior of the molecules within an assembled circuit.

As will be shown, the absolute potential energy and distribution of these orbitals in space, as well as the molecule's overall geometry, are dependent upon the molecular structure. The hemiquinone ring system shares many structural features of the related biphenyl system, especially the sterically induced twist away from a coplanar arrangement of the two

rings. However, oxidation of one ring to make a hemibiquinone greatly changes the electronic character of the molecule. Because benzene is a very weak electron donor, biphenyl is effectively a double donor (D—D) system. On the other hand, oxidation to the HBQ system converts the molecule into a donor-acceptor (D—A) system. The combination of structural and electronic features makes HBQs potential rectifying devices. Reduction of the quinone ring of an HBQ regenerates the biphenyl-like system. This switch in the electronic character of the HBQ and hydroquinone are evident from the examination of the orbital eigenvalues (shown below).

Section 2.1 Biphenyl and its Geometry

Section 2.1.1 Unsubstituted Biphenyl

Biphenyl ($C_{12}H_{10}$), or phenylbenzene, is a simple molecule easily drawn as a planar structure but naturally exists in a nonplanar conformation (Scheme 2.1). The energy stabilization from extended conjugation through the π molecular orbitals is maximized when the rings are coplanar ($\theta = 0^\circ$) and reaches zero when the ring π -systems are orthogonal ($\theta = 90^\circ$).⁵⁷⁻⁵⁹ However, steric repulsions between atoms on the peripheries of the aryl rings are maximized with coplanar rings and fall off as increasing torsion angles move substituent atoms further apart. The twisted conformations balance these two features.⁶⁰ Many experiments have been performed to determine the ring torsion angle between the rings for pure biphenyl.⁶⁰⁻⁶² Absorption spectroscopic studies show a shift attributed to conjugation of the π -systems of the two rings.^{63,64} The torsion angle between the rings of an unsubstituted biphenyl has been determined in gas-phase electron diffraction experiments as $44.4^\circ \pm 1.2^\circ$, indicating a nearly equal weight between steric and electronic effects.⁶⁵ This diminished overlap, or decoupling, creates a tunneling barrier whereby electrons are no longer delocalized about the structure.

Section 2.1.2 Substituted Biphenyls

Altering the electron distribution around the ring causes additional attractive and repulsive effects to contribute to the minimum energy structure. A perfect illustrative example of this tradeoff between steric repulsion and extended conjugation is shown by the increasing torsion angle corresponding to the increasing halogen size for a series of 2,2'-bihalogenated biphenyl molecules.⁶⁵ Unsurprisingly, an increase in *ortho*-substituent size also leads to an increase of the rotational barrier energy necessary to rotate about the 1,1'-biphenyl bond.

For 4-substituted (*para* to the 1,1'-biphenyl bond) biphenyls,⁶⁶ as well as for 4,4'-disubstituted biphenyls isomers,⁶⁷ there is some evidence that the biphenyl torsion angle is affected by resonance contributions,⁶⁶ but the overall effect of this distortion on the system is small compared to the steric effects of *ortho*-substituents.⁶⁷ The question is, then, can the lowest-energy conformation be of predictive value, when considering the degree of interplay between the two separate π -systems along the length of the molecule?

Section 2.2 Conduction through Substituted Biphenyl Derivatives

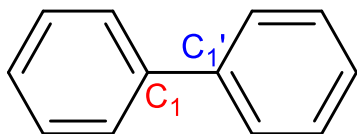
Vekataraman *et al.*²⁵ published a paper tying molecular conduction to the calculated lowest-energy torsion angle θ in a series of amine-terminated biphenyl systems. They showed a linear correlation between the $\cos^2(\theta)$ of the torsion angle θ and the statistical maximum conductance value through the molecule. Conductance at the minimum-energy conformation is determined from the center of a Gaussian distribution within the histogram plotting counts with respect to conductance.²⁶ Various substitution patterns controlled the equilibrium geometry of the molecules (Figure 2.1, Figure 2.2 [left]). Li, Mishchenko, and Wandlowski²⁹ reviewed the conductance of single-molecule biphenyl junctions in 2012 (Figure 2.2[middle, right]). They focused on symmetrically disubstituted biphenyl-dithiols and biphenyl-dinitriles, and how

controlling the torsion angle through substitution of saturated carbon side-chains affects the conductance. They report similar conclusions to Venkataraman. Through the various substituted biphenyl molecules, the conduction histogram maximum correlated to the $\cos^2(\theta)$ of the lowest-energy torsion angle. These conductance histograms were constructed because molecules in the break junction are free to rotate about the 1,1'-biphenyl bond in solution while the break junctions are being formed, and the geometry of a molecule within a single measurement greatly affects the junction conductance.

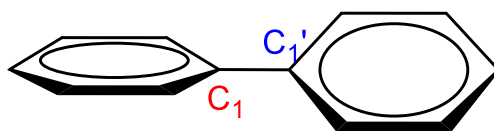
The authors note a dependence on anchor groups for the absolute conductance, thiols being a factor of ten more conductive than the corresponding nitrile.²⁹ This result agrees with the general consensus that anchor groups affect conduction efficiency through the combination of FMO eigenvalue perturbation, contact geometry, and coupling strength to the electrodes.^{12,29}

Scheme 2.1

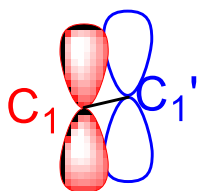
A



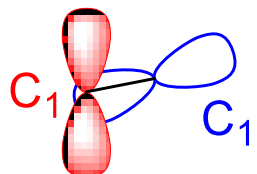
B



C



D



A) Planar representation of biphenyl. B) Better representation of biphenyl's inherent twist. C) Atomic orbital alignment looking down $C_1-C_{1'}$ bond if (A) were the true structure. D) Atomic orbital alignment looking down $C_1-C_{1'}$ bond with an inherent torsion angle.

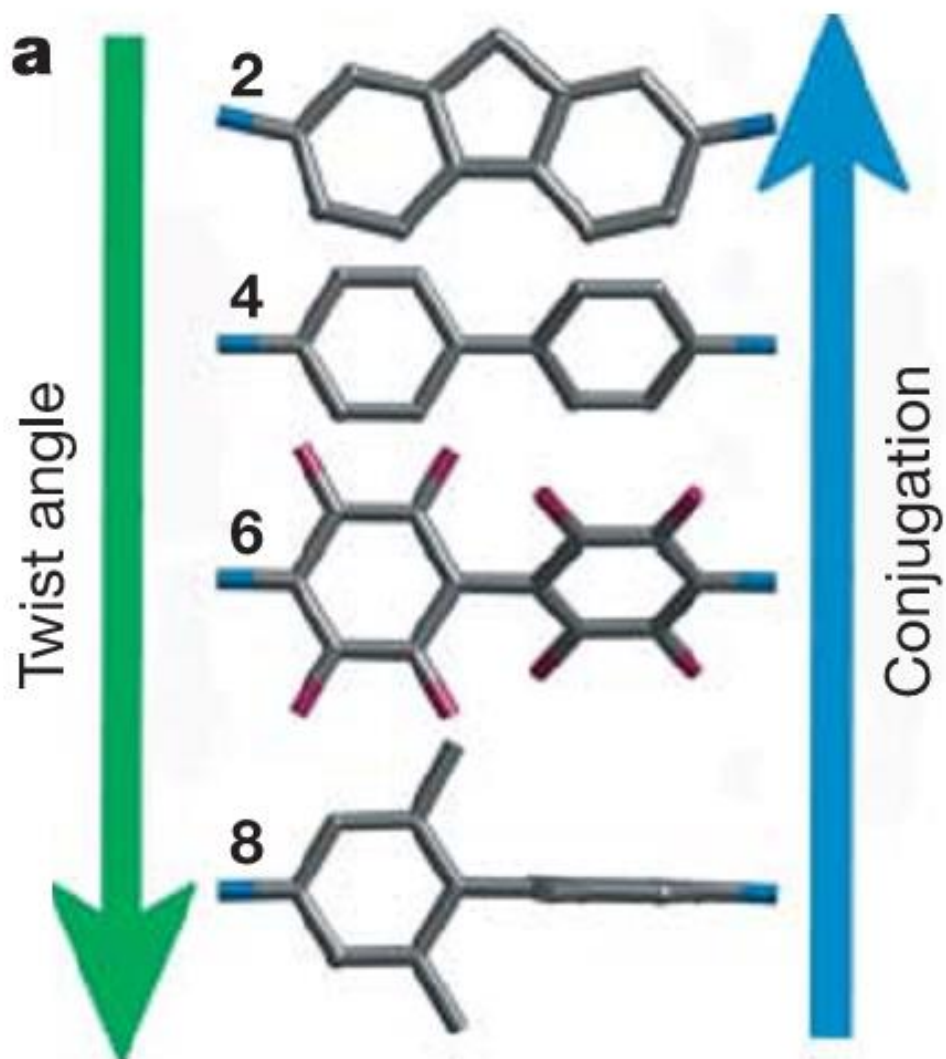


Figure 2.1 A subset of the molecules tested in Venkatamaran *et al.*²⁵ illustrating the stepwise increase in ring torsion. © 2006 Nature Publishing Group

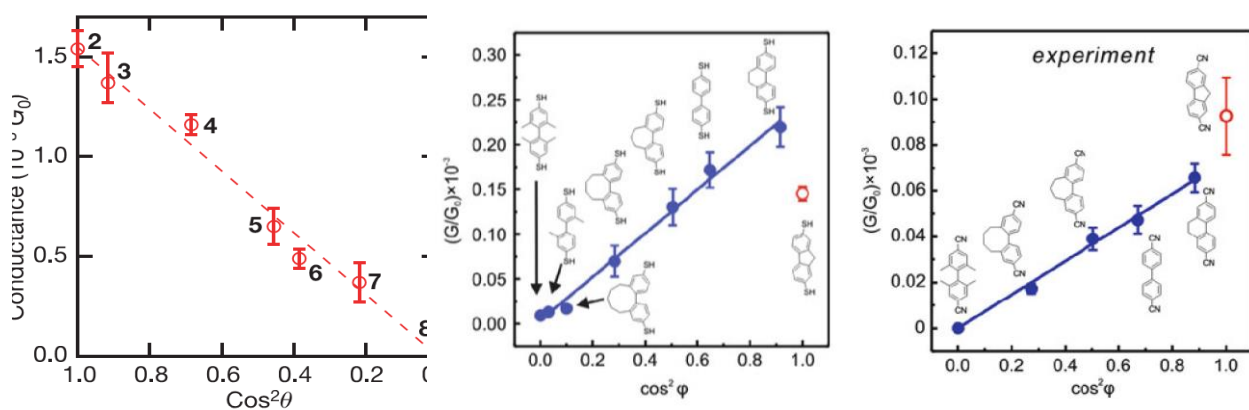


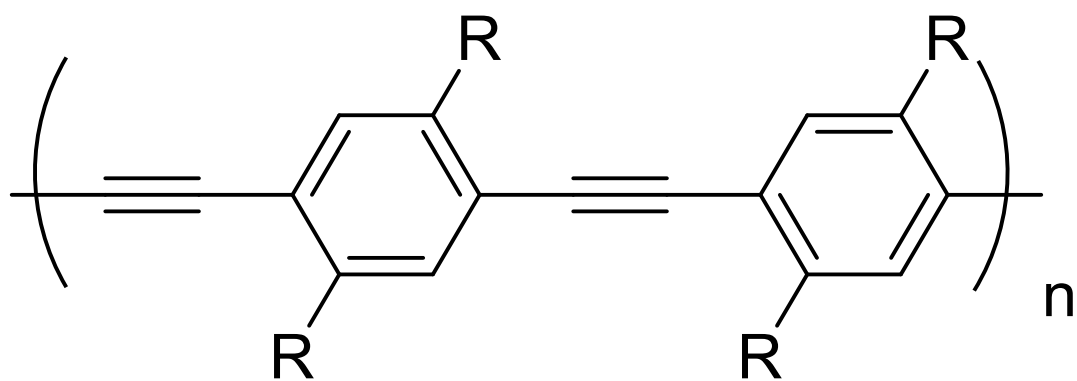
Figure 2.2 Conductance values with respect to torsion angle. As the equilibrium angle θ increases for a set of biphenyl molecules, the conductance across that molecule with respect to the $\cos^2(\theta)$. (Left) Amino-terminated biphenyl MCBJs. Adapted from Venkataraman *et al.*²⁵ © 2006 Nature Publishing Group (Middle) Thiol-terminated biphenyl MCBJs. Adapted from Mishchenko *et al.*^{27,29} © 2010 American Chemical Society (Right) Nitrile-terminated biphenyl MCBJs. Adapted from Mishchenko *et al.*^{28,29} © 2011 American Chemical Society

Section 2.3 Conduction through Other Molecular Backbones

A 2000 IEEE paper from Ellenbogen and Love²⁰ described molecular electronics from the electrical engineer's design perspective. For example, "Tour wires" (Scheme 2.2) have high conductance due to full conjugation along their length achieved by acetylene units linking phenyl rings together. Acetylenes reduce steric repulsion between the rings, such that it is no longer a contributing geometric factor ($\Delta E_{\text{rot}} \lll kT$). Electronic and physical properties of ethynyl linkers are well known and have been tested in numerous iterations of molecular electronic devices.^{11,53,56,68-77}

Despite the plentiful data available for molecules on a surface, there is still some question about the preferential geometry adopted by molecules within a packed monolayer. A report published by Abu-Husein *et al.*⁷⁸ and a reference contained therein by Liu *et al.*⁷⁹ contain conflicting accounts about the nature of oligophenylenes (of which biphenyl molecules are a subclass) within a monolayer. Abu-Husein *et al.*⁷⁸ assert that the rings lie flat to pack closely with one another and form good monolayers. This would mean that biphenyl molecules overcome steric repulsion through maximized face-to-face interactions (π -stacking). This assumption contradicts the understanding that parallel face-centered stacking is higher in energy than both parallel offset stacks, and perpendicular T-shaped interactions.⁸⁰ On the other hand, Liu *et al.*⁷⁹ report that monolayers are much less closely packed with noncoplanar rings. Further studies to determine monolayer surface geometry of basic molecular electronic backbones are necessary to better understand the correlation between monolayer conductance and the rotationally static packed monolayer.

Scheme 2.2 An example poly(p-phenylene-ethynylene) (PPE) Tour Wire.



In a series of theory papers on so-called “diblock molecular rectifiers,” there has been some investigation about the effect of both torsion angle and end-group substitution on the rectification ratio for pyrimidinyl-phenyl derivatives.^{39,40,46,81-83} The diblock moniker is a reference to two-sectioned (hence diblock) co-oligomers or copolymers in other electronic applications. All of the work so far on diblock molecular diodes focuses around calculating the rectification ratio (RR) through polyheterocyclic systems.^{39,40,50,75,82-85}

From Zhang *et al.*,³⁹ asymmetry in the binding group (“alligator clip”) choice has a greater effect on the rectifying ability of a low polarity system like the dipyrimidinyl-diphenyl set-up. There was a high amount of spatial overlap between the HOMO and LUMO of the molecule. The authors mention this affects the RR because localization of an orbital on one portion of the molecule allows that orbital to move more easily in energy with the electrical sweep. In other words, orbital energies will more easily rise with the electrode at one polarization and rise much less with the opposite polarization.¹⁸ This is akin to asymmetric-type rectification. Additional orbital polarization occurs under bias and must be taken into account within highly delocalized systems.⁸⁶ This bias-dependent evolution of MO energy is physically similar to the way density of states (DOS) shift as a system is calculated at increasing applied potential differences.¹⁸

El-Hendawy *et al.*⁸³ determine the conduction and rectification through oligomeric systems based on poly(p-phenylene ethynylene) four wires (Scheme 2.2, left). They aim to find out which molecular properties (torsion angle, polarity, junction binding strength, junction geometry) may be systematically adjusted to maximize the RR for a particular set of similar systems. A molecule’s core,³⁷ its electrode attachments,^{39,50} and the efficiency of isolation separating the electroactive components⁸⁴ all play a part in how effective a particular rectifier will be. Dipyrimidyls and substitutions therein are reported to have different RRs. Thiophenes

and thiazoles have also been modeled in an effort to demonstrate that strongly coupled FMOs can still rectify but operate under an (unspecified) alternative rectification mechanism to the unimolecular mechanism.⁸⁵

El-Hendawy *et al.*⁸³ mention that the polarity of a molecular rectifier will influence its RR as an electric field local to the junction will affect nearby electron eigenvalues. They show that the highest polarity configuration for the tested oligomers of interest occurs when all rings are coplanar with respect to one another. This would be absolutely useless for a) real molecules with steric strain and b) using the torsion angle as the decoupling mechanism between electroactive species, as the molecular orbitals are completely delocalized over the entire structure. Refs 14 and 15 in that paper discuss findings tying polarity to RR. Jiang *et al.*^{87,88} assert that polarity of the molecule, and thus of the overall junction, is a dominant characteristic governing electron flow through the junction. Polarity values for Liu's heterobiphenyl were not reported. Stadler³⁸ disagrees with El-Hendawy *et al.*, asserting that molecular dipoles play a smaller role in rectification than is usually assumed. He asserts that the more important property behind a strongly polarized molecule is the overlap of the FMOs with an electrode. That way, the FMOs eigenvalues will shift most efficiently with an applied electric field (called Fermi pinning). Poorly coupled electrodes will not shift as strongly, leading to asymmetric rectification.

Section 2.4 Molecular Orbital Isolation Requirements

Determining how individual electroactive segments connect will, in the future, become an important design parameter for useful molecule-scale circuits. At present, each molecular device in a circuit needs to be "hardwired" to a conducting surface.^{33,89,90} Often, these conducting surfaces are made from nanoscale metallic structures. Interpolating nanometallic contacts at

every junction between components would be a cost and geometry-limiting factor in commercial devices.

In addition to understanding how atoms arrange themselves in the molecule, it is important to address how the molecular orbitals most likely to be active in a device are distributed. It has been the traditional view in the field of molecular electronics that a saturated carbon bridge is required to effectively separate D's MOs from A's (Scheme 2.3, left).

In 2002, Stokbro *et al.*⁵⁸ published “Do Aviram-Ratner Diodes Rectify” in which he investigates the evolution of the density of states (DOS) as bias is introduced to a D— σ —A molecule assembled within a junction. Using a molecule proposed in the earlier paper by Ellenbogen and Love,²⁰ Stokbro *et al.*⁵⁸ calculated that the molecular orbitals associated with conduction through the junction are isolated on the donor or acceptor portions of the molecule. When a bias is placed on the system, certain voltages create resonant states where molecular orbitals align in energy. The authors note that, at these resonant states, the molecular orbitals delocalize over the whole molecule and there is a drastic increase in current that flows through a molecule.

However, Stokbro *et al.*⁵⁸ did not report rectification in this calculation, which they attribute to symmetric alignment of the Hamiltonians under bias (which leads to symmetric conduction). In other words, the potential energies of the molecular orbitals shift symmetrically from the applied potential. Closer analysis of bias-dependent RR does display some current asymmetry, in the range of 1.5–3 V. Stokbro *et al.* probably expected much greater RRs. The authors mention that the HOMO–LUMO gap of this particular molecule is high, and propose that a smaller gap may lead to favorable transport and rectification characteristics. The motif of calculating MO energy perturbations under bias is a useful and reasonably simple method to screen for molecules

that are being considered as potential rectifiers.^{45,58,91,92} The authors conclude that theoretical evaluation of rectifier candidates is an effective first step in the development of a successful device.

Recently, Van Dyck and Ratner⁴⁵ published a study in which an asymmetric D— σ —A molecule is made of two sections of n-hexatriene separated by an insulating n-butane bridge. Donor and acceptor portions in this molecule were only differentiated by their respective binding groups, a thiol D and a nitrile A. They demonstrate that electronic asymmetry induced by the molecule's anchoring groups was sufficient to localize the HOMO and LUMO on different sides of the molecule, while keeping the core backbone and electrode surface constant. This, they calculated, could lead to rectification ratios over 150. While such polyenes would probably not be very stable,⁹³ this still demonstrates that so-called “strong” D or A may not be necessary to produce a significant rectification result.

It is also important to note that the Van Dyck/Ratner molecule is predicted to conduct in the opposite direction to the Aviram and Ratner unimolecular mechanism (Figure 2.3). Figure 2.4A shows a schematic for FMOs of the molecule in Figure 2.3 in the gas phase, as compared to the Au band structure. Figure 2.4B illustrates when the molecule is attached to the gold, partial charge equilibration perturbs the FMO eigenvalues: E_{HOMO} raises and E_{LUMO} decreases. When there is an applied potential, as in Figure 2.4C, this leads to a non-conductive state as FMOs do not come into resonance. Rather, forward conduction occurs when the FMOs come into resonance ($E_{\text{LUMO}} - E_{\text{HOMO}} \approx 0$ eV, Figure 2.4D).

Metzger¹⁶ notes that all tested rectifiers thus far conduct preferentially opposite to AR. The determination of molecular geometry, FMO distribution, and FMO perturbation are critical for evaluating candidates for molecular electronic devices under bias.

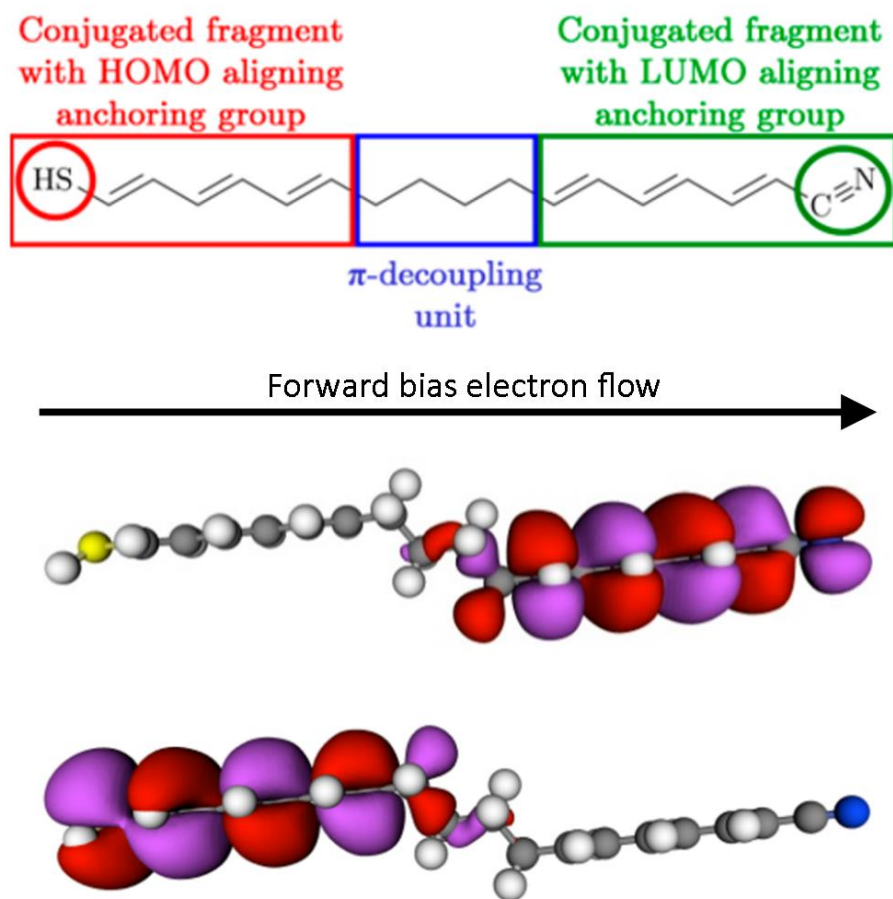


Figure 2.3 Molecule calculated within Van Dyck and Ratner.⁴⁵ Note that Forward bias electron current is opposite of AR direction. © 2015 American Chemical Society

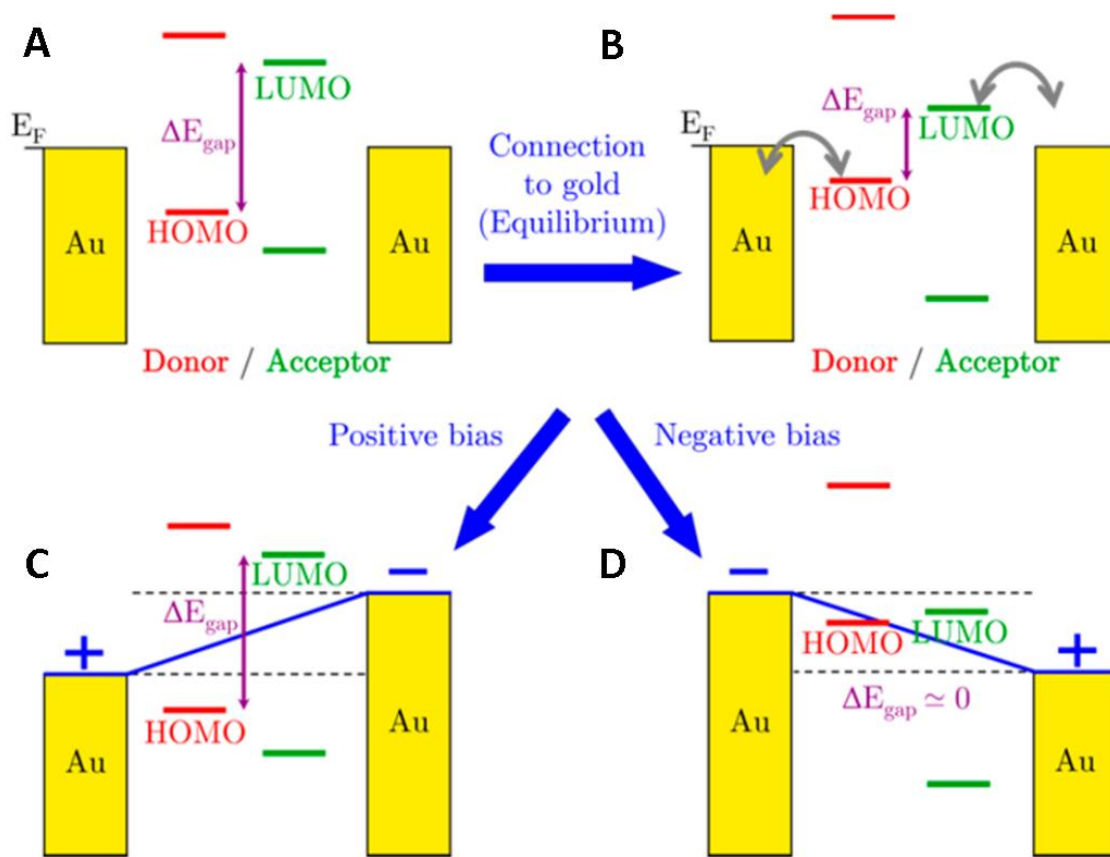


Figure 2.4 Orbital eigenvalue evolution adapted from Van Dyck and Ratner.⁴⁵ © 2015 American Chemical Society

Section 2.5 Hemibiquinone Calculation Results

In order to make reasonable predictions about the behavior of HBQs in electrical systems, one needs to determine its fully optimized structure. Density Functional Theory (DFT) calculations using Gaussian09⁹⁴ were performed on an unsubstituted HBQ molecule (Scheme 2.3) to guide optimization parameters. B3LYP^{95,96} functional with a DGDZVP2⁹⁷ basis set for light atoms (C, H, N, O) was selected. For substituted systems that included bromine, a DGDZVP basis set was used. Only 4-substituted HBQ derivatives were originally considered for synthetic targets, which is why they are the ones presented.

Section 2.5.1 Molecular Geometry Energy Minimization

Single-point calculations were performed on 10° incremental rotations to plot the molecule's energy around the 1,1'-biphenyl bond (Figure 2.5). This calculation of molecular energy with respect to the dihedral angle was used to guide the optimization process of several HBQ derivatives whose results are presented in Table 2.1. There are four local minima about the full 360° rotation, including the global minimum; the planar conformations were obviously of higher energy. The lower energy “*trans*”-planar configuration is defined as 0°, and the higher energy is defined as “*cis*”-planar 180° (Scheme 2.3). The *trans*-planar configuration sits about 6 kcal/mol above the global minimum, which exists around 40°. From there, a local maximum appears at 90°, 1.8 kcal/mol above the minimum. Another local minimum appears at 110°, 1.2 kcal/mol above the global minimum. The graph is plotted in kcal/mol relative to the global minimum. The curve is roughly symmetrical about $\theta = 180^\circ$ and rises very steeply for $130^\circ < \theta < 230^\circ$.

Evidence from the crystal structures^{98,99} demonstrates that rotation of the molecule about the central bond can pass through the planar conformation. At room temperature, the molecule is unlikely to rotate through the *cis*-planar high-energy conformation. NMR spectra (see Chapter 3)

of the HBQ molecules only show a single rotamer, so all angles between $\pm 110^\circ$ must be accessible at room temperature. If different rotamers were distinguishable in solution at RT on the timescale of the experiment, then the NMR spectrum would be more complex. As it is, all of the rotational possibilities are averaged out at RT.

Crystal structures (see Chapter 4) of HBQ molecule also show only one rotamer present, which must be energetically favored in the crystal lattice. Information about the packing interactions within the lattice, however, cannot be directly applied to intermolecular interactions in the monolayer. In the lattice, molecules packed centrosymmetrically, with intermolecular D \cdots A π -interactions dominate the packed structure. Information on the solid-state interactions is found in Chapter 4. In a monolayer, the molecules would all be oriented in the same direction and without the dipolar interactions.

Due to the increased steric burden on the rings imposed by oxygen with respect to hydrogen, the barrier of rotation for HBQ is slightly higher than barriers previously reported in the literature for biphenyl.^{100,101} While the biphenyl molecules rotate with a barrier of rotation $\leq kT$ at 300 K about the C—C inter-ring bond, HBQ molecules have less freedom due to the *ortho*-substituted oxygen atoms. The HBQ derivatives all had very similar geometrical energy minima, with an average torsion angle of $38.6 \pm 1.1^\circ$ amongst all of the derivatives tested (Table 2.1). Campanelli⁶⁶ reported that there is a slight correlation between the 4-substituted group and the precise torsion angle of a biphenyl system. The variation in exact minimum geometry is attributed to polarization of, and resonance with, the π -clouds of the structure. Campanelli⁶⁶ found that charged substituents affected the twist angle the most, although strongly π -donating or π -withdrawing substituents also had prominent effects on the structure.

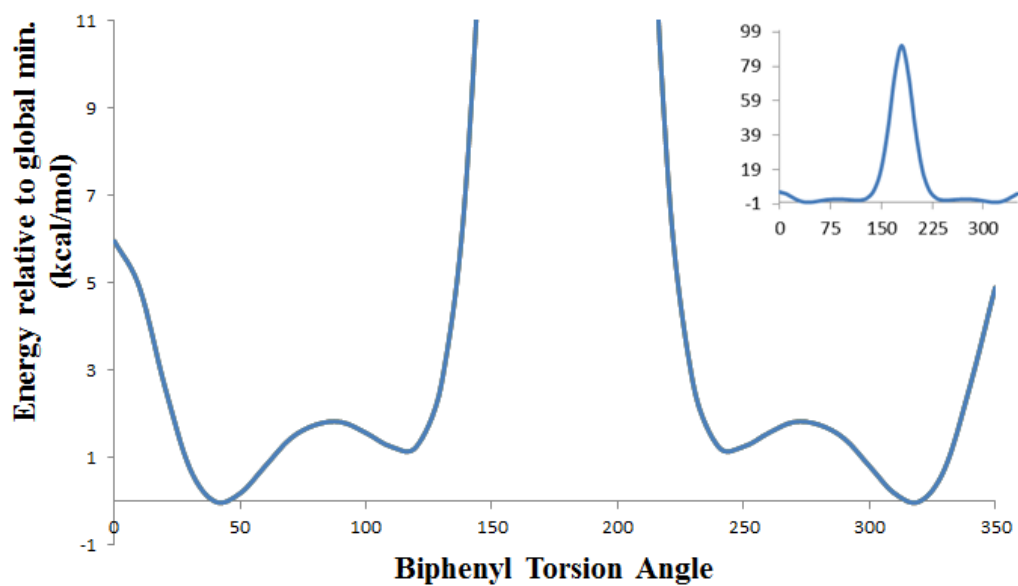
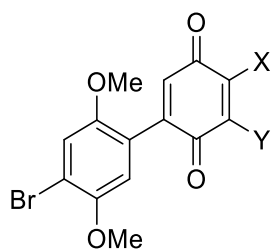


Figure 2.5 Detail of total calculated DFT molecular energy of HBQ versus torsion angle θ . The zero of energy is chosen at the global minimum ($\theta = 40^\circ$) *Inset*: Detail of the energy maximum (abscissa: degrees; ordinate: relative energy (kcal/mol)).

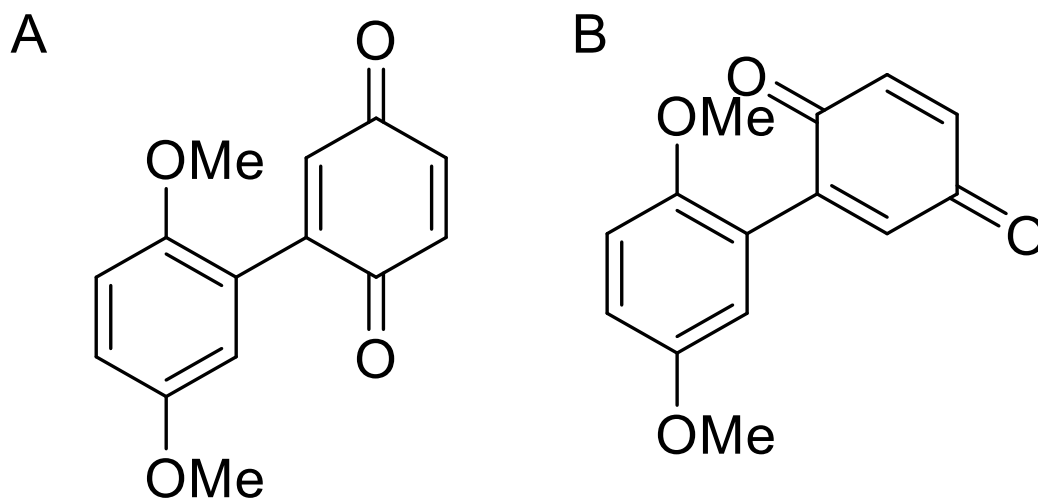
Table 2.1 Calculated molecular and electronic properties for the HBQ series. Dipoles reported at optimized structure



X	Y	Torsion Angle (°)	Dipole (D)
Br	H	38.54	1.33
N₃	H	36.41	1.35
NH₂	H	37.21	2.85
NHMe	H	39.70	3.90
NHAc	H	38.75	3.11
NHC(=O)PhH	H	38.70	3.99
NHC(=O)PhCN	H	37.95	3.87
NHC(=O)Py	H	38.58	1.92
NHC(=O)H	H	37.46	3.11
SH	H	39.69	1.21
SAc	H	38.34	3.92
isoNC	H	38.44	4.73
CN	H	39.49	5.34
COOH	H	36.74	6.01
Br	Br	41.05	1.71
CN	CN	39.71	7.79

Ph = phenyl, Py = pyridine

Scheme 2.3 *Trans*-planar (0° , A) and *Cis*-planar (180° , B) forms of the HBQ backbone.



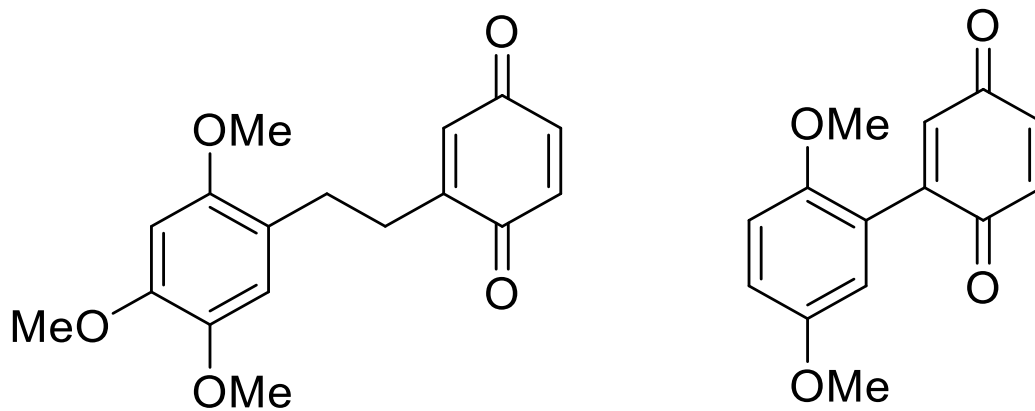
Section 2.5.2 Molecular Orbital Distribution

It is from the linked concepts of orbital localization and conjugation interruption that the HBQ backbone was hypothesized to act as a single-molecule rectifier. The HBQ molecule is reminiscent of a theoretical rectifier proposed in the seminal 1974 Aviram and Ratner¹⁰ (AR) paper (Scheme 2.4, left). The key differences are the elimination of the ethylene saturated bridge, and the addition of anchor groups for self-assembly. In AR, saturated carbon atoms between the rings disrupt conjugation of the π -orbitals, and allow for localization of the FMOs onto one ring or the other. In HBQs, the biphenyl-like structure would afford the molecule a naturally nonplanar structure (and thus the required break in conjugation for a functional bridge) while the electronic asymmetry of the dimethoxybenzene ring, compared to the quinone ring, might afford the molecular orbital alignment in a D— σ —A rectifier.

Minimized structures of several potential derivatives of the HBQ backbone were calculated in Gaussian09 (Section 2.5.1), to determine their physical and electronic properties. These results were then compared against an optimized AR molecule. The minimized energy structure of the AR molecule was achieved through similar OPT+FREQ parameters in Gaussian09, and no geometry was constrained.

Illustrated in Figure 2.6 are the FMOs of the AR molecule. In it, the planes of each ring are rotated orthogonally to one another. It is clear that the orbital probabilities are localized on a given ring—the HOMO resides entirely on the dimethoxybenzene ring, and the LUMO resides entirely on the quinone. This illustrates perfectly the idea that FMOs be spatially separated, as there is no orbital overlap on the interstitial saturated carbon atoms. Similar behavior is seen in Table 2.2, where the FMOs of BrHBQBr are displayed. See the Appendix for other derivatives. From this data, selected molecules would become synthetic targets as molecular diodes to test.

Scheme 2.4 The 1974 AR Molecule ¹⁰ (Left) vs. The HBQ backbone (Right)



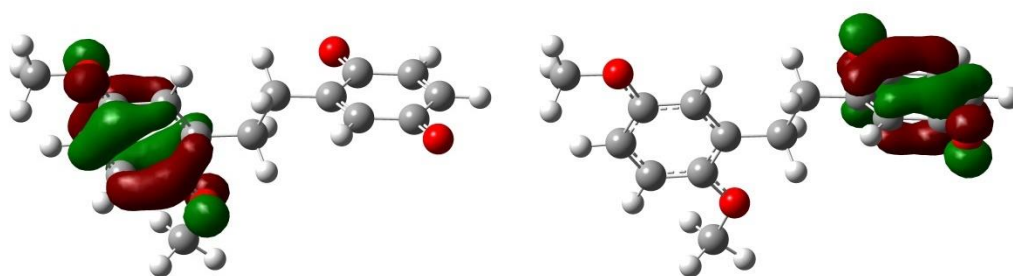


Figure 2.6 The HOMO (left) and LUMO (right) of the AR molecule at optimized geometry.

Table 2.2 The HOMO (left) and LUMO (right) of the parent HBQ Backbone through various torsion angles.

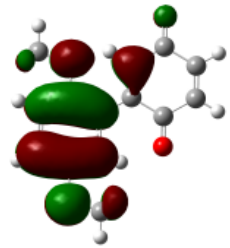
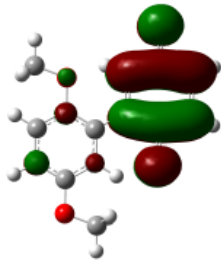
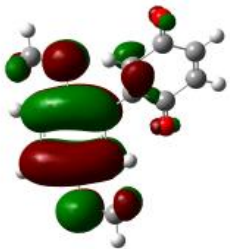
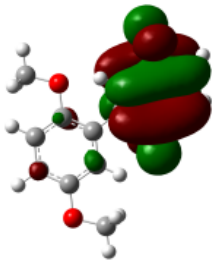
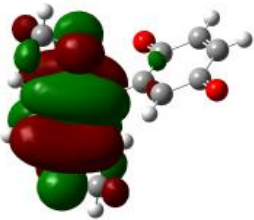
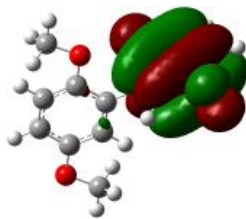
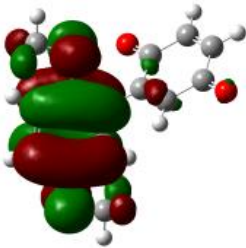
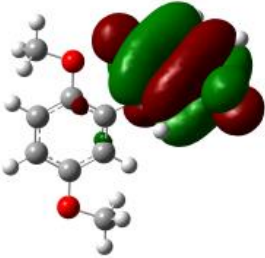
Torsion Angle	HOMO	LUMO
0°		
40°		
90°		
110°		

Table 2.2 (cont.) The HOMO (left) and LUMO (right) of the parent HBQ Backbone through various torsion angles.

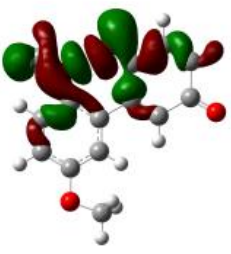
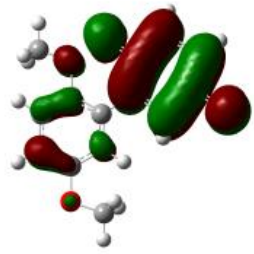
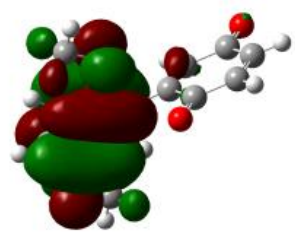
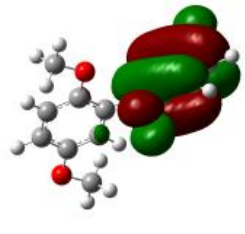
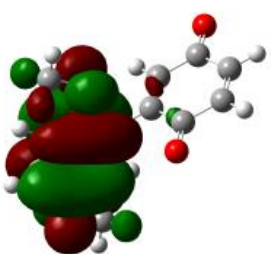
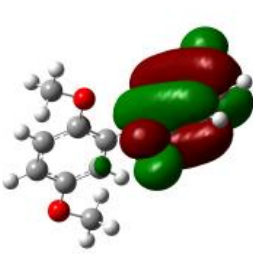
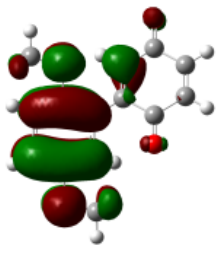
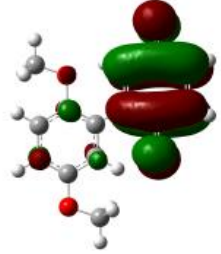
Torsion Angle	HOMO	LUMO
180°		
250°		
270°		
320°		

Table 2.2 displays the distribution of FMOs with respect to the torsion angle between the ring planes. The angles displayed are either maxima (0° , 90° , 180° , 270°) or minima (40° , 110° , 250° , 320°) from Figure 2.5. As expected from orbital geometry considerations, the planar conformations contain the greatest delocalization of electron density across the structure, while the orthogonal structures (90° , 270°) have the greatest measure of localization on each ring. Intermediate conformations have some balance between the two extremes. The minimum energy conformation ($\theta = 40^\circ$) has some delocalization apparent in the FMOs, but to a much lesser degree than the planar structures. The dependence of orbital localization on torsion angle is a result consistent with the concept of orbital overlap decrease, as outlined in Sections 2.2 and 2.4. This result should provide confidence that the donor and acceptor are sufficiently isolated without the use of a saturated carbon bridge within the structure, further allowing for a reduction in device size and complexity.

Section 2.5.3 Molecular Orbital Eigenvalues

Section 2.5.3.1 Molecular Orbital Eigenvalue Dependence on Geometry

Mapping the orbital energy levels against torsion angle, there is very little change overall until the torsion angle is between 150° and 310° (Figure 2.5). The HOMO shifts up 1.28 eV, and the LUMO shifts up 0.31 eV. Considering the unlikely possibility for the molecule to rotate to these high angles as discussed above, these rotationally-induced shifts in the FMO energies should not influence charge transport by the molecule within a device.

Zhang and Musgrave¹⁰² found that HOMO energy values are mostly dependent on the functional chosen, and less on the basis set. Even with DFT, the absolute molecular orbital energy as calculated is not a good indicator of the true energetic values that correlate with the ionization potential and electron affinity.¹⁰² These values must be found experimentally, and

calculated values are reported here with only qualitative confidence. While beyond the scope of the present work, more quantitative analyses of HOMO and LUMO transitions can be determined using time-dependent DFT methods.¹⁰²

Section 2.5.3.2 Substituent Dependence of Molecular Orbital Eigenvalues

Information from this study was used to determine the suitability of synthetically accessible HBQs in device applications. While thiols and thioacetates are ubiquitous anchor groups for self-assembly, maximizing the electron flow in one direction is believed to be most efficient when a low-lying LUMO is readily accessible for rapid charge injection from the electrode. Table 2.3 lists the DFT-calculated FMO levels for a series of HBQ derivatives. Values are reported as those generated for the optimized structures.

HOMO values are somewhat affected by quinoid anchor group choice, and span a 0.79 eV range. BrHBQNH₂ has the highest-lying potential energy and BrHBQCN has the lowest-lying potential energy. These results can be rationalized using the idea that electron-donating groups, like amines, will raise the electron-density of the ring and, therefore, will raise the energy of those electrons in the system. Conversely, strongly electron-withdrawing groups (dinitrile, carboxylic acid) decrease the potential energy of the HOMO by withdrawing local electron density.

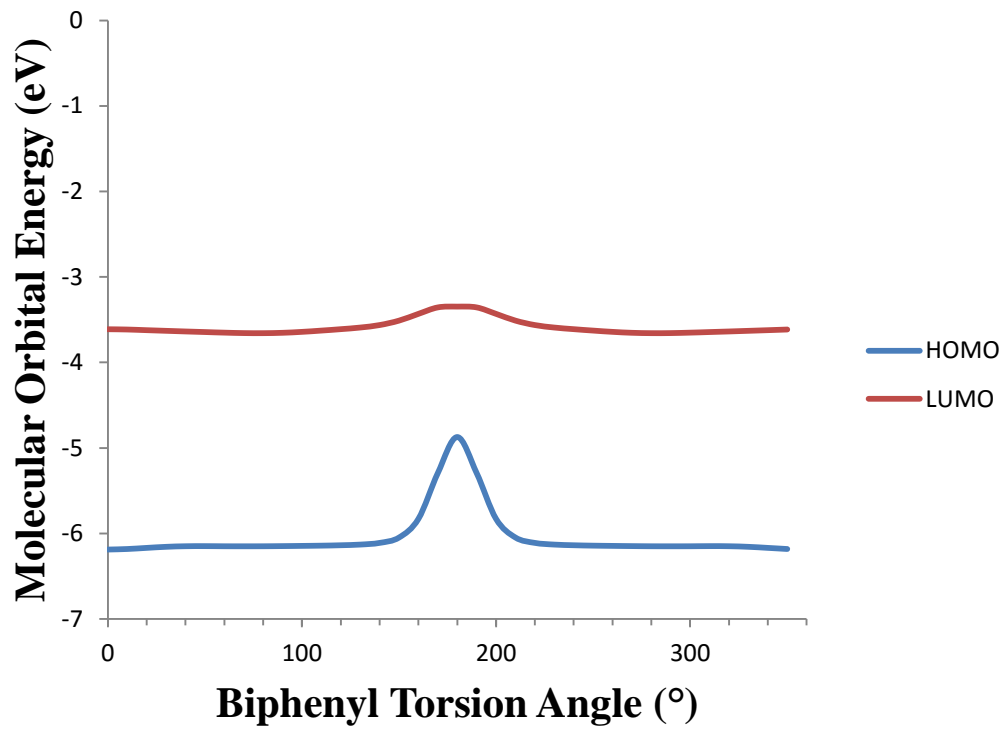
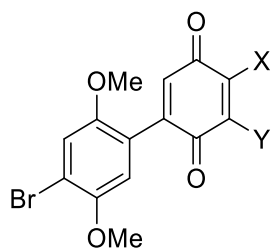


Figure 2.7 Molecular orbital energy with respect to the torsion angle. Any normally accessible geometry has essentially the same energy and thus the same HOMO–LUMO gap.

The calculated LUMO energies are more sensitive to substitution, showing a span of roughly 1.06 eV. The highest potential energies are found on the amino-substituted HBQs (BrHBQNH₂ and BrHBQNHMe). As before, the nitrile BrHBQCN has the lowest-energy LUMO owing to the especially electronegative nitrile group.

Following from these values, the methylated amine BrHBQNHMe has the highest HOMO-LUMO gap (2.83 eV) and the nitrile BrHBQCN has the lowest HOMO-LUMO gap (2.37 eV). This range of values should lead to significant differences in the absorption profile for any HBQ derivative. Localization of the HOMO on the dimethoxybenzene ring and localization of the LUMO on the quinone is the most likely explanation for the large difference in the eigenvalue ranges. If there were full conjugation across the structure, and the FMOs were entirely delocalized, then the polarization effects induced by each moiety would affect the FMOs equally.

These results informed synthetic efforts that the slightly more electron-donating thiol BrHBQSH and thioacetate BrHBQSAC were probably not ideal initial targets. Instead, the nitrile BrHBQCN was selected for both its ability to reliably self-assemble as well as maintain low FMO energies.

Table 2.3 Calculated FMO Levels by DFT

X	Y	HOMO (eV)	LUMO (eV)	HOMO-LUMO Gap (eV)
Br	H	- 6.17	- 3.93	2.24
N₃	H	- 6.16	- 3.88	2.28
NH₂	H	- 5.92	- 3.37	2.55
NHMe	H	- 6.12	- 3.28	2.83
NHAc	H	- 6.52	- 3.80	2.72
NHC(=O)PhH	H	- 5.96	- 3.54	2.42
NHC(=O)PhCN	H	- 6.19	- 3.88	2.30
NHC(=O)Py	H	- 6.05	- 3.72	2.34
NHC(=O)H	H	- 6.21	- 3.92	2.29
SH	H	- 6.44	- 3.73	2.71
SAc	H	- 6.23	- 4.05	2.18
isoNC	H	- 6.67	- 4.21	2.46
CN	H	- 6.71	- 4.34	2.37
COOH	H	- 6.41	- 4.45	2.16
Br	Br	- 6.22	- 4.03	2.24
CN	CN	- 6.91	- 4.87	2.03

Ph = phenyl, Py = pyridine

Section 2.5.4 Molecular Dipole

Section 2.5.4.1 Dipole Axes Definition

The total dipole moment of the HBQ backbone was plotted against the torsion angle. The dominant vector of the total dipole is in the x -molecular direction, aligned along the 1,1'-biphenyl bond (Figure 2.8). This is beneficial, as the electric field applied within a device will also be applied along the same vector. As discussed in Section 2.3, the molecular dipole arguably plays a part in junction conduction asymmetry, so enhanced RR from highly polar HBQ derivatives with respect to less polar derivatives is possible. This hypothesis extends beyond the scope of this dissertation and is presented in Chapter 6 as a future direction.

The z -axis is perpendicular to the xy plane formed by the dimethoxybenzene ring, the y -axis is in the same plane as the dimethoxybenzene ring but perpendicular to the 1,1'-biphenyl bond.

Section 2.5.4.2 Dipole Dependence on Torsion Angle

The dipole moments vary between 1 and 1.5 D with torsion angle within the low-energy geometries (Figure 2.8, purple). The x -directional dipole still does somewhat vary with the twist angle, but not nearly as greatly (Figure 2.8, blue). The difference between the x -vector and the total vector is made up in the contribution by the y - and z -directional vectors. The y -directional contribution begins to become more important as the quinone rotates toward the *cis*-planar conformation.

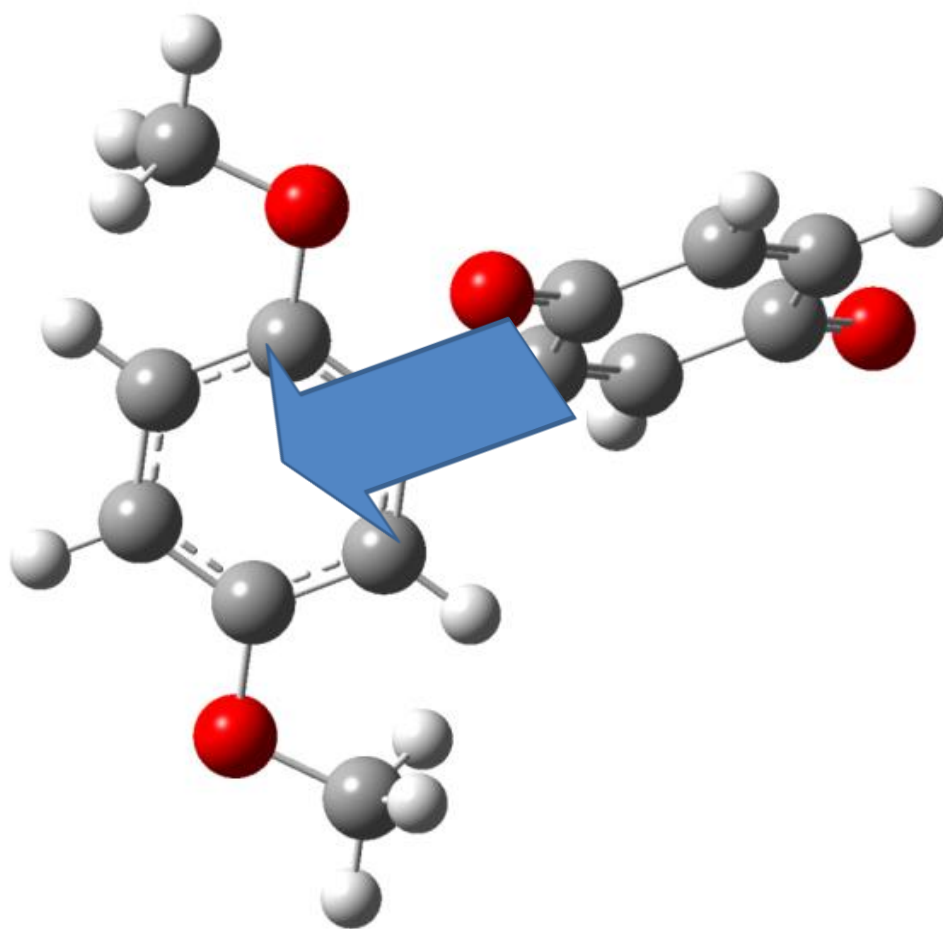


Figure 2.8 Example visualization of HBQ torsion angle calculation with corresponding dipole vector.

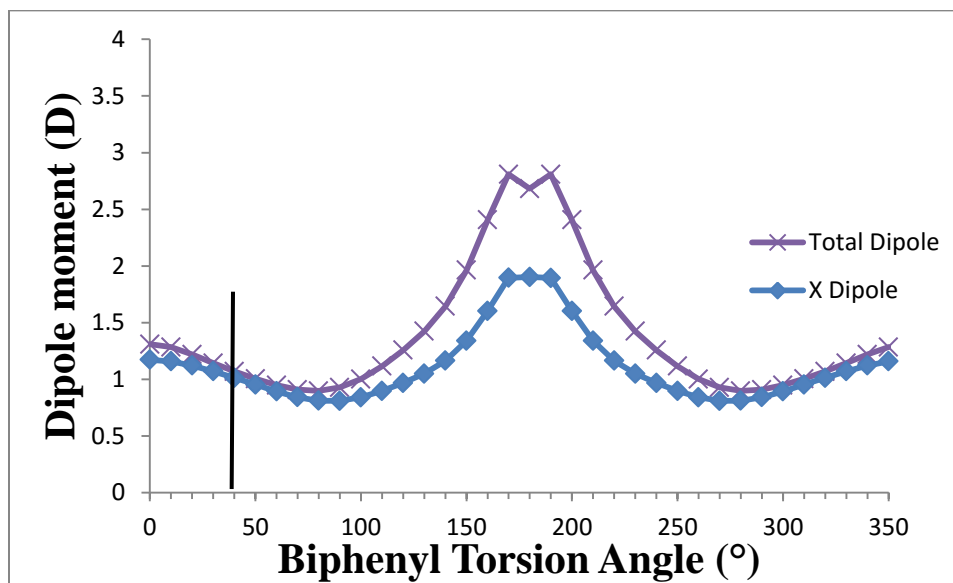


Figure 2.9 Dipole dependence on torsion angle. Purple: Total molecular dipole moment with respect to the torsion angle. Blue: x-directional molecular dipole moment with respect to the torsion angle. Black line: conformational minimum

Section 2.6 Acetylated Reduced Hemibiquinone

In the process of synthesizing a functional device (Chapter 3), direct substitution of the quinoid bromine was not always possible. Thus, the reactivity of the quinone ring was changed via reduction to the benzenoid hydroquinone. In order to retard reoxidation and protect the reactive oxygens, the hydroquinones were converted to acetyl esters.

These compounds offered inspiration for calculations to show the fundamental differences between the D—A containing HBQ and closely related asymmetric biphenyl systems. Thus, molecular geometry and orbital energies for a series of reduced HBQ molecules were calculated using DFT methods. Each HBQAc₂ derivative modeled in Table 2.4 had its electron distribution probabilities visualized, and all appear similarly to Figure 2.10. They have been tabulated in the Appendix after the HBQ derivatives.

Section 2.6.1 Molecular Geometry Energy Minimization

To determine the minimized geometry for a series for HBQAc₂ derivatives, Gaussian09 OPT+FREQ parameters were used. The average torsion angle is slightly larger than HBQ for these substituted biphenyls, at $48.9 \pm 0.9^\circ$. This is about 10° more twisted than the HBQs themselves, and about 5° more twisted than unsubstituted biphenyl.¹⁰¹ Additionally, it is rotated $\sim 1^\circ$ more than 2-methyl-4,4'-diaminobiphenyl from Venkataraman *et al.*,²⁵ which is consistent with the added steric bulk *ortho* to the 1,1'-biphenyl bond. Table 2.4 collects data for the relevant compounds. As no crystals have been grown for any reduced HBQ derivative, a comparison to the lattice structure cannot be made.

Section 2.6.2 Molecular Orbital Distribution

Delocalization of the orbitals across both rings is evident, especially for the LUMO. Orbitals originally attributed to benzoquinone became aromatic, and rise in energy (see Section 2.6.3). Unsurprisingly, this change means that the acceptor type-character on the quinone half of HBQs is lost. The π -orbitals for the diacetyl hydroquinone have a more significant overlap with the dimethoxybenzene aromatic orbitals and contribute to the delocalization over the whole structure.

Section 2.6.3 Molecular Orbital Eigenvalues

Table 2.5 presents calculated orbital eigenvalues for HBQAc₂ derivatives. As expected, HOMO and LUMO energies both more closely resemble a biaryl system, a larger gap exists between the FMOs of the reduced HBQ backbone relative to HBQ itself. Reduction of the ring increases the potential energy of the LUMO relative to benzoquinone without greatly affecting the eigenvalue of the HOMO. For example, BrHBQCN has a HOMO energy of -6.71 eV, whereas BrHBQAc₂CN has a HOMO value of -6.74 eV. However, there is a 1.75 eV increase in LUMO potential energy (-4.34 eV to -2.59 eV) upon reduction of the quinone. This potential energy increase eliminates the electron-accepting capacity inherent to the quinone. The HOMO–LUMO gap for BrHBQAc₂CN would mean that this compound has vastly different spectral characteristics than BrHBQCN. We see this visually with the compounds— synthesized HBQ derivatives are all highly colored red to blue powders, whereas the reduced versions are tan to colorless.

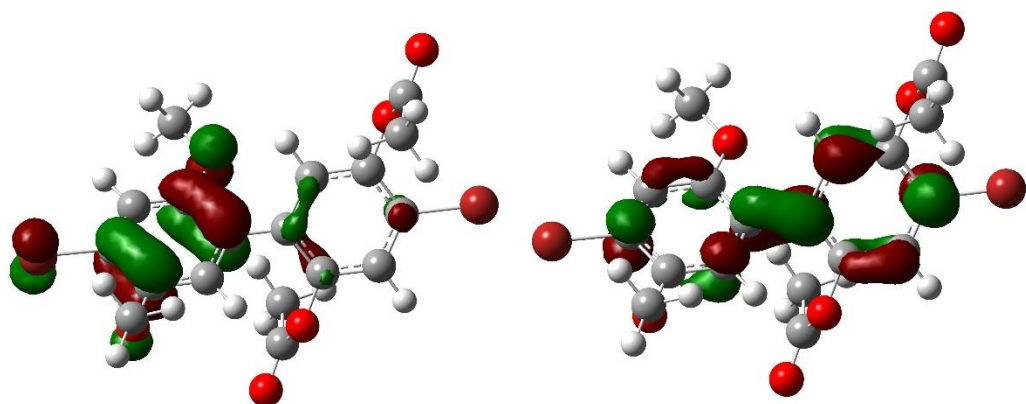
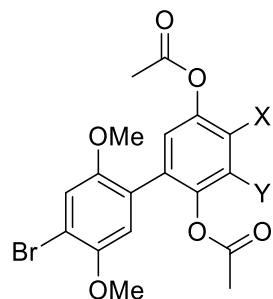


Figure 2.10 Acetylated HBQ HOMO (left) and LUMO (right)

Table 2.4 Torsion angles and dipole moments of Acetylated HBQ Molecules

X	Y	Torsion Angle (°)	Dipole (D)
Br	H	48.5	2.50
N₃	H	48.8	2.50
NH₂	H	49.2	2.61
NHMe	H	48.0	3.01
NHAc	H	49.6	4.31
NHC(=O)PhH	H	48.4	5.72
NHC(=O)PhCN	H	45.6	4.01
NHC(=O)H	H	49.6	3.88
SH	H	49.0	2.92
SAc	H	51.4	5.10
isoNC	H	48.6	4.64
CN	H	48.0	5.22
COOH	H	47.9	3.69

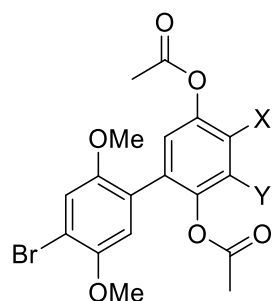
As a result of this increased potential energy alignment, the turn-on voltage for a BrHBQAc₂-based junction would shift to a higher value, due to the stronger bias required for electron injection into the LUMO. Oxidation of the dimethoxybenzene should occur at roughly the same rate as it would with the HBQ device, however, a corresponding reduction would only occur via electron tunneling through the LUMO potential energy barrier. This limitation would reduce the absolute conduction of a biaryl-based device as compared to an equivalent aryl-quinone HBQ system. Additionally, as the acceptor characteristics are lost, the mechanism of conduction through the molecule would change, preventing unimolecular rectification, as the D—A system becomes a D—D system. Therefore, any asymmetry observed within the monolayer would be due to a mechanism other than the AR unimolecular mechanism.

Section 2.7 Monomer Components and Comparison to HBQ Results

Section 2.7.1 Molecular Orbital Distribution

Because of the central hypothesis that the dimethoxybenzene and benzoquinone rings of HBQs should work as isolated units during an electron transfer processes, it is helpful to consider these individual “parents” of the HBQ series. Thus, DFT calculations of the FMO eigenfunctions for 1,4-dimethoxybenzene and 1,4-benzoquinone were performed (Figure 2.11). At the outset of this experiment, it was predicted that properties of the separated halves of HBQ would closely resemble properties from the intact HBQ. This would provide additional support for the electronic isolation of these moieties within the twisted HBQ structure. In addition to the computational approach, the spectroscopic and electrochemical behaviors of the parent halves of an HBQ are presented (Chapter 4).

Table 2.5 FMO eigenvalues and HOMO-LUMO Gap values of Acetylated HBQ Molecules



X	Y	HOMO (eV)	LUMO (eV)	HOMO-LUMO Gap (eV)
Br	H	- 6.53	- 1.91	4.62
N₃	H	- 6.45	- 2.16	4.29
NH₂	H	- 6.11	- 1.41	4.69
NHMe	H	- 5.95	- 1.35	4.59
NHAc	H	- 6.54	- 1.94	4.59
NHC(=O)PhH	H	- 6.27	- 2.05	4.21
NHC(=O)PhCN	H	- 6.11	- 2.77	3.33
NHC(=O)H	H	- 6.50	- 1.92	4.58
SH	H	- 6.36	- 1.75	4.60
SAc	H	- 6.63	- 2.14	4.49
isoNC	H	- 6.68	- 2.40	4.28
CN	H	- 6.74	- 2.59	4.14

Section 2.7.2 Molecular Orbital Eigenvalues

Table 2.6 contains calculated orbital eigenvalues for 1,4-dimethoxybenzene, 1,4-benzoquinone, the unsubstituted parent HBQ, and the AR molecule. Benzoquinone has much lower-lying orbitals as compared to dimethoxybenzene, confirming its role as an acceptor. The dimethoxybenzene HOMO is situated higher in energy, as is expected for the role of a donor. Qualitatively speaking, the HBQ backbone and AR molecule each has characteristics of both isolated “monomers.” Each HOMO for the HBQ backbone and AR have comparable eigenvalues to dimethoxybenzene, and each LUMO for HBQ and AR the benzoquinone is situated similarly in energy to the LUMO for benzoquinone.

While each of the monomers in turn have a relatively high gap, the extended FMO features of both the HBQ and AR lead to a gap well within visible wavelength energies. The HOMO–1 and LUMO+1 orbitals are situated in energy near to the HOMO of benzoquinone and LUMO of dimethoxybenzene, respectively.

Eigenvalues in Table 2.6 are visualized schematically in Figure 2.12 to illustrate the situation of the FMO energy. This shows that there should be a visible-wavelength transition for HBQ as an intramolecular electron-transfer process whereas each monomer would have a higher energy transition, in the UV range. The HOMO–LUMO gap of the AR molecule is 1.94 eV, slightly lower than that of the optimized structure of the unsubstituted-HBQ backbone at 2.51 eV (Table 2.6). See Chapters 3 and 4 for experimental confirmation.

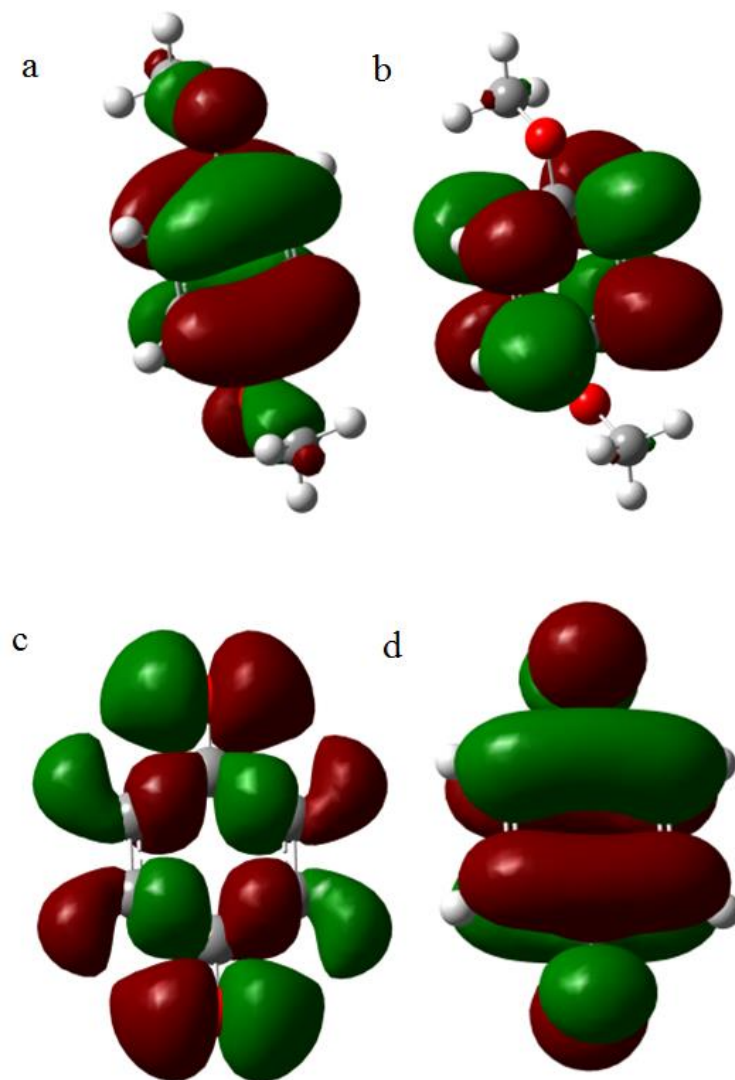


Figure 2.11 Monomer FMOs (a) Dimethoxybenzene HOMO, (b) Dimethoxybenzene LUMO, (c) Benzoquinone HOMO, (d) Benzoquinone LUMO

Table 2.6 Comparative DFT values of the FMOs for the donor, acceptor, and combined HBQ. HOMO for HBQ is similar to the donor, and the LUMO is similar to the acceptor, as expected.

Molecule	HOMO-1 (eV)	HOMO (eV)	LUMO (eV)	LUMO+1 (eV)
Dimethoxybenzene		-6.51	-0.58	
Benzoquinone		-7.79	-3.95	
Unsubstituted HBQ	-7.15	-6.14	-3.63	-1.42

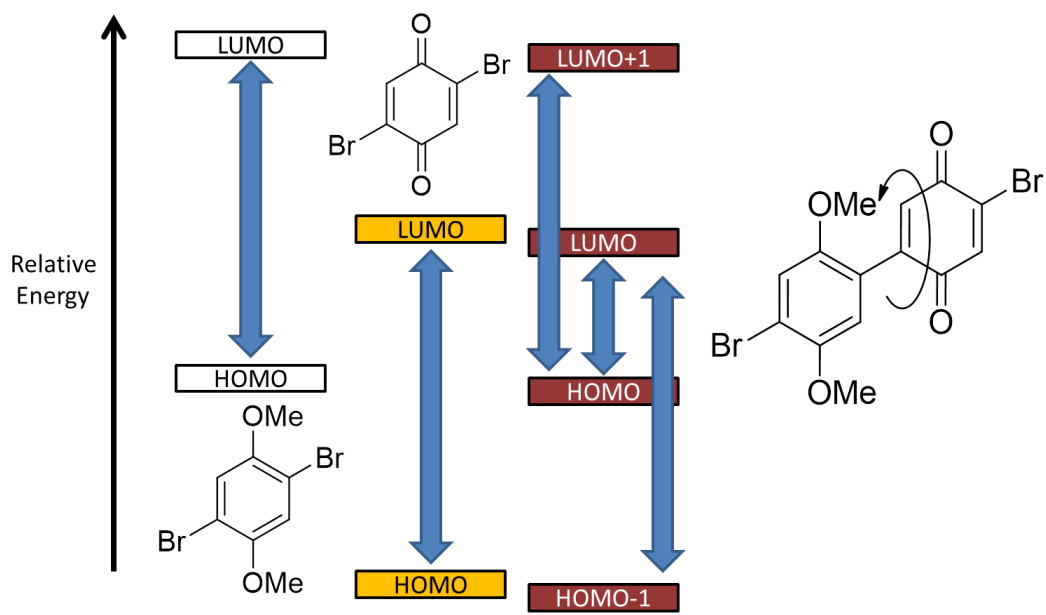


Figure 2.12 Calculated relative energy gaps of the donor and acceptor portion of the molecules

Section 2.8 Conclusions

Work presented in this chapter shows that the HBQ backbone consists of two rings twisted out of plane from one another by roughly 39° . The exact torsion angle θ is somewhat dependent on the electronics of the system, yet is still consistent with literature results on biphenyl. The rotational barrier about the bond is higher than an unsubstituted biphenyl, but rotation about the bond is still possible as supported by experimental data presented in subsequent chapters. Orbital probabilities are localized to each ring and substituent effects on the quinone affect the particular LUMO eigenvalue more so than the HOMO, which is consistent with the localization.

Reduced HBQ derivatives are slightly more twisted, but have geometry similar to that of other sterically hindered biphenyl systems. Despite the higher torsion angle, the orbitals have high overlap across the molecule, with no localization seen. When the quinone is reduced, the D—A system instead becomes a D—D system and this is reflected in the orbital eigenvalues.

The FMOs of HBQ derivatives are similar in distribution and energy as the monomeric constituents combined, dimethoxybenzene and benzoquinone. Alongside one of the original AR proposed molecules, HBQ derivatives display similar FMO separation in space. This provides evidence that a saturated carbon bridge is not the only method by which molecular orbitals are efficiently electronically isolated from one another. Information about individual components for a larger molecule may lend clues for the development of more complex D—A systems. The D and A may be selected for based on separate experimental constraints, provided that the insulator is between them. This can then lead to a more efficient use of computational resources by which to design further molecular electronic systems, as smaller portions of molecules will eliminate wasteful runtime on larger blocks.

CHAPTER 3

SYNTHESIS

Section 3.1 *In Silico to In Situ*

One goal of Molecular Electronics is to tie synthetic strategy into the rational design of single molecule electronic components.⁷⁷ Tailoring molecular structure to both function and performance is a monumental challenge, and understanding how interfacial bonding affects conductance remains a fundamental opportunity for complete understanding in this area. Researchers have made important strides forward in this field to date using both theoretical models and empirical data, but predicting electrical conductance with high quantitative confidence through single molecules is still a distant goal.¹⁰³ Experimental evidence for conduction through symmetric molecules has been well established in a variety of systems to date.^{11,12,29,104-106} Many rectifiers have been measured, mostly in monolayers.^{16,18,19} A recent study on self-assembled multilayers has also been published.¹⁰⁷ Single-molecule studies are used for collecting statistical data, as large area junctions may function differently than isolated molecules.^{76,108}

As explained in detail within Chapters 1 and 2, Molecular Electronics gained major attention in 1974 when Aviram and Ratner (AR)¹⁰ proposed an asymmetric Donor-Bridge-Acceptor molecular rectifier of electrical current (Figure 3.1). They postulated that an electron donor moiety (D) covalently linked to an electron acceptor moiety (A) through an intermediate saturated covalent bridge (B), preserves the electron-donating and -accepting characteristics of the two distal moieties. These characteristics allow for asymmetric conduction through the

molecule. The system in question for this dissertation contains an electron-rich D of dimethoxybenzene, and the electron-poor A is a quinone (Figure 3.1, top). AR explicitly details an ethylene σ -bridge between the electroactive sections of the molecule to isolate the D and A molecular orbitals. As seen in the bottom of Figure 3.1, the HOMO and LUMO are quite clearly separated from one another. Adding to this isolation, the planes of the rings are rotated roughly orthogonal to one another. This molecule unfortunately lacks the appropriate functionalization necessary to create a well-packed and stable monolayer with strong directional affinity.

In the case of hemibiquinone (HBQ) molecular diodes, D and A are directly connected to one another via a single carbon-carbon bond, using inter-ring torsion angles as the molecule's inherent break in conjugation (Figure 3.2). We hypothesize inherent decoupling of the rings due to their torsion away from planarity will serve to effectively eliminate the need for an explicit bridge. Single molecule studies demonstrating the decrease in conduction efficiency provide inspiration for the development of new single-molecule rectifiers based on asymmetric biphenyl systems.²⁹

Chapter 2 outlined the rationale behind selecting the HBQ backbone as a system of interest. The aim is for orbitals of the HBQ rings to act as isolated components, as if they were an aryl ring and a quinone not joined by a covalent bond. Isolated frontier molecular orbitals (FMOs) for HBQ derivatives are similar in both distribution and energy as calculated for the AR molecule, but synthetic versatility gives the HBQ a distinct advantage. This dissertation focuses on molecules to self-assemble on gold surfaces. For this to be possible, the HBQ must have anchor groups that selectively bind the molecule in a single direction— disorder in the monolayer leads to a signal that would be symmetric in both bias directions and thus no rectification.

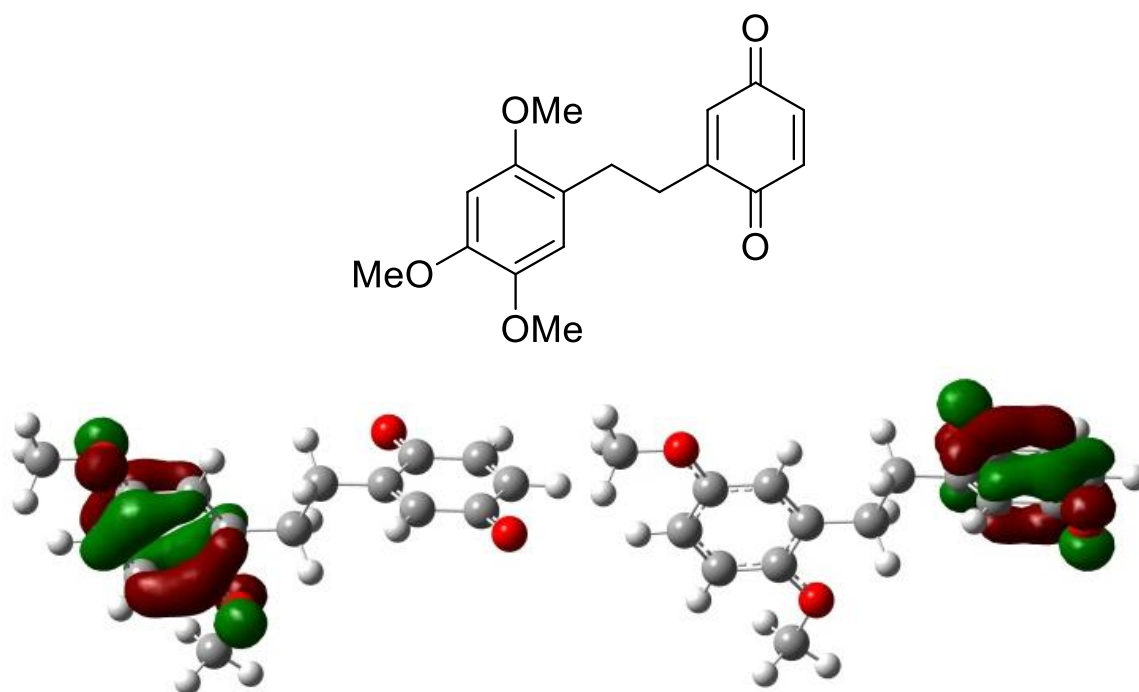


Figure 3.1 The “hemiquinone” in AR¹⁰ as inspiration for the hemibiquinone backbone (top). HOMO (bottom left) and LUMO (bottom right) are separated both spatially and energetically.

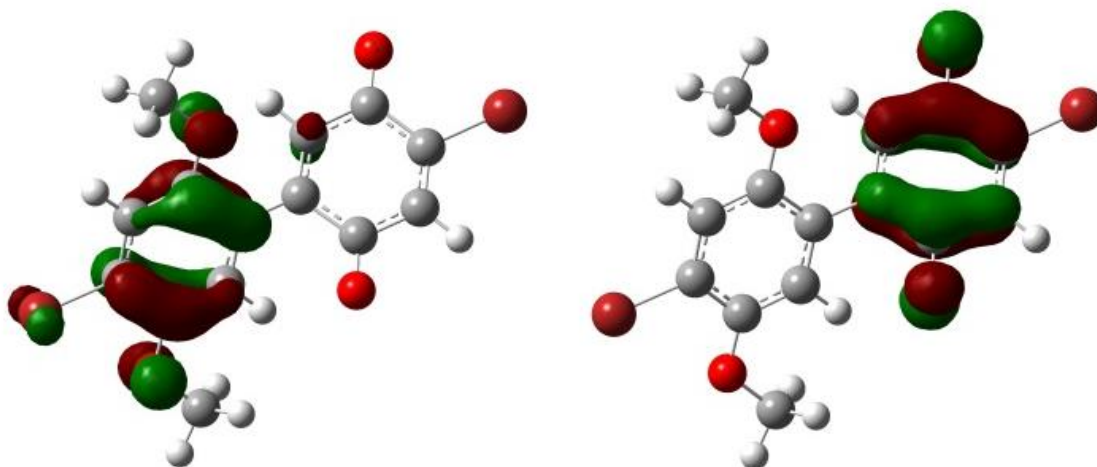


Figure 3.2. Visualization of the FMOs for BrHBQBr. They are decoupled just as in Figure 3.1.

Section 3.2 Synthesis of HBQ Backbone

Love *et al.*¹⁰⁹ suggest detecting 4,4'-dibromo-2',5'-dimethoxy-[1,1'-biphenyl]-2,5-dione (HBQ **1**) as a side product of 4,4'-dibromobiquinone synthesis, however they did not report any characterization of the molecule. Through oxidative dimerization (Scheme 3.1) we optimized a procedure to selectively produce gram quantities of **1**. Crystals of 4,4'-dibromobiquinone were isolated and characterized. Its analysis appears in Chapter 4.

To generate HBQ **1**, 2-bromo-1,4-dimethoxybenzene was synthesized according to the Zysman-Coleman technique.¹¹⁰ Since 4,4'-dibromobiquinone forms by the complete oxidation of 2-bromo-1,4-dimethoxybenzene using 3 molar equivalents of cerium ammonium nitrate (CAN),¹⁰⁹ we hypothesized that using less CAN could preferentially form the hemibiquinone. Indeed, by decreasing the ratio to 1:1.5 2-bromo-1,4-dimethoxybenzene:CAN, we were able to form the pure HBQ **1** in roughly 35% yield.

It is important to note that the mode of addition is relevant. A suspension of 2-bromo-1,4-dimethoxybenzene must be prepared separately from the CAN aqueous solution. Adding water to the solution of 2-bromo-1,4-dimethoxybenzene in acetonitrile creates a suspension that should be quickly combined with the CAN solution. Doing otherwise will result in a significant loss of efficiency. While the HBQ **1** would still form, it would coprecipitate with a large amount of 4,4'-dibromobiquinone, which would require separation by flash chromatography. Further efforts to optimize the procedure have not yielded a better synthetic strategy to form HBQ **1**.

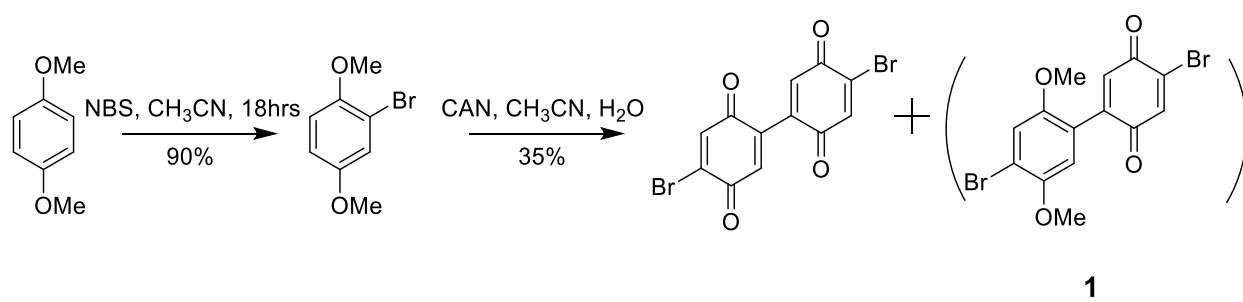
Section 3.3 Synthesis of Nitrile-Functionalized Molecular Diode

Section 3.3.1 Monomer Reactivity Differentiation

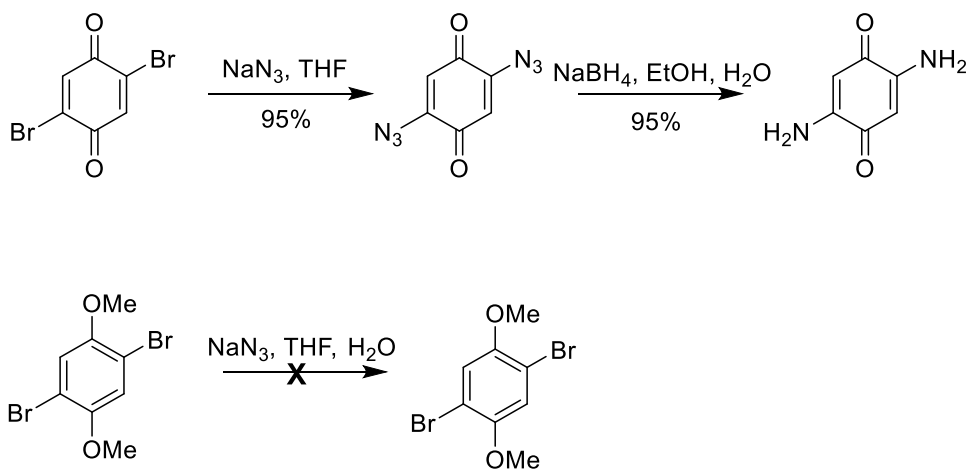
The method by which a molecule contacts an electrode will have an effect on both its conduction properties as well as its ability to rectify.⁵⁰ This fact needs to be taken into account when designing molecular systems and interpreting experimental results. Owing to the electron-withdrawing properties of the R-CN group (Chapter 2) as well as its ability to strongly couple with gold,^{73,111-113} we focused on creating **3** for exploration as single-molecule rectifiers. In addition, we have created other functionally terminated HBQs on the way to a 4-nitrile terminated molecule (Section 3.4).

As bromine will not chemisorb to gold,^{54,114} we needed to add functional groups that will. At the same time, synthesis requires selectivity for one ring or the other to produce a high quality self-assembled monolayer upon device assembly. In order to qualify chemoselectivity of the rings, we tested two analogue compounds, 2,5-dibromo-1,4-benzoquinone and 2,5-dibromo-1,4-dimethoxybenzene (Scheme 3.2). 2,5-Dibromo-1,4-benzoquinone was synthesized in nearly quantitative yield from 2,5-dibromo-1,4-dimethoxybenzene according to the procedures described by Lopez-Alvarado *et al.*¹¹⁵ The benzoquinone was converted to the diamino analog via a diazido compound,^{116,117} which was formed by dissolving the quinone in THF, stirring in an aqueous solution of sodium azide, then extracting and drying to isolate the azidoquinone. Alas, it is *very* unstable [CAUTION: EXPLOSION HAZARD], and decomposes rapidly in light and air; the reduction to the amine must be done quickly. The same reaction was tested on 2,5-dibromo-1,4-dimethoxybenzene, but only starting material was recovered. This provided evidence that nucleophiles should attach preferentially to the quinone bromine, rather than to the aromatic bromine under mild conditions.

Scheme 3.1 The synthesis of HBQ **1** and corresponding biquinone



Scheme 3.2 Quinone versus aromatic reactivity



Section 3.3.2 Reductive Disubstitution of HBQ 1

Direct conversion from the quinoid bromine to a single electron-withdrawing substituent like the nitrile proved impossible. Instead, the nitrile adds in a reductive 1,2-disubstitution.¹¹⁸⁻¹²⁰ The synthesis of the dinitrile from substitution of the 4-bromine to the 3,4-dinitrile proceeded through reductive cyanation of **1** by KCN in aqueous acetonitrile (Scheme 3.3). Attempts to synthesize the mononitrile BrHBQCN through stoichiometric control only produced the dinitrile in reduced yields. It may be that **1** undergoes nucleophilic substitution of the bromide to the mononitrile form. Excess cyanide ions can attack C-3. Tautomerization and subsequent neutralization produce the dicyanohydroquinone **2** (Scheme 3.4).

The reaction is accompanied by a rapid color change, a solution of HBQ **1** in acetonitrile is bright red, but addition of aqueous potassium cyanide solution shifts the solution color to deep purple. After the reaction is complete, addition of HCl rapidly shifts the color to vibrant orange. Evaporation of the acetonitrile precipitates a tan powder that may be recrystallized from acetone as yellow-orange prisms. Crystals of HBQH₂ **2** were grown from acetone under ambient conditions.

Oxidation of the hydroquinone **2** to HBQ **3** by ceric ammonium sulfate proceeds most efficiently overnight in chloroform, and **3** (unstable to purification by flash chromatography) can be recrystallized from benzene with hexane, ultimately producing the pure compound in 50% yield. Crystals of HBQ **3** were grown from a solution in 1:1 benzene and chloroform.

Originally, oxidation of **2** back to quinone **3** proceeded as outlined by Reynolds and VanAllan,¹²¹ by refluxing **2** with a solution of nitric acid in acetic acid. These conditions are rather harsh, and the product was only recoverable in 10% yield. A somewhat more successful method involved a tri-phasic heterogeneous system, powdered **2** was stirred in a solution of

aqueous FeCl_3 and benzene. The hydroquinone, which is not soluble in water and only sparingly soluble in benzene, was slowly oxidized by the iron (III) and the quinone dissolves into the benzene. Separation of the organic solution and washing yields the crude product as a black powder upon concentration. The crude **3** may be purified in the same manner as above, giving 29% yield.

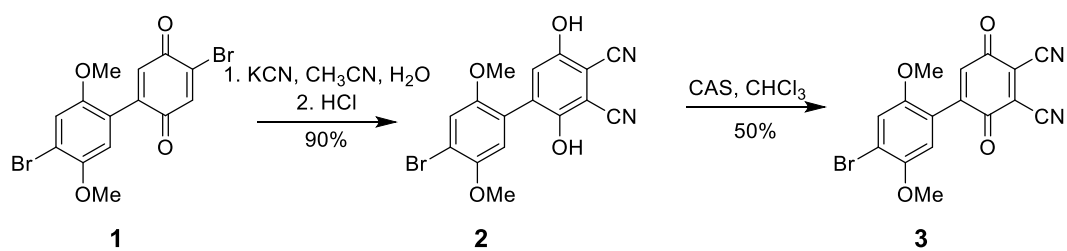
A full description of the solid-state interactions for **1**, **2**, and **3** have been published,^{98,99,122} and are presented in Chapter 4 alongside the other analytical data. Unpublished results of crystalline interactions are also included. Chapter 5 reports data collected by Marcus Johnson in Metzger lab, confirming the hypothesis that a monolayer of **3** rectifies.

Section 3.4 Ongoing Synthetic Efforts

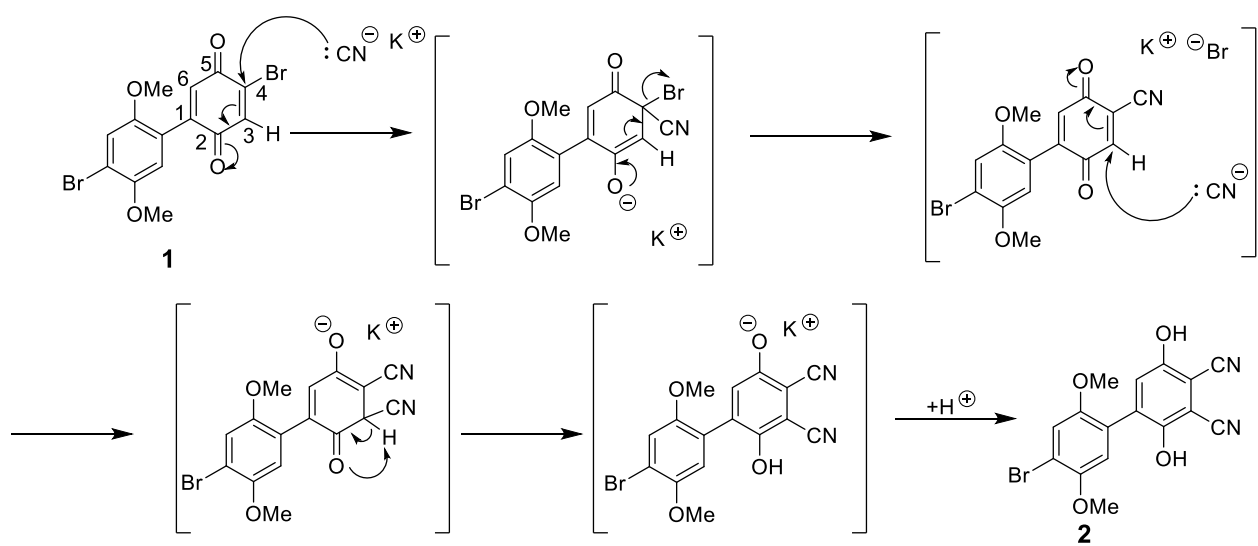
To obtain the 4-substituted mononitrile HBQ, a more lengthy but selective approach is required. Protection of the quinone is necessary to maintain synthetic possibilities, but the produced biphenyl system still needs to be chemoselective. In addition to this, quinones readily oxidize neutral metal catalysts; thus protection opens further synthetic versatility for the aromatic 4'-bromine. Reduction of HBQ **1** to the hydroquinone is possible and readily accomplished, but differentiating the bromines becomes chemically impossible unless the quinoid bromine is substituted first.

The test reactions in Scheme 3.2 provided for a facile transformation of the HBQ **1** into the HBQ **4** and the HBQ **5** (Scheme 3.5). Azides and especially azidoquinones are typically unstable as mentioned above but surprisingly **4** could be stored at ambient conditions for weeks and was not photosensitive. Crystals were recovered and analyzed, these details appear in Chapter 4.

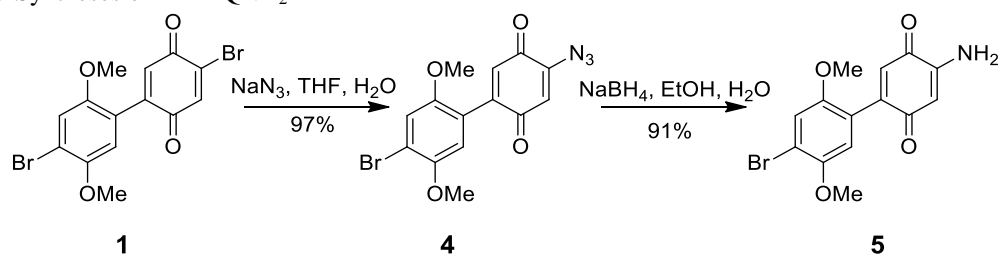
Scheme 3.3 Synthesis of BrHBQ(CN)₂



Scheme 3.4 Proposed mechanism of BrHBQ(CN)₂ formation



Scheme 3.5 Syntheses of BrHBQN_H2



Over time, the azide will auto-reduce to the amine. A quick reduction with NaBH₄ in aqueous ethanol or propanol precipitates HBQ **5** in good yield. If the amine is the desired product, a single-pot reaction to create HBQ **5** from HBQ **1** has been devised without isolating the azide and is described in Section 3.5, Experimental Details. Unfortunately, **5** does not crystallize.

We changed HBQ **1** into HBQ **5** in anticipation that it could readily undergo Sandmeyer-like reactions. However, HBQ **5** is not compatible with Sandmeyer conditions on its own, so then it becomes necessary to reduce the quinone ring to an aromatic system. Hydroxy, cyanohydrin, oxime, and acetal protection were attempted on **1**, **4**, and **5**, but were largely unsuccessful because they either did not form (acetal) or were not stable enough to purify (cyanohydrin, oxime, hydroxy). Interestingly, **1** could be reduced with NaBH₄ to the hydroquinone, but **5**'s hydroquinone auto-oxidized in air. Attempts to selectively reduce **4** to the hydroquinone were not attempted, for the obvious reason that the azide would preferentially react. This complicates the ability to isolate and characterize the compound. However, acetoxy protection of the quinone was successful on all of the tested HBQ systems to varying degrees of success (Scheme 3.6, 3.7). Acetylation of **1** resulted in **6** with about a 60% yield while acetylation of **4** resulted in **7** formed in 13% yield. Acetylation of **5** results in a complicated mixture (Scheme 3.7).

The resulting acetoxy-protected biphenyl system from **5** has three products that result from its reaction. The major product is **9**, a yellow-orange oily product. The amine is basic enough to scavenge excess acylium cations from the breakdown of the acetic anhydride, and leads to the formation of the N-acylated amides **9** and **10**. Compound **10** was isolated as a crystalline side product run by K. Williams, and the crystal structure was solved by D. Gerlach. Analysis of the

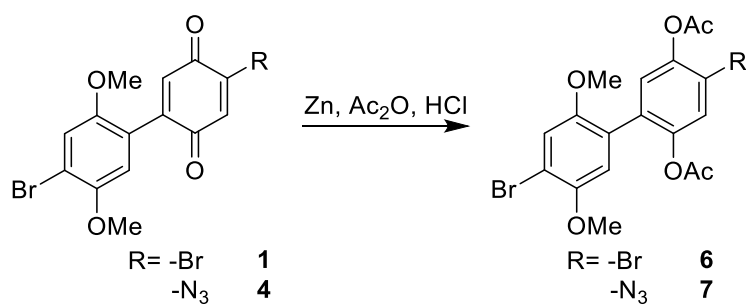
crystal structure appears below in Chapter 4. Efforts to reproduce syntheses by B. Eckhart that yielded **8** as the major product (an off-white amorphous solid) were unsuccessful.

Schemes 3.8 and 3.9 detail alternative methods by which to isolate the mononitrile HBQH₂ **12**. In the first method, HBQH₂ **8** is isolated from the crude mixture as shown in Scheme 3.7. From there, typical Sandmeyer conditions will isolate the desired material in probably low yield.

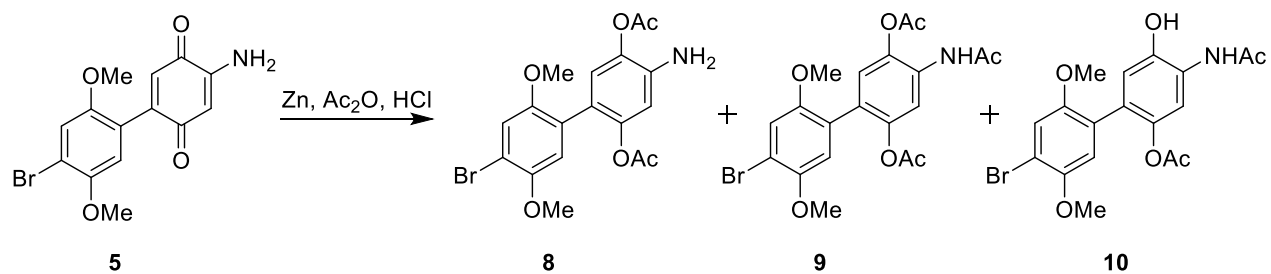
Reducing HBQ **5** in an inert atmosphere at 0 °C by NaBH₄ in isopropanol should open another pathway by which to isolate the desired product (Scheme 3.9). Sodium borohydride is unstable in methanol and ethanol, breaking down over time,¹²³ which is why isopropanol has been selected. This avoids the use of excess NaBH₄. From there, addition of aqueous HCl to the reaction will decompose unreacted reducing agents and hydrolyze borate ester intermediates. The amine will be protonated forming the ammonium salt, and solid B(OH)₃ will precipitate. If KCN is added to the reaction directly, it is possible that the cyanide anion will react with the boron, forming the tetracyanoborate salt [B(CN)₄]⁻ *in situ*, and so this must be removed prior to diazotization. The solid may be filtered from the solution under air-free conditions, and the solution can be diazotized in an ice bath (slowly) by sodium nitrite in water. Subsequent addition of the diazo salt solution to a solution of KCN in isopropanol and water would yield the mononitrile hydroquinone BrHBQH₂CN **12**.

The diazo solution would be added to the cyanide solution to keep the concentration of [CN]⁻ high compared to the diazo salt. This prevents coupling of the biphenyl molecules under homolytic cleavage of the C—N₂⁺ bond, forming N₂ gas and a radical carbon. Oxidation of HBQH₂ **12** by ceric ammonium sulfate would yield the mononitrile HBQ **13**.

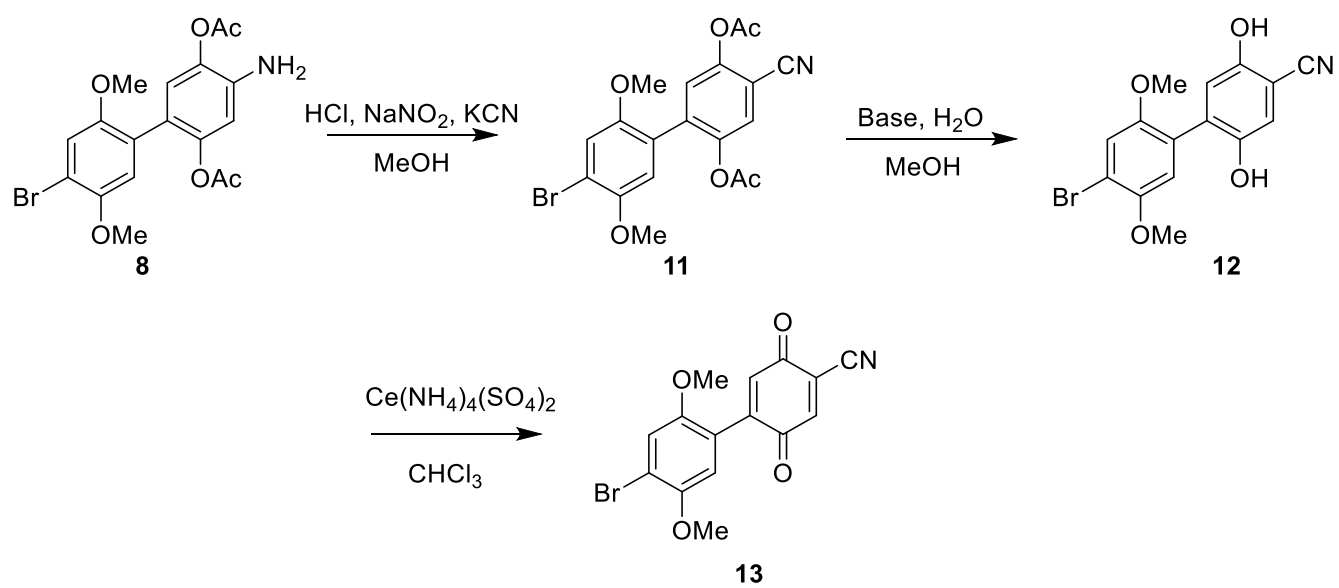
Scheme 3.6 O-Acetylation of quinones **1** and **4**



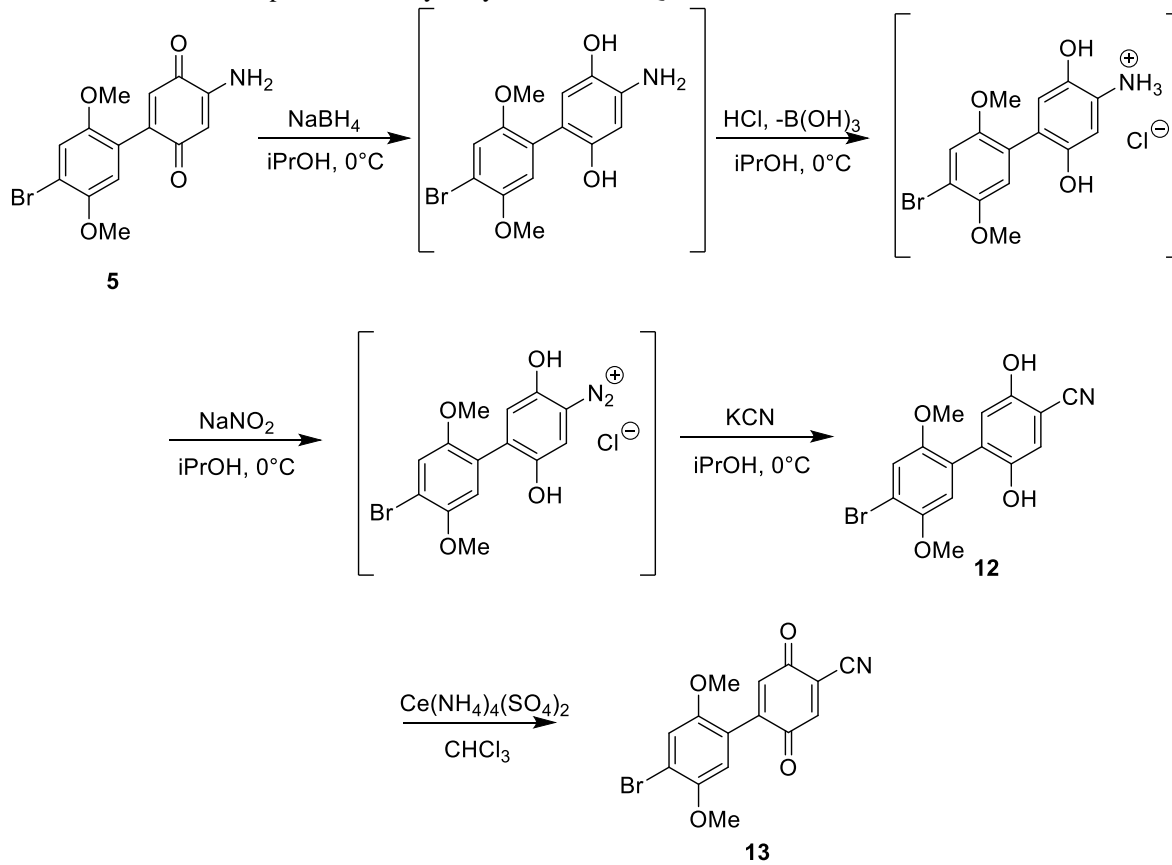
Scheme 3.7 Acetylation of HBQ **5**



Scheme 3.8 Anticipated Sandmeyer Cyanation to HBQ **13**



Scheme 3.9 Alternative Proposed Sandmeyer Cyanation to HBQ **13**



This chapter has detailed the rationale behind the design and synthesis of a molecular template containing a dimethoxybenzene ring bonded to a quinone ring with moieties attached that would self-assemble into a monolayer on gold. These reactions proceed under mostly ambient conditions and allow for a promising degree of versatility, especially for surface functionalization post-self-assembly.

Since single molecule studies in mechanically controlled break junctions require symmetric anchoring groups to work, future synthetic work will focus on the production of substitutions on both bromines at once (see Chapter 6). The hydroquinone of HBQ **1** provides the perfect starting material for this transformation into either a 4,4'-dithiol, 4,4'-dinitrile, or 4,4'-diamine.

Section 3.5 Experimental Details

All synthetic procedures were carried out in ambient conditions at room temperature unless otherwise noted. Materials were used as received from their commercial sources (Aldrich, Alfa Aesar, Fisher Scientific). ¹HNMR spectra were recorded on a Bruker 360 MHz, and ¹³CNMR were recorded on a Bruker 500 MHz spectrometer in an appropriate solvent.

2-Bromo-1,4-dimethoxybenzene

2-Bromo-1,4-dimethoxybenzene was synthesized according to literature procedure.¹¹⁰ To a flame-dried round-bottomed flask with a dry magnetic stir bar, 7.02 g (50.7 mmol) of 1,4-dimethoxybenzene and 9.04 g (50.8 mmol) of *N*-bromosuccinimide were added. The flask was capped with a rubber septum, and a nitrogen atmosphere was introduced. The flask was placed on an ice bath, and the solids were dissolved in dry acetonitrile. The solution was stirred overnight in an ice bath, and the bath was allowed to warm to room temperature. The reaction mixture was quenched in water, extracted with hexane, and the organic layers were dried over Na₂SO₄ and concentrated on vacuum. The product was sufficiently pure for use without further

purification. Orange oil, 90% yield. $d = 1.489 \text{ g/mL}$. $^1\text{H NMR}$ (360 MHz, CDCl_3): $\delta = 7.12$ (d, 1H, ArH), 6.82 (m, 2H, ArH), 3.84 (s, 3H, OCH_3), 3.75 (s, 3H, OCH_3) Values match those previously reported in the literature.

2-Bromo-5-(4-bromo-2,5-dimethoxyphenyl)cyclohexa-2,5-diene-1,4-dione 1

In a 1-L round-bottomed flask, 3.00 g (13.8 mmol) of **2** were dissolved in 300 mL of acetonitrile. Separately, 11.34 g (20.7 mmol) of cerium ammonium nitrate were dissolved in 360 mL of water. The aqueous solution was poured *into the organic solution* in one fraction and stirred for two hours. The solids were filtered *in vacuo*, rinsed with water, and dried. Product **1** was an amorphous powder that could be recrystallized as purple-black crystals from chloroform or precipitated as a dull grey-green powder from acetone with water. $^1\text{H NMR}$ (360 MHz, CDCl_3): $\delta = 7.38$ (s, 1H, ArH), 7.18 (s, 1H, ArH), 7.02 (s, 1H, ArH), 6.73 (s, 1H, ArH), 3.86 (s, 3H, OCH_3), 3.74 (s, 3H, OCH_3), 35% yield.

4'-Bromo-2,5-dihydroxy-2',5'-dimethoxy-[1,1'-biphenyl]-3,4-dicarbonitrile 2

HBQ **2** (0.30 g, 0.744 mmol) was dissolved in 350 mL of acetonitrile. Potassium cyanide (0.1237 g, 1.90 mmol) was dissolved in 50 mL of water, and this solution was poured into the acetonitrile solution with stirring. The reaction immediately changed from a vibrant red to a deep purple. After stirring for 1 h, 50 μL of concentrated HCl was added. The purple solution faded to a bright orange color. Water (50 mL) was added, and the acetonitrile was removed using rotary evaporation. A tan powder precipitated, which was recovered by filtration and washed with water to yield the crude product. Recrystallization from acetone yielded the pure product (0.1960 g, 70.4%) as yellow-orange prisms. $^1\text{H NMR}$ (360 MHz, d_6 -acetone) $\delta = 10.02$ (s, 1H, ArOH), 8.75 (s, 1H, ArOH), 7.34 (s, 1H, ArH), 7.24 (s, 1H, ArH), 7.05 (s, 1H, ArH), 3.88 (s, 3H, OCH_3), 3.82 (s, 3H, OCH_3). HRMS (EI): calcd for $\text{C}_{16}\text{H}_{11}\text{N}_2\text{O}_4\text{Br}$ 373.9902, found 373.9893.

2,3-Dicyano-5-(4'-bromo-2',5'-dimethoxyphenyl)cyclohexa-2,5-diene-1,4-dione 3

Hydroquinone **3** (0.1260 g, 0.337 mmol) was suspended in a mixture of 100 mL of water and 100 mL of benzene. FeCl₃ (0.3404 g, 2.09 mmol) was added in one portion. The resulting mixture was capped and stirred overnight. The resulting phases were separated, and the organic phase was washed with water and dried over anhydrous Na₂SO₄. Evaporation of the solvent produced a crude product. The pure product was precipitated from a chloroform solution of this material by addition of hexane, yielding 0.0460 g (36.7%). ¹H NMR (360 MHz, CDCl₃) δ = 7.22 (s, 1H, ArH), 7.12 (s, 1H, ArH), 6.71 (s, 1H, ArH), 3.87 (s, 3H, OCH₃), 3.76 (s, 3H, OCH₃). HRMS (EI): calcd for C₁₆H₉N₂O₄Br 371.9746, found 373.9896. EI in methanol reduces the molecule to the M+2H *in situ*.

2-Azido-5-(4-bromo-2,5-dimethoxyphenyl)cyclohexa-2,5-diene-1,4-dione 4

In a 100-mL round-bottom flask, 1.00 g (2.5 mmol) of **3** in 60 mL of tetrahydrofuran was stirred. In a separate vessel, 0.1620 g (2.5 mmol) NaN₃ was dissolved in 4.5 mL of water. The aqueous solution was added to the organic solution all at once, and the solution stirred for 30 minutes. The reaction was quenched with water and extracted in CH₂Cl₂. The organic layers were dried on Na₂SO₄ and dried in vacuum. The product **4** was purified on a silica gel column, eluted with CHCl₃ (85% yield). ¹H NMR (360 MHz, CDCl₃): δ = 7.18 (s, 1H, ArH), 6.86 (s, 1H, ArH), 6.73 (s, 1H, ArH), 6.33 (s, 1H, ArH), 3.86 (s, 3H, OCH₃), 3.74 (s, 3H, OCH₃). HRMS (EI): calcd for C₁₄H₁₀N₃O₄Br 362.9855, found 362.9850.

2-Amino-5-(4-bromo-2,5-dimethoxyphenyl)cyclohexa-2,5-diene-1,4-dione 5

In a 100-mL round-bottom flask, 1.3650 g (3.76 mmol) of **4** was suspended in 50 mL of a 70% ethanol/water solution. While stirring, 0.2528 g (6.58 mmol) of NaBH₄ was added in one portion. The reaction was stirred until the product had precipitated, and the mixture was a deep

rust red. The product was filtered on vacuum, rinsed with cold H₂O, and dried (80% yield). ¹H NMR (360 MHz, CDCl₃): δ = 7.16 (s, 1H, ArH), 6.76 (s, 1H, ArH), 6.73 (s, 1H, ArH), 5.83 (s, 1H, ArH), 4.93 (br s, 2H, NH₂), 3.85 (s, 3H, OCH₃), 3.75 (s, 3H, OCH₃). HRMS (EI): calcd for C₁₄H₁₂NO₄Br 336.9950, found 336.9945.

4-Bromo-4'-bromo-2',5'-dimethoxy-[1,1'-biphenyl]-2,5-diyl diacetate 6

To a 25-mL round-bottomed flask with a stir bar, 104.0 mg (0.25 mmol) of BrHBQBr and 170.3 mg (2.60 mmol) of Zn powder were mixed together. The mixture was capped and set to stir in an ice bath. Acetic anhydride (0.49 mL, 5.18 mmol) was added via syringe and left to stir on ice for two hours, replacing the ice as necessary to maintain the low temp. After the color had faded, the colorless reaction was diluted with 20 mL of CHCl₃ and gravity filtered to remove unreacted zinc into a separatory funnel containing ice. The filter paper was rinsed with another 15 mL of CHCl₃. The organic layer was washed twice with DI H₂O, dried on Na₂SO₄, and concentrated on vacuum to yield the crude product as a waxy solid. Product was purified on a silica column eluted by chloroform→ethyl acetate to yield 73.8 mg (0.15 mmol, 58.5% yield) ¹H NMR (360 MHz, CDCl₃): δ = 7.44 (s, 1H, ArH), 7.15 (s, 1H, ArH), 7.13 (s, 1H, ArH), 6.77 (s, 1H, ArH), 3.84 (s, 3H, OCH₃), 3.70 (s, 3H, OCH₃) 2.36 (s, 3H, C(=O)CH₃), 2.07 (s, 3H, C(=O)CH₃). HRMS (EI): calcd for C₁₈H₁₆O₆Br₂ 485.9314, found 485.9328.

4-Azido-4'-bromo-2',5'-dimethoxy-[1,1'-biphenyl]-2,5-diyl diacetate 7

To an oven-dried 5-mL round-bottomed flask, 90.4 mg (0.25 mmol) of the azide **4** and 115.7 mg (1.74 mmol) of activated Zn powder were mixed together. The mixture was cooled on an ice bath. In a separate vessel, on ice, 0.1870 mL (2.2 mmol) of concentrated HCl was added and mixed with 1.260 mL (13.2 mmol) of acetic anhydride. The anhydride solution was poured onto the rapidly stirring solid mixture and left to stir for 10 minutes, after which the color of the

quinone had disappeared. The suspension was diluted with chloroform, and gravity filtered into a separatory funnel to remove unreacted zinc. The solution was washed twice with water. The organic layer was dried with Na₂SO₄ and rotovaped to remove the chloroform and excess anhydride, yielding the crude product as a waxy pale yellow solid. Product was purified on a silica column eluted with 2:1 hexane:ethyl acetate to yield 14.2 mg (0.03 mmol, 13%). ¹H NMR (360 MHz, CDCl₃): δ = 7.14 (s, 1H, ArH), 7.07 (s, 1H, ArH), 6.98 (s, 1H, ArH), 6.77 (s, 1H, ArH), 3.84 (s, 3H, OCH₃), 3.69 (s, 3H, OCH₃) 2.33 (s, 3H, C(=O)CH₃), 2.07 (s, 3H, C(=O)CH₃). HRMS (EI): calcd for C₁₈H₁₆N₃O₆Br 449.0222, found 449.0209.

4-Amino-4'-bromo-2',5'-dimethoxy-[1,1'-biphenyl]-2,5-diyl diacetate 8

To an oven-dried 20-mL round-bottomed flask, 727.2 mg (2.15 mmol) of azide **4** and 983.9 mg (15.0 mmol) of activated Zn powder were mixed together. The mixture was cooled on a dry ice/acetonitrile bath. In a separate vessel, on ice, 1.613 mL (19.4 mmol) of concentrated HCl was added and mixed with 10.5 mL (109.7 mmol) of acetic anhydride. The anhydride solution was poured onto the rapidly stirring solid mixture. After stirring for 10 minutes, the color of the quinone had disappeared. The suspension was diluted with chloroform, and gravity filtered into a separatory funnel to remove unreacted zinc. The solution was washed three times with water and once with brine. The organic layer was dried with Na₂SO₄ and rotovaped to remove the chloroform and excess anhydride, yielding the crude product as a waxy pale yellow solid. Product was purified on a silica column eluted with 2:1 hexane:ethyl acetate to yield 114.2 mg (0.30 mmol, 42%).

4-Acetamido-4'-bromo-2',5'-dimethoxy-[1,1'-biphenyl]-2,5-diyl diacetate **9**

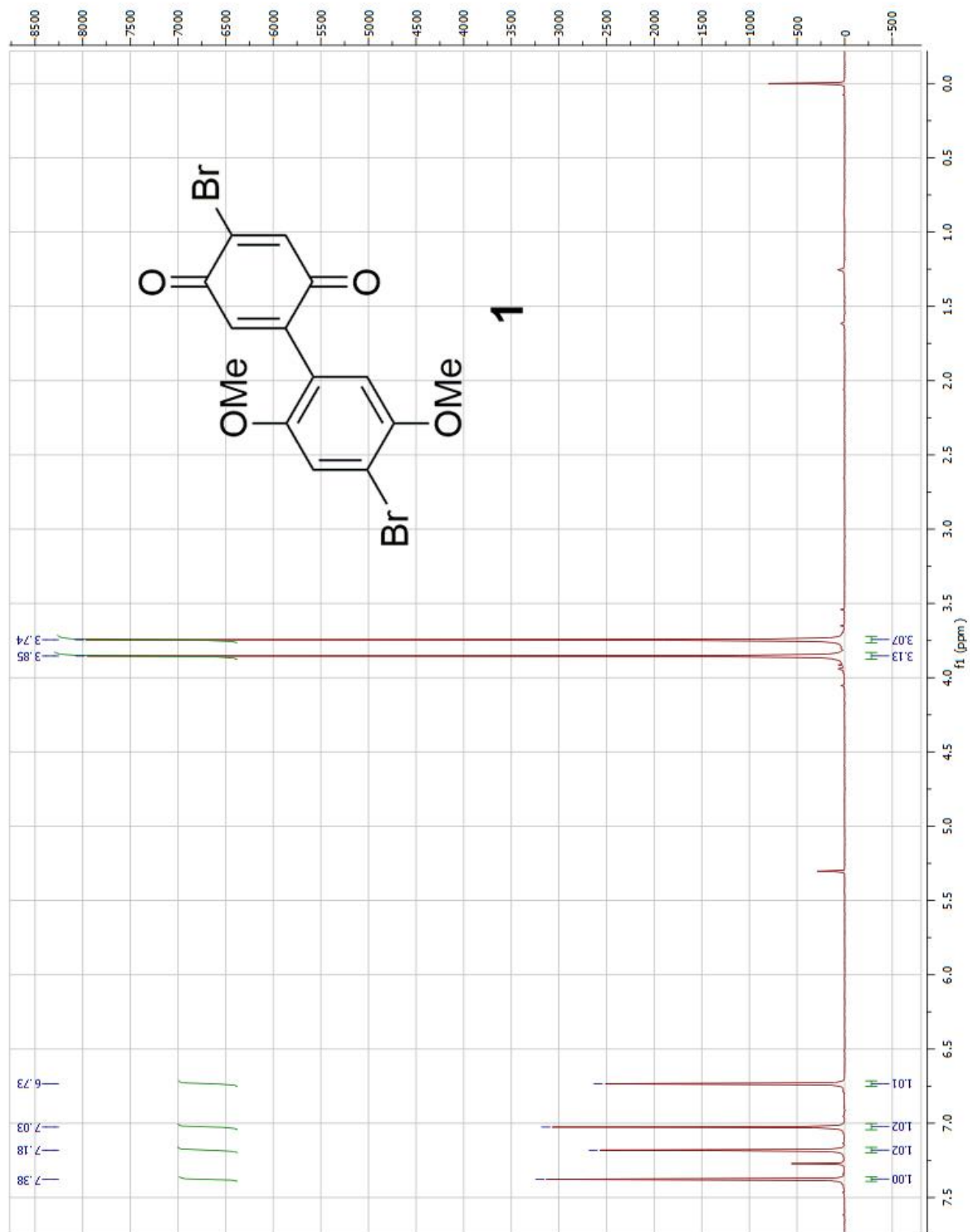
Side product of above.

4-Acetamido-4'-bromo-5-hydroxy-2',5'-dimethoxy-[1,1'-biphenyl]-2-yl acetate **10**

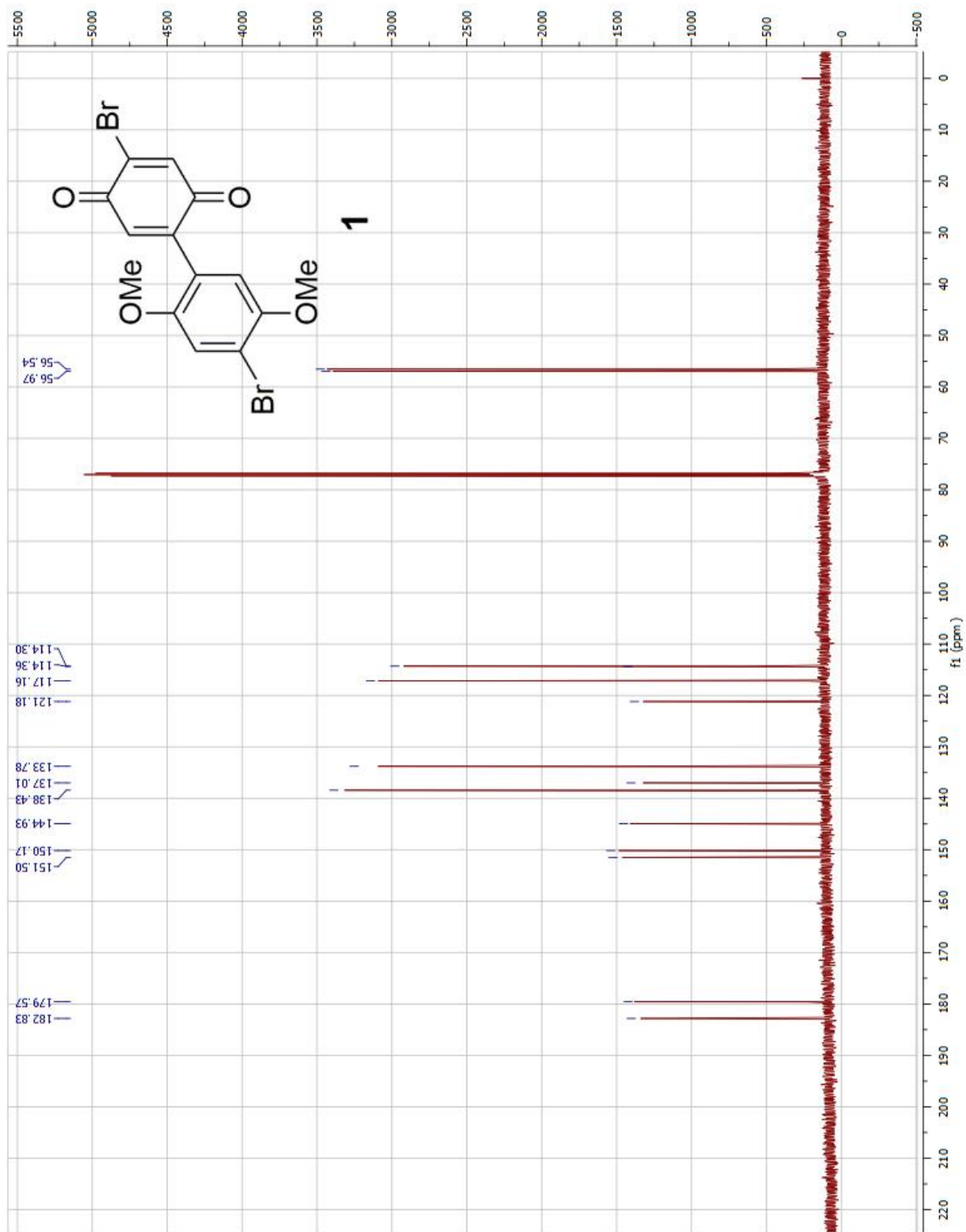
Side product of above.

Spectra

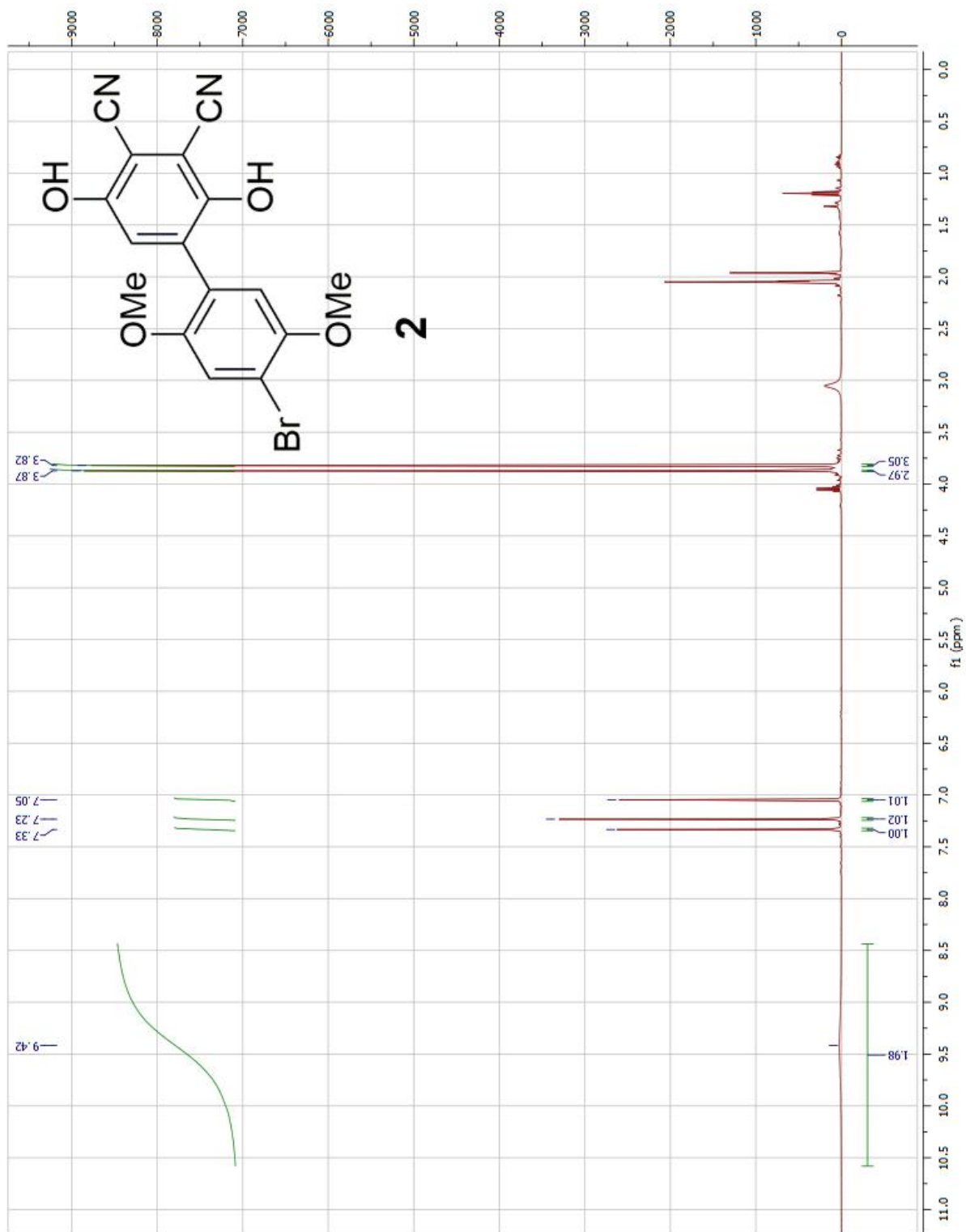
2-Bromo-5-(4-bromo-2,5-dimethoxyphenyl)cyclohexa-2,5-diene-1,4-dione **1** ^1H NMR



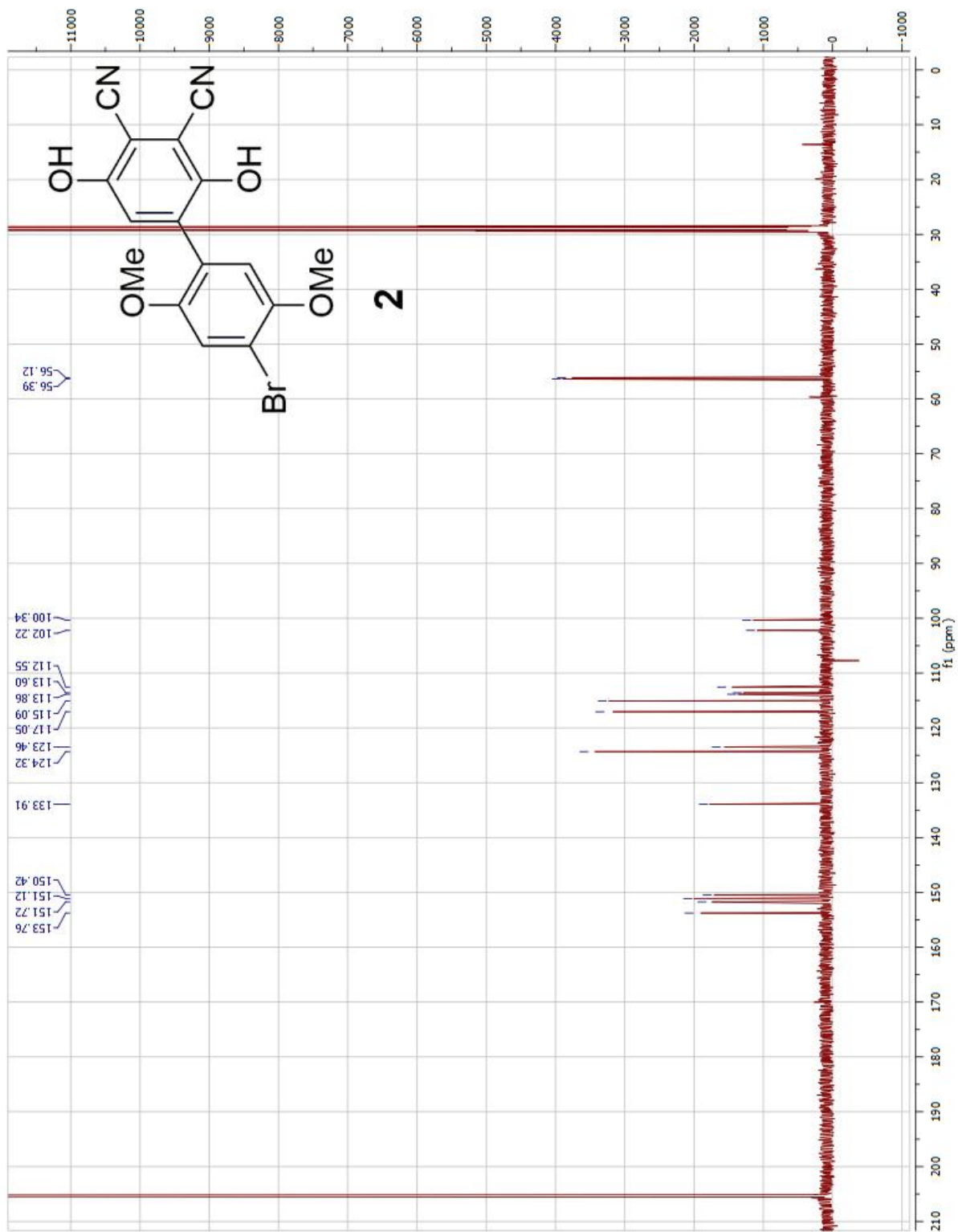
2-Bromo-5-(4-bromo-2,5-dimethoxyphenyl)cyclohexa-2,5-diene-1,4-dione **1** ^{13}C NMR



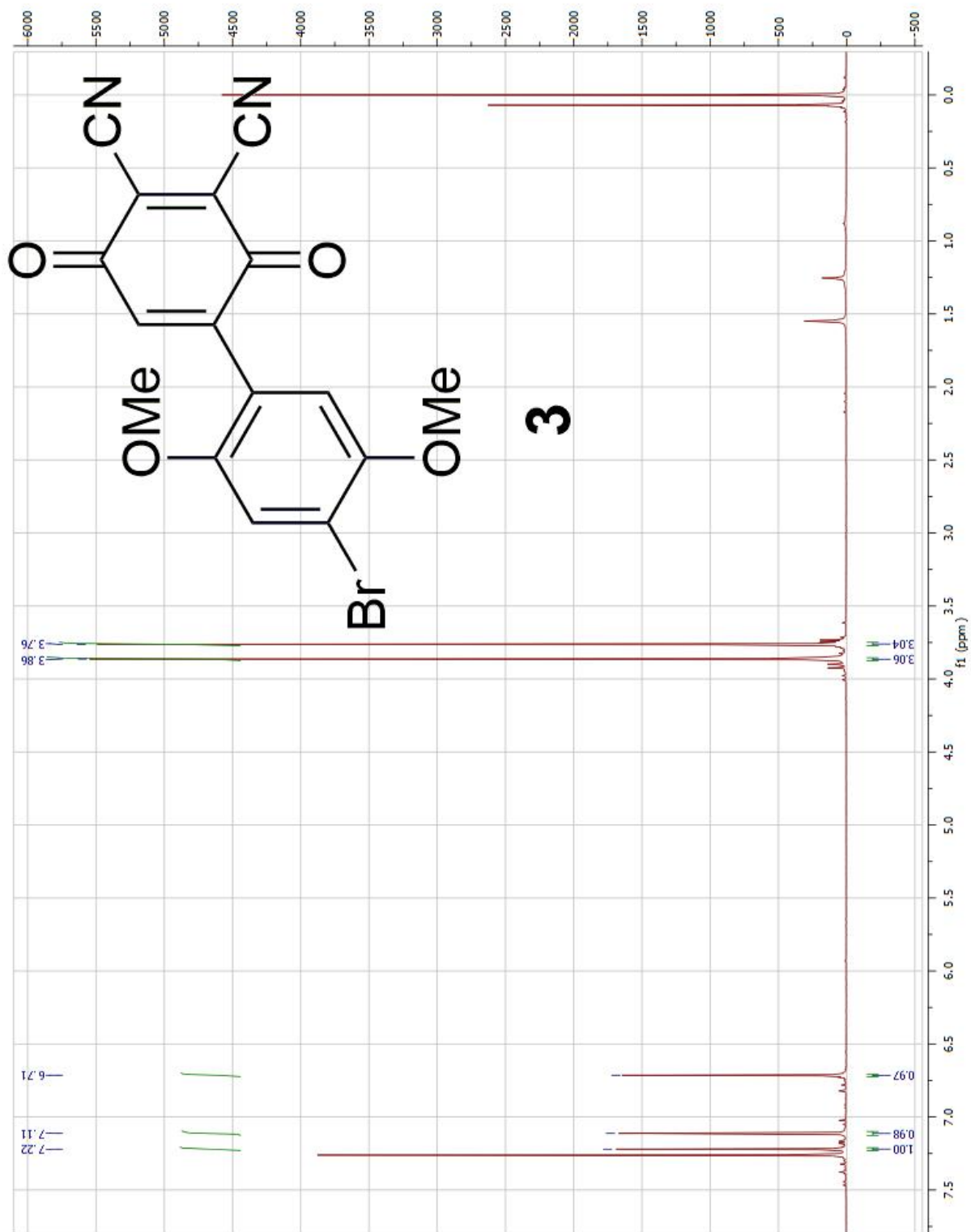
4'-Bromo-2,5-dihydroxy-2',5'-dimethoxy-[1,1'-biphenyl]-3,4-dicarbonitrile **2** ^1H NMR



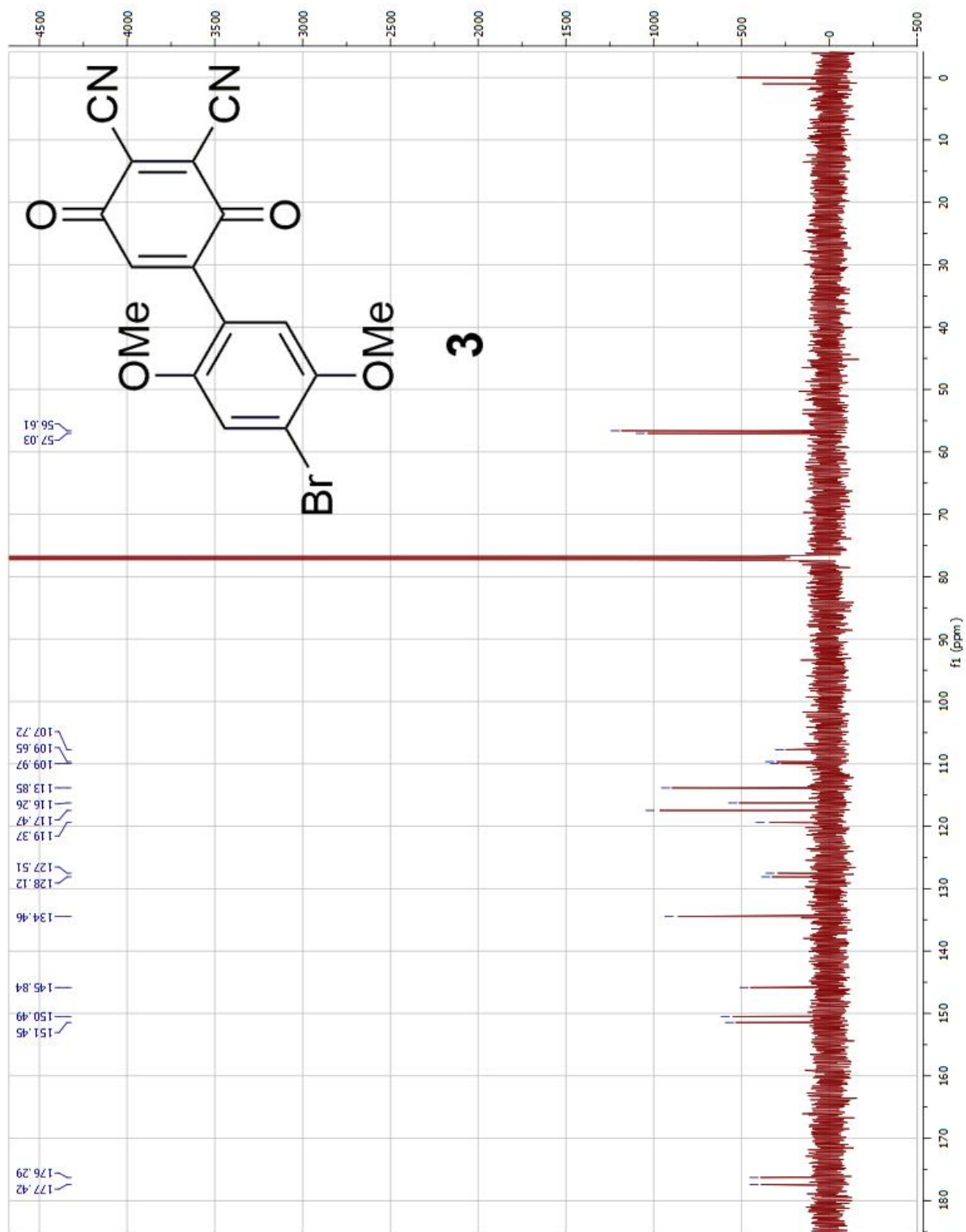
4'-Bromo-2,5-dihydroxy-2',5'-dimethoxy-[1,1'-biphenyl]-3,4-dicarbonitrile **2** ^{13}C NMR



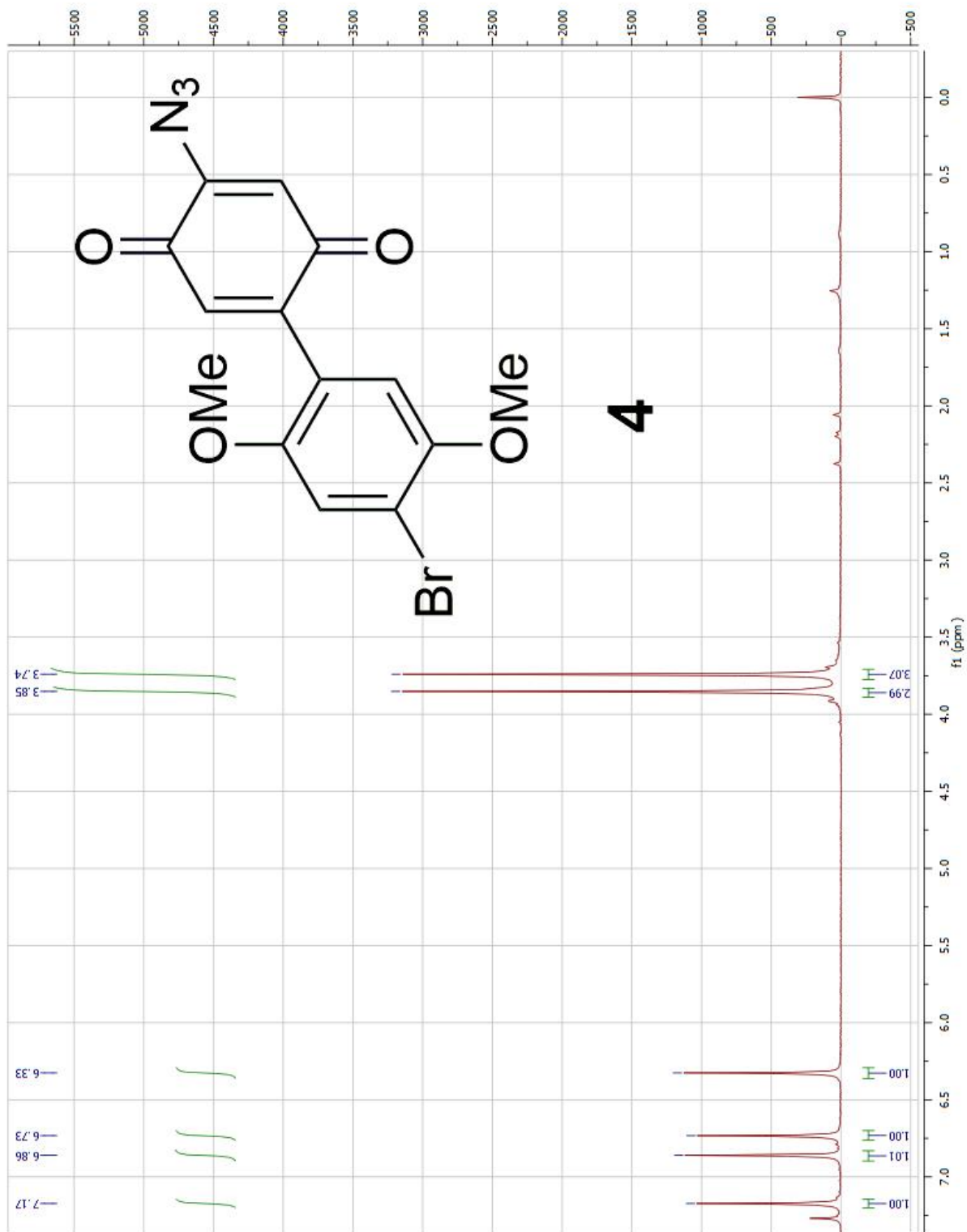
2,3-Dicyano-5-(4'-bromo-2',5'-dimethoxyphenyl)cyclohexa-2,5-diene-1,4-dione **3** $^1\text{H NMR}$



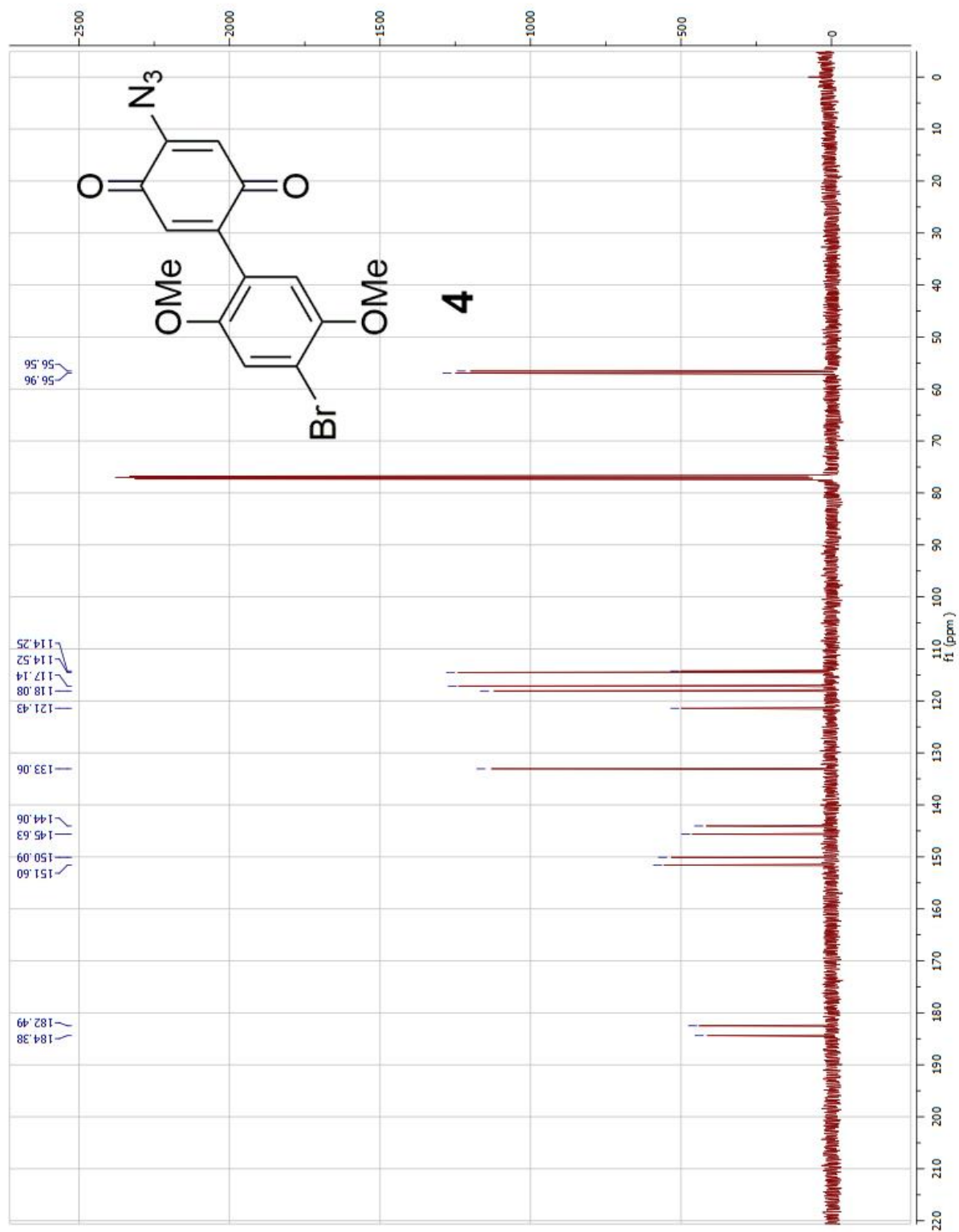
2,3-Dicyano-5-(4'-bromo-2',5'-dimethoxyphenyl)cyclohexa-2,5-diene-1,4-dione **3** ^{13}C NMR



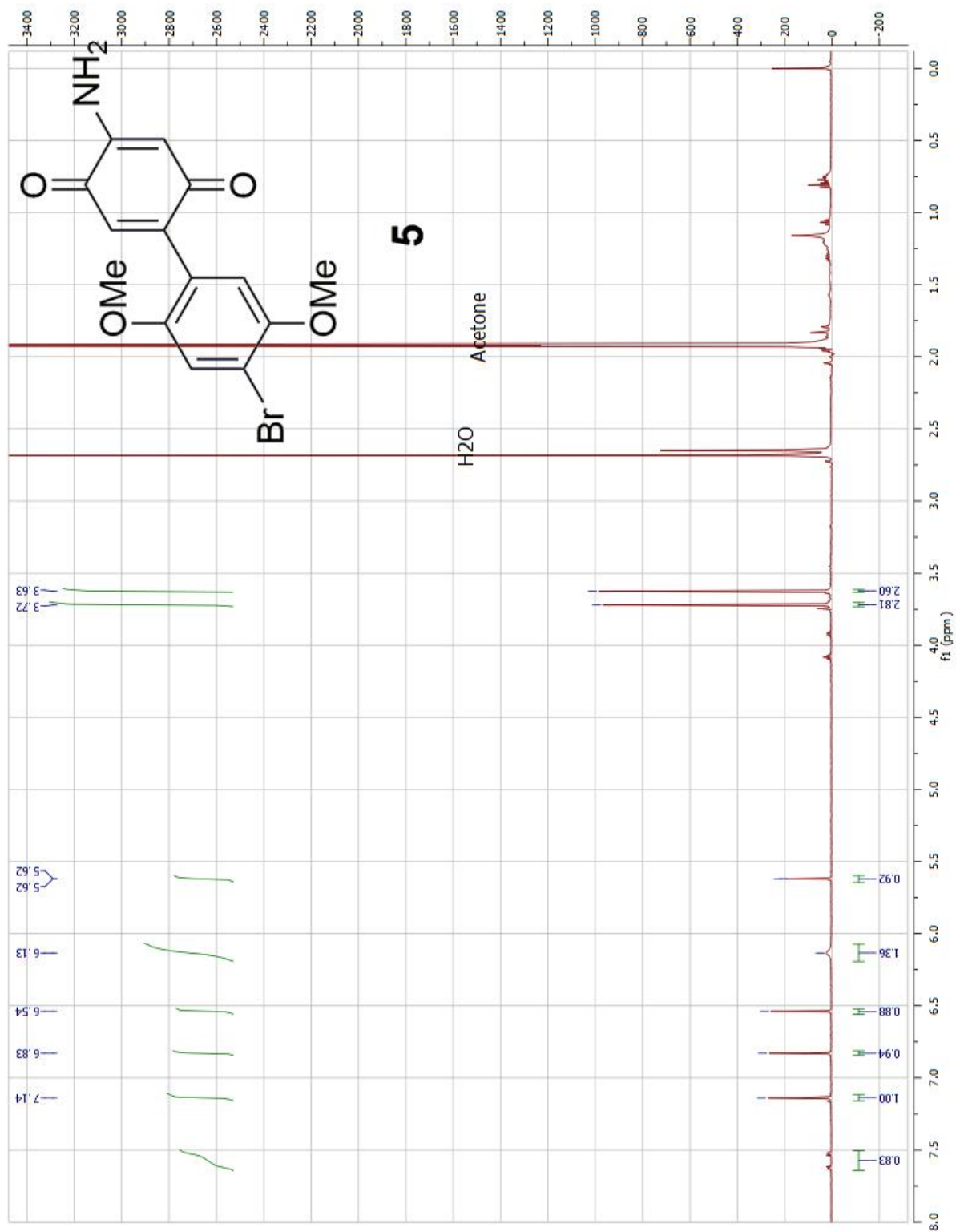
2-Azido-5-(4-bromo-2,5-dimethoxyphenyl)cyclohexa-2,5-diene-1,4-dione **4** ¹HNMR



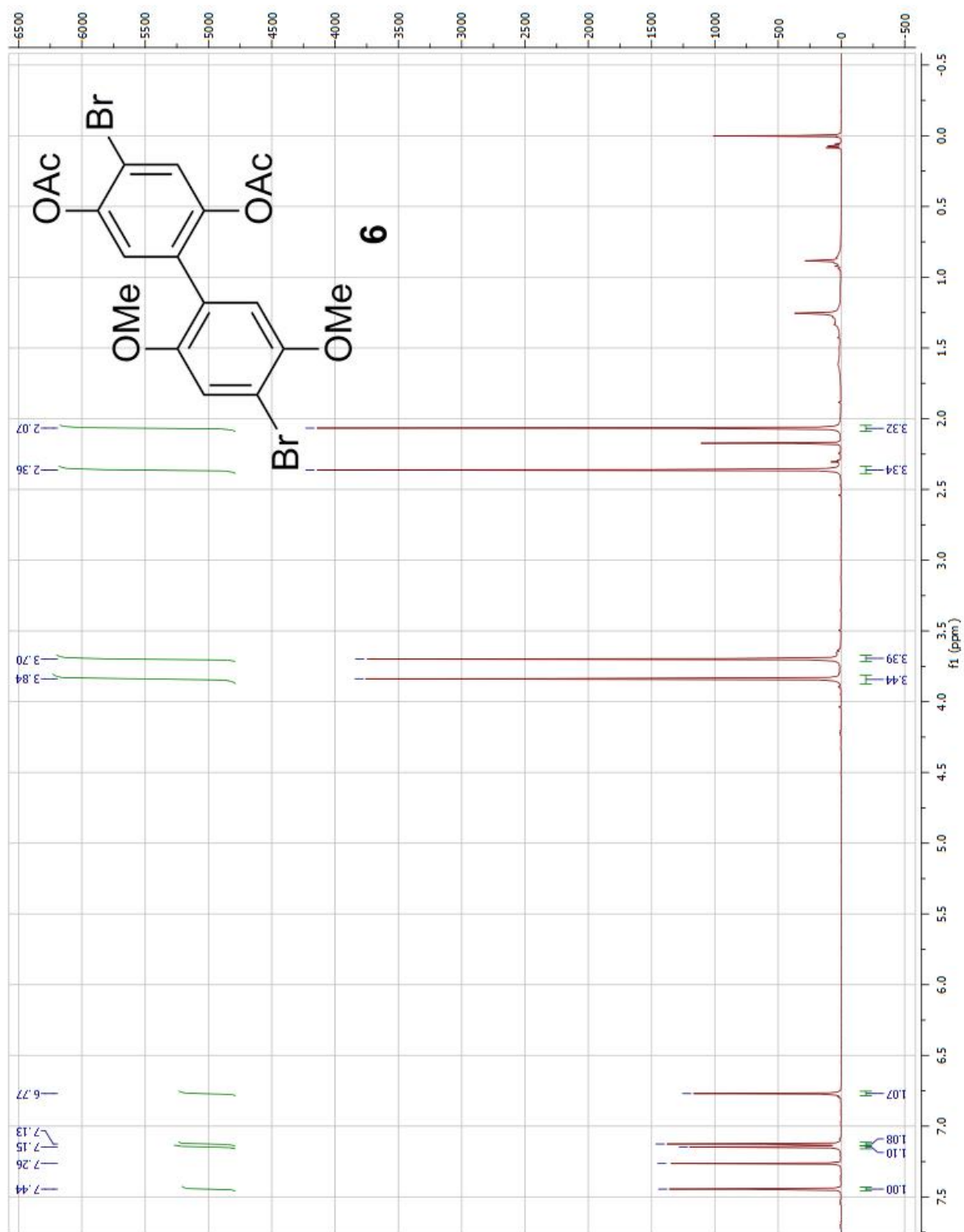
2-Azido-5-(4-bromo-2,5-dimethoxyphenyl)cyclohexa-2,5-diene-1,4-dione **4** ^{13}C NMR



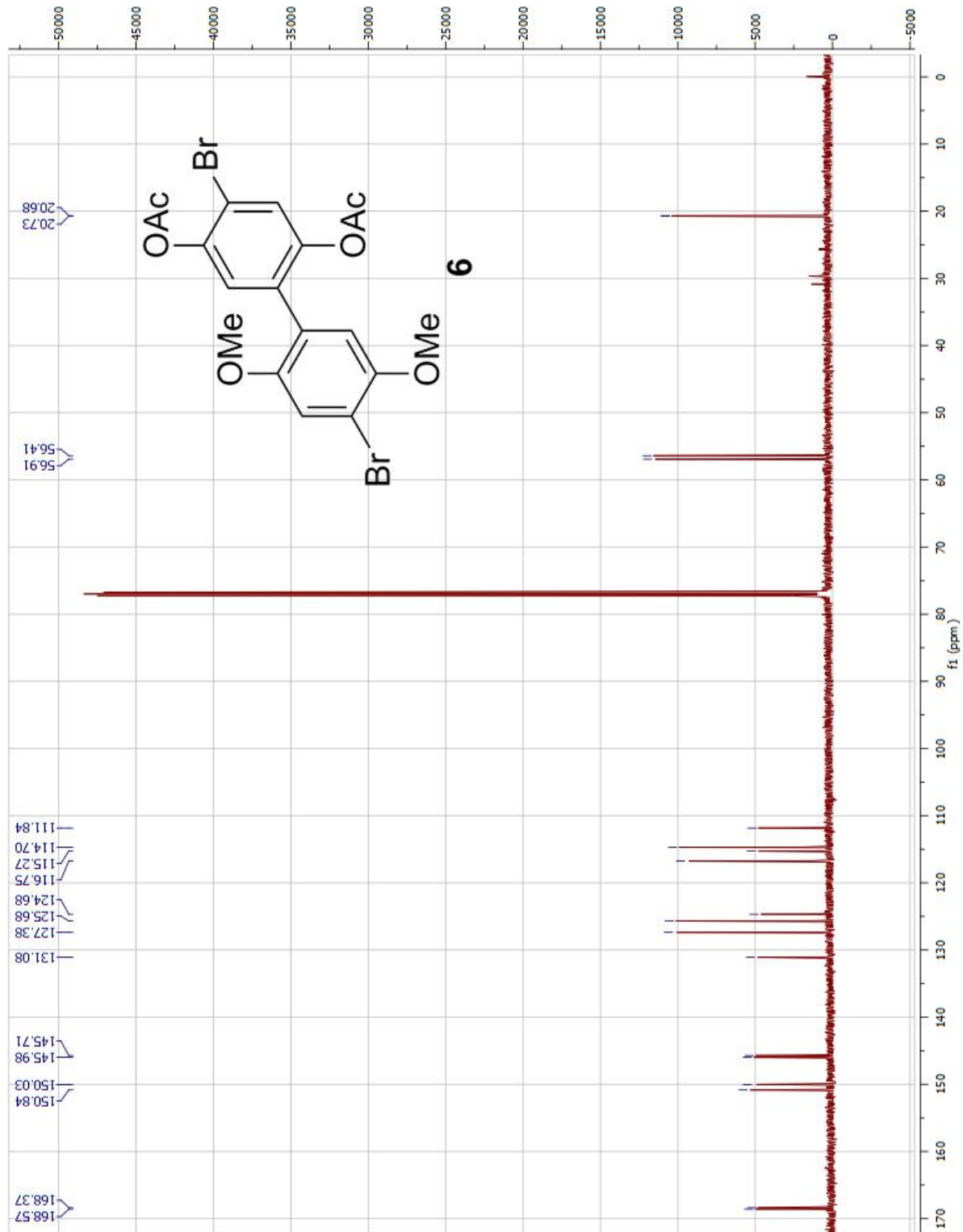
2-Amino-5-(4-bromo-2,5-dimethoxyphenyl)cyclohexa-2,5-diene-1,4-dione **5** ^1H NMR



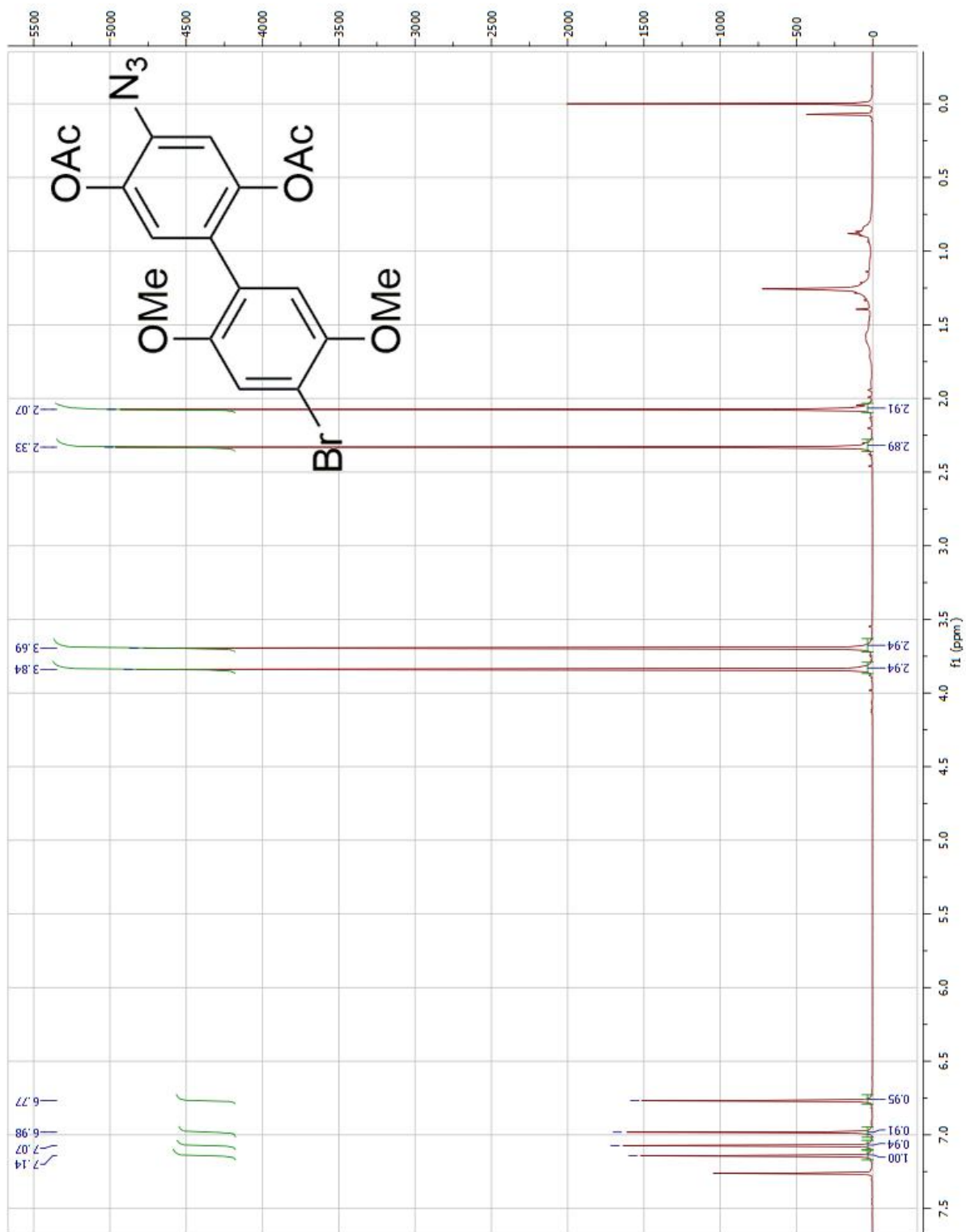
4-Bromo-4'-bromo-2',5'-dimethoxy-[1,1'-biphenyl]-2,5-diyl diacetate **10** ^1H NMR



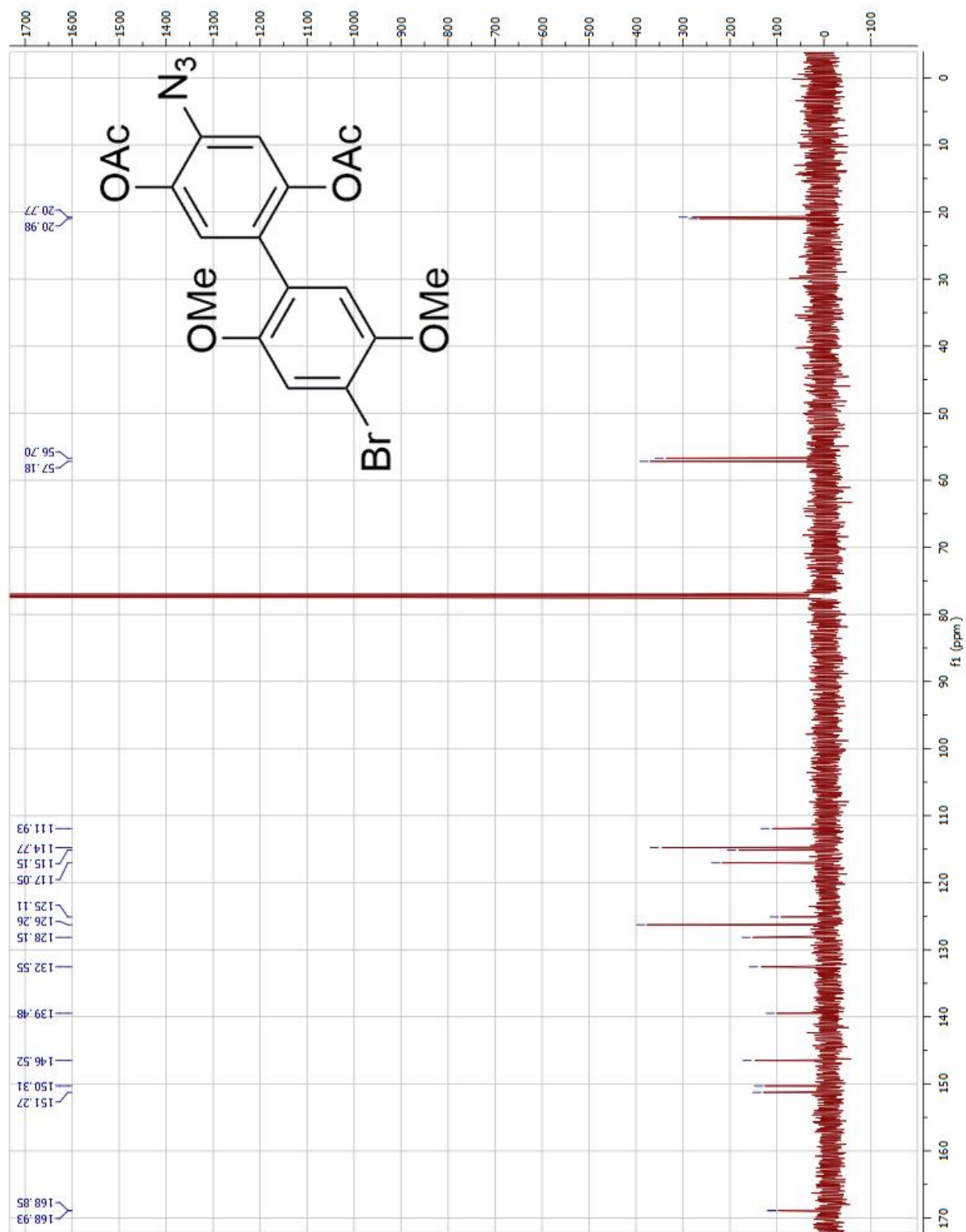
4-Bromo-4'-bromo-2',5'-dimethoxy-[1,1'-biphenyl]-2,5-diyl diacetate **10** ^{13}C NMR



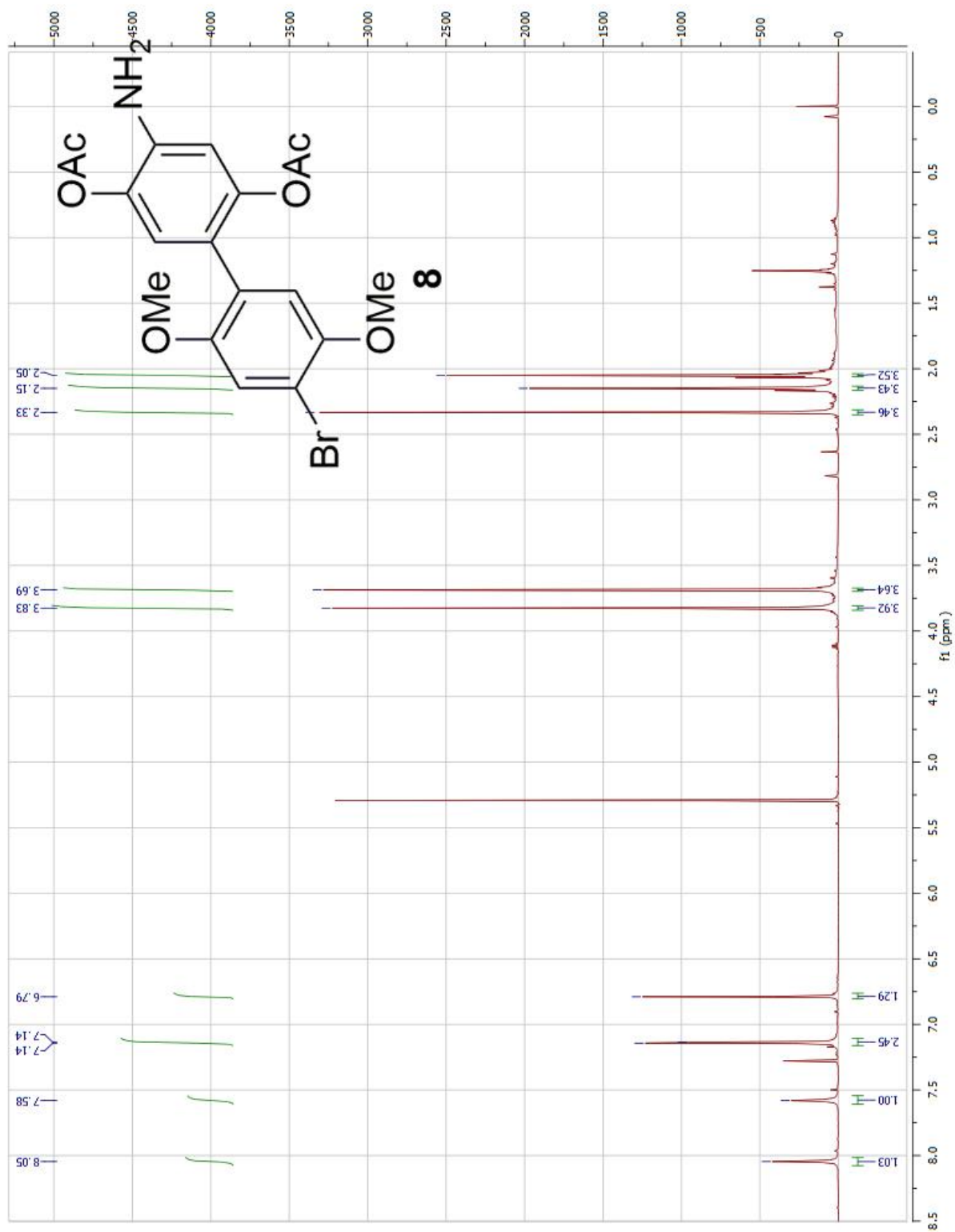
4-Azido-4'-bromo-2,5'-dimethoxy-[1,1'-biphenyl]-2,5-diyl diacetate **11** ¹HNMR



4-Azido-4'-bromo-2',5'-dimethoxy-[1,1'-biphenyl]-2,5-diyl diacetate **11** ^{13}C NMR



4-amino-4'-bromo-2',5'-dimethoxy-[1,1'-biphenyl]-2,5-diyl diacetate **12** ^1H NMR



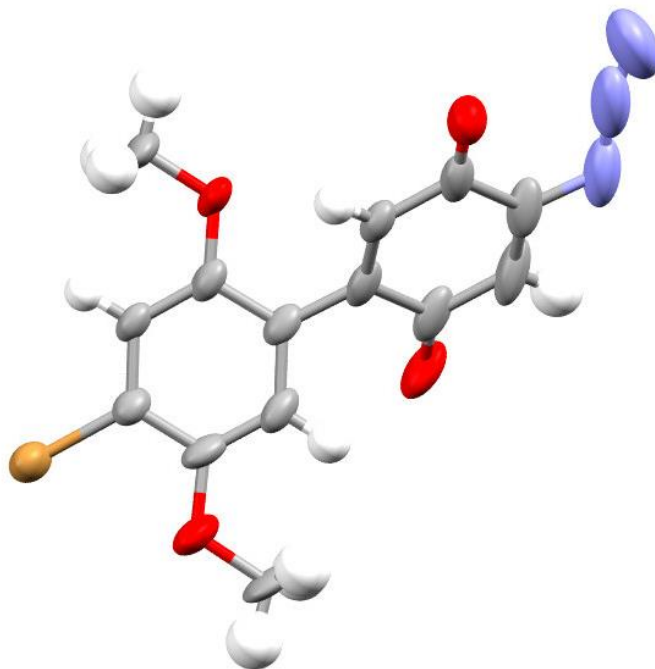


Figure 3.3 Crystal structure data for **4**. Ellipsoid display at 50% probability and fixed hydrogen diameter.

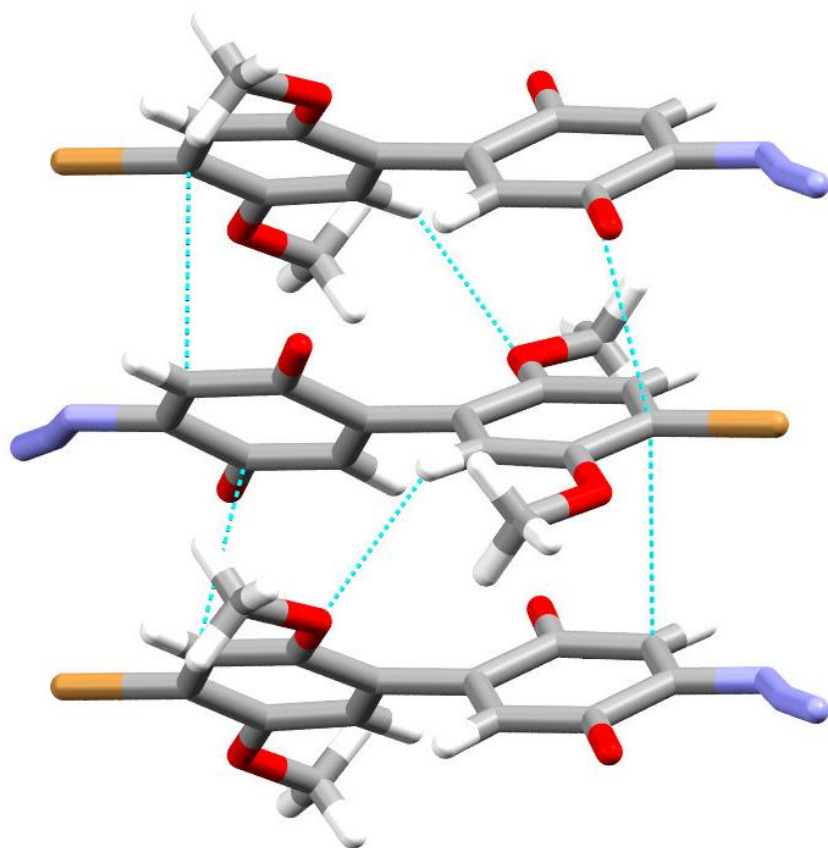


Figure 3.4 Crystal structure data for **4**, packing along *a* direction.

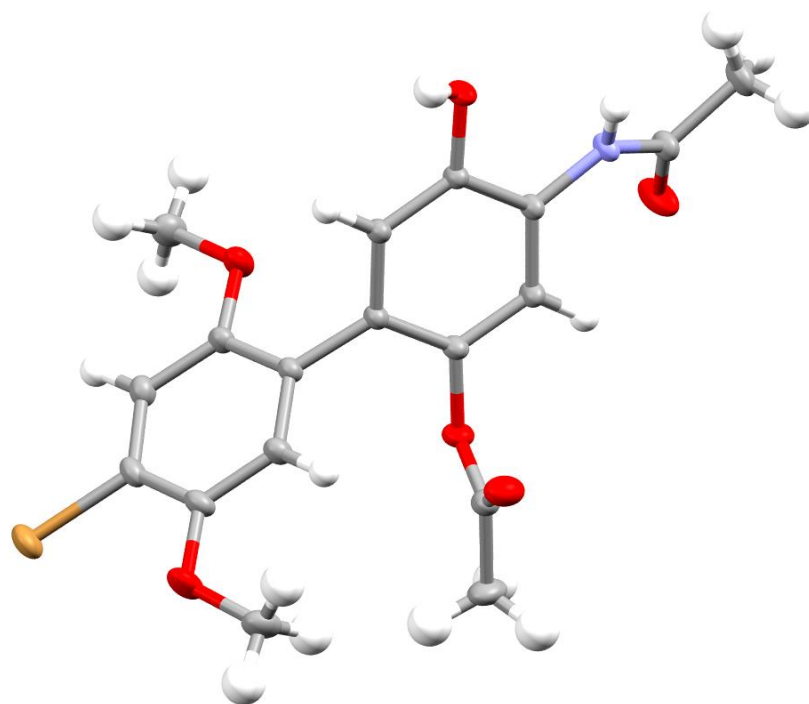


Figure 3.5 Crystal structure data for **10**. Ellipsoid display at 50% probability and fixed hydrogen diameter.

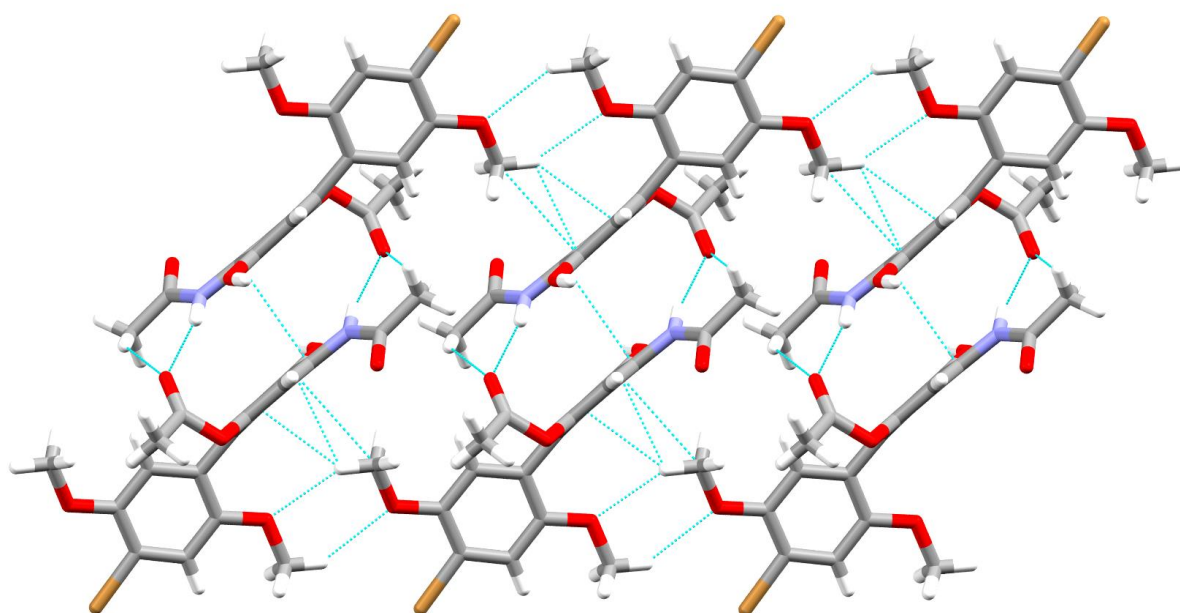


Figure 3.6 Crystal structure data for **10**, packing along *a* direction.

CHAPTER 4

SOLUTION AND CRYSTAL CHARACTERIZATION OF HBQS

Section 4.1 Experimental Validation of Calculations

Chapter 2 detailed the calculated physical and electronic properties of HBQ derivatives. In order to understand the geometry of the molecule, the minimum geometry was carefully determined. Estimates of the HOMO and LUMO eigenvalues as well as the distributions of their probabilities over the molecule were calculated as well. This information was used to make decisions about which derivative(s) to synthesize, based upon the ability of a molecule to selectively self-assemble on a gold substrate and maintain strong D and A orbital separation. Basic characterization of chemical identity was described in the experimental section of Chapter 3. This chapter contains analytical data obtained on the HBQ derivatives. Ultraviolet-visible (UV-Vis) absorption spectra and cyclic voltammetry behavior are presented alongside a discussion correlating their behavior to structure. UV-Vis spectra of the monomeric compounds, and some discussion of the transitions are presented, with reference to the data presented in the earlier chapters. Included within the discussion on the solution UV-Vis data are the shifts in λ_{\max} with the change in the quinone substituent. Following that are the electrochemical analyses of the redox behavior of the HBQ series of compounds.

Over the course of making each derivative, several compounds crystallized neatly enough to isolate single crystals. X-ray diffraction (XRD) crystallographic data for these single crystals were collected and analyzed by either Dr. Steven Kelley (Rogers Lab) or Dr. Deidra Gerlach

(Papish Lab). A discussion of the solid-state interactions within crystal structures for relevant compounds has been included. Finally, Marcus Johnson (Metzger group) performed analytical work on the HBQ molecules within a monolayer. An abridged summary of those data appears in Chapter 5.

Section 4.2 Ultraviolet-Visible Spectroscopy

Section 4.2.1 Experimental Details

Solution absorption spectra for different HBQ derivatives were recorded using 1 cm quartz cuvettes within a Varian Cary 100 spectrometer in the range 190–800 nm. Spectrophotometric grade acetonitrile was selected for its 190 nm cutoff; the concentration of each solution was 75 μM .

Section 4.2.2 Dimethoxybenzene and Benzoquinone

In order to properly interpret the electronic transitions of HBQ molecules in solution, it is necessary to establish comparative data for the constituent donor and acceptor parts of 2,5-dibromo-1,4-dimethoxybenzene and 2,5-dibromo-1,4-benzoquinone, respectively. The spectra presented within this section are used to validate the calculations presented in Chapter 2 and establish structure-property relationships.

The absorption spectra for 2,5-dibromo-1,4-benzoquinone and 2,5-dibromo-1,4-dimethoxybenzene are shown in Figure 4.1. Each has multiple absorption peaks in the scan range. Table 4.1 presents the wavelength of maximum absorption λ_{max} and the molar extinction coefficient ϵ at each λ_{max} . Both molecules have similar excitation wavelengths for their lowest energy ($n \rightarrow \pi^*$) transitions. 2,5-Dibromo-1,4-benzoquinone has a higher molar absorptivity for this transition. Each molecule has a shoulder absorption characteristic of aromatic compounds at about 250 nm. Both spectra show $\pi \rightarrow \pi^*$ absorption at ~ 200 nm, with that of 2,5-dibromo-1,4-

benzoquinone appearing at 192 nm and 2,5-dibromo-1,4-dimethoxybenzene with a dual peak at 206/200 nm.

It was predicted in Chapter 2 that both 2,5-dibromo-1,4-dimethoxybenzene and 2,5-dibromo-1,4-benzoquinone would have roughly similar relative distribution of FMO eigenvalues in the gas phase. These measurements help to substantiate that claim by demonstrating that they absorb at relatively similar wavelengths. As predicted in Chapter 2, the HOMO of the dimethoxybenzene lies higher in energy than the HOMO of benzoquinone, consistent with dimethoxybenzene's classification as an electron donor. The LUMO of benzoquinone lies lower in energy than that of dimethoxybenzene, consistent with benzoquinone's classification as an electron acceptor. The next section will illustrate the importance behind understanding absolute FMO eigenvalues when the donor and acceptor systems are co-dissolved but not conjugated.

Section 4.2.3 HBQ Absorption Spectra

Absorption spectra were recorded for HBQ molecules as described above. Analysis presented in Chapter 2 predicted that the HBQ class of molecules would have lower HOMO→LUMO transition energies than either of the monomers by themselves, as the HBQ FMO eigenvalues should be a linear combination of the monomer eigenvalues. Figure 4.2 depicts a schematic representation as predicted by the calculations.

Table 4.1 Absorbance details of 2,5-dibromobenzoquinone and 2,5-dibromo-1,4-dimethoxybenzene.

Molecule	λ_{\max} (nm)	ϵ (cm⁻¹·M⁻¹)
2,5-dibromobenzoquinone	339	293
	283	13000
	192	16600
2,5-dibromo-1,4-dimethoxybenzene	300	6266
	206	30906
	200	31373

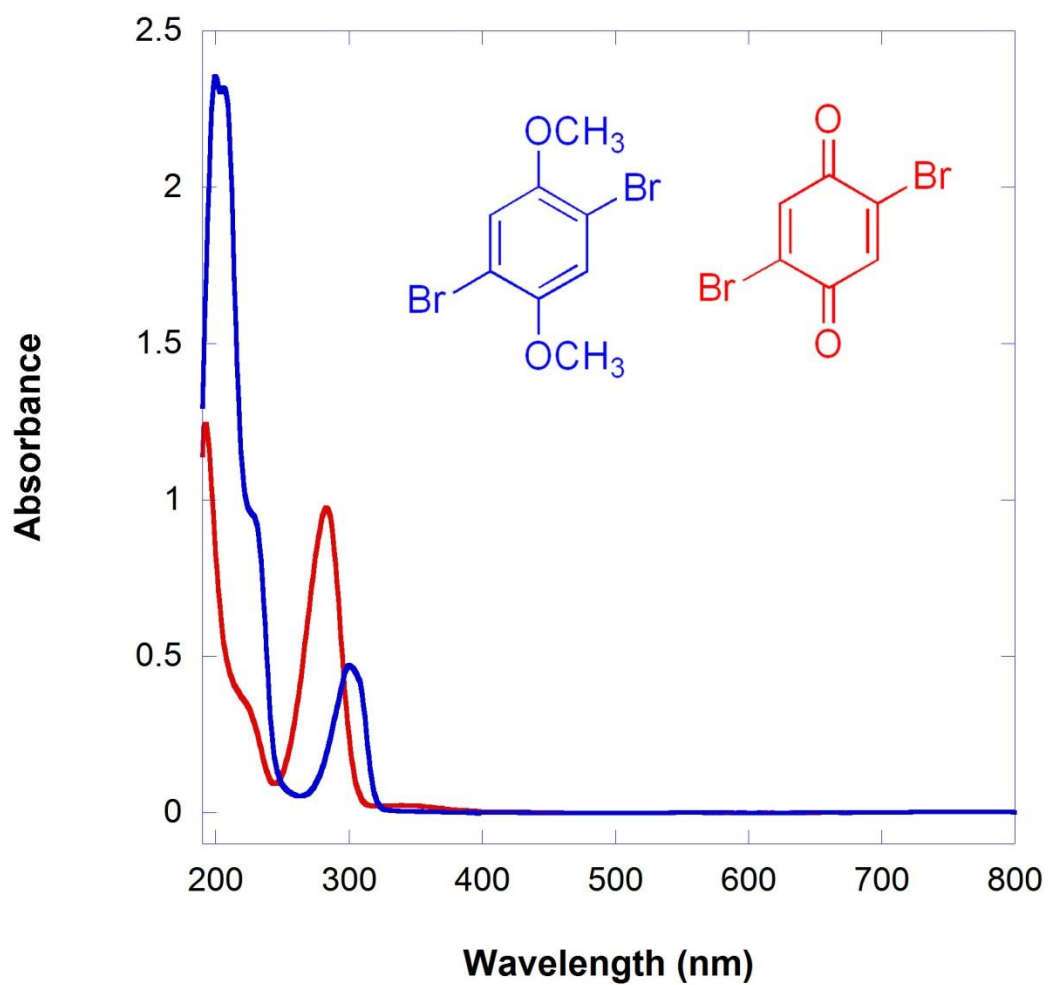


Figure 4.1 Absorption spectrum of 2,5-dibromo-1,4-dimethoxybenzene (blue) compared with 2,5-dibromobenzoquinone (red)

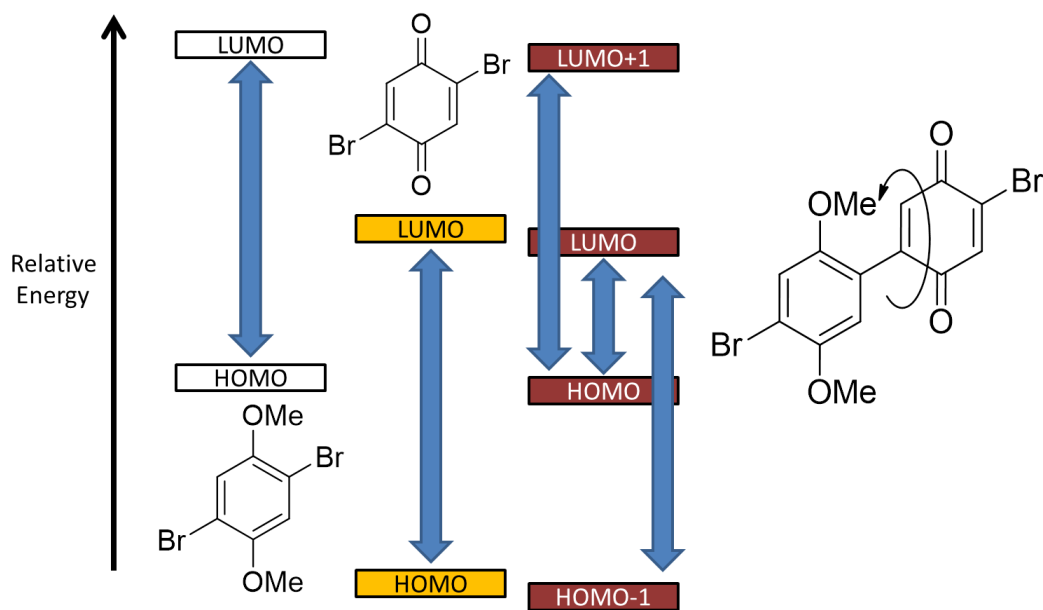


Figure 4.2 Calculated energy gaps of the donor and acceptor portions of the molecules

The low-energy absorption for the HOMO→LUMO transition was observed for all tested HBQ derivatives. In Figure 4.3, a low-energy transition at 452 nm is apparent. Table 4.2 summarizes all spectral data collected for the HBQ derivatives and related compounds. The absorption spectra of the HBQ “halves” show similar transitions in the high-energy region, but individually lack the low-energy transitions seen in the linked HBQ molecules corresponding to the HBQ HOMO-LUMO gap, consistent with an interacting D—A system. The HBQ molecule was predicted to contain both of these characteristics with a high-lying HOMO and a low-lying LUMO.

The HOMO-1 and LUMO+1 orbitals of HBQ are localized on the benzoquinone and dimethoxybenzene rings, respectively. From the calculations outlined in Chapter 2, the data suggests that FMO transitions in each of the monomers would have similar energetic magnitudes as HOMO→LUMO+1 transitions and HOMO-1→LUMO in HBQ. We see this confirmed in the electronic transitions (Figure 4.3). High-energy transitions exist for the BrHBQBr at 209 and 299 nm, which corresponds well with expected values for the intra-ring absorptions. Conversion of the solution absorption wavelengths are well matched with calculated gas-phase excitation energies.

Inspection of the ϵ value for HBQ HOMO→LUMO transition shows that the absorption is on a similar order of magnitude for that of an interaction between non-conjoined D···A intermolecular electron transfer “exciplexes.”^{124,125} Formation of the D⁺—A⁻ (in either the exciplex or HBQ molecule) excited state induces a change in the dipole moment, whereas intra-ring excitement does not. This leads to the small observed ϵ for HBQ HOMO→LUMO transition as compared to HOMO→LUMO+1 and HOMO-1→LUMO transitions.

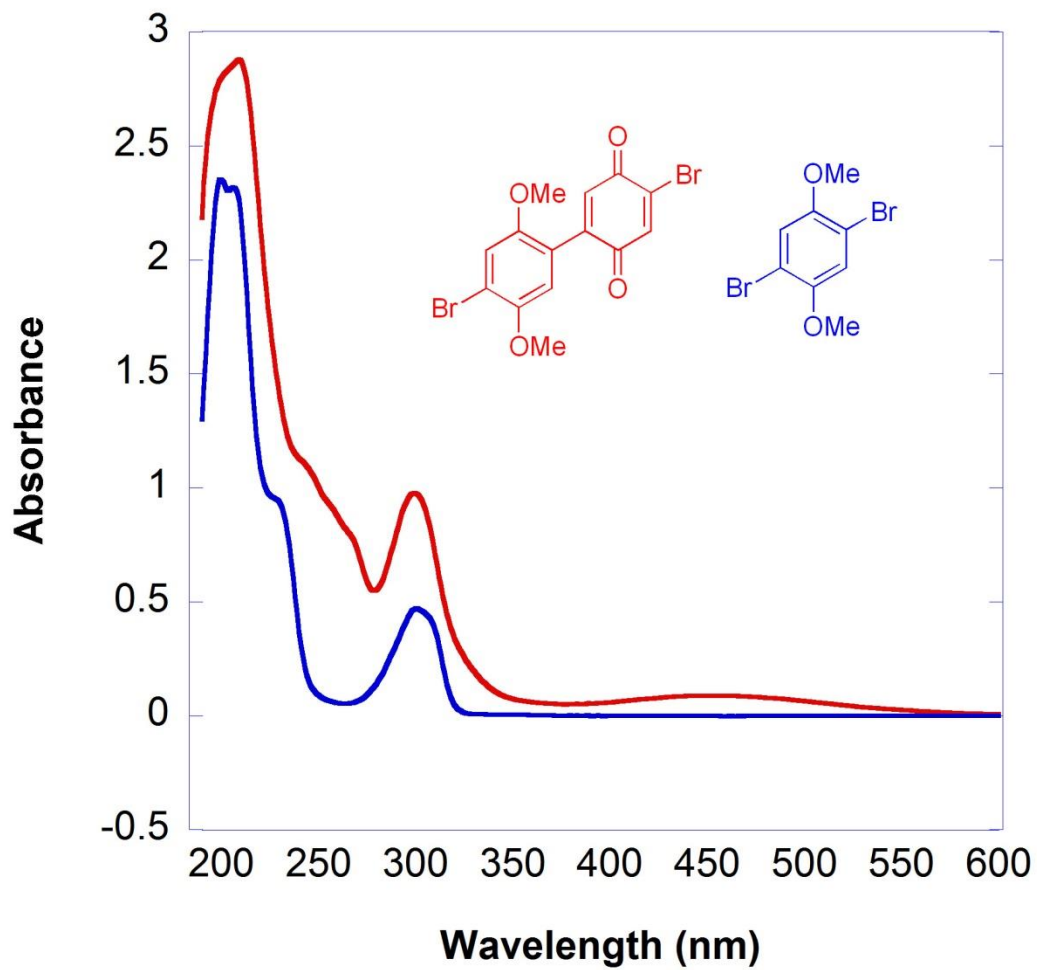


Figure 4.3 Comparison of UV-Vis absorption spectra of BrHBQBr (red) and 2,5-dibromo-1,4-dimethoxybenzene (blue)

Table 4.2 Absorbance details of various HBQ derivatives

Molecule	λ_{\max} (nm)	ϵ
BrHBQBr	452	1160
	299	13013
	209	38386
BrHBQH ₂ (CN) ₂	352	8480
	211	39400
BrHBQ(CN) ₂	556	920
	306	5920
	249	19653
	197	35346
BrHBQNH ₂	395	2693
	291	1044
	206	36613

The exact λ_{max} for the low-energy HOMO→LUMO transition is highly dependent on the 4-substituent on the quinone; the low-energy absorption redshifts by ~100 nm from BrHBQBr to BrHBQ(CN)₂ (Figure 4.4) or BrHBQNH₂ (Figure 4.5). This supports the predictions in Chapter 2 that BrHBQ(CN)₂ has the smallest predicted absorption energy. Figure 4.5 illustrates the effect of adding an electron donor onto the quinone. Electron density from the amine is donated back into the quinone system, increasing the gap between the FMOs, and thus blueshifting the HOMO→LUMO transition with respect to the HBQ backbone. This is consistent with the pattern found in the FMO energies presented in Chapter 2, Table 2.1.

In Chapter 2, it was asserted that reducing HBQ derivatives will affect the electronic characteristics of the molecule. In theory, reduction of the quinone to an aromatic ring would raise the LUMO beyond the energy range associated with the benzoquinone. Instead, the LUMO would exist in the aromatic range as the molecule becomes a D—D system, and the FMOs would delocalize across the whole molecule. The absorption spectrum for BrHBQH₂(CN)₂ as compared to BrHBQ(CN)₂ appears in Figure 4.6. The transitions are consistent with FMO transitions as seen in other HBQ molecules, as well as 2,5-dibromo-1,4-benzoquinone and 2,5-dibromo-1,4-dimethoxybenzene. However, the spectrum for BrHBQH₂(CN)₂ lacks the low-energy transition ~450 nm characteristic of D—A HBQ molecules. This outcome is consistent with expectations. Moving the LUMO level up in potential energy creates a conduction barrier that should prevent conduction through BrHBQH₂(CN)₂ via the Aviram and Ratner model described in Chapter 1.

A monolayer UV-Vis spectrum for BrHBQ(CN)₂ was collected by Marcus Johnson and appears in Figure 4.7. The monolayer spectrum shows a transition bathochromically shifted from 300–350 nm, possibly due to nitrile n→π* stabilization on the surface. The low-energy transition is not visible as a monolayer. This result is inconclusive, and may likely be due to the weak ϵ .

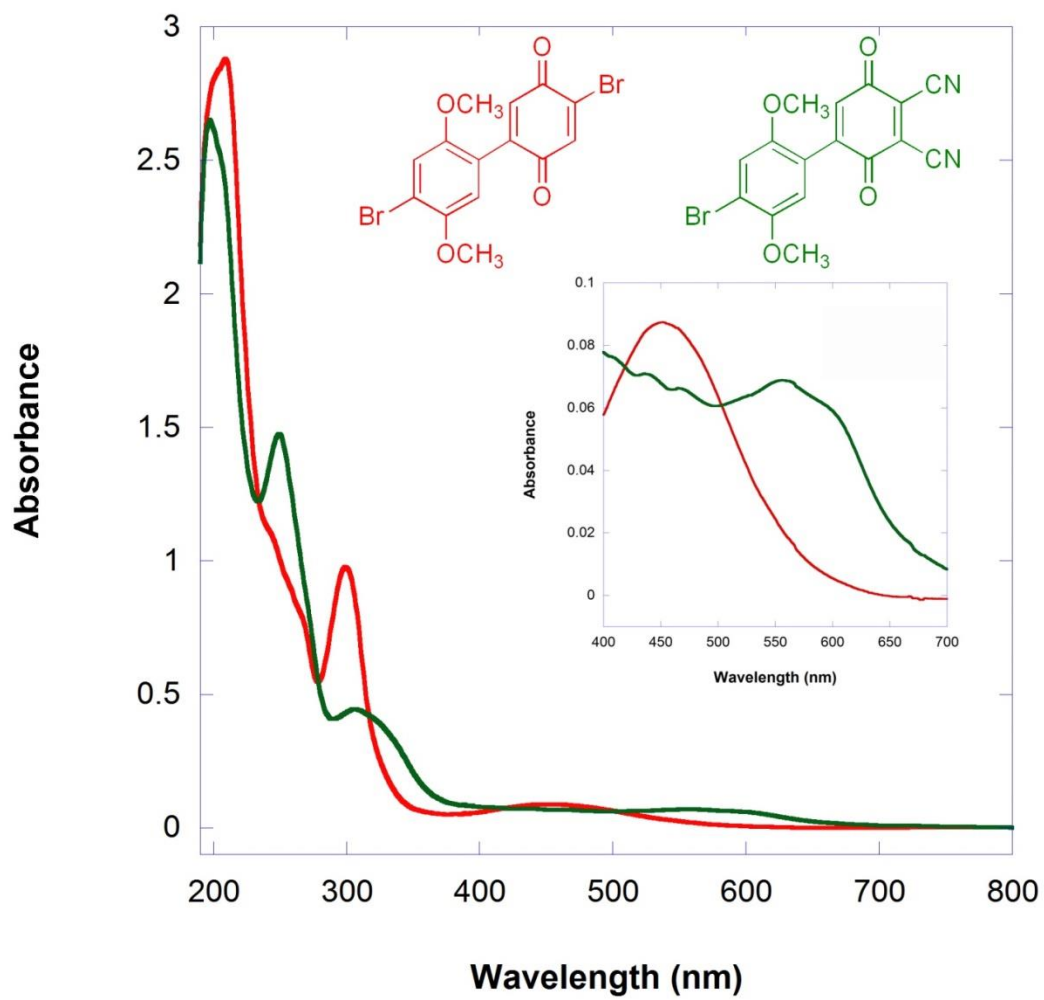


Figure 4.4 Comparison of UV-Vis absorption spectra of BrHBQBr (red) and BrHBQ(CN)₂ (green)
Inset: Expansion of low-energy bands

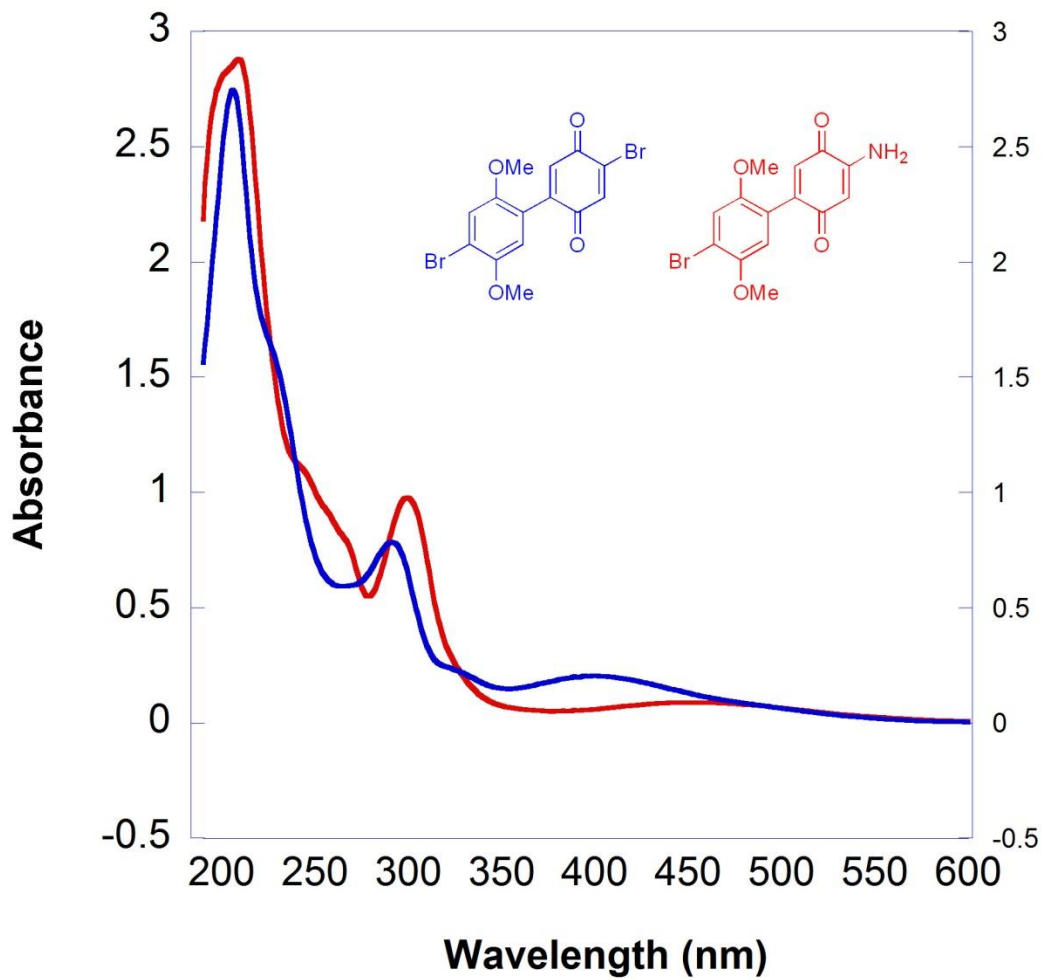


Figure 4.5 Comparison UV-Vis absorption spectra of BrHBQBr (red) and BrHBQNH₂ (blue). Note the higher energy HOMO→LUMO transition for BrHBQNH₂.

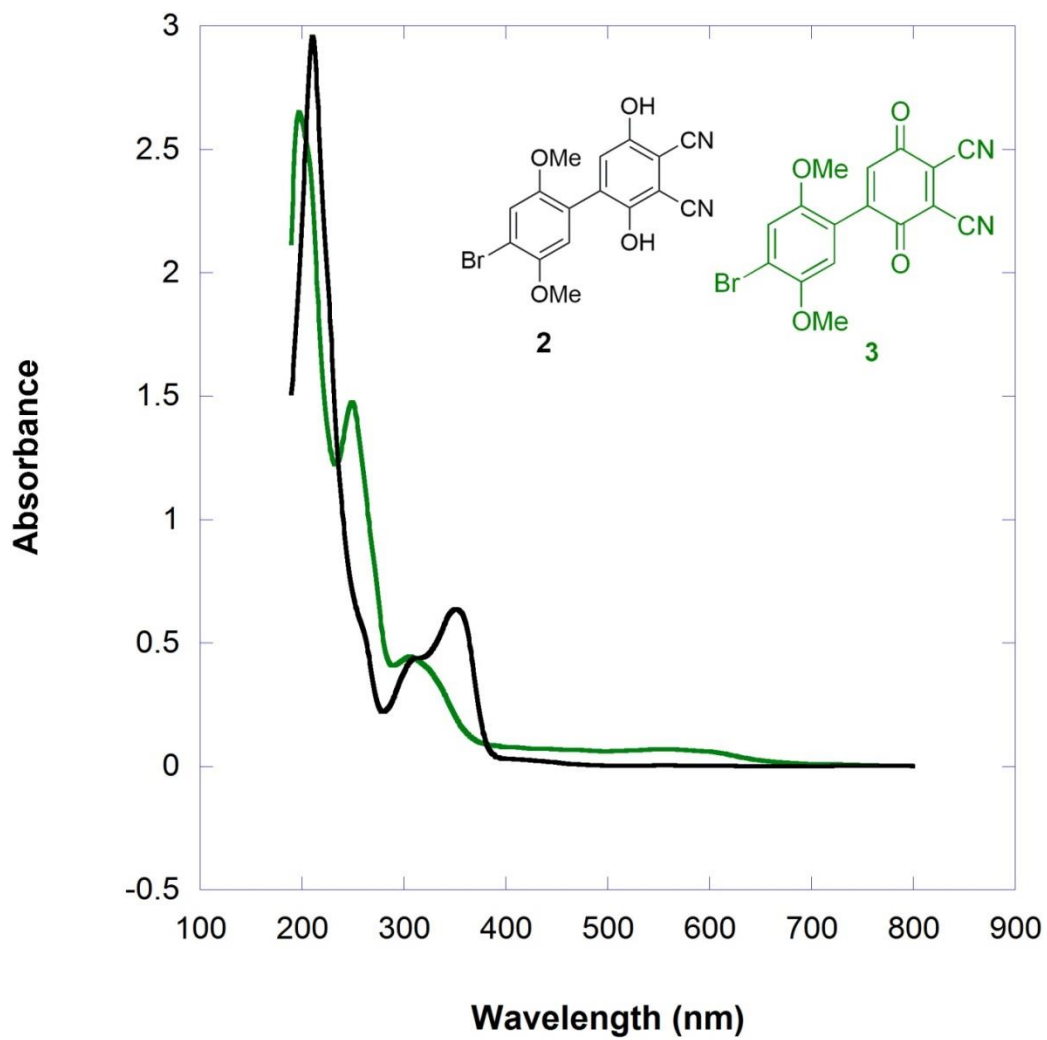


Figure 4.6 Comparison UV-Vis absorption spectra of BrHBQ(CN)₂ (green) and BrHBQH₂(CN)₂ (black).

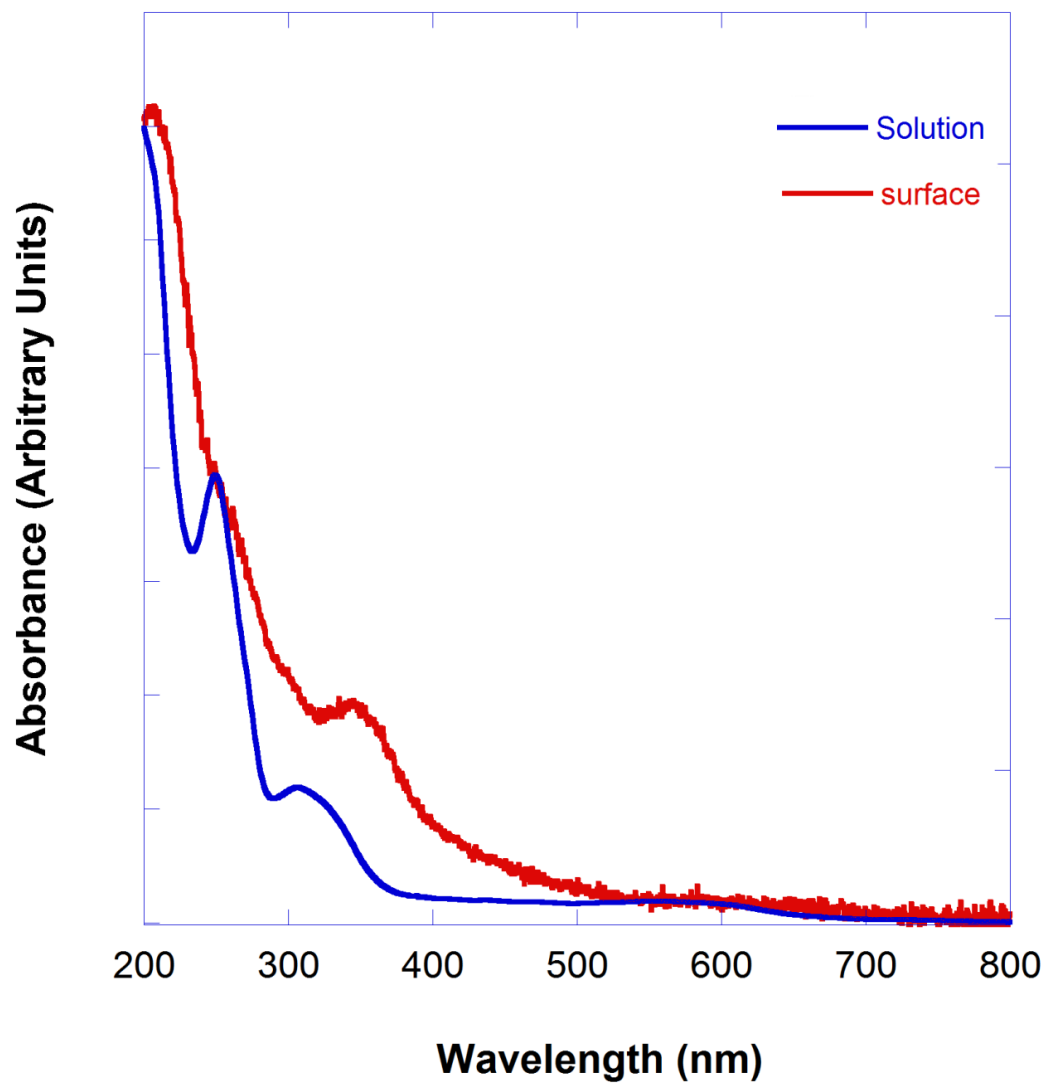


Figure 4.7 Comparison UV-Vis absorption spectra of BrHBQ(CN)₂ in solution (blue) vs. as a monolayer supported on a glass slide (red).

Section 4.3 Cyclic Voltammetry

Section 4.3.1 Experimental Details

Cyclic voltammograms were measured in a CH Instruments 600 E potentiostat with a 7.07 mm² glassy carbon working electrode (GCE), a graphite counter electrode, and a saturated calomel electrode (SCE) as the reference. Data were recorded at room temperature under inert conditions using 1 mM solutions in dry, degassed acetonitrile with 0.1 M Bu₄NPF₆ as the supporting electrolyte. A sample of 1mM ferrocene was used as an external reference on the same system. In order to minimize any possibility of atmospheric contamination, the measurements were run in a glove box.

Section 4.3.2 Dimethoxybenzene and Benzoquinone Electrochemical Characteristics

As in Section 4.2, it is necessary to establish the behavior of simple molecules by which to then compare the more complex behavior of HBQ molecules. Three derivatives of dimethoxybenzene were analyzed to determine the effect that bromine substitution has on electrochemical behavior. 1,4-Dimethoxybenzene derivatives have one reversible redox peak in the solvent window (Figure 4.8). Outside of the solvent window, decomposition of the acetonitrile occurs and the currents become convoluted with side reactions, particularly once the solvent window is reached (not shown). Bromine atoms withdraw electron density from the aromatic ring, which stabilizes it with respect to vacuum and makes oxidation progressively more difficult as demonstrated by the increasing oxidation potential between 1,4-dimethoxybenzene, 2-bromo-1,4-dimethoxybenzene and 2,5-dibromo-1,4-dimethoxybenzene (Table 4.3). No significant current attributable to the analyte was observed under negative potential bias.

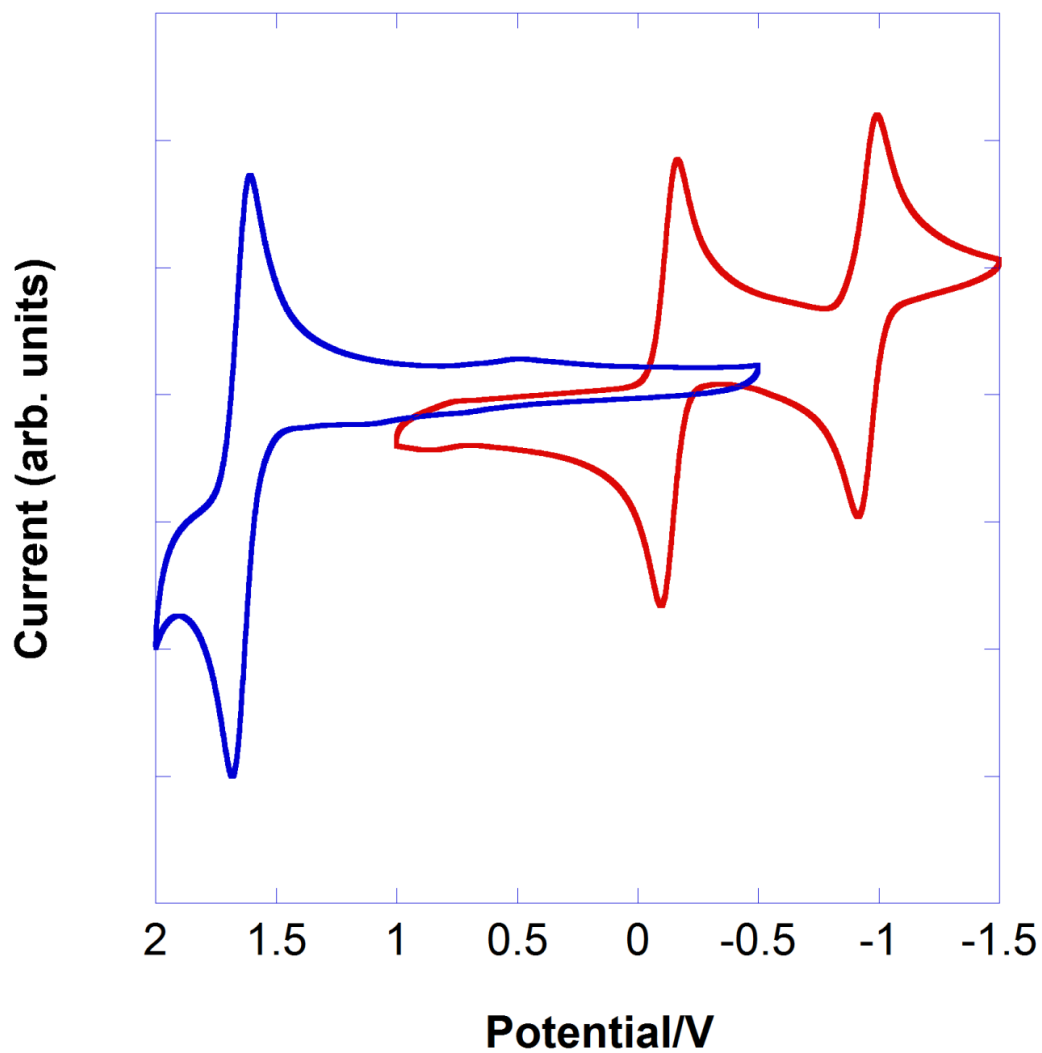


Figure 4.8 Comparison of CVs of 2,5-dibromo-1,4-dimethoxybenzene (blue) and 2,5-dibromo-1,4-benzoquinone.

Both 1,4-dimethoxybenzene and 2,5-dibromo-1,4-dimethoxybenzene show fully reversible behavior, even in scan ranges that extend to ± 2 V. Oxidation of 2-bromo-1,4-dimethoxybenzene is not fully reversible at the scan rate measured (Figure 4.9), possibly due to nucleophilic attack at the C5 *para* position to the bromine. This is evident as the cathodic peak current on reducing the oxidized 2-bromo-1,4-dimethoxybenzene ring is unequal to the anodic peak for the oxidation. Attempts to synthesize 2-bromo-1,4-benzoquinone were unsuccessful, so the same substitution effects for the quinone rings as dimethoxybenzene were not attempted. 2,5-Dibromo-1,4-benzoquinone exhibits two reversible one-electron reductions (Figure 4.8), which is a well-known aspect of quinone chemistry.^{126,127} Thus, the semiquinone radical anion is produced first, followed by the singlet dianion. An oxidation current does start to appear around +2 V; however, it is not reversible (not shown).

In preparation for electrochemical studies of reduced HBQH₂, 2,5-dibromo-1,4-hydroquinone was characterized in solution. In agreement with previously published work characterizing hydroquinone in non-aqueous solvents,¹²⁸ scanning in an initially anodic direction showed complicated redox behavior in the potential window (Figure 4.10). The anodic peak current at 1.281 V is irreversible, but a cathodic peak current at 0.026 V may be the same species as found by Sharma.¹²⁸ Due to this complication, it was predicted that limited useful information would come from testing the HBQH₂ molecule, so this was not attempted.

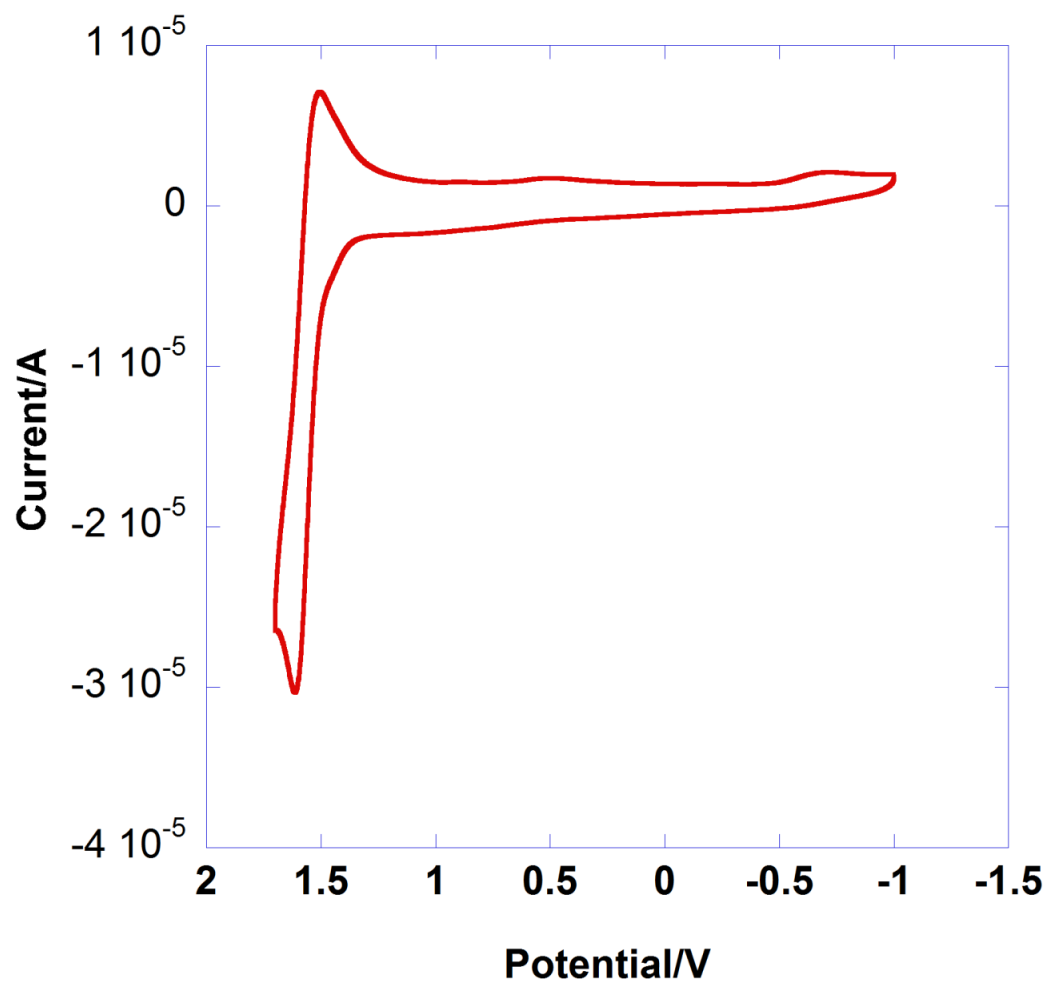


Figure 4.9 CV of 2-bromo-1,4-dimethoxybenzene.

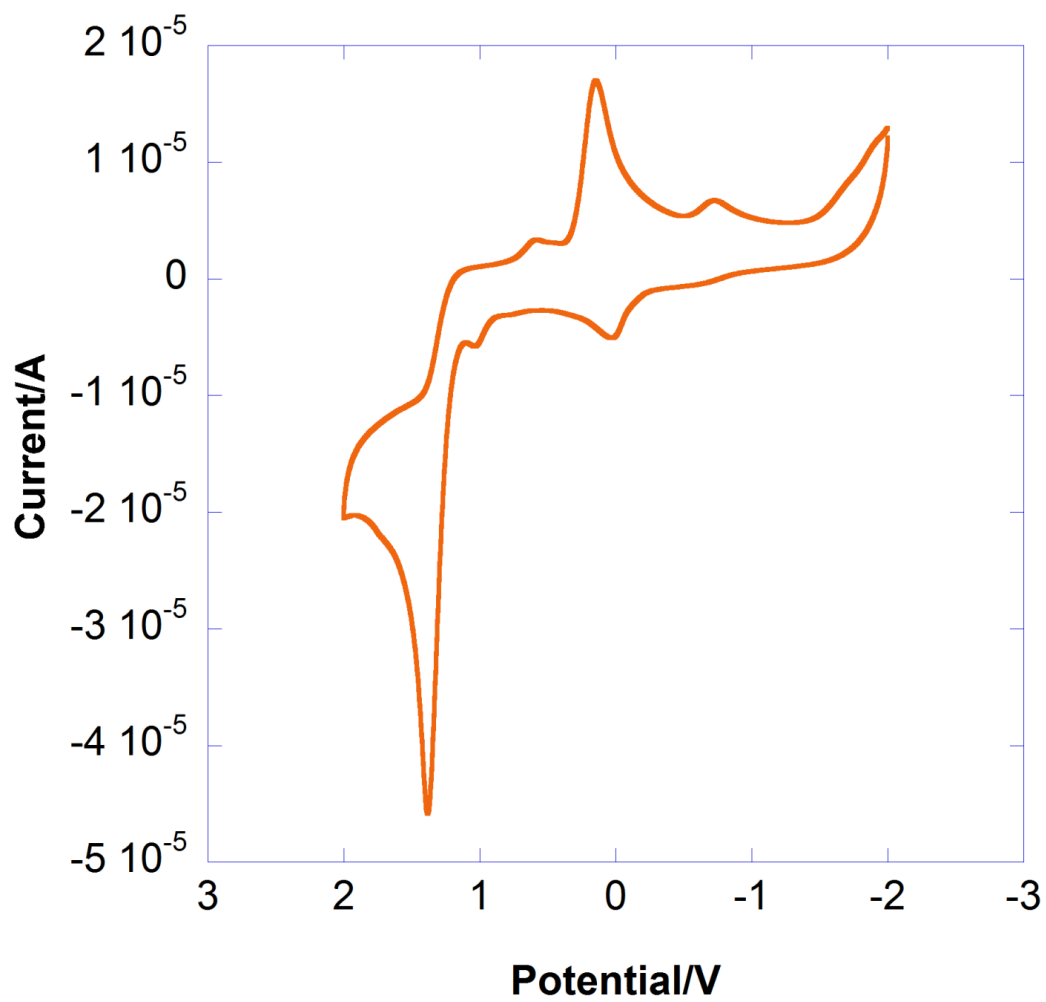


Figure 4.10 CV of 2,5-dibromo-1,4-hydroquinone. Complex redox behavior suggests many reactions in solution.

Table 4.3 Peak Potentials (V vs. SCE)

Molecule	${}^1E_{1/2}^R$	${}^2E_{1/2}^R$	${}^1E_{1/2}^O$
1,4-dimethoxybenzene	—	—	1.323
2-bromo-1,4-dimethoxybenzene	—	—	1.459
2,5-dibromo-1,4-dimethoxybenzene	—	—	1.547
2,5-dibromo-1,4-benzoquinone	-0.235	-1.058	—

Section 4.3.2 HBQ Electrochemical Characteristics

It remains important to determine the electrochemical characteristics of HBQ derivatives, because spectral characteristics alone cannot demonstrate by themselves how FMOs influence one another with respect to charge transfer.¹²⁹ Leading from the predictions in Chapter 2 and preliminary results demonstrated in Section 4.2, the data so far has supported the idea that dimethoxybenzene derivatives have distinct behavior separate from that of benzoquinone derivatives. Fully conjugated polycyclic systems like naphthoquinones show similar characteristic two single-electron reductions, but lack an accessible oxidation typical for aromatic compounds.¹³⁰⁻¹³² Decoupling the ring orbitals, and thus breaking conjugation, should present behaviors characteristic of dimethoxybenzene and benzoquinone, as seen in the previous section.

Table 4.4 presents the redox potentials of tested HBQ derivatives. BrHBQBr showed behaviors that resemble each of the respective components' subunits— there was a single reversible oxidation peak similar to that of dimethoxybenzene and two reversible reduction peaks resembling benzoquinone (Figure 4.11, Scheme 4.1). The oxidation potential of BrHBQBr is decreased with respect to 2,5-dibromo-1,4-benzoquinone by 78 mV, and reduction potentials are increased by 113 mV apiece. The oxidation peak is intermediate to 2-bromo-1,4-dimethoxybenzene and 2,5-dibromo-1,4-dimethoxybenzene, consistent with the idea that although the quinone ring is supposed to be electron-withdrawing, it is not fully deconjugated with the dimethoxybenzene ring because of the twist angle for the C—C biphenyl bond. This supports the calculations presented in Chapter 2, where the HBQ molecules have a HOMO on the order of dimethoxybenzene, but a LUMO on the order of benzoquinone. This allows both orbitals to be present within the sweep window.

Table 4.4 Peak Potentials (V vs. SCE)

Molecule	${}^1E_{1/2}^R$	${}^2E_{1/2}^R$	${}^1E_{1/2}^O$
BrHBQBr	-0.348	-1.171	1.469
BrHBQ(Br) ₂	-0.411	-1.233	1.312
BrHBQ(CN) ₂	-0.046	-0.856	1.197
BrHBQNH ₂	-0.703	-1.437	—*

*While an onset potential is observed, the electron transfer is irreversible so no $E_{1/2}$ is observable.

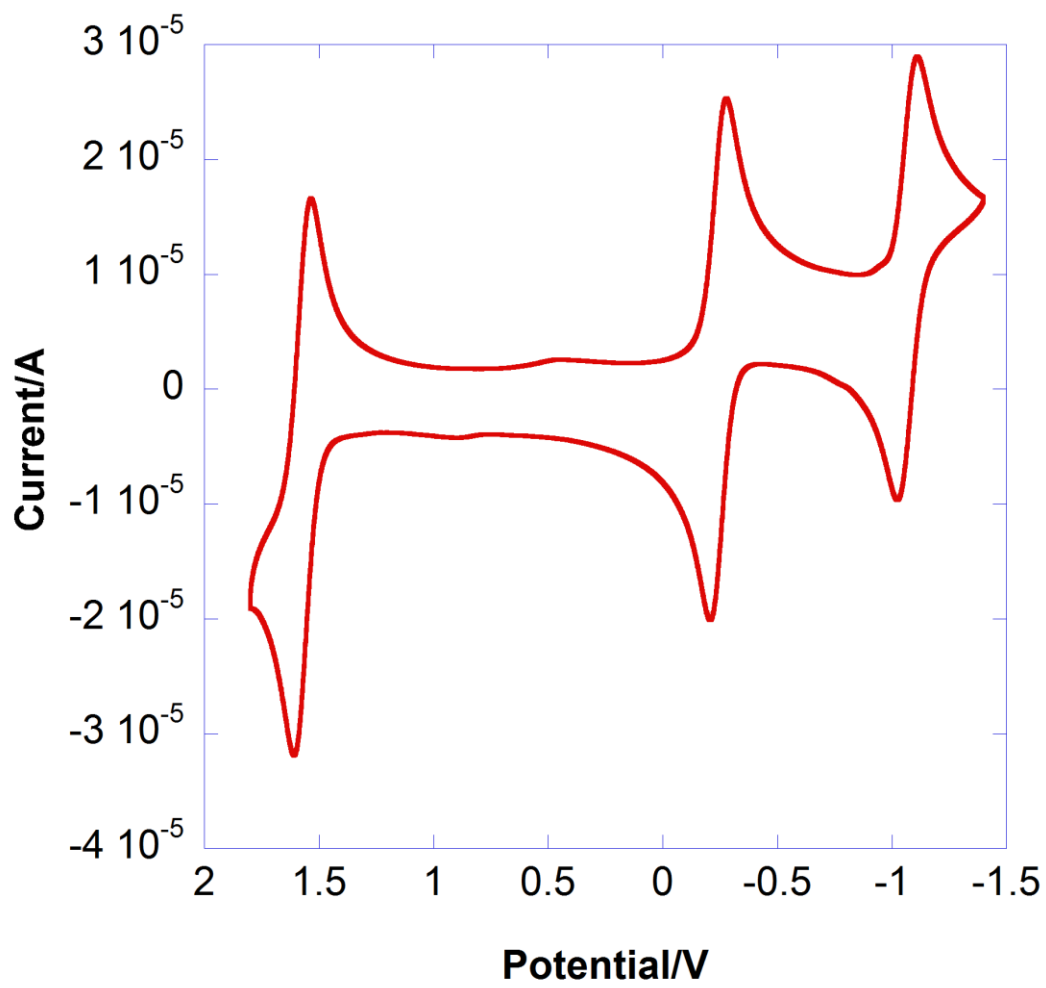
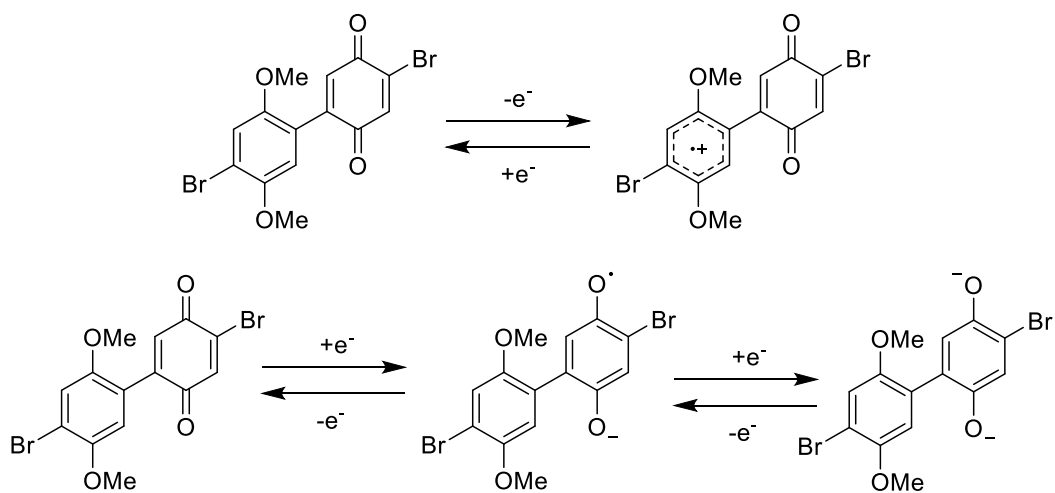


Figure 4.11 CV of BrHBQBr.

Scheme 4.1



If HBQ molecular orbitals were strongly interacting, the electron-withdrawing nature of the quinone on the HBQ backbone should stabilize the HOMO with respect to dimethoxybenzene, decreasing its energy (and therefore increasing the oxidation potential). This is not observed in BrHBQBr, however, as the oxidation potential is slightly reduced, meaning the HOMO energy is somewhat raised relative to the work function of the electrode. The electron-donating nature of the 1,4-dimethoxybenzene ring is also diminished because of the break in conjugation. Without the second bromine attached to the quinone, LUMO eigenvalue slightly decreases and leads to the slightly higher onset potentials for BrHBQBr relative to 2,5-dibromo-1,4-benzoquinone.

Substitution of the quinone 3- and 4-carbon on the HBQ backbone affects the redox behavior. Adding another bromine to the quinone, as in BrHBQ(Br)₂, further increases the reduction potentials while only very slightly reduces the oxidation potential (Figure 4.12). Adding nitrile groups to the HBQ greatly reduces the gap between the redox onsets, the oxidation and reduction peaks are all shifted much closer together (Figure 4.13). The first reduction peak is -46 meV relative to SCE, and the work function of the GCE is slightly negative compared to the first reduction potential of the HBQ in the experiment. While background current from nonfaradaic processes begins to become non-negligible within the cell at higher potentials, the second reduction of BrHBQ(CN)₂ is still quasireversible in a potential window of +1.3 V to -1.2 V. Extending the scan between ±2 V leads to significant irreversible side reactions (not shown). As was expected from theory and spectral results, the amino HBQ, BrHBQN₂, had the highest reduction potential.

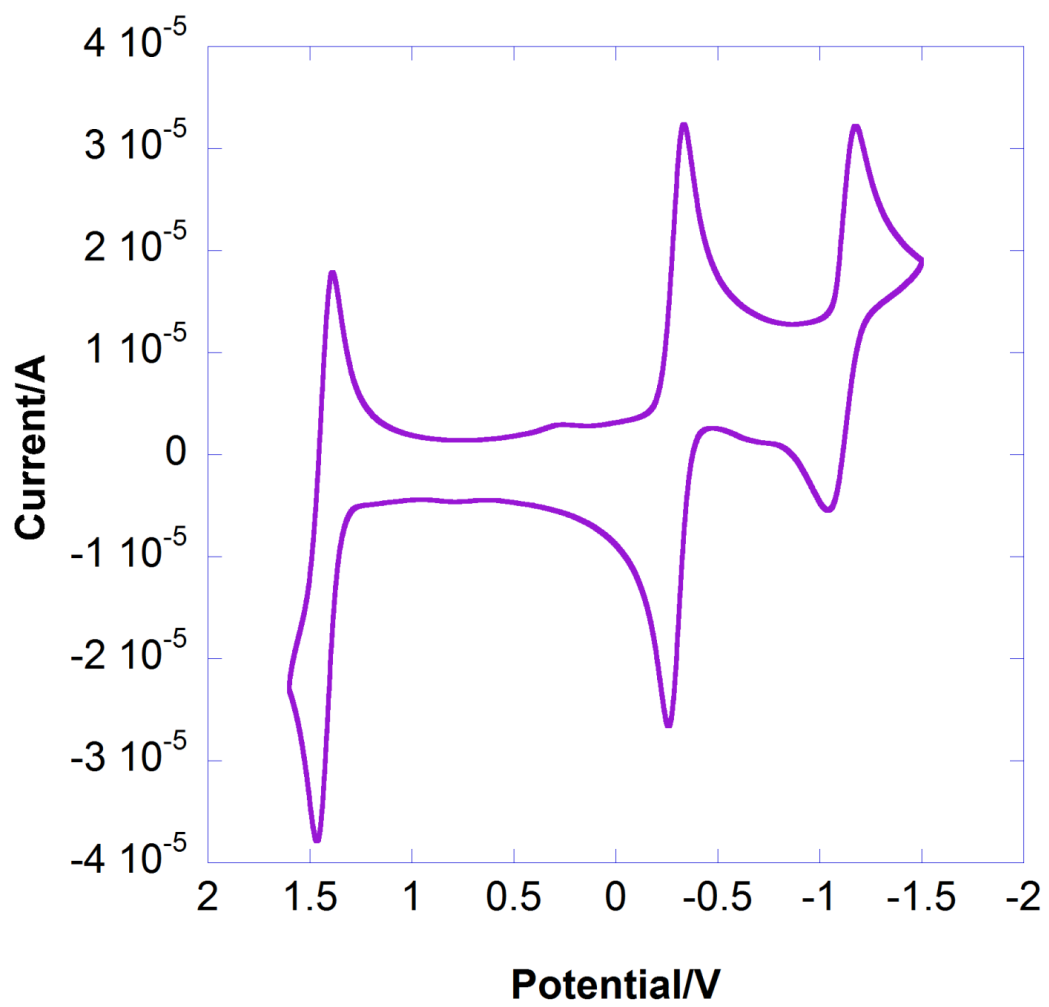


Figure 4.12 CV of BrHBQ(Br)₂.

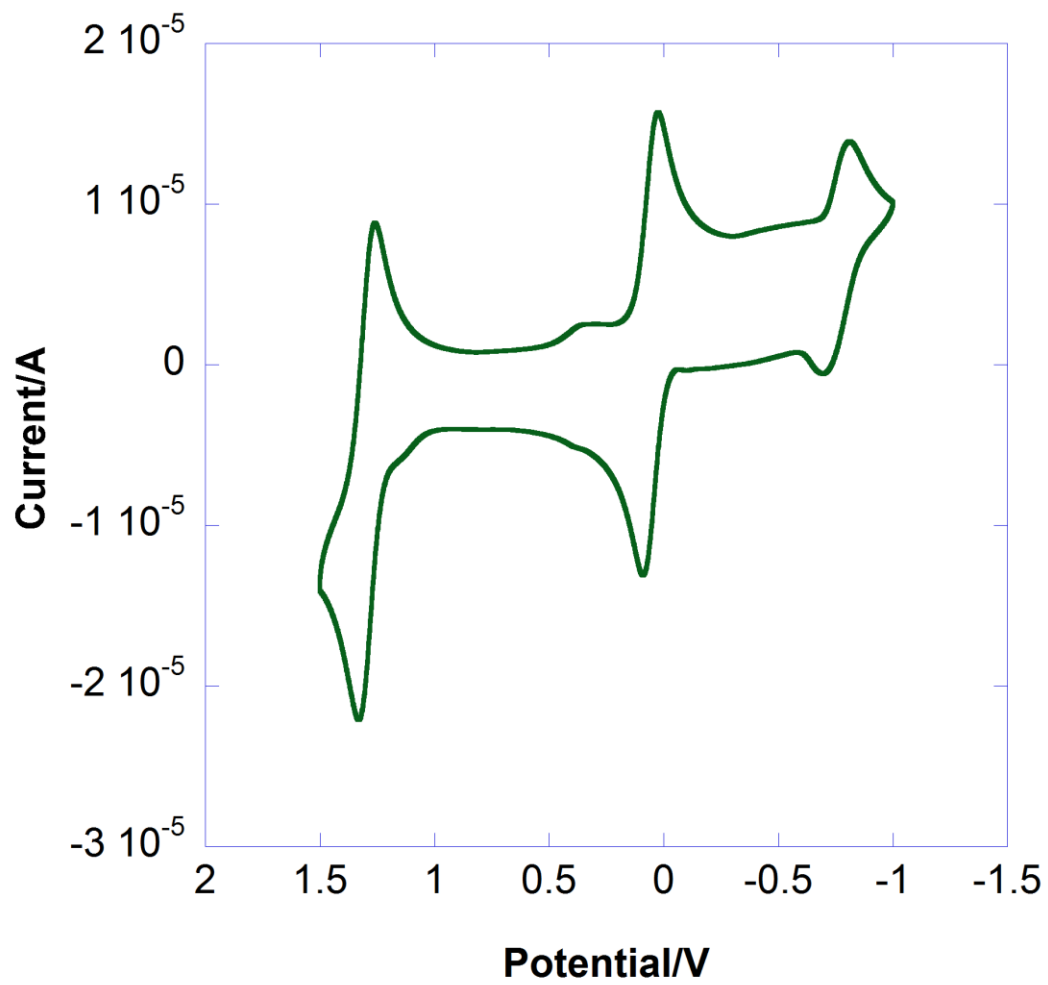


Figure 4.13 CV of BrHBQ(CN)₂.

With the exception of BrHBQNH₂ (Figure 4.14), other HBQ derivatives show very similar electrochemical behavior to BrHBQBr. All reduction peaks and oxidation peaks are fully reversible. The oxidation wave for BrHBQNH₂ is fully irreversible, and leads to significant side reactions in the window of ± 2 V (not shown). The irreversible oxidation of BrHBQNH₂ probably derives from electropolymerization in solution.¹³³⁻¹³⁵ Narrowing the window to 1.5 V to -1.7 V somewhat simplifies the voltammogram, the oxidation still being irreversible but with less noise present from other nonfaradaic processes. It may be that the first oxidation process only leads to a dimerization rather than an uncontrolled polymerization and deposition onto the electrode.¹³³ Formation of an insulating film, resulting in the decrease of current over subsequent scans,¹³⁵ is not observed (data not shown). Even under limited potential windows, the second reduction of BrHBQNH₂ is only quasireversible, where the first remains fully reversible.

The single oxidation peak is due to the presence of dimethoxybenzene which is decoupled from the quinone ring- preserving the characteristics of each donor and acceptor at once. This means that the orbitals are, in fact, decoupled from one another to create a D—A system. The next challenge is to use the electrochemical data in order to determine the actual magnitude of the orbital eigenvalues.

Section 4.3.3 HBQ Ionization Potential and Electron Affinity Estimation

The previous section corroborated predictions made in Chapter 2 about the electrochemical nature of HBQs in solution. Dimethoxybenzene derivatives do not have a LUMO capable of electron injection in the solvent window, and benzoquinone derivatives do not have a HOMO capable of oxidation in the solvent window. Both rings together, however, produce a molecule which is capable of reversible redox chemistry in both scan directions.

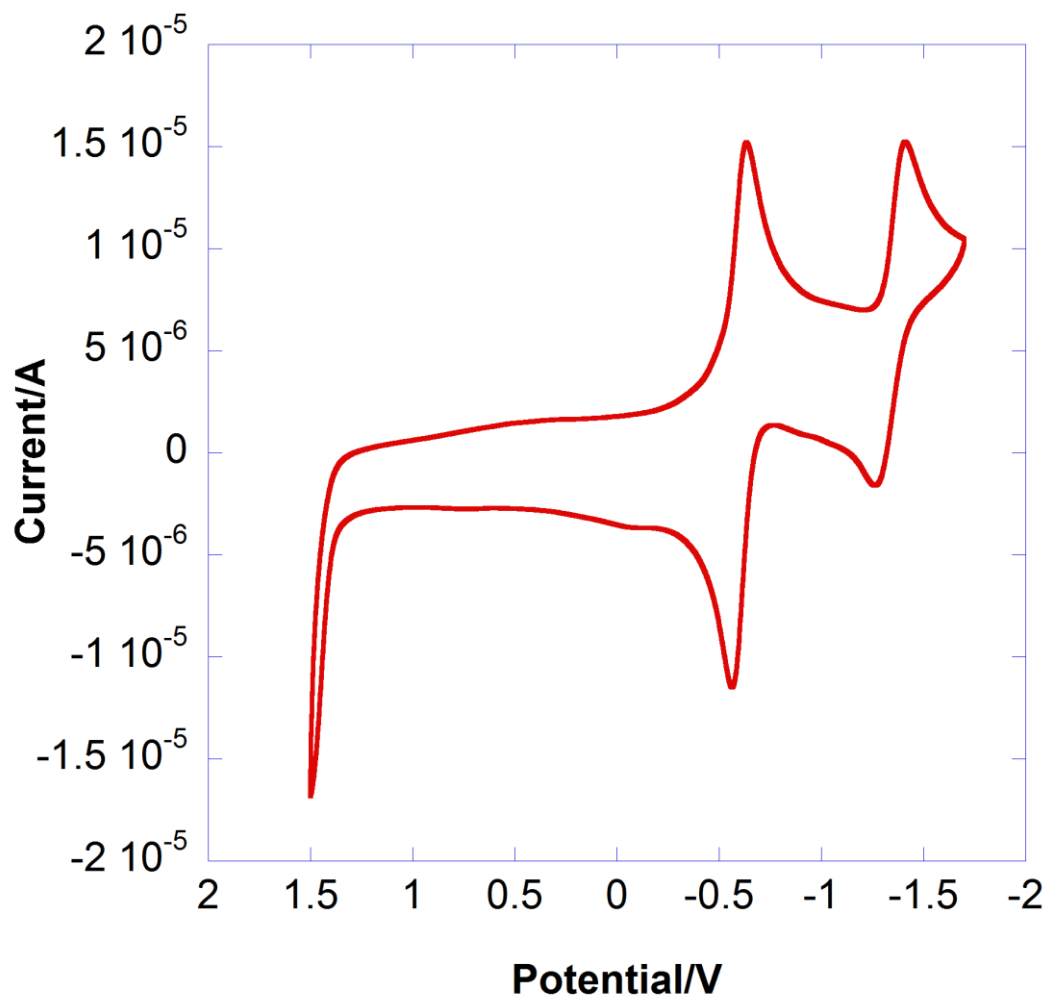


Figure 4.14. CV of BrHBQNH₂.

It is possible to experimentally estimate the energy of the HOMO and LUMO for a molecule, in order to be able to construct a schematic energy diagram of the junction. This aids researchers in understanding the conduction mechanism through the junction. To determine the absolute energy of the HOMO and LUMO, it is necessary to approximate the HOMO as the ionization potential and the LUMO as the electron affinity. By Koopmans' Theorem, ionization potential is estimated as the energy required to vertically excite an electron to the vacuum level. Likewise, electron affinity is estimated as the energy of vertically injecting an electron into the LUMO. While these values do not take into account electron correlation values or molecular rearrangement energy, approximations of this sort are acceptable to determine where molecular orbitals lie with respect to the work function of metal electrodes. Photoelectron spectroscopy, especially ultraviolet photoelectron spectroscopy (UPS) and inverse photoelectron spectroscopy (IPES) have been staple methods for examining ionization potentials and electron affinities, respectively, in organic molecules.^{136,137} However, UPS may not always be available to an experimentalist, and CV may act as a sufficient substitute.¹³⁶

By using an experimentally well-understood standard such as ferrocene, the solution FMO levels for such molecules may be estimated using the $E_{1/2}$ potentials.¹³⁸ Cardona *et al.*¹³⁸ outline that Fc^+/Fc redox couple is 0.40 V vs. SCE in acetonitrile, which correlates to a HOMO value of -5.1 eV vs. vacuum. They review that up until that time, no values had been standardized across the field of organic photovoltaics, for which these values are especially important. The authors concede that solution values are only an estimation of the gas-phase values, and even the most accurate attempt to standardize reported values still gives error of $\sim\pm 0.1$ V.

$$E_{\text{LUMO}} = -(E_{1/2}^{\text{R}} + 5.1 \text{ eV})$$

$$E_{\text{HOMO}} = -(E_{1/2}^{\text{O}} + 5.1 \text{ eV})$$

From the equations above, approximations of the FMO eigenvalues may be calculated from experiment. Table 4.4 presents the calculated FMO values for several compounds. Contrary to the results predicted in Chapter 2, BrHBQ(CN)₂ actually has a *higher*-lying HOMO value and is easier to oxidize than either of the other derivatives presented. The molecule has a lower-lying LUMO than the other derivatives, consistent with the predictions. As the Fermi level of Au is -5.2 eV,¹³⁹ the experimental FMO values give high confidence that the Fermi level of Au lies well in between the orbital eigenvalues for HBQ derivatives.

Determination of the orbital eigenvalues, even to within $\sim\pm 0.1$ V, is helpful for selecting the appropriate electrode material(s). Chapter 1 showed a schematic where the electrode Fermi level was located equally between the HOMO and LUMO eigenvalues of the example molecule. When a molecule is situated within a junction, charges local to the molecule equilibrate slightly with the electrodes. This perturbs the orbital eigenvalues from their gaseous energies. Recall that orbital eigenvalues shift under applied bias. The direction of preferential conduction is going to be the direction which most easily provides a channel for electrons to conduct. If AR hopping is achieved at a lower absolute magnitude bias $|V|$ than resonant tunneling, then the AR conduction mechanism will be preferred. On the other hand, if resonant tunneling is achieved at lower bias than hopping, then forward bias will be opposite to AR.

The ability to determine conduction mechanisms through a molecule requires knowledge of three primary parameters:

1. FMO Eigenvalues.
2. Electrode Fermi energy
3. Coupling strength of FMOs to electrode

Table 4.5 Orbital Potentials (vs. SCE)

Molecule	HOMO (eV)	LUMO (eV)
1,4-dimethoxybenzene	-6.4	—
2-bromo-1,4-dimethoxybenzene	-6.6	—
2,5-dibromo-1,4-dimethoxybenzene	-6.6	—
2,5-dibromo-1,4-benzoquinone	—	-4.8
BrHBQBr	-6.6	-4.7
BrHBQ(Br) ₂	-6.4	-4.7
BrHBQ(CN) ₂	-6.3	-5.1
BrHBQNH ₂	—*	-4.4

*No HOMO calculated for oxidation $E_{1/2}$.

The first two parameters are now known about the HBQ system. The first has been presented within this section for several HBQ derivatives and the second is obtained through standard UPS techniques for any given electrode. The third parameter, however, is a more complex matter and should include thorough experimental investigation as well as theoretical modelling in future studies (see Chapter 6).

Section 4.4 Crystallography

In addition to electronic information, the majority of the discussion within Chapter 2 focused on the importance of calculating the physical structure of HBQ derivatives in the gaseous phase. As the defining tunneling barrier within the system, the HBQ interring torsion is an important metric to understand. Furthermore, having information about the types and strengths of intermolecular interactions may provide additional detail whereby the HBQ molecules can interact as they pack into a monolayer. The following subsections are descriptions of several HBQ derivatives that produced crystals of sufficient quality for analysis by XRD.

The following descriptions detail the kinds of interactions possible in transitioning from the solvated state to the adsorbed state. Intramolecular steric repulsion and intermolecular donor-acceptor interactions cause these molecules to deviate from the torsion angle calculated for the gaseous state, around 39° (Chapter 2), so monolayer geometry may not correspond to the calculated lowest-energy geometry. These descriptions are more relevant for functionalized HBQs that adsorb on the surface ($-\text{NH}_2$, $-\text{CN}$) than for functionalities that do not (Br), but understanding the differences between each derivative gives context to subsequent molecules. For example, in $\text{BrHBQH}_2(\text{CN})_2$, an intramolecular hydrogen bond bends an aromatic ring slightly out of planarity, and the molecule adopts an entirely unique geometry compared to the oxidized HBQ derivatives (Section 4.4.2). All of the crystals pack in centrosymmetric space

groups, where head-to-tail interactions would not be directly applicable to monolayer formation. As all molecules in a monolayer would need to be aligned in the same fashion, this changes the nature of intermolecular interactions.

Section 4.4.1 BrHBQBr Structure

Due to the role that the twist angle between rings plays in the electronic properties of the molecule, the determination of the C12—C7—C4—C5 torsion angle is the key observation in this structural analysis. This angle measures -110.89° in the BrHBQBr crystal structure. Calculations performed on the target molecule in the gas phase (Chapter 2) predict an angle of -38.54° . This significant discrepancy is due to packing interactions in the solid phase, as outlined below.

Substituents on the HBQ system behave as expected. The C—Br bond distances reflect the natures of the electron-deficient quinone and electron-rich dimethoxybenzene rings: the C1—Br1 bond distance is 1.872(5) Å, while the C10—Br2 bond is 1.898(4) Å. Thus Br1 has a slightly stronger π -donating character into the quinone moiety, strengthening the bond relative to the Br2—C bond of the dimethoxybenzene ring. The methoxy substituents are nearly coplanar to the benzene ring, with a C12—C11—O4—C14 torsion angle of 1.47° and a C9—C8—O3—C13 torsion angle of -4.41° . The methyl portions of each of these groups point away from the sterically restricting groups ortho to these positions. Finally, the quinone ring is slightly buckled, probably due to supramolecular packing effects.

Each molecule is surrounded by eight neighboring molecules which interact through hydrogen bonding, halogen bonding, and $\pi\cdots\pi$ interactions (Figure 4.15). The strongest interactions appear to be between functional groups on the quinone ring of one molecule with those on the dimethoxybenzene ring of another. These include especially short but non-

directional C—H \cdots O hydrogen bonds between the quinone carbonyl groups and dimethoxybenzene ring hydrogen atoms of two neighbors. Interactions between like parts of neighboring molecules include edge-to-edge stacking of quinone rings with quinone rings, dimethoxybenzene rings with dimethoxybenzene rings, and dimeric hydrogen bonding between methoxy groups. Quinone rings on adjacent molecules along the *c* axis show some face-to-face π -stacking.

Along the *a* crystallographic axis, the benzene rings nestle closely to one another in an antiparallel geometry, where one quinone points up and the layer behind it points down. Along the *cb* plane the benzene rings are coplanar; hydrogen atoms from C14 on one molecule project closely to O3 on the adjacent molecule and vice versa for a hydrogen on C13 to the adjacent O4. Symmetric C—H $\cdots\pi$ short contacts exist between pairs of C13—H13C \cdots dimethoxybenzene. Molecules are aligned linearly in a head-to-tail manner where the bromines participate in intermolecular halogen bonding. As discussed above, Br1 is electron deficient with respect to Br2, and a distinct halogen interaction forms along the molecular *x*-axis (the C7—C4 biphenyl bond). The Br1 \cdots Br2 interaction is 3.420 Å and is nearly linear, with a Br1 \cdots Br2—C10 interaction angle of 170.94°. Equivalent rings from molecules packed along this axis are parallel to one another, quinones and benzene rings aligned coplanar to the corresponding ring in the next molecule.

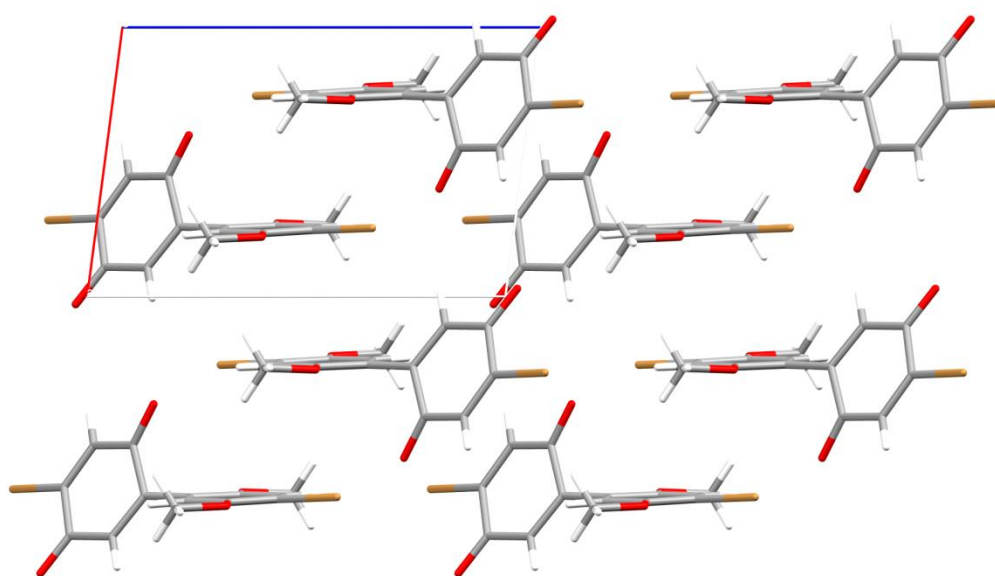


Figure 4.15 Crystal structure of BrHBQBr viewed down the *a* crystallographic axis.¹²²

Section 4.4.2 BrHBQH₂(CN)₂ Structure

For this structure, the benzene rings are twisted out of a common plane, forming a dihedral angle of 53.59(7)°, which appears to optimize the 2.758(2) Å O3—H···O2 intramolecular hydrogen bond. The rings are essentially planar although the O3—H group which participates in the intramolecular hydrogen bond is deflected slightly out of the plane. Also, the rings are not coaxial with the C4—C7 bond that bridges them. This can be seen in torsion angles involving three carbon atoms from one ring and the bridging carbon atom from the other, which deviate from linearity by ~5° (C2—C3—C4—C7 = 173.9(1)°, C6—C5—C4—C7 = -175.4(1)°, C4—C7—C8—C9 = 174.9(1)°, C4—C7—C11—C12 = -175.6(1)°). This bending of the molecule about its long axis may also be due to hydrogen bonding as it causes the methoxy group to approach the OH group more closely. The aromatic C—C bonds of both rings have a narrow range of distances [from 1.387(2) to 1.412(2) Å]. The C—C, C—O, C—N, and C≡N distances for the molecule are similar to the corresponding distances in 2,3,5,6-tetracyanoquinone.¹⁴⁰ The C—C bond distances around the bromodimethoxybenzene ring are close to those in the other hemibiquinone molecules containing this ring.^{99,122} The C9—C10 bond in BrHBQH₂(CN)₂ [1.408(2) Å] is longer than the corresponding C1—C6 bond in BrHBQBr (1.334 Å).¹²² The stronger polarization of BrHBQH₂(CN)₂ relative to the starting material should weaken the bond through repulsive effects. The Br1—C1 bond is slightly shorter in BrHBQH₂(CN)₂ (1.885(1) Å) compared to the starting material (1.898(4) Å) as well, also suggesting decreased electron density on the dimethoxybenzene ring due to increased polarization. The calculated dipole of BrHBQBr is only 1.33 D, compared to that of BrHBQH₂(CN)₂ (6.17 D).

As in the other reported hemibiquinone molecules,¹²² we seek to use and compare the inter-ring torsion angles in the crystals as a guide against gas-phase calculated values. The

intramolecular hydrogen bond from the C8 phenol to the O2 methoxy group causes a greater torsion angle than that in the starting HBQ.¹²² In this molecule, the C5—C4—C7—C8 torsion is $-126.5(2)^\circ$, compared to an angle of $-110.9(5)^\circ$. DFT calculations performed on the target molecule in the gas phase predict an angle of 48.85° . This significant discrepancy is due to packing interactions in the solid phase as well as the additional hydrogen bond.

The O3—H \cdots O2 intramolecular hydrogen bond points toward the nonbonded electrons on O2 with a total bond angle of $151(3)^\circ$. Due to the influence of other short contacts and supramolecular interactions (see below), the phenolic C—O—H bond angles deviate when compared to the methoxy C—O—C bond angles. C8—O3—H is calculated at 107.90° , C11—O4—H is calculated at 112.21° , C3—O2—C14 is measured at $117.9(1)^\circ$, and C6—O1—C13 is measured at $117.2(1)^\circ$. As in other structures, the methoxy groups are aligned mostly in-plane with the benzene ring, C5—C6—O1—C13 being bent out of plane by $-4.5(2)^\circ$ and C2—C3—O2—C14 bent out of plane by $-1.3(2)^\circ$. The C12—C11—O4—H phenol group is also nearly planar, being bent out of plane by 1.3° . However, the hydrogen-bonded phenol is unsurprisingly bent out of plane, C7—C8—O3—H = $38(2)^\circ$. The methoxy methyl groups point away from the sterically restricting groups ortho to these positions.

Each molecule makes short (less than the sum of the VdW radii) contacts to 6 neighboring molecules. Rings of like identity are aligned in parallel planes. All short contacts are associated with Lewis acid-base interactions of some kind, and for each interaction there is one neighboring molecule that acts as a donor and second that acts as an acceptor. Two central molecules in the unit cell stack antiparallel to one another, the quinone rings shifted off-center from one another in the *a* direction. Both nitrile groups are involved in intermolecular hydrogen-bonding interactions, the first one (O4—H \cdots N1) strong, the second one (C2—H \cdots N2) weaker but still highly

directional. These interactions link molecules along the crystallographic *a* and *b* directions, respectively, forming sheets parallel to (010). The quinone rings are aligned parallel to the *bc* plane diagonal.

The remaining two molecules in the unit cell are oriented orthogonally to the central molecules. These molecules are antiparallel to each other, where the dimethoxybenzene rings stack with those of the central pair. Centroid distances for the rings are longer than expected for close π -interactions at 4.107 Å. However, since the rings are slightly offset from one another, this is not the correct centroid to use. Instead, a close 3.598 Å π -interaction between two intermolecular C9—C10 centroids exists. A centroid calculated for the C7—C8—C9—C11—C12 ring sits 3.574 Å from a centroid for N1—C15—C9—C10—C16—N2, which may be explained by the electron donating character of the hydroquinone as compared to the dinitrile substituents. The planes of the dimethoxybenzene rings are oriented parallel to the short diagonal of the *ac* plane.

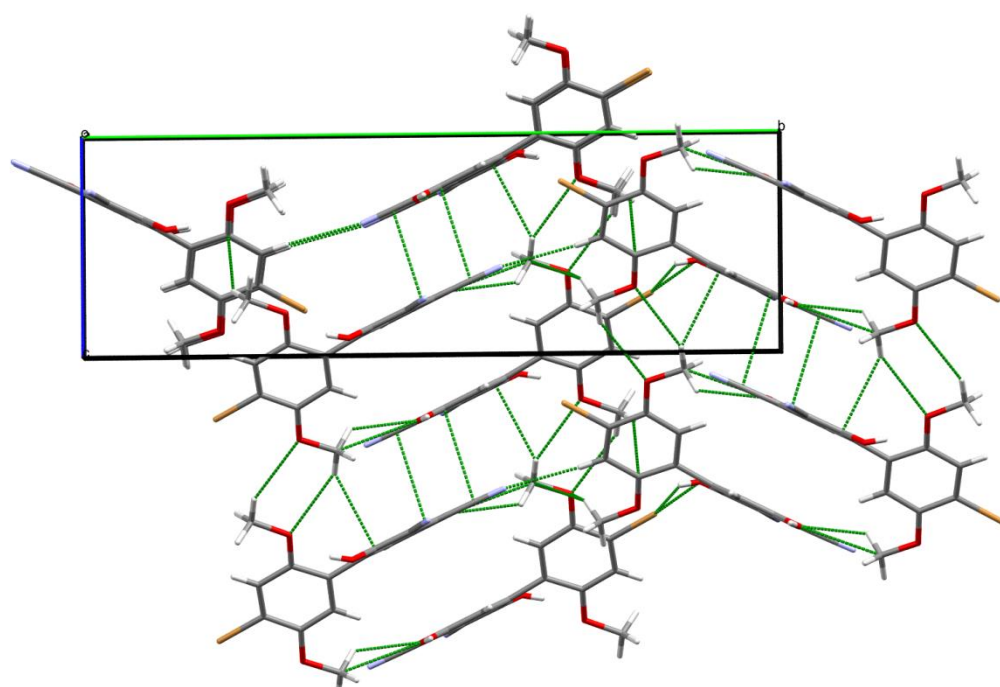


Figure 4.16 Crystal structure of BrHBQH₂(CN)₂ viewed down the *c* crystallographic axis.

Section 4.4.3 BrHBQ(CN)₂ Structure

As in the other reported HBQ molecules,¹²² we seek to use and compare the inter-ring torsion angles in the crystals as a guide against gas-phase calculated values. However, benzene inside the crystal structure prevents us from drawing direct conclusions about the geometry. Packing effects distort the biphenyl molecule out of plane in the opposite direction as the hydroquinone starting material BrHBQH₂(CN)₂. The C—C biphenyl bond (1.481(2) Å) is slightly shorter in BrHBQ(CN)₂ compared to the hydroquinone (1.481(2) Å). In this molecule, the C5—C4—C7—C8 torsion is 125.4 (2)°, compared to the hydroquinone torsion angle of -126.50°. ⁹⁸ DFT calculations performed on the target molecule in the gas phase predict an angle of -39.71°. This significant discrepancy is due to packing interactions in the solid phase, especially from benzene. Finally, the quinone ring is slightly buckled, likely due to supramolecular packing effects.

As in other structures, the methoxy groups are aligned nearly in-plane with the benzene ring, C2—C3—O2—C13 being bent out of plane by 2.9(3)° and C5—C6—O1—C14 bent out of plane by -7.0(3)°. The methoxy group C3—O2—C13 is measured at 117.4(1)°, and C6—O1—C14 is measured at 117.3(1)°. The methyl portions of each of these groups point away from the sterically restricting groups ortho to these positions, typical for this class.

Continuing the trend from the hydroquinone, the C9—C10 bond in **1** (1.346(2) Å) is shorter than than the corresponding hydroquinone C9—C10 bond (1.408(2) Å) and the C1—C6 bond (1.334(6) Å) of BrHBQBr.¹²² The stronger polarization of **1** due to the dicyanoquinone relative to the starting materials weakens the bond through repulsive effects. The Br1—C1 bond is slightly longer in **1** (1.893(2) Å) compared to the same bond in the hydroquinone precursor (1.885(1) Å), but is still shorter than that of the starting material BrHBQBr (1.898(4) Å).¹²² The calculated dipole of BrHBQH₂(CN)₂ is 6.17 D, compared to a dipole moment of 7.78 D for BrHBQ(CN)₂.

The molecule packs in a P-1 space group with two HBQ molecules and one solvent molecule. The molecules align antiparallel to one another in the unit cell primarily along the *c* crystallographic axis. The quinone rings are mostly parallel to the *ac* plane and sandwich, in a 2:1 ratio, a benzene solvent molecule. The plane of the dimethoxybenzene ring aligns with the diagonal of the *ab* plane.

Analysis of the short contacts shows an off-center donor-acceptor type $\pi\cdots\pi$ interaction between benzene and the HBQ molecule. Figure 4.17 shows the great extent of π overlap between benzene and BrHBQ(CN)₂. It is readily apparent that the benzene ring, rather than being centered between the quinone rings exactly, is actually slightly off-center. Instead, the electron density of the benzene is centered over the slightly electropositive C9—C10 bond.

Each HBQ molecule interacts with a total of three benzene molecules by short contacts. As mentioned above, one molecule of benzene is sandwiched between two quinone rings. Additionally, the 3-substituted nitrile hydrogen-bonds to a second solvent molecule C16≡N1 \cdots H17 at 2.812 Å and 146.74° that is π -stacking between two separated molecules. The third benzene molecule short contacts to the 4'-bromine on the opposite end of the molecule, where H17 and H18 are bridged almost symmetrically H17 \cdots Br1 \cdots H18 where H17 \cdots Br1 is 3.052 Å and Br1 \cdots H18 is 3.042 Å long. The benzene solvent molecule π -stacks parallel to the quinones. Although, in previous HBQ crystals the 4 and 4' groups show evidence of intermolecular halogen bonding, due to the excess electron density around the aryl bromine and the nitriles, an attractive interaction is not possible, rather a slightly repulsive interaction is favored. Instead, the protons on C17 and C18 bifurcate Br1 as an acceptor forming slightly asymmetric hydrogen bonds between the dimethoxybenzene ring and the benzene solvent molecule. As discussed above, the quinone carbonyls are deflected from perfect planarity. In

previous structures, methoxy oxygens tended to deflect the carbonyls through repulsive effects. However, this structure contains some attractive intermolecular hydrogen bonding character between the C14—H14B···O4, which is a moderate interaction at 2.570 Å and a bond angle of 157.26°. A second weaker intermolecular interaction occurs between O4 and the dimethoxybenzene hydrogen C5—H5···O4 at 2.639 Å and 133.72°. Projection of the O4 carbonyl to a neighboring quinoid proton H12 is also evident at a bond length of 2.654 Å and a C12—H12···O4 angle of 147.33°. There is a fourth and weakest interaction with O4, between the C16≡N1···O4 at a N1···O4 bond length of 3.159 Å and overall bond angle of 129.91°. Two contacts are made with O3; O3 has a short contact to H2 through C2, at 2.649 Å and a C2—H2···O3 angle of 141.60° and C10 and C11 interact with O3 via weak π interactions, at 3.251 and 3.187 Å respectively. Additionally, C10 packs closely to C8, at 3.486 Å. The N2 nitrile only has one pair of close interactions between methoxy C13 and H13A. This is a long, very weak hydrogen bond of C13—H13A···N2 97.33° and H13A···N2 2.820 Å. There is a long C13···N2 (3.101 Å) interaction as well. Even longer than those interactions, H13 also has a weak H··· π interaction with the dimethoxybenzene ring on an adjacent molecule 2.883 Å long.

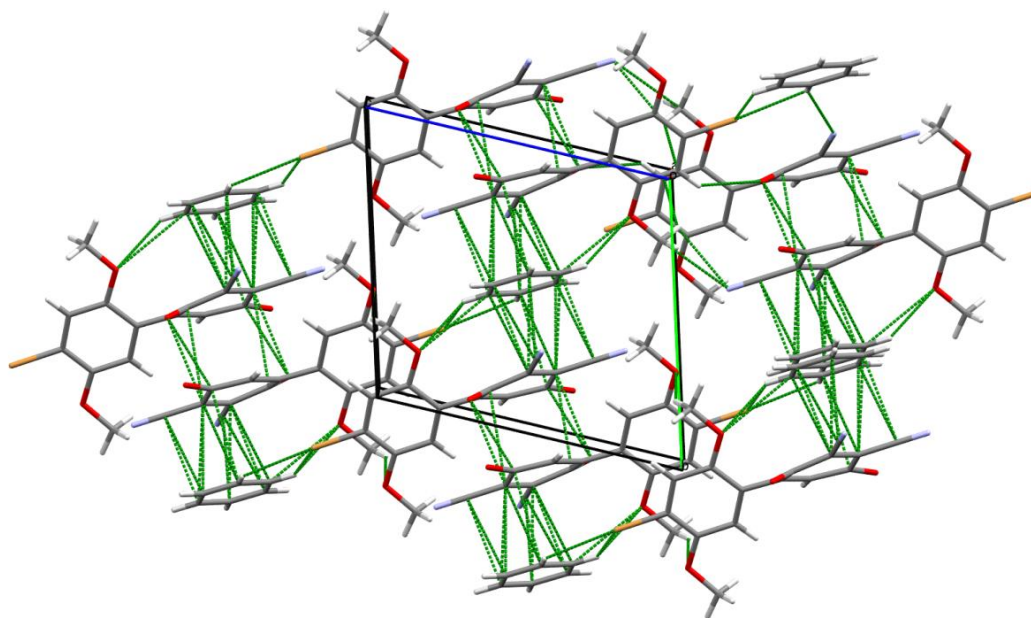


Figure 4.17 Crystal structure of BrHBQ(CN)₂ viewed down the *b* crystallographic axis.

Section 4.4.4 BrHBQ(Br)₂ Structure

The HBQ backbone is defined by its highly twisted intermolecular conformation between the two rings as its functional electronic characteristic. The twist angle between the rings is of interest since it determines the amount of overlap of the rings' molecular orbitals and is defined as $C12-C7-C5-C4 = 116.16^\circ$. DFT calculations performed on the target molecule in the gas phase predict an angle of 41.05° . This significant discrepancy is due to packing interactions in the solid phase, as is discussed below.

Substituents on the HBQ system behave as expected. The C—Br bond distances reflect the natures of the electron-deficient quinone and electron-rich dimethoxybenzene rings: the C2—Br1 and C3—Br2 bond distances are nearly identical at 1.866(3) Å and 1.866(4) Å, respectively. The C10—Br2 bond is 1.887(3) Å. Thus Br1 and Br2 have slightly stronger π -donating character into the quinone moiety, strengthening the bond relative to the C10—Br2 bond of the dimethoxybenzene ring. The two methoxy groups on the benzene ring are almost entirely planar, with a dihedral angle of only 3.77° and 4.81° . The aromatic C—C bond distances of the dimethoxybenzene ring are quite close to one another. The C9—C10 bond is statistically shorter than the others (1.373(4) Å), while the remainder are within one to two standard deviations of each other (C7—C8 = 1.392(4) Å, C8—C9 = 1.391(4) Å, C10—C11 = 1.393(4) Å, C11—C12 = 1.390(4) Å, C12—C7 = 1.384(6) Å). The quinone ring has markedly different single bond (C1—C2 = 1.492(5) Å, C1—C6 = 1.467(5) Å, C3—C4 = 1.497(4) Å, C4—C5 = 1.493(5) Å) and double bond distances (C2—C3 = 1.340(4), C5—C6 = 1.331(4) Å). The carbonyl group at C4 is noticeably deflected from the plane of the ring, with the oxygen atom O2 residing 0.279 Å outside of the mean plane of the aromatic ring. This appears to be due to steric repulsion from methoxy oxygen atom O3.

The molecule packs in a P-1 space group with two molecules in the unit cell. Each molecule is surrounded by 8 neighboring molecules which interact through hydrogen bonding, halogen bonding, and $\pi\cdots\pi$ interactions. In the unit cell, the molecular *x*-axis is aligned along the diagonal of the *bc* plane. All dimethoxybenzene rings are parallel to this plane, and the quinone rings are rotated relative to the *a*-axis.

Each molecule makes short (less than the sum of the van der Waals radii) contacts to 8 neighboring molecules. Two molecules interact through either donating or receiving halogen bonds between Br3 and Br1. Two other molecules donate or receive halogen bonds between Br2 and O1. Two more interact through hydrogen bonds between two methoxy groups on adjacent molecules. One neighbor, forms a centrosymmetric, hydrogen bonded dimer through aromatic C—H to carbonyl O hydrogen bonds, and the last one neighbor also forms a centrosymmetric dimer through weaker methoxy C—H to carbonyl O hydrogen bonds. The halogen bonds and methoxy-to-methoxy hydrogen bonds link the molecules into infinite head-to-tail chains in mutually orthogonal directions, linking the structure into an overall 3-dimensional network.

Planar interactions occur between neighboring methoxy groups along the *b* crystallographic axis. Along the *bc* plane the dimethoxybenzene rings are coplanar; hydrogen atom H14A from C14 on one molecule projects closely to O3 on the adjacent molecule and vice versa for a hydrogen H13A on C13 to the adjacent O4. Dimeric C—H $\cdots\pi$ short contacts exist between centrosymmetric pairs of C14—H14A \cdots quinone. There is some centrosymmetric $\pi\cdots\pi$ interaction between a directionally adjacent dimethoxybenzene rings. H13C projects closely to the bond between C11—O4.

As mentioned above, supramolecular packing interactions determine the intermolecular geometry around the C—C biphenyl bond between C5 and C7. Molecules are aligned linearly in a head-to-tail manner where the bromines participate in intermolecular halogen bonding (Figure 4.18). In the case of the starting material HBQ, crystal packing was somewhat driven by both the attractive as well as steric forces. In this molecule, additional opportunity for halogen bonding exists because of the extra quinone bromine; which in turn leads to the molecular geometry outlined above.

As in BrHBQBr,¹²² there is a distinct halogen interaction between the 4- and 4'-bromine atoms, Br1···Br3. This interaction is longer than in the starting material, 3.488 Å versus the 3.420 Å.¹²² This halogen bond is mostly linear, at 168.04°. The halogen bond Br2···O1 is much shorter, with a bond length of 3.073 Å and 121.84°. It is this interaction that primarily determines the crystal packing geometry. Equivalent rings from molecules packed along this axis are parallel to one another, quinones and benzene rings aligned coplanar to the corresponding ring in the next molecule. In addition to the Br2···O1 interaction from one molecule to another, O1 also has some close interaction with a second molecule. The C14 methyl group and the C12 proton complete the triad of interactions stemming from O1.

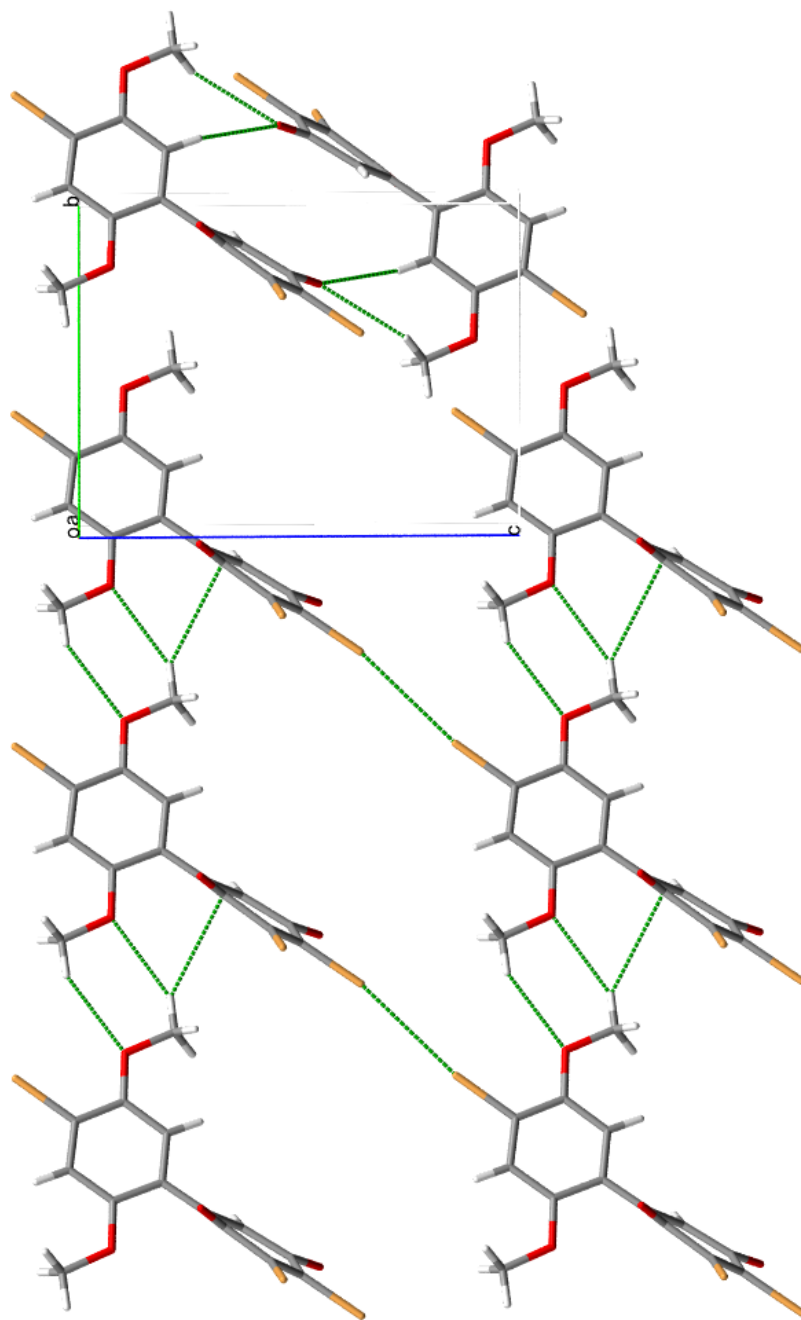


Figure 4.18 Crystal structure of BrHBQ(CN)₂ viewed down the *b* crystallographic axis.

Section 4.4.5 BrHBQN₃ Structure

This particular HBQ backbone is twisted in a direction opposite that of BrHBQBr. The C5—C4—C7—C12 torsion is measured as $-45.9(7)^\circ$ (the negative to show directionality relative to the *trans*-planar conformation), whereas DFT calculations performed on the target molecule in the gas phase predict an angle of 36.41° , in the same direction as all other HBQ molecules. This significant discrepancy is due to packing interactions in the solid phase, particularly with respect to π -interactions between molecules in the crystal.

The aromatic C1—Br1 bond distance is somewhat shorter than in the starting material,¹²² at $1.877(5)$ Å. The two methoxy groups on the benzene ring, while still almost planar, have slightly larger dihedral angles comparatively of $9.0(8)^\circ$ and $-5.1(8)^\circ$. The methoxy groups do display short contact behavior in the extended lattice (see below), and this may be the cause of these deviations from planarity.

The aromatic C—C bond distances of the dimethoxybenzene ring are quite close to one another. The C4—C7 bond is slightly longer ($1.476(7)$ Å) than the starting material. Previously discussed derivatives showed the quinone ring buckles slightly outside of the mean plane of the aromatic ring due to a combination of steric repulsion and attractive intermolecular π -interactions with a neighboring dimethoxybenzene ring. In this structure, however, no such attractions nor repulsions are present, and the quinone ring lies flat.

The azido group lies on the quinone, rotated away from the C11 proton. It is not completely planar with the ring, however, and has a C11—C10—N1—N2 torsion of $169.0(8)^\circ$. Due to the positive formal charge on N2, there is some electrostatic attraction between it and carbonyl O3 on the quinone ring. The C10—N1—N2 bond angle is $118.0(7)^\circ$, which deviates from the ideal

angle of 120° . The N1—N2—N3 bond angle is $166.3(1)^\circ$, very obviously deviating from linearity. The N1=N2 bond is significantly longer ($1.30(2)$ Å) than the N2=N3 bond ($1.10(2)$ Å). Each molecule makes short intermolecular contacts to five neighboring molecules. Columns of molecules pack in the *b* direction centrosymmetrically, where the aromatic ring on one molecule closely packs to the quinone ring “below” it, and the quinone ring of the first molecule closely packs to the aromatic ring of the second (Figure 4.19). C1 contacts C9 at $3.398(8)$ Å, and contacts C11 at $3.353(9)$ Å. H5A projects from the aromatic ring closely to O2 at 2.653 Å. O3 projects closely to a highly directional methoxy proton, at 2.507 Å and 155.6° . All other interactions are related by symmetry in the lattice.

There are four molecules in the unit cell, with two pairs of *b*-directionally stacked molecules, as described above. There are no short interactions between the two pairs. The molecules line up parallel to the diagonal of *ac*, with molecules of the same *b* stack oriented slightly off-center from one another. In previous HBQ molecules, such as BrHBQBr¹²² and BrHBQ(Br)₂, there were direct linear interactions between the aryl bromine and the quinone substituent. This is the only case in which there is no linear chain to link the molecules. Molecules at the same stack still line up head-to-tail, with the bromine projecting toward the azide, but the zig-zag pattern prevents them from interacting. Stacked rings within the *b* columns are parallel to one another, and rings across stacks are antiparallel to one another.

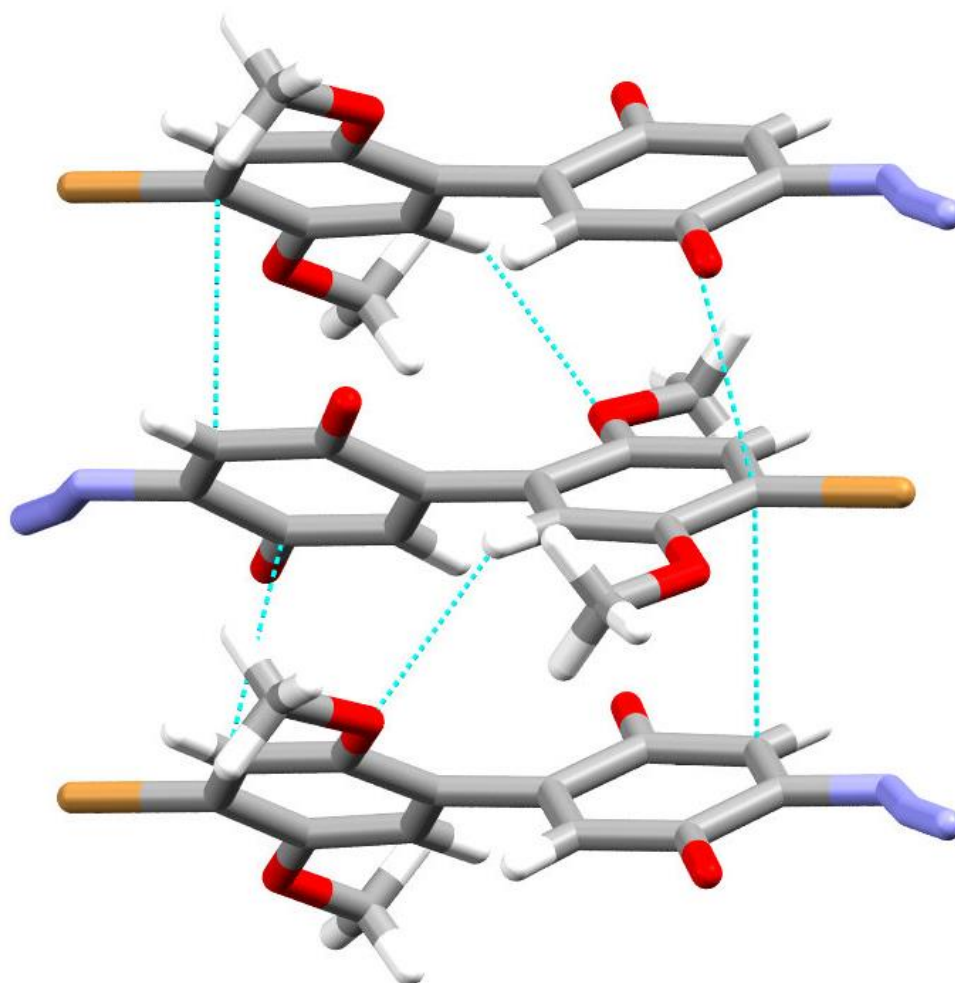


Figure 4.19 Crystal structure of BrHBQN₃ viewed along the *b* crystallographic axis.

Section 4.4.6 4,4'-Dibromobiquinone Structure

This molecule was created as an intended acceptor within a larger synthetic target before the HBQ backbone had been hypothesized to act as a D— σ —A rectifier. This crystal is peculiar, though, because while all previous HBQ molecules had a single molecule as a part of their asymmetric unit, this crystal structure contains two whole molecules as the asymmetric unit. This is even more interesting, considering the overall geometric symmetry of the molecule itself.

All four of the C—Br bonds are of different length (C7B—Br4, 1.869(5) Å; C1B—Br3, 1.873(4) Å; C1A—Br1A 1.861(5) Å; and C7A—Br2A, 1.878(5) Å) as are all eight of the C=O carbonyl bonds. Both 1,1'-biphenyl bonds are different, one is 1.488(6) Å long, and the other is 1.468(6) Å long. There are no appended substituents such as the methoxy groups by which rotation is possible, only the torsion between rings themselves are possible. These angles are different between molecules, too, at $-40.4(7)^\circ$ and $38.9(7)^\circ$. These angles are affected largely by intermolecular packing effects in the lattice. Due to the large number of interactions within the crystal, all of the quinones are puckered to some degree or another.

There is a highly directional C—H \cdots O hydrogen bond (2.392 Å, 171.4°) from H3AA to O2B that helps constrain geometry. There is also a C=O $\cdots\pi$ interaction (2.924 Å) of the O1A carbonyl to the centroid between C7B and C8B. Interestingly, there is a Br1A \cdots Br2A short contact (3.3275(7) Å), although no obvious Lewis acid-base interaction is present. These two bromine atoms are on symmetry-equivalent molecules, and are attached in a head-to-tail fashion. Similarly, Br3 and Br4 appear short contacted on symmetry equivalent chains in a 3.3818(6) Å Br3 \cdots Br4 interaction. O3A projects closely to an adjacent quinone, 2.843 Å from the centroid of C10B, C11B, and C12B.

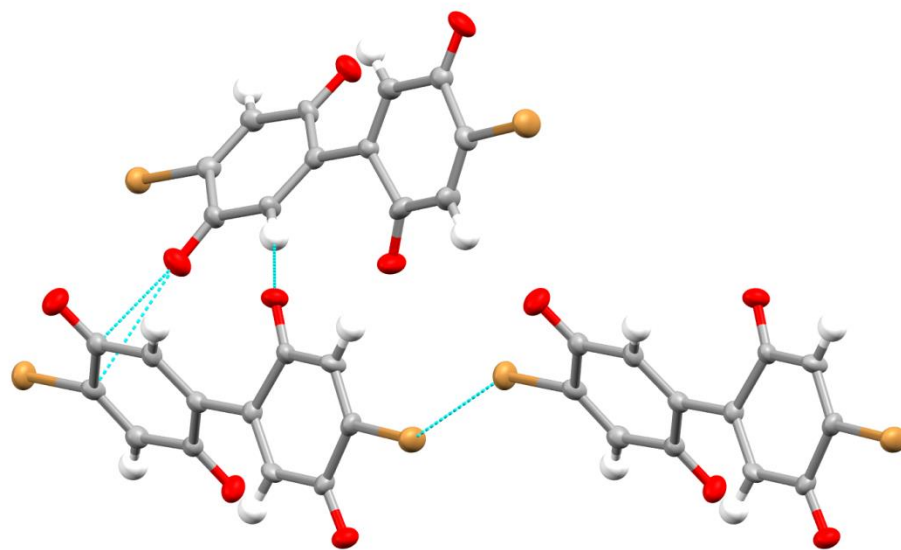


Figure 4.20 Crystal structure of biquinone BrBQBr depicted down the *b* crystallographic axis.

Section 4.5 Conclusion

In this chapter I presented the optical behaviors of HBQs in solution using UV-Vis spectroscopy, and the electrochemical behavior using cyclic voltammetry. These data were compared to the calculated predictions presented within Chapter 2. Optical absorption of the HBQ derivatives supports the assertion that each half of the molecule acts as if it were the two separate monomers in solution together. A low-energy ICT band confirms the HOMO→LUMO transition of similar energy to that calculated for the gas-phase molecules. Electrochemical determination of the FMO values in solution also confirms the hypothesized behavior as both a one-electron donor and two-electron acceptor. As expected, substitution on the quinone affects the half-wave potentials.

The crystal structures of five HBQ derivatives, determined by x-ray diffraction, are reported. The structures show great diversity that is highly dependent on the nature of inter- and intramolecular forces, and do not correlate well with gas-phase calculations. Substitutions on the quinone are especially important in determining the shape of the unit cell. The two rings of all HBQ derivatives remain twisted from coplanarity, although crystal symmetry arguments prevent a direct analogy from being drawn between the lattice and monolayer.

The results presented herein add strength to the hypothesis that the dimethoxybenzene ring and quinone ring are able to act as isolated donors and acceptors, respectively.

CHAPTER 5

MONOLAYER ASSEMBLY AND ANALYSIS

Section 5.1 Relevance to Previous Results

Throughout the preceding chapters, the preparation and characterization of hemibiquinones (HBQs) have been described. This work was in support of the hypothesis that the intramolecular twist of the lowest-energy conformations of the HBQs will provide electronic isolation of the donor and acceptor constituents of the HBQ. It has been proposed that HBQs would rectify current running through the molecule when arrayed between two electrodes and completing a circuit. This chapter presents the results of experiments performed by Marcus Johnson in the laboratory of Professor Robert Metzger at the University of Alabama. These data will show that one of the HBQ molecules, *2,3-dicyano-5-(4'-bromo-2',5'-dimethoxyphenyl)cyclohexa-2,5-diene-1,4-dione* (BrHBQ(CN)₂), forms ordered monolayers on gold surfaces^{141,142}. Further experiments demonstrate that current passes in one direction through junctions composed of BrHBQ(CN)₂. This is a confirmation that my hypothesis was correct and HBQs are structurally adequate to act as molecular-scale electronic devices.

Section 5.2 Monolayer Deposition

Template stripped gold, Au^{TS}, was chosen as the substrate onto which BrHBQ(CN)₂ and the hydroquinone derivative BrHBQH₂(CN)₂ would be self-assembled as a monolayer. Template-stripped gold is formed by thermally evaporating gold, and depositing it onto freshly cleaved

mica.^{143,144} Applying an adhesive to the deposited gold and stripping the mica leaves a freshly exposed surface of gold atoms of up to $25 \mu\text{m}^2$ in area and 3 \AA in roughness.¹⁴³ This allows for quickly-formed atomically-flat gold surfaces.

Au^{TS} was prepared by Marcus Johnson using a literature procedure.¹⁴⁴ Acetonitrile was chosen as the solvent for self-assembly. $\text{BrHBQ}(\text{CN})_2$ is soluble in polar or aromatic solvents such as acetonitrile, methanol, ethanol, and benzene. However, alcohols and aromatic solvents are incompatible with Au^{TS} . Typical Au^{TS} solvents, such as hexane and cyclohexane, were poor solvents for $\text{BrHBQ}(\text{CN})_2$; therefore, acetonitrile was selected.

I have observed that HBQs in general decompose at ambient temperature in acetonitrile solutions. The culprit appears to be adventitious moisture. Therefore, all acetonitrile used in HBQ monolayer experiments was freshly distilled from anhydrous calcium hydride and stored over 3 \AA molecular sieves under a blanket of dry nitrogen. The container was sealed with a rubber septum and stored at $0 \text{ }^\circ\text{C}$; fresh aliquots were syringed for each experiment.

Section 5.2.1 Self-Assembly Procedure

Self-assembled monolayers were prepared by M. Johnson by exposing Au^{TS} substrates to a 1 mM anhydrous acetonitrile solution of $\text{BrHBQ}(\text{CN})_2$ for 6 hours. Formation of the monolayer was monitored by atomic force microscopy (AFM). AFM images taken at different intervals showed that the coverage reached after 6 hours was the same as the coverage reached after longer periods (out to 24 h). Initially, large aggregates, 60 nm tall, form on the surface. Over time, these structures become smaller, and the underlying monolayer becomes smoother. The monolayer film was then rinsed with fresh CH_3CN to remove non-chemisorbed molecules, and dried overnight under a stream of nitrogen.

Section 5.2.2 Monolayer Characterization

X-Ray photoelectron spectra (XPS) for the BrHBQ(CN)₂ monolayers were recorded by Marcus Johnson. The absence of signals assignable to iron or cerium indicate that no metal impurities are present from previous oxidation steps. Comparison of the data from BrHBQ(CN)₂ as a monolayer on Au^{TS} and as an aggregated cluster on Au^{TS} supported the idea that the molecule would interact with the gold surface along one edge of the molecule via the nitrile nitrogen atoms. A single N 1s peak was observed at 399 eV for the monolayer; in comparison, this peak is found at 402.5 eV in the spectrum of “bulk” material. The shift to lower binding energies in the monolayer compared to the bulk solid is indicative of increased electron density on the nitrogen, the expected result for nitrile groups chemisorbed on the Au surface.¹⁴ The binding energy observed in the monolayer is similar to those reported for benzonitrile adsorbed via η¹ N-bonded complexes on Pd and Ni surfaces (399.6 eV and 399.8, respectively).¹¹¹

Interestingly, the N 1s binding energy in bulk BrHBQ(CN)₂ is higher than the ~400 eV normally seen for condensed organic nitriles such as benzonitrile (399.8 eV) and acetonitrile (400.2 eV).^{145,146} This suggests that the nitrile nitrogens in BrHBQ(CN)₂ are relatively electropositive.⁹⁹ This may be partly due to resonance with the quinone system; however, a CN—Br halogen bond in the solid phase cannot be ruled out. The shift in the Br 3p XPS peak at 70.7 eV in the monolayer to a broad shoulder with peak at 66.4 eV in the cluster suggests an increase of electron density, supporting the notion of a halogen bond. The X-ray crystal structure of BrHBQ(CN)₂ does not show a close N—Br interaction. However, this does not exclude the possibility of halogen bonding in the nanocrystalline state produced in the absence of benzene.

Because only a single nitrogen binding energy environment was evident, I conclude that both nitrogen atoms are chemisorbed to the surface. Bromine peaks were strong, consistent with unbound electrons having the highest mean free-path due to the element's position at the top of the monolayer. Thus, this data support a model where BrHBQ(CN)_2 forms a monolayer on Au^{TS} where the molecules stand on the surface via two simultaneous η^1 contacts of the nitrile nitrogens to the gold.

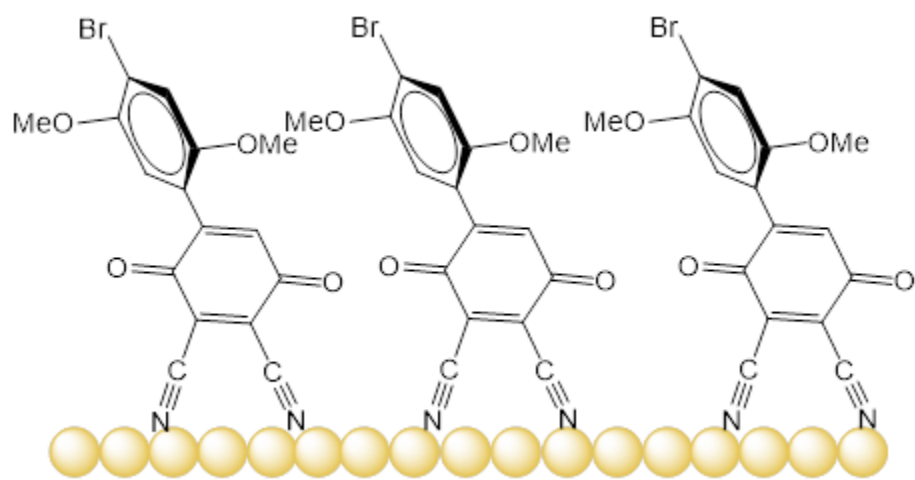


Figure 5.1 Diagram of molecules self-assembled on flat template-stripped gold.

Section 5.3 Conduction Measurements

In order to test the conduction through the HBQ monolayer, a junction was required to complete the circuit. Each of the junctions formed a sandwich with HBQ and is expressed as “Top contact | HBQ monolayer | Au^{TS}”. The first top contact was a droplet of eutectic gallium-indium amalgam (EGaIn) on the bare monolayer surface (Figure 5.2, Section 5.3.1). Following this, in Section 5.3.2, conduction measurements for the hydroquinone precursor are presented. The second top contact was a cold-gold deposited electrode contacted to the circuit in series by EGaIn (Figure 5.6, Section 5.3.3). The third contact was a scanning tunneling microscope (STM) tip made from a Pt/Ir alloy (Figure 5.8).

Complete details of the experimental setup may be found in Marcus Johnson’s dissertation.¹⁴² Forthcoming publications will fully discuss the results,¹⁴¹ and additional analysis of the data is expected to provide some mechanistic insights of the electron transfer.

Section 5.3.1 EGaIn Top Contact

The first monolayer sandwich tested was constructed as EGaIn | BrHBQ(CN)₂ | Au^{TS} (Figure 5.2). The circuit was tested between ± 2.5 V within a Faraday cage under ambient conditions.^{141,142} M. Johnson reports that 50% of the assemblies did not short immediately and could maintain stable conduction through several sweeps. However, only a single pad was stable after an hour of measurement. Data was reported for only this pad.

Figure 5.3 shows a single example conduction trace for this circuit. Note the greater current in the negative bias conduction. The schematic in Figure 5.2 illustrates electron flow through the monolayer; electrons preferentially transfer from the top contact through the monolayer and into the Au^{TS}. This result was unexpected, because it is in the *opposite* direction to AR. Metzger and

Johnson argue that this is due to an electric-field induced auto-excitation forming $D^+ - \sigma - A^-$.^{141,142} An alternative explanation may be that the FMOs shift under bias (as discussed in Chapter 2), and conduction increases when a resonance state is reached.¹⁶ When a negative bias is placed on the system, the Fermi energy of Au^{TS} electrons drops. This leads to a decrease in energy of the acceptor orbitals along with it.^{18,147} Concurrently, the Fermi energy of the EGaIn rises in energy. This, in turn, increases the energy of the donor molecular orbitals. When the HOMO and LUMO are at the same energy (or within a thermally excitable energy difference), electron transfer from D to A becomes possible. In this way, conduction begins.

As the scan numbers are increased, the conduction at $-V$ moves to more positive values while the conduction at $+V$ are largely unaffected (not shown). This leads to the growth of the rectification values (Section 5.4.1). The explanation for this phenomenon is an area for further inquiry. A similar trend is seen in Section 5.3.3 for the EGaIn | Cold Au | BrHBQ(CN)₂ | Au^{TS} sandwiches.

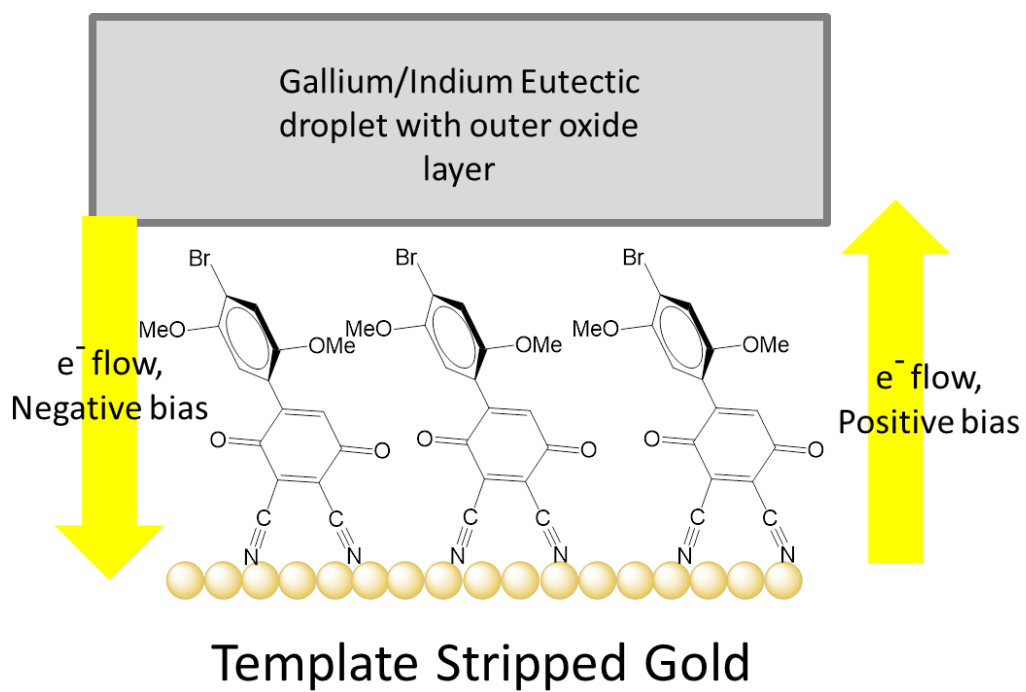


Figure 5.2 Schematic of the monolayer with EGaln top contact. The droplet contacts many molecules at once. Arrows show direction of electron flow.

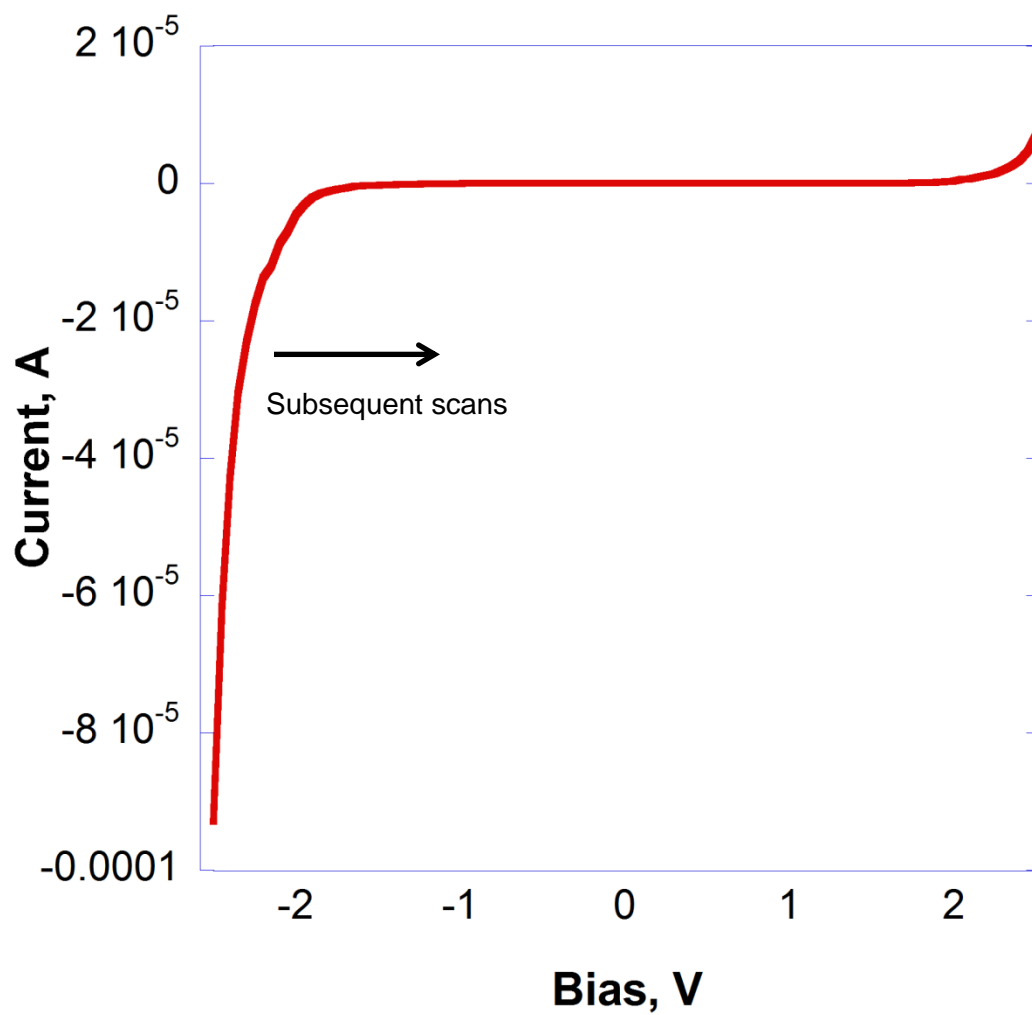


Figure 5.3 Representative *IV* curve with EGaIn top contact. Data has been smoothed for clarity using Kaleidagraph 4.5™. Arrow indicates onset of conduction becomes more positive on scanning.

Section 5.3.2 BrHBQH₂(CN)₂ EGaIn Top Contact

The reduced hydroquinone analog of BrHBQ(CN)₂, BrHBQH₂(CN)₂, was self-assembled onto Au^{TS} as was described above. Despite the loss of the quinone structure, this compound formed well-packed monolayers, presumably “standing” on the surface via the two nitrile groups.

Conduction was recorded for the EGaIn | BrHBQH₂(CN)₂ | Au^{TS} assembly (Figure 5.4) by M. Johnson.¹⁴² The circuit was initially tested between ± 2.5 V within a Faraday cage under ambient conditions, but none of the junctions were stable beyond 0.5 V (Figure 5.5). Cycling a junction to ± 0.5 V still led to a decrease in the conduction over subsequent scans. Conduction was symmetric through the monolayer. This observation is likely a result of the reduction of the quinone ring to an aromatic (hydroquinone) system.

As discussed in Chapters 2 and 4, reduction of the quinone to the hydroquinone raises the LUMO level of the molecule to roughly the same energies as the dimethoxybenzene ring. If the conduction mechanism followed typical charge-injection (hopping) models, this new eigenvalue would prevent electron injection from the electrode into the molecule because the LUMO has moved well beyond the bias window. This is analogous to the electrochemical characterization, where reduction of the aromatic compounds is not possible within the scan range. If the electric-field induced auto-excitation hypothesis is correct,¹⁴¹ then monolayer degradation may be due to electric field-induced thermal decomposition

Nevertheless, reduction of the quinone ring is enough to eliminate the rectifying characteristics of the HBQ system. This result suggests that rectification through the monolayer is due at least in some part to the D— σ —A structure, rather than to the other mechanisms described in Chapter 1.

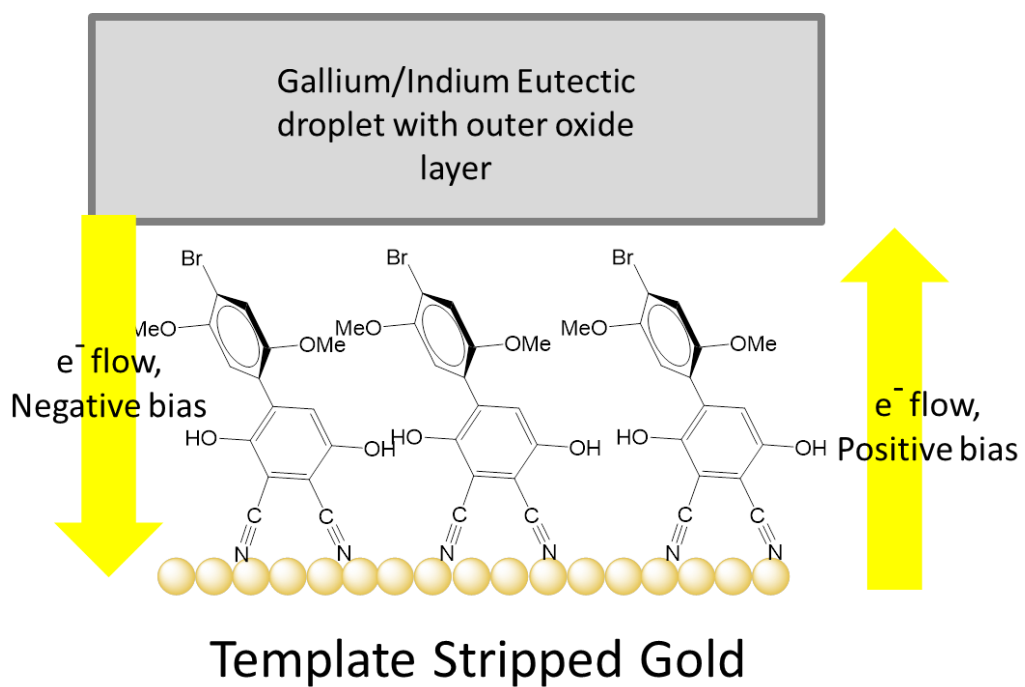


Figure 5.4 Schematic of the monolayer with EGaIn top contact. The droplet contacts many molecules at once.

Arrows show direction of electron flow.

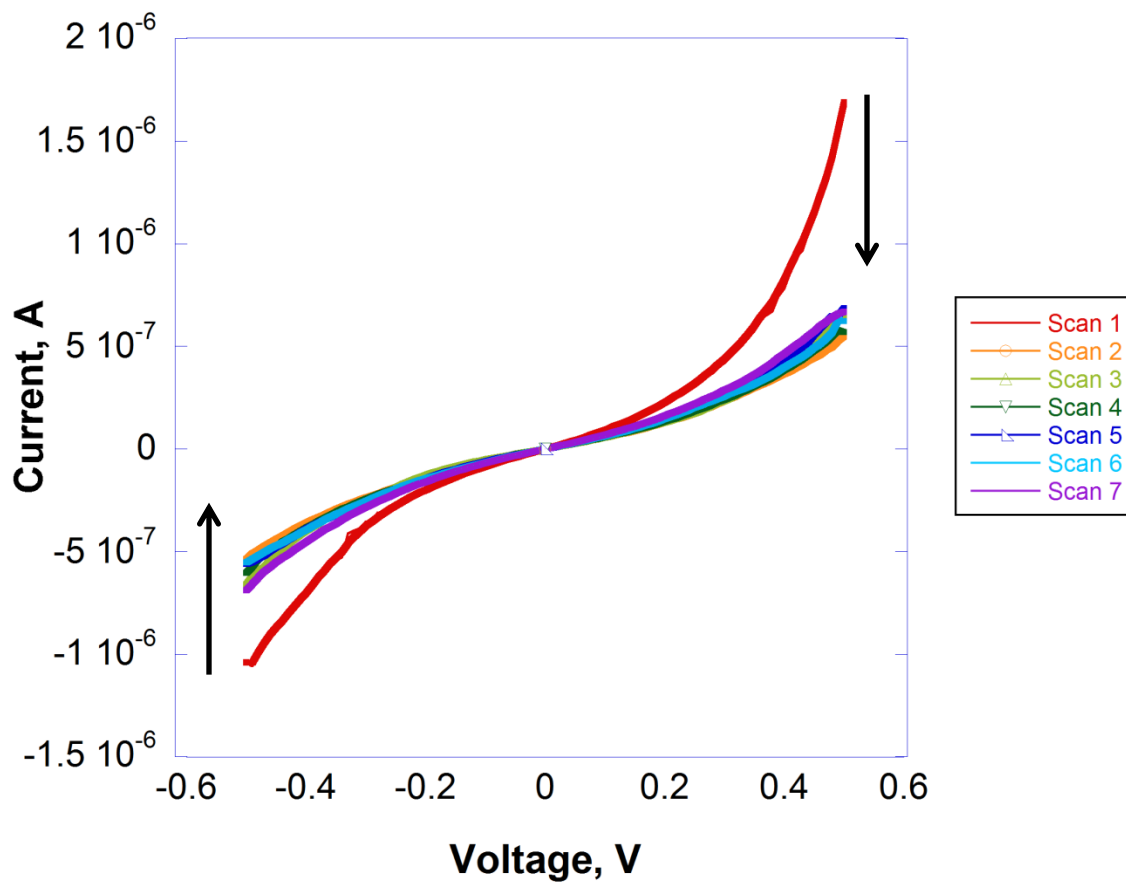


Figure 5.5 Representative *IV* curves for BrHBQH₂(CN)₂ with an EGaIn top contact. Scans after the first have diminished conductances. Data has been smoothed for clarity using Kaleidagraph 4.5™.

Section 5.3.3 Cold Au Top Contact

To further ensure that rectification through the monolayer is due to the molecule and not due to the asymmetry imposed by different electrodes, constructions with a gold top electrode were constructed by M. Johnson.^{141,142} Thus, “cold gold” was vapor deposited onto HBQ monolayers on Au^{TS}, forming electrodes 1 mm² in area and 15–20 nm thick. In order to connect this cold Au | BrHBQ(CN)₂ | Au sandwich to the larger circuit, it was still necessary to use an EGaIn droplet (Figure 5.6), as a silver adhesive paste destroyed the sandwich.¹⁴² If an amalgam of the Ga component were formed with Au, then no Ga₂O₃ should be present; if the contacting is only partially amalgamated, then some Ga₂O₃ may be present. The actual species present is unknown and is not taken into account.

Forty-five sandwiches were generated: of these, 20 were studied by EGaIn probes, of which 1 sandwich remained stable to ± 2.5 V, while the remainder showed either short or open circuits.¹⁴² The data are presented in Figure 5.7. As with the EGaIn electrode alone, the monolayer asymmetrically conducts with forward bias in the negative voltage range. However, the magnitude of the conductance is greatly diminished (by about a factor of 70) with respect to the bare EGaIn sandwich. Whether this is due to ohmic losses from the gold pad or from some other source, is unclear. The conduction traces for this setup do not reveal any further information about the mechanism of conduction through the monolayer, and further work is required to explore conduction through the low-bias voltages. As was observed for the EGaIn | BrHBQ(CN)₂ | Au^{TS} device, the conductance in $-V$ moves to more positive values as the scan numbers are increased while the conduction at $+V$ are largely unaffected (not shown). This leads to the growth of the rectification values (Section 5.4.2).

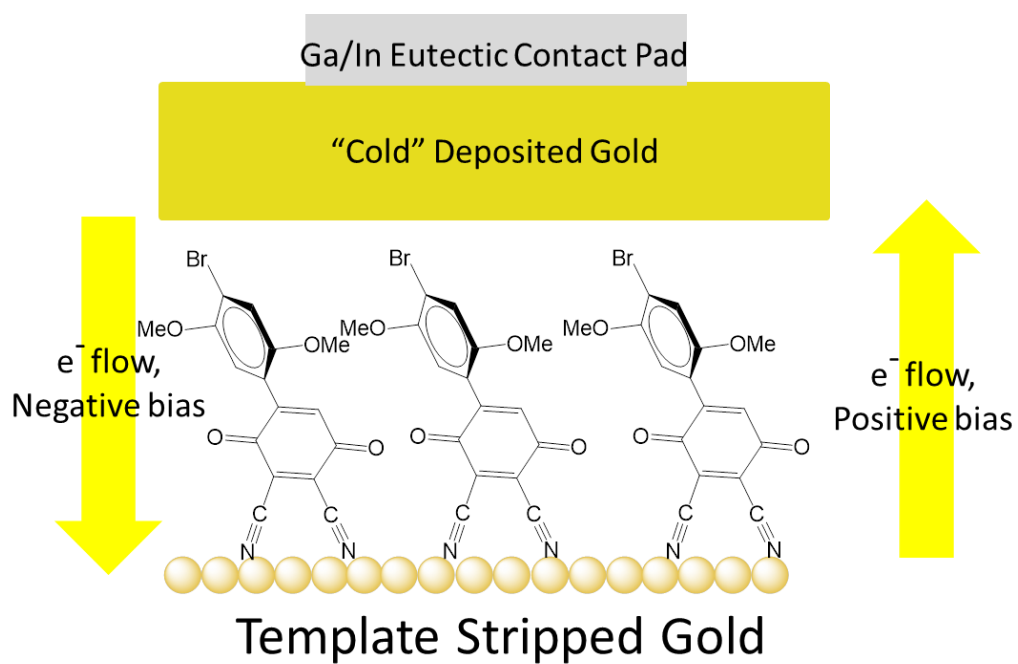


Figure 5.6 Schematic of the monolayer with Cold Au top contact. The EGaIn droplet connects the junction to the circuit. Arrows show direction of electron flow.

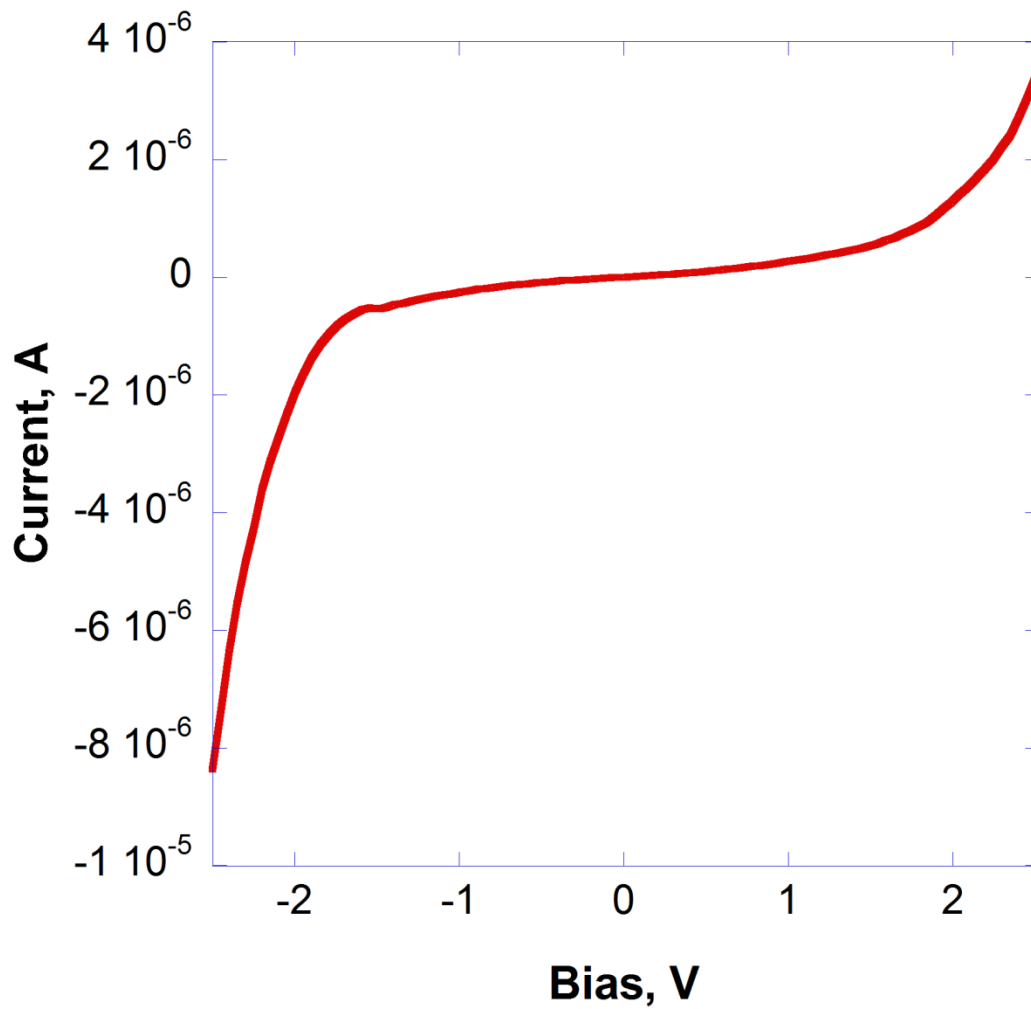


Figure 5.7 Representative *IV* curve with “Cold Au | EGaIn” top contact. Data has been smoothed for clarity using Kaleidagraph 4.5™.

Section 5.3.4 Pt/Ir STM Contact

Conductance traces were also recorded using monolayers of $\text{BrHBQ}(\text{CN})_2 | \text{Au}^{\text{TS}}$ as probed by a Pt/Ir STM tip (Figure 5.8). Scanning tunneling spectroscopy traces were generated from the same samples as were used to record the AFM images (Section 5.2.2). The conductance traces were recorded by moving the tip to a desired spot, then sweeping the voltage applied to the sample over that spot. Afterwards, the voltage range was extended to ± 1.5 V. Rectifying characteristics occurred roughly 50% of the time.

Figure 5.9 illustrates a conductance trace through $\text{Pt/Ir} | \text{BrHBQ}(\text{CN})_2 | \text{Au}^{\text{TS}}$. In this experiment, the forward bias occurs in the positive voltage range, which happens because electrical ground in the STM system is connected to the STM tip, rather than the sample (as is the case for Au^{TS}). An unusual result from the low-energy turn-on voltage in the negative bias leads to preferential conduction at $V < -0.5$ V, but just above $\sim V = +0.5$ V the conduction rises exponentially. The voltage continues to increase more quickly in the positive direction than the negative direction out to ± 1.5 V. The effect this conductance switching has on rectification is discussed in Section 5.4.3.

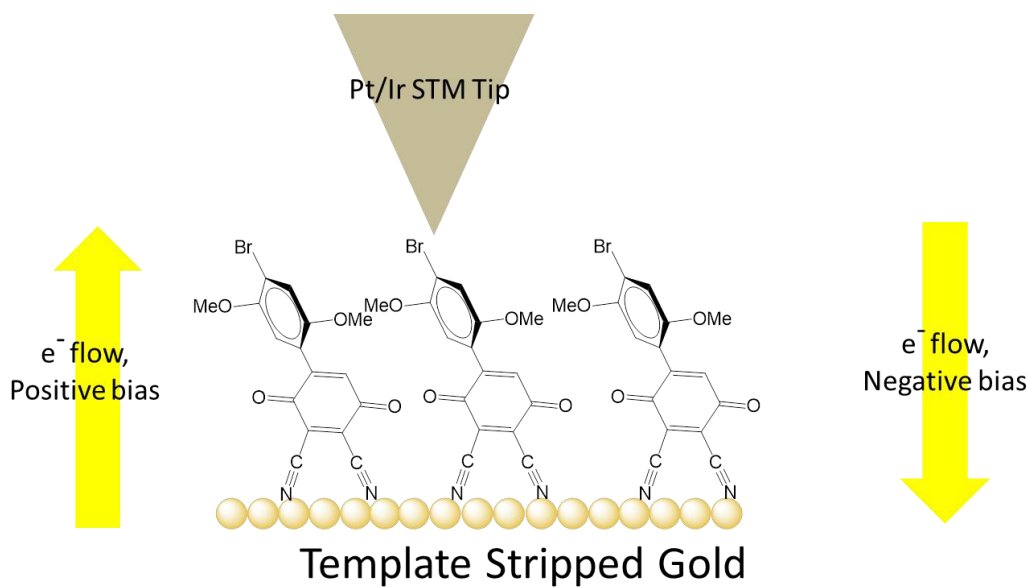


Figure 5.8 Schematic of the monolayer with Cold Au top contact. The EGaIn droplet connects the junction to the circuit. Arrows show direction of electron flow.

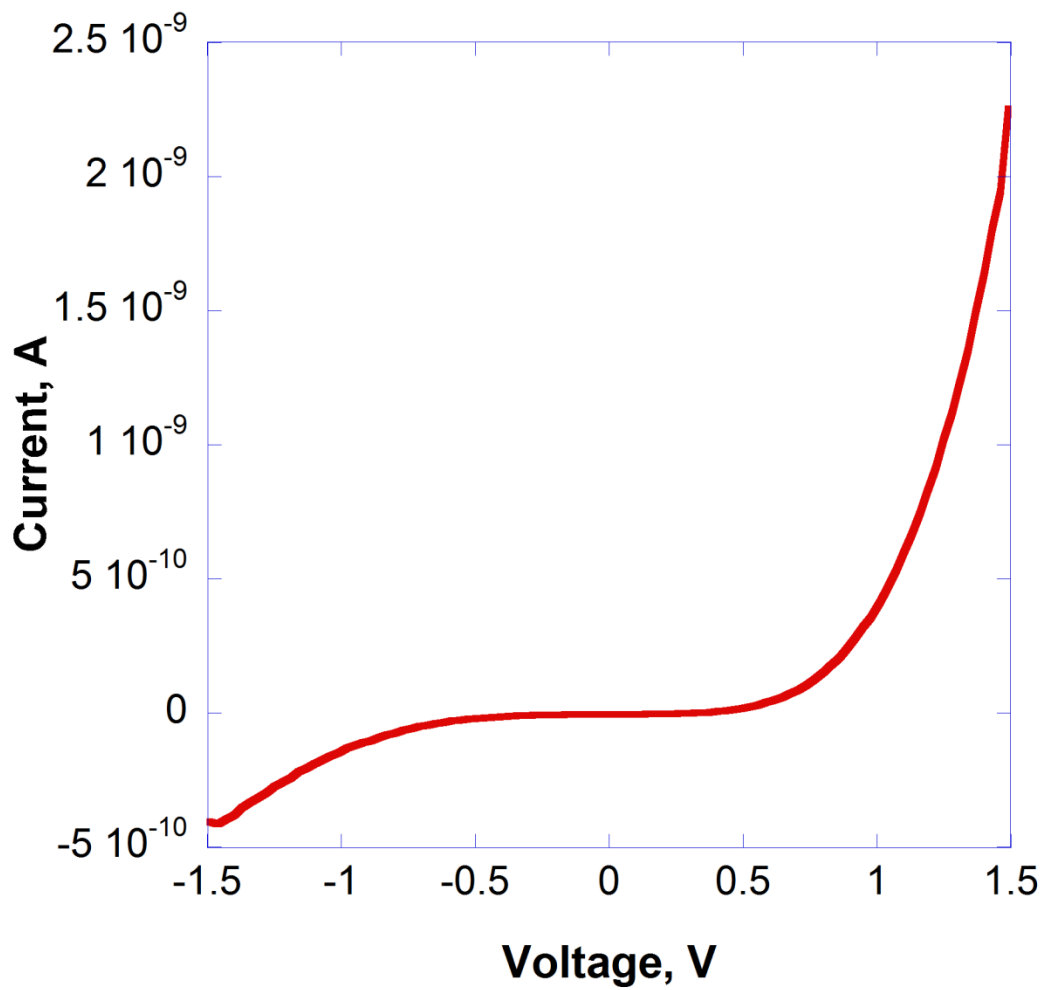


Figure 5.9 Representative *IV* curve with STM Pt/Ir top contact. Data has been smoothed for clarity using Kaleidagraph 4.5™.

Section 5.4 Rectification

Analyses of the conduction traces recorded for the three top-contact electrodes by M. Johnson provide the bias dependent rectification ratios $RR(V)$.¹⁴² Results of the RR analyses are only presented for $\text{BrHBQ}(\text{CN})_2$, because the hydroquinone $\text{BrHBQH}_2(\text{CN})_2$ conducted symmetrically for the potentials in which it was stable. Due to the placement of electrical ground, the forward bias operated at negative potentials for the monolayer conduction measurements, and $RR(V)$ is defined as

$$RR(V) = \frac{-I(-V)}{I(V)}$$

Forward bias due to placement of ground was demonstrated at positive bias for STM conduction measurements, and so RR for that system is defined as

$$RR(V) = \frac{I(V)}{-I(-V)}$$

Section 5.4.1 EGaIn Top Contact

A plot of the rectification ratio with respect to voltage is presented in Figure 5.10. Rectification is low ($RR < 10$) for biases under 1.0 V. After that, a sharp increase in rectification is seen. The rectification continues to increase until about 1.8 V, where it reaches a maximum and inverts. After this, the rectification drops until ~2.3 V, where it inverts again and rises out to the edge of the scan window.

As mentioned in Section 5.3.1, successive scans changed the behavior of the conduction traces, and this is seen in the increase of the RR over successive scan numbers. Figure 5.10 illustrates this with three example traces over subsequent scans. The earliest scan (lowest scan number) has the shallowest rise in rectification ratio, whereas later scans begin to increase in magnitude. The traces generally display the same behavior as described above, it is their

magnitude which changes with subsequent sweeps. If the monolayer were unstable, RR would decrease.¹⁴⁸ It stands to reason, then, that the monolayer is unaffected by the high bias fields and there is another change within the system.

The RR maxed out at the last scan at ~ 150 , which is several orders of magnitude lower than commercial semiconductor diodes ($RR \approx 10^6$).¹⁶ However, it is a respectable rectification ratio for an all-organic rectifier; previous studies utilizing only torsion angles as a barrier received much lower rectification ratios.^{149,150,150}

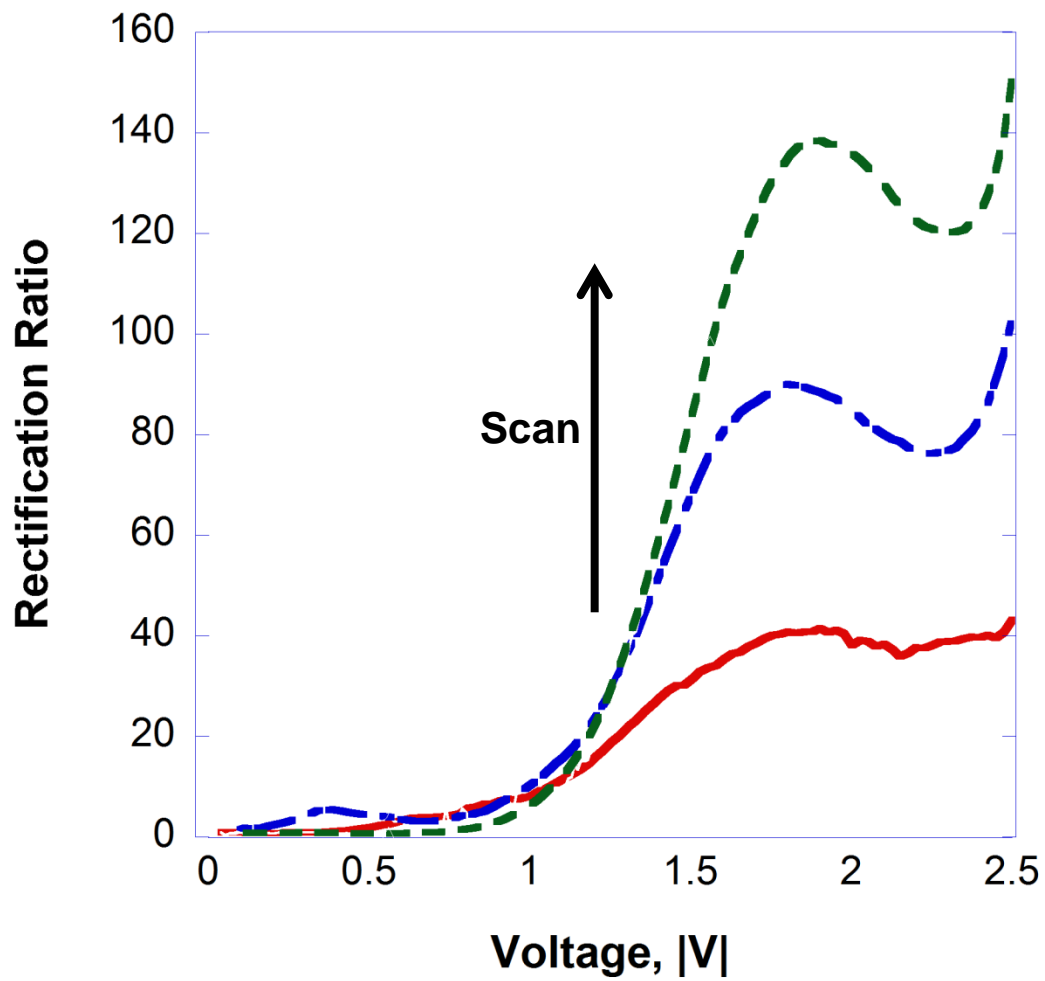


Figure 5.10 Representative RR traces for EGaIn | BrHBQ(CN)₂ | Au^{TS} sandwich. Data has been smoothed for clarity using Kaleidagraph 4.5TM. Red, green, and blue lines denote results at 7th, 15th, and 20th scans.

Section 5.4.2 Cold Au Top Contact

The chart of rectification ratios with respect to voltage is presented in Figure 5.11. Rectification is low ($RR < 1$) for biases under 2 V. Rectification onset grows more slightly out to 2.5 V to a maximum of 5–35. The conduction traces from Section 5.3.3 show lower overall conduction by about a factor of 70 in the negative bias direction, which may be a factor in the diminished RR.

As mentioned in Section 5.3.3, successive scans changed the behavior of the conduction traces, and this is witnessed by the increase of the RR over successive scan numbers. The traces generally display the same behavior as described above, it is their magnitude which changes with subsequent sweeps. It stands to reason, then, that the monolayer is still unaffected by the high bias fields, and there is another change within the system. The maximum RR (~35) was seen for the last scan, which was significantly reduced with respect to the EGaIn top contact alone. The rationalization for this effect has yet to be explored in detail.

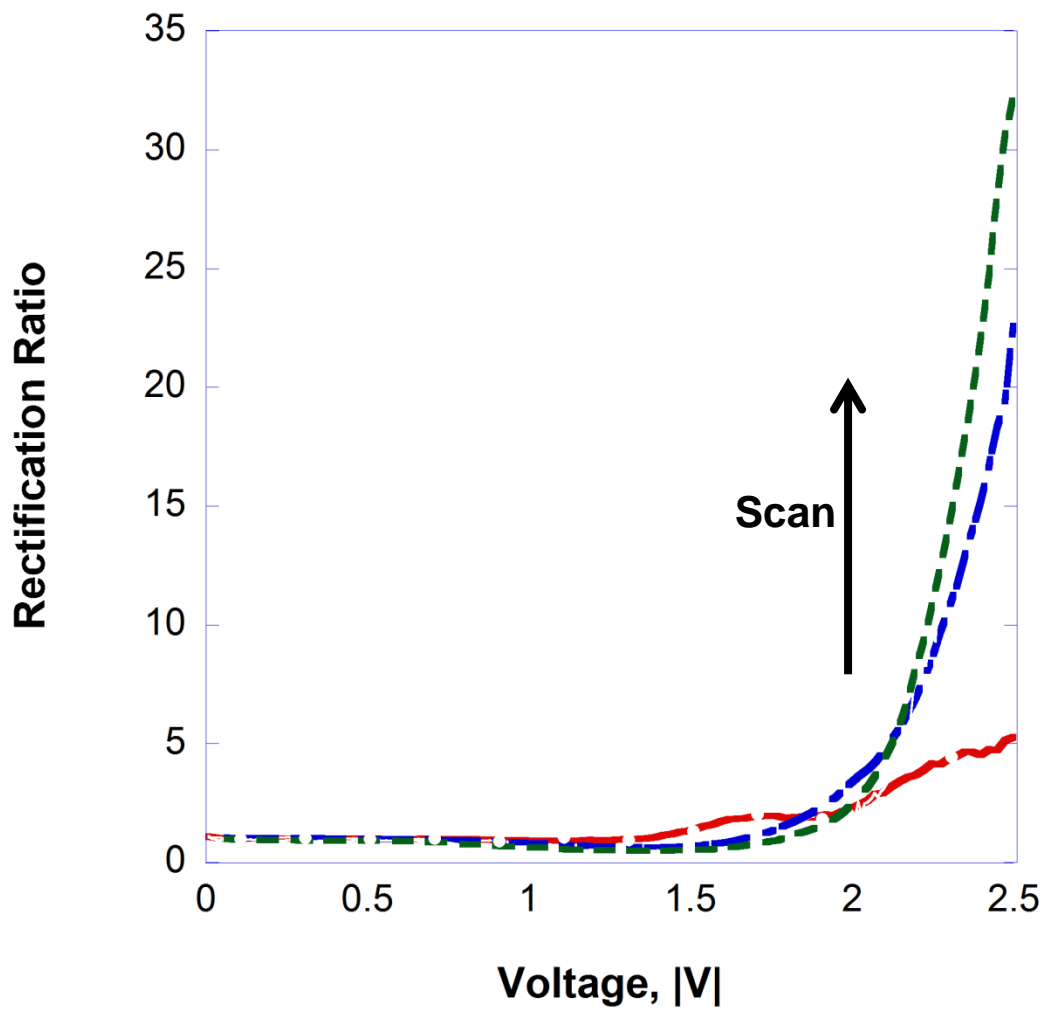


Figure 5.11 Representative RR traces for EGaIn | Au | BrHBQ(CN)₂ | Au^{TS} sandwich. Data has been smoothed for clarity using Kaleidagraph 4.5TM. Red, green, and blue lines denote results at 5th, 12th, and 17th scans.

Section 5.4.3 Pt/Ir STM Contact

Figure 5.12 illustrates the rectification ratios that resulted from averaged measurements within the STM conduction measurements in Section 5.3.4. The measured rectification ratio is much smaller than either macroscopic measurements of the monolayer. The initial dip in RR below 1 is due to the early onset of conduction in $-V$. As conduction begins in $+V$, and increases above 0.5 V, the rectification direction reverses.

The single molecule measurements taken on the monolayer have a much smaller conduction and rectification ratio than the macroscopic measurements. While single-molecule conductance is understandably smaller, if rectification through the monolayer were due only to the molecule itself, then there should ideally be a 1:1 correlation to the tested area and conductance. This, in turn, would lead to a scale correlation to the rectification ratio. However, this is not the case¹⁰⁸ and remains an area of further inquiry.

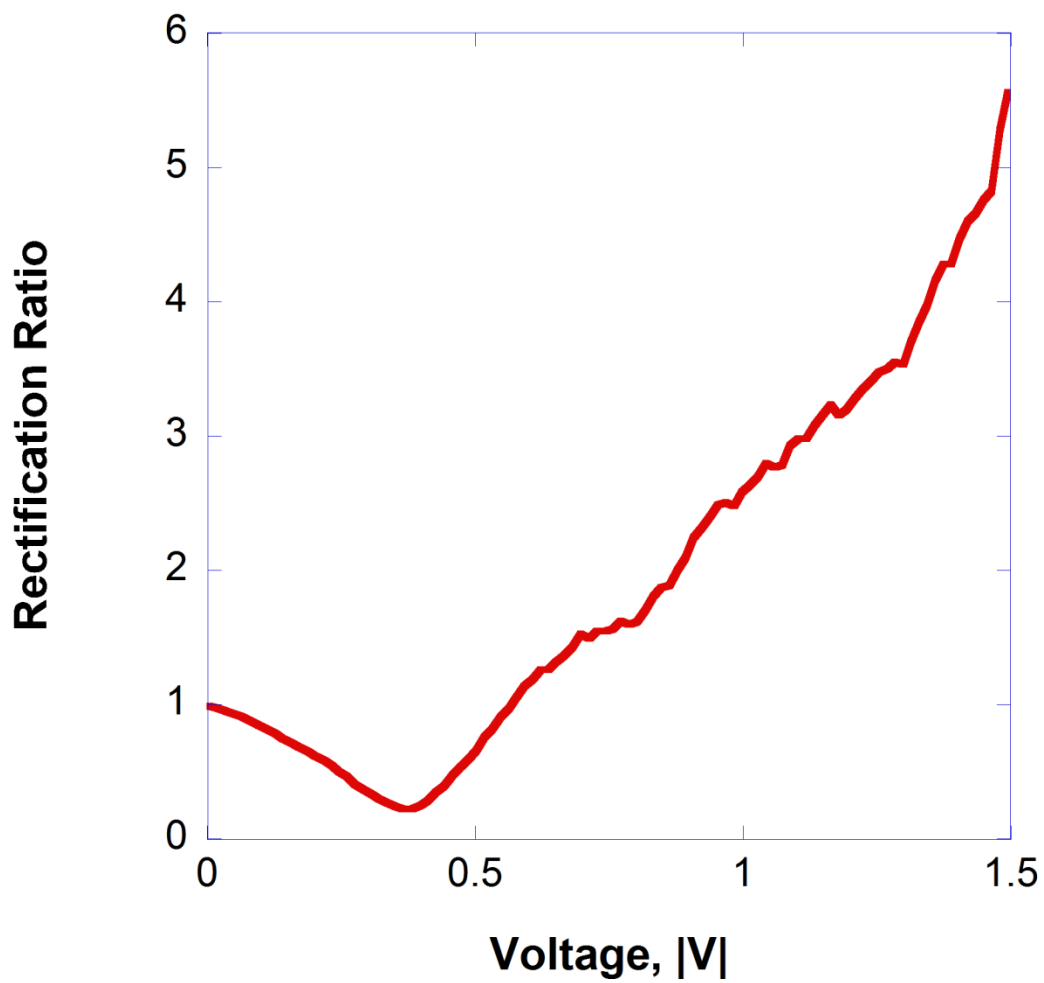


Figure 5.12 Representative RR trace for Pt/Ir | BrHBQ(CN)₂ | Au^{TS} sandwich. Data has been smoothed for clarity using Kaleidagraph 4.5TM.

Section 5.5 Summary

In this chapter we present the confirmation that BrHBQ(CN)₂, self-assembled into a monolayer and sandwiched by various top electrodes, rectifies. Likewise, the hydroquinone derivative tested did not rectify within the junction. Conduction through the monolayer using macroscopic pads was inconsistent; on subsequent scans of the junction, a change in the conduction behavior was evident. Future work within the Metzger lab will analyze the cause(s) behind this change.

Conduction through a single molecule by STS, on the other hand, was consistent upon multiple scans which allowed for statistical analysis of the junction at lower biases. The direction of electron flow is reported to be the same for that of the monolayers.

The rectification ratios for EGaIn-contacted monolayers (both with and without the Au pad) increase with scan number until the junction eventually fails. This effect is related to the change in conduction, although the root cause remains unclear. It is believed that the gallium oxide which coats the EGaIn droplet grows over successive scans at high bias (>1.5 V), and this layer causes complex changes within the junction structure. The single molecule rectification ratio, tested by STS, remains stable under the experimental conditions.

The molecule, BrHBQ(CN)₂, rectified as predicted under three separate conditions. While specific details concerning the mechanisms of electron transfer remain unclear, future studies will focus on elucidating the specific contributions to rectification. The next chapter will review the information presented within all preceding chapters, and address open questions such as this with regard to HBQ rectification.

CHAPTER 6

CONCLUSIONS AND FUTURE DIRECTIONS

Molecular Electronics, a subdiscipline of nanotechnology, holds promise for exploring the interface between classical and quantum electronics. As researchers gain a better understanding of the variables and effects which govern electron transport through a junction (and eventually, several junctions), we gain a better understanding of the underlying physical principles which dominate on the quantum level—and which ones do not. By carefully altering molecular structure and controlling the variables under which the experiments are run, structure–property relationships may be drawn.

In Chapter 1, concepts critical to the understanding of molecular circuits and components were reviewed, and major scientific milestones were presented to construct context for the current work. The major physical principles behind molecular conduction and rectification were outlined. Emphasis was placed on the parameters limiting the scope of the current work. Based on these principles, we were able to confidently explore the notion that HBQs might rectify.

Chapter 2 detailed the computational work which presented the idea that the lowest energy conformations for HBQ derivative systems would be twisted out of plane. Spectral and electrochemical data presented in Chapter 4 supports the idea that the twisted conformation, leading to orbital isolation, should predominate. FMOs calculated for twisted conformations indicate that torsions are sufficient to localize the HOMO and LUMO densities to the dimethoxybenzene and benzoquinone rings, respectively. Molecular geometry, orbital distribution, and orbital eigenvalues were calculated for several other molecules by which to

draw comparative conclusions. “Monomer” dimethoxybenzene and benzoquinone displayed behaviors that are characteristic of their contribution to the HBQ system. Diaryl reduced-HBQ systems have largely delocalized orbitals with high overlap across both rings.

Chapter 3 detailed the stepwise synthesis and purification of the HBQ systems, showing the reactivity difference between aromatic and quinone systems. The synthesis of BrHBQCN was presented, a much more challenging synthetic target than was originally supposed. From there, a primary synthetic target has been isolated. BrHBQ(CN)₂, a 2,3-dicyanobenzoquinone derivative, was prepared from its hydroquinone. These compounds were the focus of later rectification efforts. Ongoing work to isolate the monocyanted BrHBQCN is presented with data to assist for its isolation by a future group member.

Chapter 4 presented the spectroscopic and electrochemical characterization of several HBQ derivatives and related compounds. Additionally, XRD analyses on single crystals and the solid-state interactions of the molecular lattice were discussed. The spectral and electrochemical data provide important support for Chapter 2 calculations, needed to analyze HBQ device behavior.

Chapter 5 presents brief confirmation that the HBQ molecule BrHBQ(CN)₂ rectifies on an atomically flat layer of gold, while a monolayer of BrHBQH₂(CN)₂ does not. This data is being drafted for publication, and appears unabridged in Marcus Johnson’s dissertation.

Finally, this chapter is to gather the most important messages from each of the preceding experimental chapters and put them in context with respect to a) ongoing investigation within Woski lab, b) near-term collaborative work outside of the scope of this manuscript, and c) near-to-mid-term synthetic and spectrometric investigations that will grow the body of work relating to the HBQ backbone as a molecular rectifier.

Much investigation still needs to be performed whereby the mechanisms behind conduction in the HBQ molecules are carefully and conclusively investigated. Electrode choice in the system has some effect on the rectification ratio, although clearly construction of the junction overall has a notable effect on determining currents at both forward and reverse bias.^{151,152}

Section 6.1 Calculation of NEGF-DFT DOS

Section 6.1.1 DOS evolution under bias

In addition to the theoretical work already discussed in Chapter 2, another set of computations would add to the understanding of HBQ molecules. A full conductance treatment, consisting of the molecule placed between two Au electrodes and subjected to a bias using non-equilibrium Green functions (NEGF),^{22,153,154} would help develop understanding about how electrons move through the molecule in a device. The fundamental concepts underlying NEGF as they apply to Molecular Electronics are outlined in the text by Cuevas and Sheer.²²

Wang³⁹ and Bin⁸⁴ correlate behavior of Molecular Projected Self Consistent Hamiltonians (MPSH) calculated in a particular bias window alongside the calculated conductance curves. Other reports of the use of this method include Elbing *et al.*,¹⁴⁹ El-Hendawy *et al.*,^{82,83} and Nakamura *et al.*,⁴⁰ among others. The authors correlate the energy of the molecular orbitals in a junction as they change with the applied bias to the Fermi energy of the junction's electrodes. Typically, as FMO eigenvalues shift into and out of resonance, conduction increases and drops off again.¹⁵⁵ This is the basis for the dependence of RR on V . Wang⁵⁹ and Bin⁸⁴ also comment on the shape of the molecular orbitals without a bias, and discuss how the charge transfer mechanism through them is affected as the HOMO and LUMO are perturbed.

This computational treatment may be directly applied to the HBQ molecules. Generating MPSH graphs in addition to transmission coefficients would be important to discuss conduction

mechanisms, this type of study would require a collaboration with a more experienced computational chemist. Additionally, the results of experiments would be required to validate the output from calculations.

Section 6.1.2 Monomer Monolayer Comparison to Experiment

In a manner similar to that of Van Dyck,⁴⁵ it would be an interesting exercise to compute an asymmetrically substituted benzene— one with two differently polarizing alligator clips and test the rectification through that. The benzene itself would simply be a molecular wire, but that would be sufficient when simply trying to tease out the *pure* effects of Schottky rectification. An example molecule could be 4-mercaptobenzonitrile. It is commercially available, which would decrease the amount of effort required for experimental set-up. Then, similar conduction measurements through 2-cyano-5-mercaptobenzoquinone (heretofore unreported in the literature) could be both experimentally determined and calculated. That way, these results could be compared side by side quickly to the results generated for the HBQ molecules. 4-Mercaptobenzonitrile is not expected to act as a traditional unimolecular rectifier as the HOMO–LUMO gap is large owing to the aromatic ring, and no isolation between the Donor thiol and Acceptor nitrile. The same is true for 2-cyano-5-mercaptobenzoquinone, although a difference in their conduction profiles is expected, due to the much more accessible LUMO level of benzoquinone (Chapter 2).

The simplest experimental setup for testing the rectification ability of a SAM of molecules would be a pure 4-mercaptobenzonitrile SAM on the gold surface (similar to the mercury drop experiment, with only Au electrodes). 4-Bromo-2,5-dimethoxybenzonitrile has already been prepared and isolated, which would need only a simple substitution on the bromine for the thiol or thioacetate (reactions easily found in SciFinder to accommodate the nitrile in one step).

Holze¹⁵⁶ in 2013 measured the binding competition of 4-mercaptobenzonitrile and found that only Au-S bonds exist, which suggests that those bonds are formed preferentially to Au-N bonds through the nitrile. He notes that the polarity of the molecule (2.9 D) weakens the Au-S bond somewhat, but not enough to cause competition with Au-N bonds when the system has equilibrated. Benzonitrile and benzylocyanide were both tested as well, and bonding geometries were suggested based on the data. These findings impact the design choices of molecular electronics researchers, as competitive adsorption would prevent high order in a monolayer (See Section 6.3).

Section 6.1.3 Monolayer Geometry Effects on Conduction

Querebillo *et al.*¹⁵⁷ measured the static conductance of several mercapto-arylnitriles in 2013. They constructed self-assembled monolayers of the aryl nitriles adsorbed on a gold surface *only through the thiol* and were able to get certain electrochemical measurements from the devices. This further supports the findings by Holze,¹⁵⁶ although the Au-S-Ph contact geometry is inconsistent between the two. Holze¹⁵⁶ shows the angle to be 180°, and Querebillo *et al.*¹⁵⁷ show the angle to be 120°. This is peculiar, because Hamoudi *et al.*¹⁵⁸ published a follow-up paper in 2012 that determined the bond angle (by XPS) of three S-Ar-CN (Ar=Bz, diPhenylethynyl, triphenyldiethynyl) molecules which had a deviation from surface normal between 33° and 36°.

Surface geometry is an important parameter to determine packing effects on a surface, but it is also a necessary parameter to understand the geometry of break junctions. The apparent molecular length normal to the electrode surface is dependent on binding geometry. Break-junctions measure conductance as a function of electrode separation, and well-defined conduction measurements require understanding of the junction interface. This is especially true to determine whether a molecule is bridging only two atoms between the contacts, or if one (or

both) of the contacts maintains contact to >1 electrode atoms.¹⁵⁹ For a monolayer, angle resolved XPS (ARXPS) is the best way to determine surface morphology. While XPS performed on the HBQ and HBQH₂ monolayers do *imply* that the nitriles adsorb onto the gold, ARXPS would provide clearer evidence that the terminal nitrogens are in fact both adsorbed on the surface.

In 2015, Ossowski *et al.*¹⁶⁰ used 2-thiolate and 2-selenate substituted naphthonitriles in order to measure the relative contact strength between the two, and used Core-Hole Clock Spectroscopy¹⁶¹ to investigate the femtosecond electron transfer processes within these molecules. This allowed the authors to better understand the mechanisms of electron transfer across fully conjugated molecules with different coupling strengths to Au(111). If a setup like this were available for 4-mercaptobenzonitrile, 2-cyano-5-mercaptobenzoquinone, and HBQ derivatives, time-resolved conduction processes could determine the differential contributions of tunneling and hopping charge transfer in the overall conduction regimes.

Section 6.2 TCNQ- and DCNQI-Substituted HBQ Derivatives

The end group alligator clips are not the only portion of the HBQ backbone susceptible to systematic alterations that might provide asymmetric conduction traces. TCNQ and DCNQI derivative molecules are synthetically accessible from BrHBQBr within a few steps (Figure 6.1). They would be promising candidates for a full theoretical treatment due to their similar geometry but much higher electron affinity than a bare HBQ. Fully optimized structures and associated information (orbitals, polarity, total energy) have already been calculated for the TCNQ molecule as well as all conformational isomers of the DCNQI structure; taking it from there to a complete set of calculations alongside synthetic, spectral, and electrochemical characterization would be important in securing the relevance of the HBQ structure in the literature. Additionally, the TCNQ and DCNQI acceptors are traditionally known as especially strong acceptors. This

would allow for a way to compare CT rate to the HBQ backbone, based on the Marcus Theory approach. As UV-Vis absorption presents an easily quantifiable ICT probability response, equimolar solutions of various derivatives will demonstrate the efficiency of the ICT within solution.

Presentation of the theoretical conduction, geometry, FMO eigenvalues, and MPSH's for TCNQ and DCNQI molecules in a junction could each be their own papers, referencing a first HBQ computational paper. Altering the structures in this way (especially among the different conformers of DCNQI) could really help give additional data on the correlation of polarity-based rectification. Table 6.1 lists the relevant characteristics of the HBQ backbone alongside the derivatives from Figure 1 to directly compare physical and electronic information. The A, B, and C labels for the DCNQI labels refer to Figure 6.1 and the different geometries in which the quinoimine can exist. Perhaps somewhat surprising is that DCNQI-C is the most stable of the conformers according to our calculations. Geometry measurements are reported in the same manner as outlined in Chapter 2. TCNQ and DCNQI-A are rotated in the opposite direction as the HBQ backbone. Future calculations will be run to determine the barriers of rotation for each of these derivatives and ascertain as to why these particular geometries are favored.

Images of the FMOs for each molecule are presented in the Appendix. In general, these derivatives show greater HOMO delocalization across the system than the HBQ backbone. The LUMOs, on the other hand, are very efficiently localized on the acceptor ring.

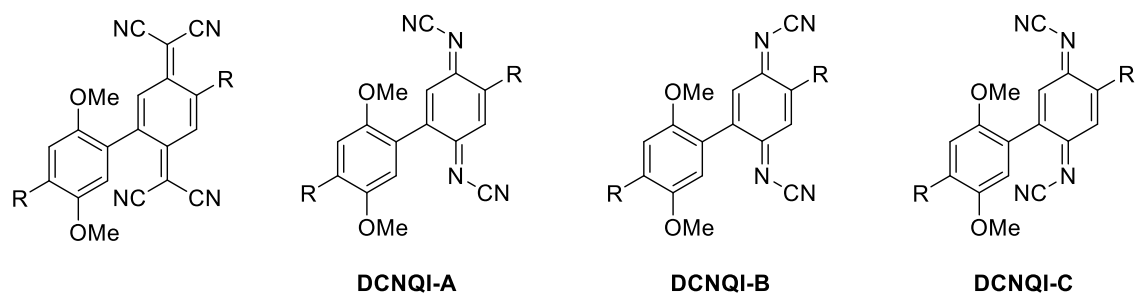


Figure 6.1 TCNQ derivative of HBQ (left), the four configurational isomers of DCNQI-derived HBQ

Table 6.1 DFT minimization of compounds in Figure 6.1

	Torsion Angle (°)	Dipole (D)
BrHBQBr	38	1.33
DMB-TCNQ	118	3.35
DCNQI-A	122	1.76
DCNQI-B	47	4.73
DCNQI-C	45	2.97

Using these derivatives in an actual device would present a challenge within the circuit design— nitrile groups on the quinoid positions would competitively bind to a gold substrate if an improper alligator clip were selected. This is why, in Figure 1, the termini are left as R groups. Thiols remain a possibility, but the increased steric burden (especially from TCNQ) might require these molecules to have some sort of nonspecific spacer to attach to a planar electrode. MCBJ techniques would be incompatible with these molecules because too many junction geometries are possible across the molecules.

Section 6.3 Synthesis of NCHBQCN

Considering the poor interaction (and therefore appendant FMO overlap) of bromine with typical electrode materials, further synthetic developments should endeavor to create the symmetrically substituted NCHBQCN. The weak bromine...gold interaction is an area of unforeseen complication in the original charge-transport experiments, because a molecular end group's interaction strength with an adjacent electrode directly affect the charge-transfer rate across the junction.^{39,44-46,59} As outlined in Chapter 1, the nonequivalent coupling of the FMOs to their respective electrode would equate to a nonequivalent shift of the FMO eigenvalues under bias. This would then lead to asymmetric rectification across the molecular system. Thus by changing the HBQ backbone to a symmetrically terminated backbone, direct conclusions may be drawn from the inherent design of the backbone itself, rather than be conflated with other conduction effects.

This molecule will not form a suitable self-assembled monolayer since the alligator clips are insufficiently differentiable and would ultimately lead to a symmetric signal in the junction (Figure 6.2).

Geometry optimization of the proposed molecule gives an intermolecular torsion angle of 41° . While there might be an expectation that the molecule would have the same dipole as BrHBQBr (because of the 4,4'-group symmetry), the electron withdrawing nature of the nitrile groups make the quinone a more efficient acceptor. It gives NCHBQCN an overall dipole moment of 2.1 D compared to BrHBQBr's dipole of 1.3 D.

Synthesizing an HBQ core with symmetrical alligator clips may be a straightforward procedure using chemistry already developed in Woski lab. A proposed synthetic scheme is outlined below in Scheme 6.1. From the starting material BrHBQBr, reduction in methanol by NaBH_4 will yield the hydroquinone. Subsequent cyanation in acetonitrile by a metal cyanide assisted by a Pd catalyst was reported by Ushkov to proceed in high yield with good tolerance for diverse functional groups.¹⁶² Reduction prior to cyanation is necessary to prevent oxidation of the Pd catalyst as well as dicyanation of the quinone. Oxidation of the hydroquinone back to the quinone by ceric ammonium sulfate should proceed under mild conditions.

Once this is accomplished, a group able to measure the NCHBQCN via MCBJ at reduced temperature should provide statistical conductance data for the system.

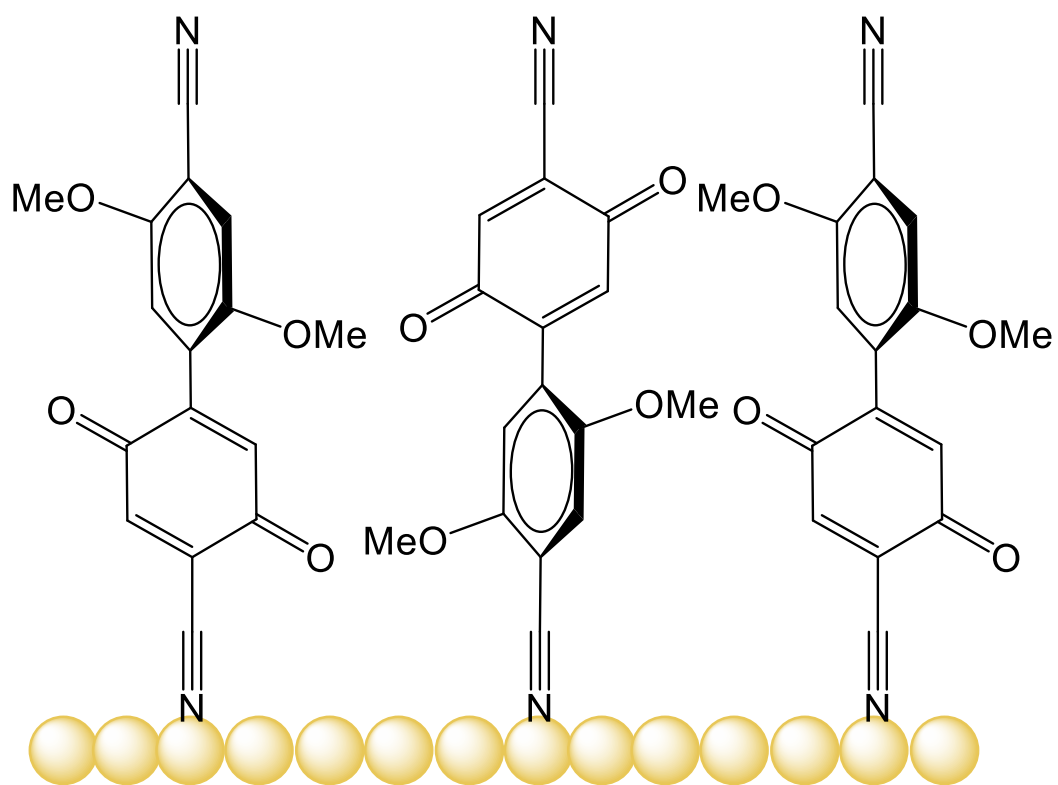
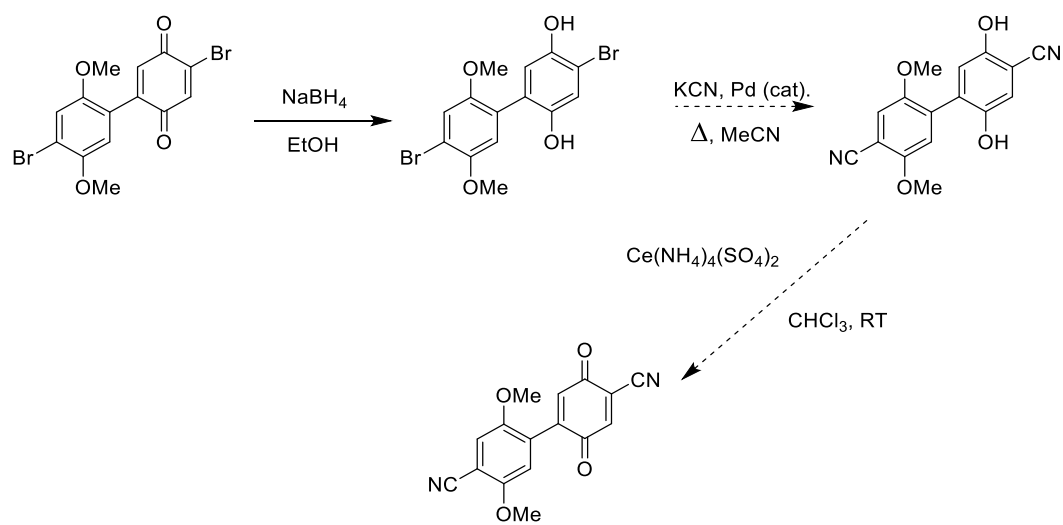


Figure 6.2 Symmetric binding groups on the molecule lead to random order under self-assembly. This cannot be accounted for in a packed monolayer.

Scheme 6.1



Section 6.4 Deposition of BrHBQN₃

Reactions of the azido-group with metals are a complex subject. No literature catalogued by CAS contains an azide-metal bond which forms a self-assembled monolayer. A review by Cenini *et al.*¹⁶³ details the structure of the azide and its reactivity, particularly with respect to its reactivity in metal complexes. All azides as a part of a SAM are deposited with the R—N₃ functionality sticking up away from the surface, which is then used in a copper-catalyzed cycloaddition in order to variously functionalize the surface for characterization. The azide→metal coordination in Cenini *et al.*¹⁶³ indicates that coordination complexes of azides (at least those which have been characterized) tend to bind through the N_γ (see Figure 6.3) and may either be η¹ or bridged across two metal centers. A handful of examples show binding through the N_α, but as expected no examples bind through the deficient N_β.

An azide→metal surface bond would provide for an interesting characterization problem: is the azide functionality attached to the surface in an η³ or an η¹ format (Figure 6.4) or some combination thereof? Is the hapticity coverage dependent? The XPS signal of the individual nitrogen atoms should change depending on the junction geometry, which would allow for one characterization method of the surface. Oxidative addition of the azide to a metal in an η² format have similar geometric characteristics as 1,3-cycloaddition to a dipolarophile. If, however, the azide is not stable on the surface, N₂ may be released from the molecule, forming a HBQ—η¹-nitrene→metal coordination. This would result in a strong, high-energy C—N vibration visible to surface-enhanced IR (Figure 6.5). Surface-enhanced IR absorption spectroscopy should also lend itself to characterization of the monolayer. In the η¹-bonded azide, the two N=N stretching vibrations would be visible where as in the η³-bonded azide no azide stretch would be visible. Carbonyl stretching in the η³-bonded azide would be greatly diminished with respect to the η¹-

bonded azide, due to the fact that there are fewer allowed geometries where a perpendicular contribution to the C=O stretch would be significant enough for surface-enhanced absorption. On the other hand, the η^1 -bonded azide should have significant C=O absorption peaks. C—O stretching peaks for the aryl methoxy groups would likely have enhancement in the η^1 -bonded azide over the η^3 -bonded azide for the same reasons just stated.

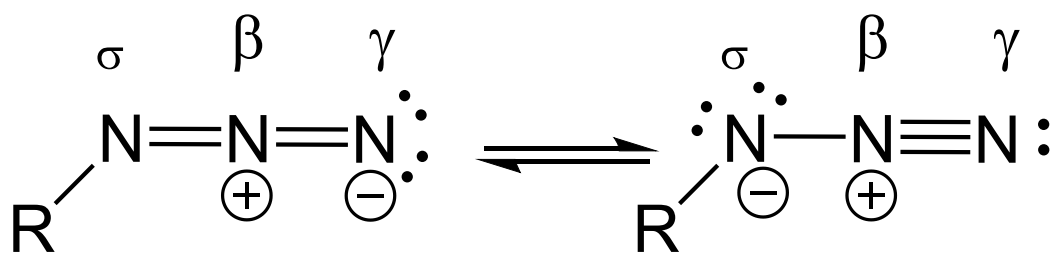


Figure 6.3. Structure and labeling of an azide functional group (adapted from Cenini).¹⁶³

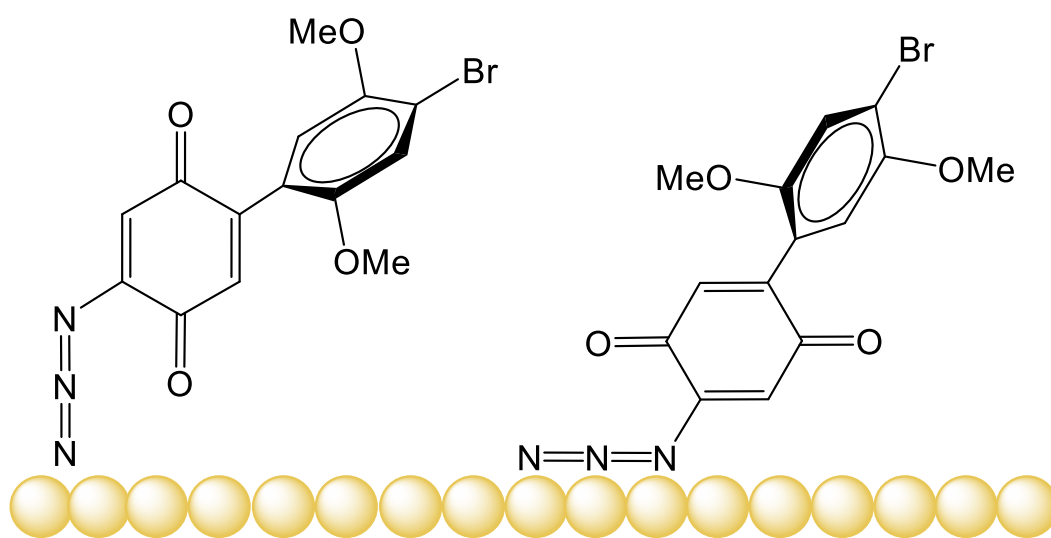


Figure 6.4. An η^1 -bonded azide (left) and an η^3 -bonded azide (right).

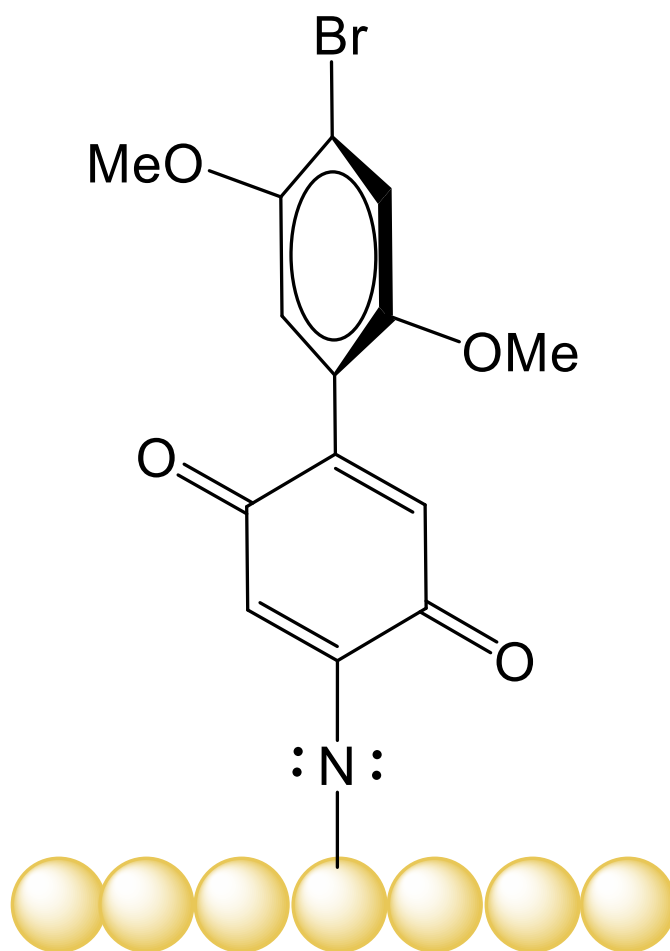


Figure 6.5 An η^1 -bonded nitrene.

Section 6.5 Final Thoughts

It might be possible that the diodes we create with molecular electronics are not simply describable as replacements for silicon or Schottky diodes. But a third kind of device, a Zener diode, could possibly be most congruent device in the semiconductor industry.³⁰ Zener diodes are appropriate analogs for molecular semiconductor devices, because they are built with a specific reverse bias at which they begin to conduct. They have high conduction in the forward bias direction, and low conduction in reverse bias. However, beyond a certain voltage the p and n bands bend into resonance, allowing a turn-on in the reverse direction. This is analogous to the molecular orbitals coming into resonance that finally allow a sharp increase in hopping current through the molecule. As molecular energy levels move into and out of resonance, rectification ratio changes with the applied bias sweep.

Thus, the bias dependence of $RR(V)$ is not desirable in systems where high RR is the dominating design consideration. Organic molecules, at present, simply cannot compete with the high RR afforded by inorganic based diodes. However, organic electronics have a benefit over inorganic electronics due to their ease of manufacture and tunability,²⁰ this will ultimately be useful in niche applications until such time that organic diode achieve $RRs > 10^6-10^9$.

Many factors affect a particular system's rectification ratio. Interfacial effects, molecular torsions, conjugation, length, polarity, and orbital asymmetry all affect one another in some level and play a part in a given system's ability to conduct electrons in one direction and yet hamper their flow in the other. This is further complicated when binding geometry and binding strength of a system are taken into consideration.

“The performance of a material in an engineering application is the sum of the processes of synthesis, shaping, and joining. Certainly our progressive ability to manipulate, characterize,

and design at the nanoscale or even single atoms has transformed the landscape of materials choice in virtually every engineering discipline.”¹

With the advent of Additive Manufacturing (popularly known as 3D printing), new structural architectures are possible that are otherwise impossible to achieve with traditional machining techniques.¹⁶⁵ Advances in the complexity of these 3D printed pieces designing electronic architecture embedded within the substrate becomes possible.¹⁶⁶ Eventually, as mentioned in the quote above, researchers and engineers will have such control over additive manufacturing processes so as to make extremely complicated systems with seamless integrated electrical circuits.

The results presented in this dissertation lay groundwork for future studies involving new synthetic possibilities, and are laid out to ensure that the HBQ backbone remains a topic of interest in the conversation about how far “Moore’s Law” can really extend. Ultimately, fundamental understanding of the complex interactions within molecular scale junctions will lead to functional consumer devices, which will satisfy the mission set forward by the Air Force in the 1950’s. The HBQ monomer bypasses size limitations by providing evidence that careful choice of molecular formula and geometry can govern electron transport at the single nanometer level.

It is tempting, to be sure, to say that information developed in the field over the past several years will help grow molecular electronics— but the researchers in the field continue to learn the difficult lesson of just how much further we have to go to realize a commercial quantum device. Until a stronger understanding of the underlying physical principles important on the quantum level is obtained, engineering a useful device that will be able to complement or compete with CMOS technology still lies beyond the horizon.

"And he lived happily ever after, to the end of his days."

~Bilbo Baggins.

REFERENCES

1. Banerjee, D.; Williams, J. Materials and Engineering: An Evolving Landscape. *MRS Bull.* **2015**, *40*, 999-1008.
2. Cuevas, J.; Sheer, E. The Birth of Molecular Electronics. In *Molecular Electronics: An Introduction to Theory and Experiment*. WORLD SCIENTIFIC: 2010; Vol. 1, pp 3-17.
3. Choi, H.; Mody, C. The Long History of Molecular Electronics: Microelectronics Origins of Nanotechnology. *Soc. Stud. Sci.* **2009**, *39*, 11-50.
4. Feynman, R. Tiny Machines. **2012**, *Video*.
5. Fuller, R. *Nine Chains to the Moon*; Anchor Books: Garden City, NY, 1971; .
6. Balzani, V.; Credi, A.; Raymo, F.; Stoddart, J. Artificial Molecular Machines. *Angew. Chem. Int. Ed.* **2000**, *39*, 3348-3391.
7. Moore, G. Cramming More Components onto Integrated Circuits. *Electronics* **1965**, *38*, 114.
8. Moore, G. Cramming More Components onto Integrated Circuits. *Proc. IEEE* **1998**, *86*, 82-85.
9. Vu, C. IBM Research Alliance Produces Industry's First 7nm Node Test Chips. <https://www-03.ibm.com/press/us/en/pressrelease/47301.wss#resource> (accessed 11/02, 2015).
10. Aviram, A.; Ratner, M. Molecular Rectifiers. *Chem. Phys. Lett.* **1974**, *29*, 277-283.
11. Reed, M.; Zhou, C.; Muller, C.; Burgin, T.; Tour, J. Conductance of a Molecular Junction. *Science* **1997**, *278*, 252-254.
12. Kiguchi, M.; Kaneko, S. Electron Transport through Single π -Conjugated Molecules Bridging between Metal Electrodes. *ChemPhysChem* **2012**, *13*, 1116-1126.
13. Metzger, R.; Chen, B.; Hopfner, U.; Lakshmikantham, M.; Vuillaume, D.; Kawai, T.; Wu, X.; Tachibana, H.; Hughes, T.; Sakurai, H.; Baldwin, J.; Hosch, C.; Cava, M.; Brehmer, L.; Ashwell, G. Unimolecular Electrical Rectification in Hexadecylquinolinium Tricyanoquinodimethanide. *J. Am. Chem. Soc.* **1997**, *119*, 10455-10466.

14. Baldwin, J.; Chen, B.; Street, S.; Konovalov, V.; Sakurai, H.; Hughes, T.; Simpson, C.; Lakshmikantham, M.; Cava, M.; Kispert, L.; Metzger, R. Spectroscopic Studies of Hexadecylquinolinium Tricyanoquinodimethanide. *J. Phys. Chem. B* **1999**, *103*, 4269-4277.
15. Krzeminski, C.; Delerue, C.; Allan, G.; Vuillaume, D.; Metzger, R. Theory of Electrical Rectification in a Molecular Monolayer. *Phys. Rev. B* **2001**, *64*, 085405.
16. Metzger, R. Unimolecular Electronics. *Chem. Rev.* **2015**, *115*, 5056-5115.
17. Metzger, R. Unimolecular Electrical Rectifiers. *Chem. Rev.* **2003**, *103*, 3803-3834.
18. Metzger, R. Unimolecular Electronics. *J. Mater. Chem.* **2008**, *18*, 4364-4396.
19. Metzger, R.; Mattern, D. Unimolecular Electronic Devices. *Top. Curr. Chem.* **2012**, *313*, 39-84.
20. Ellenbogen, J.; Love, J. Architectures for Molecular Electronic Computers. I. Logic Structures and an Adder Designed from Molecular Electronic Diodes. *Proc. IEEE* **2000**, *88*, 386-426.
21. Stokbro, K.; Taylor, J.; Brandbyge, M.; Guo, H. Ab-initio based Non-equilibrium Green's Function Formalism for Calculating Electron Transport in Molecular Devices. In *Introducing Molecular Electronics, Springer Lecture Notes in Physics. 680.* **2005**; pp 117-151.
22. Cuevas, J.; Sheer, E. Nonequilibrium Green's Functions Formalism. In *Molecular Electronics: An Introduction to Theory and Experiment.* WORLD SCIENTIFIC: 2010; Vol. 1, pp 179-203.
23. Luisier, M. Atomistic Simulation of Transport Phenomena in Nanoelectronic Devices. *Chem. Soc. Rev.* **2014**, *43*, 4357-4367.
24. Hybertsen, M.; Venkataraman, L.; Klare, J.; Whalley, A.; Steigerwald, M.; Nuckolls, C. Amine-Linked Single-Molecule Circuits: Systematic Trends across Molecular Families. *J. Phys. Condens. Matter* **2008**, *20*, 374115.
25. Venkataraman, L.; Klare, J.; Nuckolls, C.; Hybertsen, M.; Steigerwald, M. Dependence of Single-Molecule Junction Conductance on Molecular Conformation. *Nature* **2010**, *442*, 904-907.
26. Venkataraman, L.; Klare, J.; Tam, I.; Nuckolls, C.; Hybertsen, M.; Steigerwald, M. Single-Molecule Circuits with Well-Defined Molecular Conductance. *Nano Lett.* **2006**, *6*, 458-462.
27. Mishchenko, A.; Vonlanthen, D.; Meded, V.; Burkle, M.; Li, C.; Pobelov, I.; Bagrets, A.; Viljas, J.; Pauly, F.; Evers, F.; Mayor, M.; Wandlowski, T. Influence of Conformation on Conductance of Biphenyl-Dithiol Single-Molecule Contacts. *Nano Lett.* **2010**, *10*, 156-163.

28. Mishchenko, A.; Zotti, L.; Vonlanthen, D.; Burkle, M.; Pauly, F.; Cuevas, J.; Mayor, M.; Wandlowski, T. Single-Molecule Junctions Based on Nitrile-Terminated Biphenyls: A Promising New Anchoring Group. *J. Am. Chem. Soc.* **2011**, *133*, 184-187.
29. Li, C.; Mishchenko, A.; Wandlowski, T. Charge Transport in Single Molecular Junctions at the Solid/Liquid Interface. In *Unimolecular and Supramolecular Electronics*_Metzger, R. M., Ed.; Springer Berlin Heidelberg: 2012; Vol. 313, pp 121-188.
30. Diefenderfer, J.; Holton, B. *Principles of Electronic Instrumentation, 3rd Ed.* Saunders College Publishing: Philadelphia PA, 1994; .
31. Aviram, A.; Joachim, C.; Pomerantz, M. Evidence of Switching and Rectification by a Single Molecule Effected with a Scanning Tunneling Microscope. *Chem. Phys. Lett.* **1988**, *146*, 490-495.
32. Aviram, A.; Joachim, C.; Pomerantz, M. Evidence of Switching and Rectification by a Single Molecule Effected by a Scanning Tunneling Microscope: Chem. Phys. Letters 146 (1988) 490. *Chem. Phys. Lett.* **1989**, *162*, 416.
33. Cuevas, J.; Sheer, E. Contacting Single Molecules: Experimental Techniques. In *Molecular Electronics: An Introduction to Theory and Experiment*. WORLD SCIENTIFIC: 2010; Vol. 1, pp 45-73.
34. Cuevas, J.; Sheer, E. The Conductance of a Single Atom. In *Molecular Electronics: An Introduction to Theory and Experiment*. WORLD SCIENTIFIC: 2010; Vol. 1, pp 295-333.
35. Cuevas, J.; Sheer, E. Coherent Transport through Molecular Junctions I: Basic Concepts. In *Molecular Electronics: An Introduction to Theory and Experiment*. WORLD SCIENTIFIC: 2010; Vol. 1, pp 357-390.
36. Chabinyk, M.; Chen, X.; Holmlin, R.; Jacobs, H.; Skulason, H.; Frisbie, C.; Mujica, V.; Ratner, M.; Rampi, M.; Whitesides, G. Molecular Rectification in a Metal-Insulator-Metal Junction Based on Self-Assembled Monolayers. *J. Am. Chem. Soc.* **2002**, *124*, 11730-11736.
37. Kornilovitch, P.; Bratkovsky, A.; Stanley Williams, R. Current Rectification by Molecules with Asymmetric Tunneling Barriers. *Phys. Rev. B* **2002**, *66*, 165436.
38. Stadler, R. Conformation Dependence of Charge Transfer and Level Alignment in Nitrobenzene Junctions with Pyridyl Anchor Groups. *Phys. Rev. B* **2010**, *81*, 165429.
39. Zhang, G.; Hu, G.; Song, Y.; Li, Z.; Wang, C. Modulation of Rectification in Diblock Co-oligomer Diodes by Adjusting Anchoring Groups for Both Symmetric and Asymmetric Electrodes. *J. Phys. Chem. C* **2012**, *116*, 22009-22014.

40. Nakamura, H.; Asai, Y.; Hihath, J.; Bruot, C.; Tao, N. Switch of Conducting Orbital by Bias-Induced Electronic Contact Asymmetry in a Bipyrimidinyl-biphenyl Diblock Molecule: Mechanism to Achieve a pn Directional Molecular Diode. *J. Phys. Chem. C* **2011**, *115*, 19931-19938.
41. Hihath, J.; and Tao, N. The role of Molecule–Electrode Contact in Single-Molecule Electronics. *Semicond. Sci. Technol.* **2014**, *29*, 054007.
42. Schottky, W. Halbleitertheorie der Sperrschicht. *Naturwissenschaften* **1938**, *26*, 843-843.
43. Schroder, D. *Semiconductor Material and Device Characterization, 2nd Ed.* John Wiley & Sons, Inc.: New York, 1998; , pp 759.
44. Zhang, G.; Ratner, M.; Reuter, M. Is Molecular Rectification Caused by Asymmetric Electrode Couplings or by a Molecular Bias Drop? *J. Phys. Chem. C* **2015**, *119*, 6254-6260.
45. Van Dyck, C.; Ratner, M. Molecular Rectifiers: A New Design Based on Asymmetric Anchoring Moieties. *Nano Lett.* **2015**, *15*, 1577-1584.
46. Song, Y.; Bao, D.; Xie, Z.; Zhang, G.; Wang, C. Obvious Variation of Rectification Behaviors Induced by Isomeric Anchoring Groups for Dipyrimidinyl–Diphenyl Molecular Junctions. *Phys. Lett. A* **2013**, *377*, 3228-3234.
47. Jiang, P.; Morales, G.; You, W.; Yu, L. Synthesis of Diode Molecules and their Sequential Assembly to Control Electron Transport. *Angew. Chem. Int. Ed.* **2004**, *43*, 4471-4475.
48. Capozzi, B.; Xia, J.; Adak, O.; Dell, E. J.; Liu, Z.; Taylor, J.; Neaton, J.; Campos, L.; Venkataraman, L. Single-Molecule Diodes with High Rectification Ratios through Environmental Control. *Nat. Nanotechnol.* **2015**, *10*, 522-527.
49. Ashwell, G.; Urasinska, B.; Tyrrell, W. Molecules that Mimic Schottky Diodes. *Phys. Chem. Chem. Phys.* **2006**, *8*, 3314-3319.
50. Lee, Y.; Carsten, B.; Yu, L. Understanding the Anchoring Group Effect of Molecular Diodes on Rectification. *Langmuir* **2009**, *25*, 1495-1499.
51. Pelayo Garcia, d. A.; Mihi, A.; Konstantatos, G. Molecular Interfaces for Plasmonic Hot Electron Photovoltaics. *Nanoscale* **2015**, *7*, 2281-2288.
52. Seminario, J.; Zacarias, A.; Tour, J. Molecular Alligator Clips for Single Molecule Electronics. Studies of Group 16 and Isonitriles Interfaced with Au Contacts. *J. Am. Chem. Soc.* **1999**, *121*, 411-416.
53. Dirk, S.; Price, D.; Chanteau, S.; Kosynkin, D.; Tour, J. Accoutrements of a Molecular Computer: Switches, Memory Components and Alligator Clips. *Tetrahedron* **2001**, *57*, 5109-5121.

54. Schomaker, S.; Holze, R. The Adsorption of 1,4-Dibromobenzene on Gold Electrodes: A Combined in situ Infrared and Surface-Enhanced Raman Spectroscopic Investigation. *Electroanal.* **1994**, *6*, 1024-1028.
55. Kwong, G.; Zhang, Z.; Pan, J. Rectifying and Negative Differential Resistance Behaviors of a Functionalized Tour Wire: The Position Effects of Functional Groups. *Appl. Phys. Lett.* **2011**, *99*, 123108.
56. James, D.; Tour, J. Electrical Measurements in Molecular Electronics. *Chem. Mater.* **2004**, *16*, 4423-4435.
57. Brédas, J.; Street, G.; Thémans, B.; André, J. Organic Polymers Based on Aromatic Rings (Polyparaphenylene, Polypyrrole, Polythiophene): Evolution of the Electronic Properties as a Function of the Torsion Angle between Adjacent Rings. *J. Chem. Phys.* **1985**, *83*, 1323.
58. Stokbro, K.; Taylor, J.; Brandbyge, M. Do Aviram-Ratner Diodes Rectify? *J. Am. Chem. Soc.* **2003**, *125*, 3674-3675.
59. Wang, L.; Guo, Y.; Tian, C.; Song, X.; Ding, B. Torsion Angle Dependence of the Rectifying Performance in Molecular Device with Asymmetrical Anchoring Groups. *Phys. Lett. A* **2010**, *374*, 4876-4879.
60. Jia, J.; Wu, H.; Chen, Z.; Mo, Y. Elucidation of the Forces Governing the Stereochemistry of Biphenyl. *Eur. J. Org. Chem.* **2013**, *2013*, 611-616.
61. Almenningen, A.; Bastiansen, O.; Fernholt, L.; Cyvin, B.; Cyvin, S.; Samdal, S. Structure and Barrier of Internal Rotation of Biphenyl Derivatives in the Gaseous State: Part 1. The Molecular Structure and Normal Coordinate Analysis of Normal Biphenyl And Pedeuterated Biphenyl. *J. Mol. Struct.* **1985**, *128*, 59-76.
62. Potzel, O.; Taubmann, G. The Pressure Dependence of the Solid-State Structure of Biphenyl from DFT Calculations. *Phys. Chem. Chem. Phys.* **2013**, *15*, 20288-20293.
63. Pickett, L.; Walter, G.; France, H. The Ultraviolet Absorption Spectra of Substituted Biphenyls. *J. Am. Chem. Soc.* **1936**, *58*, 2296-2299.
64. Bastiansen, O. The Molecular Structure of Biphenyl and some of its Derivatives. *Acta Chem. Scand.* **1949**, *3*, 408-414.
65. Grein, F. Twist Angles and Rotational Energy Barriers of Biphenyl and Substituted Biphenyls. *J. Phys. Chem. A* **2002**, *106*, 3823-3827.
66. Campanelli, A.; Domenicano, A. A Computational Study of 4-Substituted Biphenyls in their Minimum Energy Conformation: Twist Angles, Structural Variation, and Substituent Effects. *Struct. Chem.* **2013**, *24*, 867-876.

67. Gómez-Gallego, M.; Martín-Ortiz, M.; Sierra, M. Concerning the Electronic Control of Torsion Angles in Biphenyls. *Eur. J. Org. Chem.* **2011**, *2011*, 6502-6506.
68. Schumm, J.; Pearson, D.; Jones, L.; Hara, R.; Tour, J. Potential Molecular Wires and Molecular Alligator Clips. *Nanotechnology* **1996**, *7*, 430.
69. Kosynkin, D.; Tour, J. Phenylene Ethynylene Diazonium Salts as Potential Self-Assembling Molecular Devices. *Org. Lett.* **2001**, *3*, 993-995.
70. Reed, M.; Chen, J.; Rawlett, A.; Price, D.; Tour, J. Relationship between Local Structure and Phase Transitions of a Disordered Solid Solution. *Appl. Phys. Lett.* **2001**, *78*, 3735.
71. Chanteau, S.; Tour, J. Synthesis of Potential Molecular Electronic Devices containing Pyridine Units. *Tetrahedron Lett.* **2001**, *42*, 3057-3060.
72. Price, D.; Dirk, S.; Maya, F.; Tour, J. Improved and New Syntheses of Potential Molecular Electronics Devices. *Tetrahedron* **2003**, *59*, 2497-2518.
73. Dirk, S.; Tour, J. Synthesis of Nitrile-Terminated Potential Molecular Electronic Devices. *Tetrahedron* **2003**, *59*, 287-293.
74. Flatt, A.; Dirk, S.; Henderson, J.; Shen, D.; Su, J.; Reed, M.; Tour, J. Synthesis and Testing of New End-Functionalized Oligomers for Molecular Electronics. *Tetrahedron* **2003**, *59*, 8555-8570.
75. Dameron, A.; Ciszek, J.; Tour, J.; Weiss, P. Effects of Hindered Internal Rotation on Packing and Conductance of Self-Assembled Monolayers. *J. Phys. Chem. B* **2004**, *108*, 16761-16767.
76. Selzer, Y.; Cai, L.; Cabassi, M.; Yao, Y.; Tour, J.; Mayer, T.; Allara, D. Effect of Local Environment on Molecular Conduction: Isolated Molecule Versus Self-Assembled Monolayer. *Nano Lett.* **2005**, *5*, 61-65.
77. Tour, J.; James, D. In *Molecular Electronic Computing Architectures*. Section Title: Electric Phenomena; 2007; , pp 2/1-2/28.
78. Abu-Husein, T.; Schuster, S.; Egger, D.; Kind, M.; Santowski, T.; Wiesner, A.; Chiechi, R.; Zojer, E.; Terfort, A.; Zharnikov, M. The Effects of Embedded Dipoles in Aromatic Self-Assembled Monolayers. *Adv. Funct. Mater.* **2015**, *25*, 3943-3957.
79. Liu, J.; Schupbach, B.; Bashir, A.; Shekhah, O.; Nefedov, A.; Kind, M.; Terfort, A.; Woll, C. Structural Characterization of Self-Assembled Monolayers of Pyridine-Terminated Thiolates on Gold. *Phys. Chem. Chem. Phys.* **2010**, *12*, 4459-4472.
80. Martinez, C.; Iverson, B. Rethinking the Term Pi-Stacking. *Chem. Sci.* **2012**, *3*, 2191-2201.

81. Lortscher, E.; Gotsmann, B.; Lee, Y.; Yu, L.; Rettner, C.; Riel, H. Transport Properties of a Single-Molecule Diode. *ACS Nano* **2012**, *6*, 4931-4939.
82. El-Hendawy, M.; El-Nahas, A.; Awad, M. Effect of Applied Voltage on the Geometrical and Electronic Structures of Dipyrimidinyl-Diphenyl Diblock as a Molecular Diode: A DFT Study. *J. Phys. Chem. C* **2010**, *114*, 21728-21735.
83. El-Hendawy, M.; El-Nahas, A.; Awad, M. The Effect of Constitutional and Conformational Isomerization on the Electrical Properties of Diblock Molecular Diode. *Org. Electron.* **2011**, *12*, 1080-1092.
84. Cui, B.; Zhao, W.; Wang, H.; Zhao, J.; Zhao, H.; Li, D.; Jiang, X.; Zhao, P.; Liu, D. Effect of Geometrical Torsion on the Rectification Properties of Diblock Conjugated Molecular Diodes. *J. Appl. Phys.* **2014**, *116*.
85. Li, Y.; Yao, J.; Yang, C.; Zhong, S.; Yin, G. Ab Initio Investigations on the Geometric and Electronic Structures of a Diblock Molecular Diode under the Influence of an External Bias. *Mol. Simul.* **2009**, *35*, 301-307.
86. Van Dyck, C.; Geskin, V.; Cornil, J. Fermi Level Pinning and Orbital Polarization Effects in Molecular Junctions: The Role of Metal Induced Gap States. *Adv. Funct. Mater.* **2014**, *24*, 6154-6165.
87. Jiang, P.; Morales, G.; You, W.; Yu, L. Synthesis of Diode Molecules and Their Sequential Assembly to Control Electron Transport. *Angew. Chem. Int. Ed.* **2004**, *43*, 4471-4475.
88. Morales, G.; Jiang, P.; Yuan, S.; Lee, Y.; Sanchez, A.; You, W.; Yu, L. Inversion of the Rectifying Effect in Diblock Molecular Diodes by Protonation. *J. Am. Chem. Soc.* **2005**, *127*, 10456-10457.
89. Cuevas, J.; Sheer, E. Fabrication of Metallic Atomic-Size Contacts. In *Molecular Electronics: An Introduction to Theory and Experiment* WORLD SCIENTIFIC: 2010; Vol. 1, pp 19-44.
90. Xiang, D.; Wang, X.; Jia, C.; Lee, T.; Guo, X. Molecular-Scale Electronics: From Concept to Function. *Chem. Rev.* **2016**, *116*, 4318-4440.
91. Mizuseki, H.; Niimura, K.; Majumder, C.; Belosludov, R.; Farajian, A.; Kawazoe, Y.; Majumder, C. Theoretical Study of Donor-Spacer-Acceptor Structure Molecule for Stable Molecular Rectifier. *Mol. Cryst. Liq. Cryst.* **2003**, *406*, 205-211.
92. Mizuseki, H.; Niimura, K.; Majumder, C.; Kawazoe, Y. Theoretical Study of the Alkyl Derivative C₃₇H₅₀N₄O₄ Molecule for Use as a Stable Molecular Rectifier: Geometric and Electronic Structures. *Comput. Mater. Sci.* **2003**, *27*, 161-165.

93. Bock, C.; George, P.; Trachtman, M. A Molecular Orbital Study of Ethylene and the All-Trans Conjugated Polyenes: C₄H₆, C₆H₈, C₈H₁₀ and C₁₀H₁₂. *J. Mol. Struct.: THEOCHEM* **1984**, *109*, 1-16.
94. Frisch, M. J.; Trucks, G. W.; Schlegel, H. B.; Scuseria, G. E.; Robb, M. A.; Cheeseman, J. R.; Scalmani, G.; Barone, V.; Mennucci, B.; Petersson, G. A.; Nakatsuji, H.; Caricato, M.; Li, X.; Hratchian, H. P.; Izmaylov, A. F.; Bloino, J.; Zheng, G.; Sonnenberg, J. L.; Hada, M.; Ehara, M.; Toyota, K.; Fukuda, R.; Hasegawa, J.; Ishida, M.; Nakajima, T.; Honda, Y.; Kitao, O.; Nakai, H.; Vreven, T.; Montgomery, J. A., Jr.; Peralta, J. E.; Ogliaro, F.; Bearpark, M.; Heyd, J. J.; Brothers, E.; Kudin, K. N.; Staroverov, V. N.; Kobayashi, R.; Normand, J.; Raghavachari, K.; Rendell, A.; Burant, J. C.; Iyengar, S. S.; Tomasi, J.; Cossi, M.; Rega, N.; Millam, J. M.; Klene, M.; Knox, J. E.; Cross, J. B.; Bakken, V.; Adamo, C.; Jaramillo, J.; Gomperts, R.; Stratmann, R. E.; Yazyev, O.; Austin, A. J.; Cammi, R.; Pomelli, C.; Ochterski, J. W.; Martin, R. L.; Morokuma, K.; Zakrzewski, V. G.; Voth, G. A.; Salvador, P.; Dannenberg, J. J.; Dapprich, S.; Daniels, A. D.; Farkas, Ö; Foresman, J. B.; Ortiz, J. V.; Cioslowski, J.; Fox, D. J. Gaussian 09, Revision **D.01**, **2009**.
95. Becke, A. Density-Functional Exchange-Energy Approximation with Correct Asymptotic Behavior. *Phys. Rev. A* **1988**, *38*, 3098-3100.
96. Lee, C.; Yang, W.; Parr, R. Development of the Colle-Salvetti Correlation-Energy Formula into a Functional of the Electron Density. *Phys. Rev. B* **1988**, *37*, 785-789.
97. Godbout, N.; Salahub, D.; Andzelm, J.; Wimmer, E. Optimization of Gaussian-type Basis Sets for Local Spin Density Functional Calculations. Part I. Boron through Neon, Optimization Technique and Validation. *Can. J. Chem.* **1992**, *70*, 560-571.
98. Meany, J.; Kelley, S.; Rogers, R.; Woski, S. Crystal Structure of 4'-Bromo-2,5-dihydroxy-2',5'-dimethoxy-[1,1'-biphenyl]-3,4-dicarbonitrile. *Acta Cryst. E* **2016**, *72*, 667-670.
99. Meany, J.; Gerlach, D.; Papish, E.; Woski, S. Crystal Structure of 4'-Bromo-2',5'-dimethoxy-2,5-dioxo-[1,1'-biphenyl]-3,4-dicarbonitrile [BrHBQ(CN)₂] Benzene Hemisolvate. *Acta Cryst. E* **2016**, *72*, 600-603.
100. Göller, A.; Grummt, U. Torsional Barriers in Biphenyl, 2,2'-Bipyridine and 2-Phenylpyridine. *Chem. Phys. Lett.* **2000**, *321*, 399-405.
101. Dahlgren, M.; Schyman, P.; Tirado-Rives, J.; Jorgensen, W. Characterization of Biaryl Torsional Energetics and its Treatment in OPLS All-Atom Force Fields. *J. Chem. Inf. Model.* **2013**, *53*, 1191-1199.
102. Zhang, G.; Musgrave, C. Comparison of DFT Methods for Molecular Orbital Eigenvalue Calculations. *J. Phys. Chem. A* **2007**, *111*, 1554-1561.
103. Lindsay, S.; Ratner, M. Molecular Transport Junctions: Clearing Mists. *Adv. Mater.* **2007**, *19*, 23-31.

104. Park, J.; Pasupathy, A.; Goldsmith, J.; Chang, C.; Yaish, Y.; Petta, J.; Rinkoski, M.; Sethna, J.; Abruna, H.; McEuen, P.; Ralph, D. Coulomb Blockade and the Kondo Effect in Single-Atom Transistors. *Nature* **2002**, *417*, 722-725.
105. Xu, B.; Tao, N. Measurement of Single-Molecule Resistance by Repeated Formation of Molecular Junctions. *Science* **2003**, *301*, 1221-1223.
106. Reed, M. Prospects for Molecular-Scale Electronics. *MRS Bull.* **2001**, *26*, 113-120.
107. Hamoudi, H.; Uosaki, K.; Ariga, K.; Esaulov, V. Going Beyond the Self-Assembled Monolayer: Metal Intercalated Dithiol Multilayers and their Conductance. *RSC Adv.* **2014**, *4*, 39657-39666.
108. Schuckman, A.; Ewers, B.; Yu, L.; Tome, J.; Perez, L.; Drain, C.; Kushmerick, J.; Batteas, J. Utilizing Nearest-Neighbor Interactions To Alter Charge Transport Mechanisms in Molecular Assemblies of Porphyrins on Surfaces. *J. Phys. Chem. C* **2015**, *119*, 13569-13579.
109. Love, B.; Bonner-Stewart, J.; Forrest, L. Improved Synthesis of Diquinones. *Synlett* **2009**, 813-817.
110. Zysman-Colman, E.; Arias, K.; Siegel, J. Synthesis of Aryl Bromides from Arenes and N-bromosuccinimide (NBS) in Acetonitrile. A Convenient Method for Aromatic Bromination. *Can. J. Chem.* **2009**, *87*, 440-447.
111. Nakayama, T.; Inamura, K.; Inoue, Y.; Ikeda, S.; Kishi, K. Adsorption of Benzonitrile and Alkyl Cyanides on Evaporated Nickel and Palladium Films Studied by XPS. *Surf. Sci.* **1987**, *179*, 47-58.
112. Steiner, U.; Caseri, W.; Suter, U. Adsorption of Alkanenitriles and Alkanedinitriles on Gold and Copper. *Langmuir* **1992**, *8*, 2771-2777.
113. Okuno, Y.; Yokoyama, T.; Yokoyama, S.; Kamikado, T.; Mashiko, S. Theoretical Study of Benzonitrile Clusters in the Gas Phase and Their Adsorption onto a Au(111) Surface. *J. Am. Chem. Soc.* **2002**, *124*, 7218-7225.
114. Gao, P.; Weaver, M. Surface-Enhanced Raman Spectroscopy as a Probe of Adsorbate-Surface Bonding: Benzene and Monosubstituted Benzenes Adsorbed at Gold Electrodes. *J. Phys. Chem.* **1985**, *89*, 5040-5046.
115. Lopez-Alvarado, P.; Avendano, C.; Menendez, J. Efficient, Multigram-Scale Synthesis of Three 2,5-Dihalobenzoquinones. *Synth. Commun.* **2002**, *32*, 3233-3239.
116. Strahle, J. Reactions of Coordinated Azido Groups. *Comment. Inorg. Chem.* **1985**, *4*, 295-321.

117. Moore, H.; Shelden, H.; Shellhamer, D. Rearrangement of Azidoquinones. III. Reaction of 1,4-Benzoquinone with Sodium Azide. *J. Org. Chem.* **1969**, *34*, 1999-2001.
118. Thiele, J.; Meisenheimer, J. Ueber die Addition von Blausäure an Chinon. *Ber. Dtsch. Chem. Ges.* **1900**, *33*, 675-676.
119. Perry, G.; Sutherland, M. The hydrocyanation of Free and Polymer-Bound Benzoquinone. *Tetrahedron* **1982**, *38*, 1471-1476.
120. Allen, C.; Wilson, C. The Mechanism of the Addition of Hydrogen Cyanide to Benzoquinone. *J. Am. Chem. Soc.* **1941**, *63*, 1756-1757.
121. Reynolds, G.; VanAllan, J. The Reactions of 2,3-Dichloro-1,4-naphthoquinone with Alkali Metal Cyanides. *J. Org. Chem.* **1964**, *29*, 3591-3593.
122. Meany, J.; Kelley, S.; Metzger, R.; Rogers, R.; Woski, S. Crystal structure of 4,4'-Dibromo-2',5'-dimethoxy-[1,1'-biphenyl]-2,5-dione (BrHBQBr). *Acta Cryst. E* **2015**, *71*, 1454-1456.
123. Davis, R.; Gottbrath, J. Boron Hydrides. V. Methanolysis of Sodium Borohydride. *J. Am. Chem. Soc.* **1962**, *84*, 895-898.
124. Pasman, P.; Rob, F.; Verhoeven, J. Intramolecular Charge-Transfer Absorption and emission Resulting from Through-Bond Interaction in Bichromophoric Molecules. *J. Am. Chem. Soc.* **1982**, *104*, 5127-5133.
125. Tsuji, Y.; Staykov, A.; Yoshizawa, K. Molecular Rectifier Based on π - π Stacked Charge Transfer Complex. *J. Phys. Chem. C* **2012**, *116*, 2575-2580.
126. Eggins, B. Interpretation of Electrochemical Reduction and Oxidation Waves of Quinone-Hydroquinone System in Acetonitrile. *J. Chem. Soc. D* **1969**, 1267-1268.
127. Tsutsui, S.; Sakamoto, K.; Yoshida, H.; Kunai, A. Cyclic Voltammetry and Theoretical Calculations of Silyl-Substituted 1,4-Benzoquinones. *J. Organomet. Chem.* **2005**, *690*, 1324-1331.
128. Sharma, L.; Sharma, A.; Singh, G. Redox Behavior of Hydroquinone in Aqueous and Non-Aqueous Solutions. *Ind. J. Chem.* **1987**, *26A*, 659.
129. Jansen, G.; Kahlert, B.; Klarner, F.; Boese, R.; Blaser, D. Intramolecular Electronic Interactions between Nonconjugated Arene and Quinone Chromophores. *J. Am. Chem. Soc.* **2010**, *132*, 8581-8592.
130. Ibis, C.; Ayla, S.; Asar, H. Synthesis and Spectral and Electrochemical Characterization of Novel Substituted 1,4-Naphthoquinone Derivatives. *Syn. Comm.* **2014**, *44*, 121-126.

131. Chen, J.; Jin, B. Investigation on Redox Mechanism of 1,4-Naphthoquinone by in situ FT-IR Spectroelectrochemistry. *J. Electroanal. Chem.* **2015**, *756*, 36-42.
132. Elhabiri, M.; Sidorov, P.; Cesar-Rodo, E.; Marcou, G.; Lanfranchi, D.; Davioud-Charvet, E.; Horvath, D.; Varnek, A. Electrochemical Properties of Substituted 2-Methyl-1,4-Naphthoquinones: Redox Behavior Predictions. *Chem. Eur. J.* **2015**, *21*, 3415-3424.
133. Gater, V.; Love, M.; Liu, M.; Leidner, C. Quinone Molecular Films Derived from 1,5-Diaminoanthraquinone. *J. Electroanal. Chem. Interfacial Electrochem.* **1987**, *235*, 381-385.
134. Gater, V.; Liu, M.; Love, M.; Leidner, C. Quinone Molecular Films Derived from Aminoquinones. *J. Electroanal. Chem. Interfacial Electrochem.* **1988**, *257*, 133-146.
135. Ramiz, M.; Hassan, K.; Khudaish, E.; Deronzier, A.; Chardon-Noblat, S.; Abdel Azzem, M. Anodic Polymerization of 1-Amino-2-methyl-9,10-anthraquinone in Mixed Solvent. *J. Electroanal. Chem.* **2010**, *647*, 35-42.
136. D'Andrade, B.; Datta, S.; Forrest, S.; Djurovich, P.; Polikarpov, E.; Thompson, M. Relationship Between the Ionization and Oxidation Potentials of Molecular Organic Semiconductors. *Org. Electron.* **2005**, *6*, 11-20.
137. Djurovich, P.; Mayo, E.; Forrest, S.; Thompson, M. Measurement of the Lowest Unoccupied Molecular Orbital Energies of Molecular Organic Semiconductors. *Org. Electron.* **2009**, *10*, 515-520.
138. Cardona, C.; Li, W.; Kaifer, A.; Stockdale, D.; Bazan, G. Electrochemical Considerations for Determining Absolute Frontier Orbital Energy Levels of Conjugated Polymers for Solar Cell Applications. *Adv. Mater.* **2011**, *23*, 2367-2371.
139. Hansson, G.; Flodstrom, S. Photoemission Study of the Bulk and Surface Electronic Structure of Single Crystals of Gold. *Phys. Rev. B* **1978**, *18*, 1572-1585.
140. Bock, H.; Seitz, W.; Sievert, M.; Kleine, M.; Bats, J. Donor/Acceptor Complexes in Hydrogen-Bonded Networks: pH-Dependent Self-Organization. *Angew. Chem. Int. Ed.* **1996**, *35*, 2244-2246.
141. Meany, J.; Johnson, M.; Woski, S.; Metzger, R. Manuscript in preparation **2016**.
142. Johnson, M. Electrical Characterization of Large-Area Donor-Acceptor Molecular Junctions, The University of Alabama, Tuscaloosa, AL, 2016.
143. Hegner, M.; Wagner, P.; Semenza, G. Ultralarge Atomically Flat Template-Stripped Au Surfaces for Scanning Probe Microscopy. *Surf. Sci.* **1993**, *291*, 39-46.

144. Wagner, P.; Hegner, M.; Guentherodt, H.; Semenza, G. Formation and in Situ Modification of Monolayers Chemisorbed on Ultraflat Template-Stripped Gold Surfaces. *Langmuir* **1995**, *11*, 3867-3875.
145. Vannerberg, N. The ESCA-spectra of Sodium and Potassium Cyanide and of the Sodium and Potassium Salts of the Hexacyanometallates of the First Transition Metal Series. *Chem. Scr.* **1976**, *9*, 122-126.
146. Kosaku, K.; Shigero, I. Adsorption of Acetonitrile on Evaporated Nickel and Palladium Films Studied by X-ray Photoelectron Spectroscopy. *Surf. Sci.* **1981**, *107*, 405-416.
147. Stadler, R.; Geskin, V. Cornil, J. A Theoretical View of Unimolecular Rectification. *J. Phys. Condens. Matter* **2008**, *20*, 374105.
148. Wimbush, K.; Fratila, R.; Wang, D.; Qi, D.; Liang, C.; Yuan, L.; Yakovlev, N.; Loh, K.; Reinhoudt, D.; Velders, A.; Nijhuis, C. Bias Induced Transition from an Ohmic to a Non-Ohmic Interface in Supramolecular Tunneling Junctions with Ga₂O₃/EGaIn Top Electrodes. *Nanoscale* **2014**, *6*, 11246-11258.
149. Elbing, M.; Ochs, R.; Koentopp, M.; Fischer, M.; von Hänisch, C.; Weigend, F.; Evers, F.; Weber, H.; Mayor, M. A Single-Molecule Diode. *Proc. Natl. Acad. Sci. USA* **2005**, *102*, 8815-8820.
150. Yee, S.; Sun, J.; Darancet, P.; Tilley, T.; Majumdar, A.; Neaton, J.; Segalman, R. Inverse Rectification in Donor-Acceptor Molecular Heterojunctions. *ACS Nano* **2011**, *5*, 9256-9263.
151. Nijhuis, C.; Reus, W.; Whitesides, G. Molecular Rectification in Metal-SAM-Metal Oxide-Metal Junctions. *J. Am. Chem. Soc.* **2009**, *131*, 17814.
152. Salomon, A.; Bocking, T.; Gooding, J.; Cahen, D. How Important Is the Interfacial Chemical Bond for Electron Transport through Alkyl Chain Monolayers? *Nano Lett.* **2006**, *6*, 2873.
153. Derosa, P.; Seminario, J. Electron Transport through Single Molecules: Scattering Treatment Using Density Functional and Green Function Theories. *J. Phys. Chem. B* **2001**, *105*, 471-481.
154. Damle, P.; Ghosh, A.; Datta, S. First-Principles Analysis of Molecular Conduction using Quantum Chemistry Software. *Chem. Phys.* **2002**, *281*, 171-187.
155. Lake, R.; Datta, S. Nonequilibrium Green's-function Method Applied to Double-Barrier Resonant-Tunneling Diodes. *Phys. Rev. B* **1992**, *45*, 6670-6685.
156. Holze, R. Competition of Anchoring Groups in Adsorption on Gold Electrodes-A Comparative Spectroelectrochemical Study of 4-Mercaptobenzonitrile and Aromatic Nitriles. *J. Solid State Electrochem.* **2013**, *17*, 1869-1879.

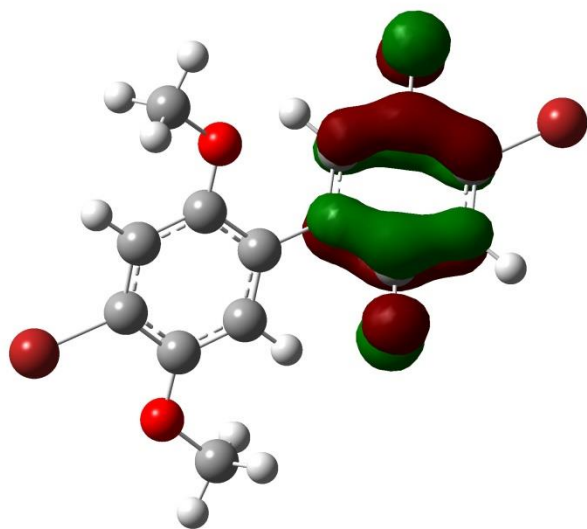
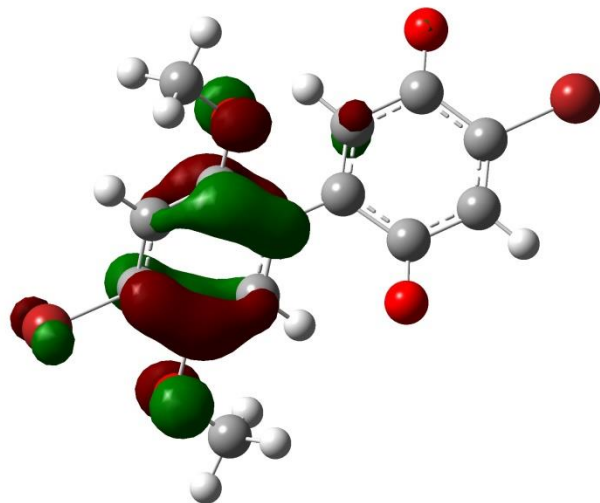
157. Querebillo, C.; Terfort, A.; Allara, D.; Zharnikov, M. Static Conductance of Nitrile-Substituted Oligophenylene and Oligo(phenylene ethynylene) Self-Assembled Monolayers Studied by the Mercury-Drop Method. *J. Phys. Chem. C* **2013**, *117*, 25556-25561.
158. Hamoudi, H.; Kao, P.; Nefedov, A.; Allara, D.; Zharnikov, M. X-ray Spectroscopy Characterization of Self-Assembled Monolayers of Nitrile-Substituted Oligo(Phenylene Ethynylene)s with Variable Chain Length. *Beilstein J. Nanotechnol.* **2012**, *3*, 12-24.
159. Li, C.; Pobelov, I.; Wandlowski, T.; Bagrets, A.; Arnold, A.; Evers, F. Charge Transport in Single Au | Alkanedithiol | Au Junctions: Coordination Geometries and Conformational Degrees of Freedom. *J. Am. Chem. Soc.* **2008**, *130*, 318-326.
160. Ossowski, J.; Wachter, T.; Silies, L.; Kind, M.; Noworolska, A.; Blobner, F.; Gnatek, D.; Rysz, J.; Bolte, M.; Feulner, P.; Terfort, A.; Cyganik, P.; Zharnikov, M. Thiolate versus Selenolate: Structure, Stability, and Charge Transfer Properties. *ACS Nano* **2015**, *9*, 4508-4526.
161. Cao, L.; Gao, X.; Wee, A. T.; Qi, D. Quantitative Femtosecond Charge Transfer Dynamics at Organic/Electrode Interfaces Studied by Core-Hole Clock Spectroscopy. *Adv. Mater.* **2014**, *26*, 7880-7888.
162. Ushkov, A.; Grushin, V. Rational Catalysis Design on the Basis of Mechanistic Understanding: Highly Efficient Pd-Catalyzed Cyanation of Aryl Bromides with NaCN in Recyclable Solvents. *J. Am. Chem. Soc.* **2011**, *133*, 10999-11005.
163. Cenini, S.; Gallo, E.; Caselli, A.; Ragaini, F.; Fantauzzi, S.; Piangiolo, C. Coordination Chemistry of Organic Azides and Amination Reactions Catalyzed by Transition Metal Complexes. *Coord. Chem. Rev.* **2006**, *250*, 1234-1253.
164. Pawlicki, A.; Avery, E.; Jurow, M.; Ewers, B.; Vilan, A.; Drain, C.; Batteas, J. Studies of the Structure and Phase Transitions of Nano-Confined Pentanedithiol and its Application in Directing Hierarchical Molecular Assemblies on Au(111). *J. Phys. Condens. Matter* **2016**, *28*, 094013.
165. Huang, Y.; Leu, M.; Mazumder, J.; Donmez, A. Additive Manufacturing: Current State, Future Potential, Gaps and Needs, and Recommendations. *J. Manuf. Sci. Eng.* **2015**, *137*, 014001-014001.
166. Parker, E.; Narveson, B.; Alderman, A.; Burgyan, L. In *In Embedding active and passive components in PCBs and inorganic substrates for power electronics*; Integrated Power Packaging (IWIPP), 2015 IEEE International Workshop on; 2015; pp 107-110.
167. Obersteiner, V.; Egger, D.; Zojer, E. Impact of Anchoring Groups on Ballistic Transport: Single Molecule vs Monolayer Junctions. *J. Phys. Chem. C* **2015**, *119*, 21198-21208.

168. Cygan, M.; Dunbar, T.; Arnold, J.; Bumm, L.; Shedlock, N.; Burgin, T.; Jones, L.; Allara, D.; Tour, J.; Weiss, P. Insertion, Conductivity, and Structures of Conjugated Organic Oligomers in Self-Assembled Alkanethiol Monolayers on Au{111}. *J. Am. Chem. Soc.* **1998**, *120*, 2721-2732.
169. Meany, J.; Woski, S.; Metzger, R. Manuscript in preparation.

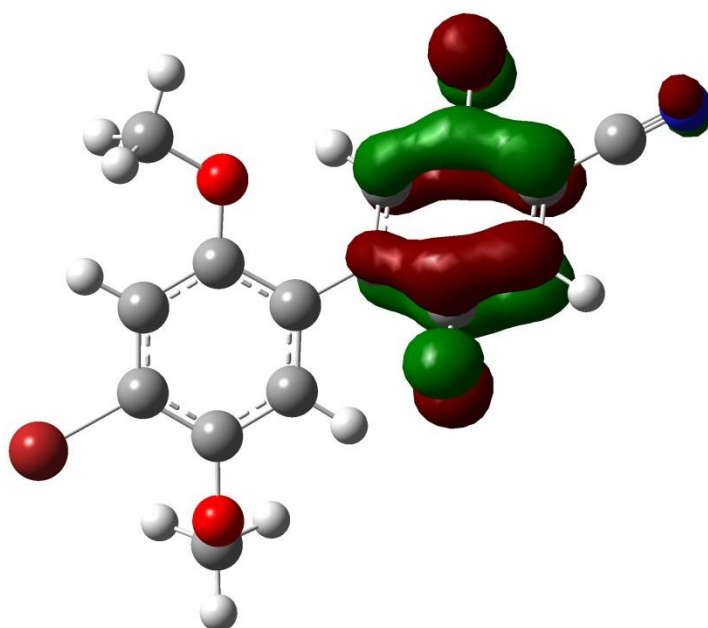
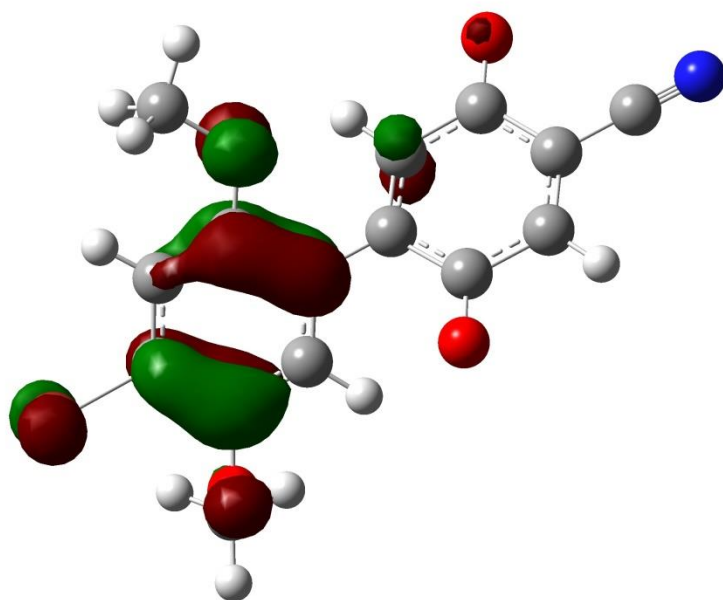
APPENDICES

APPENDIX A

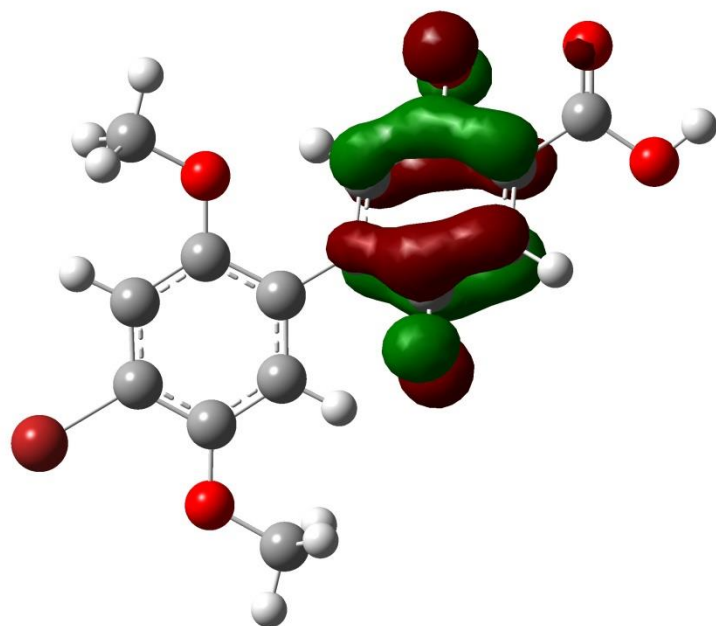
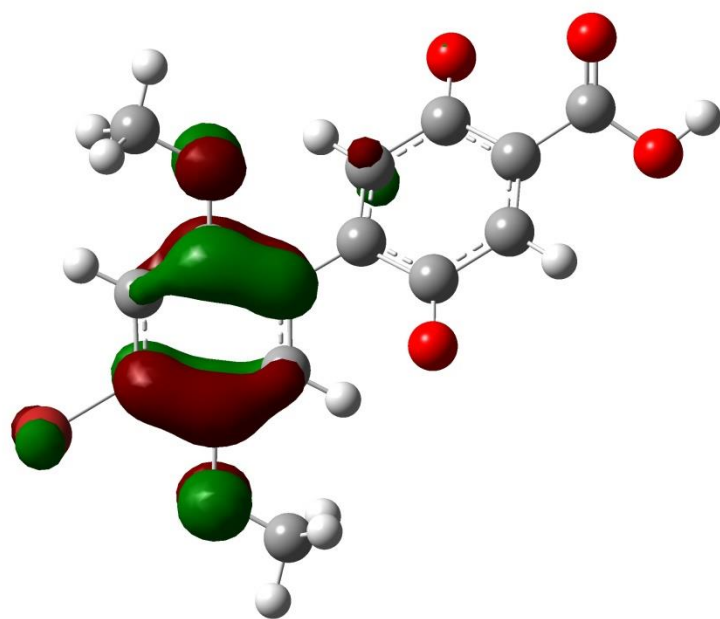
HBQ FMO Visualizations



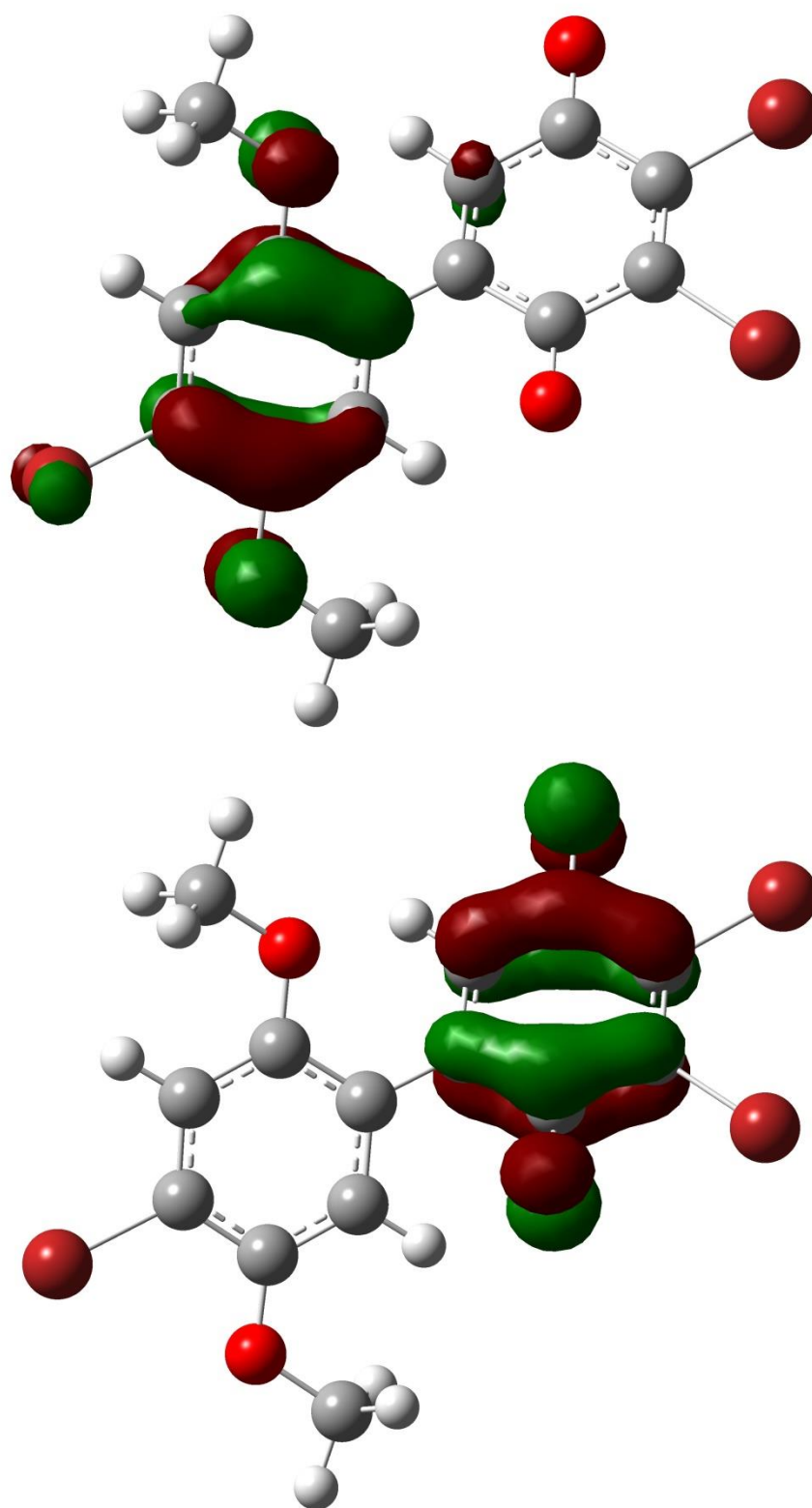
HOMO (top) and LUMO (bottom) of BrHBQBr



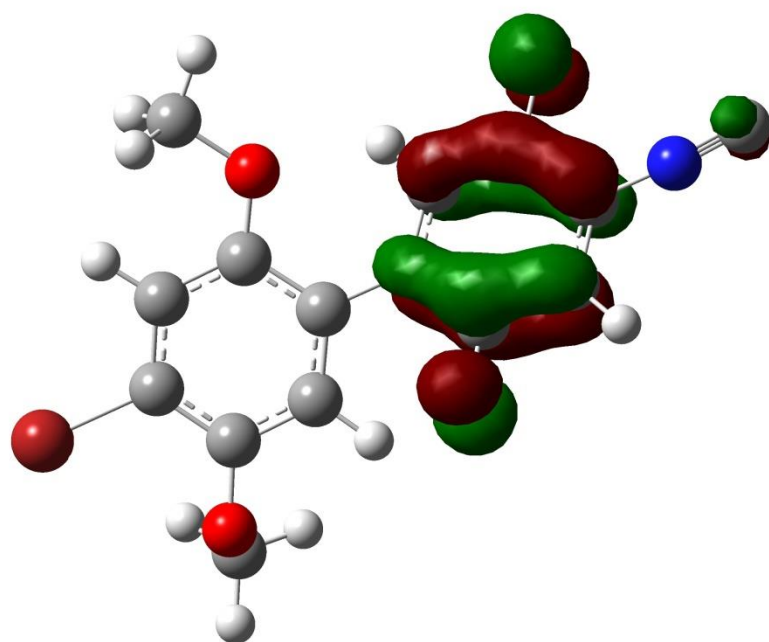
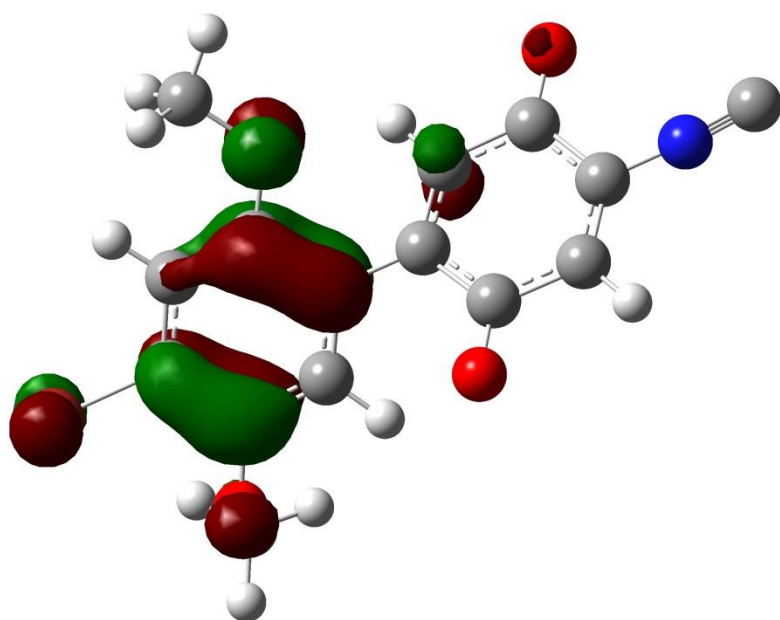
HOMO (top) and LUMO (bottom) of BrHBQCN



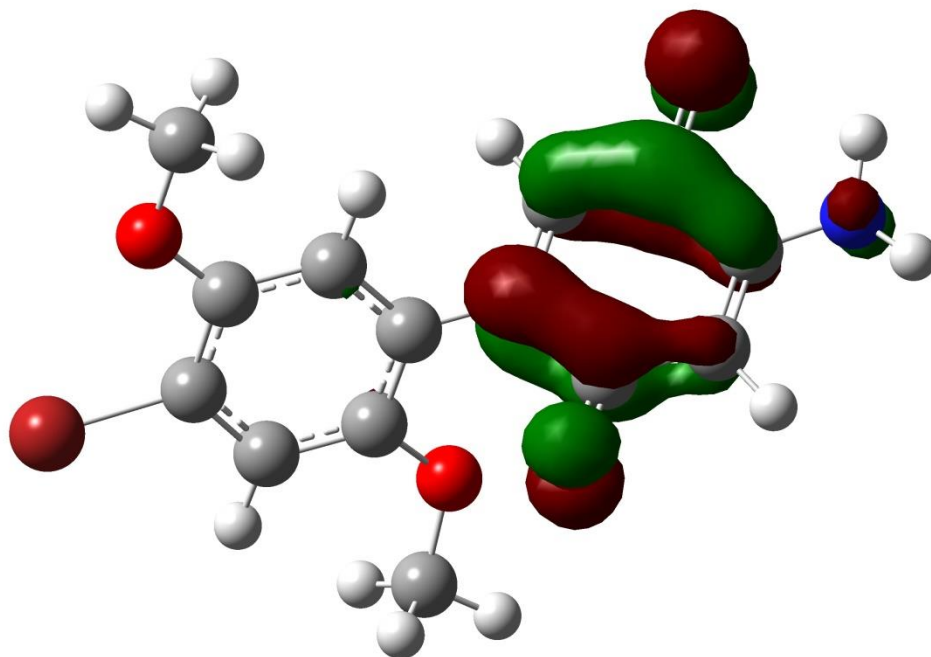
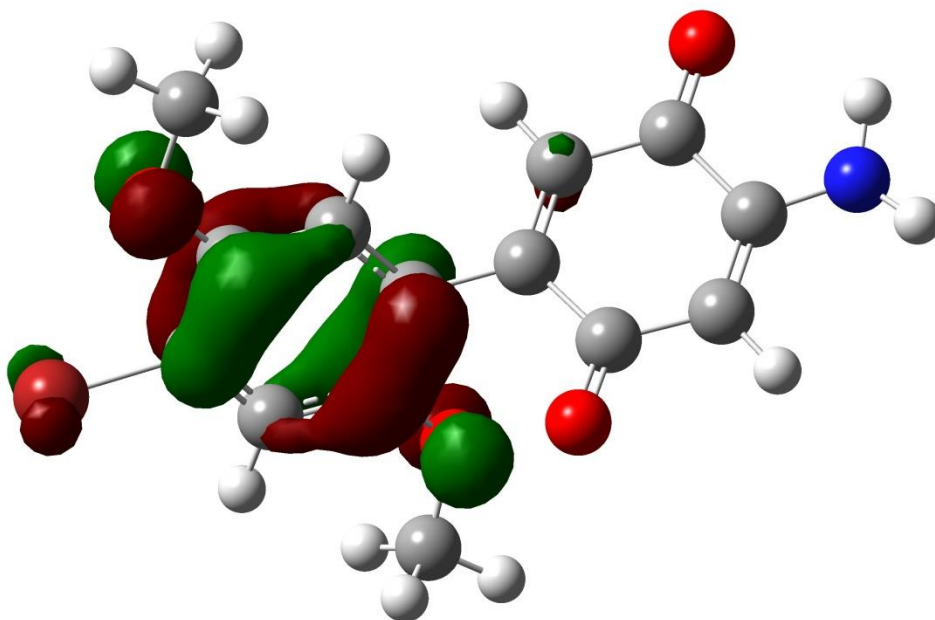
HOMO (top) and LUMO (bottom) of BrHBQCOOH



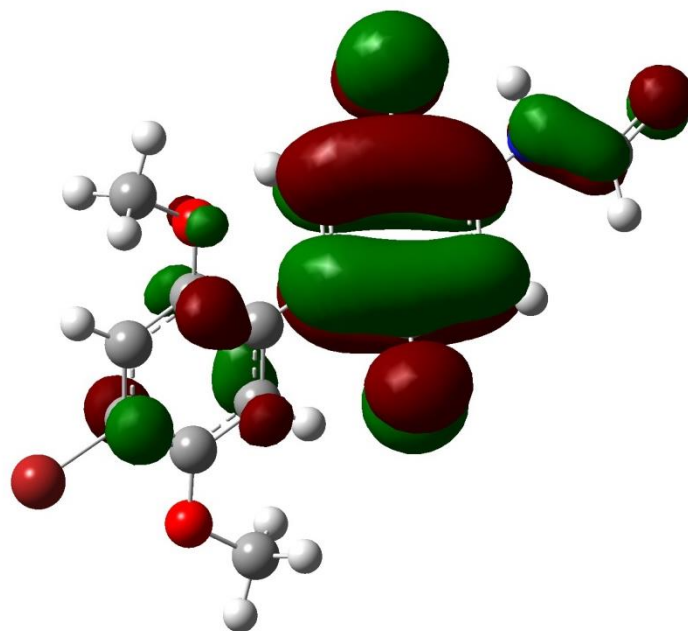
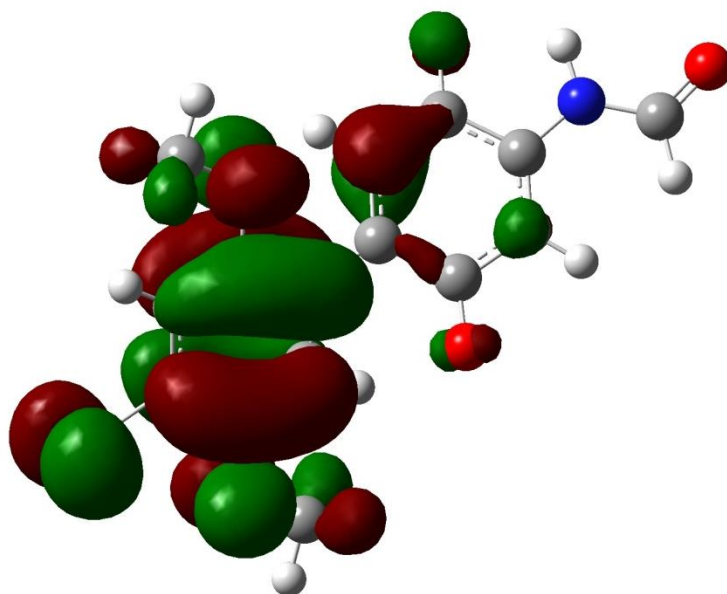
HOMO (top) and LUMO (bottom) of BrHBQBr₂



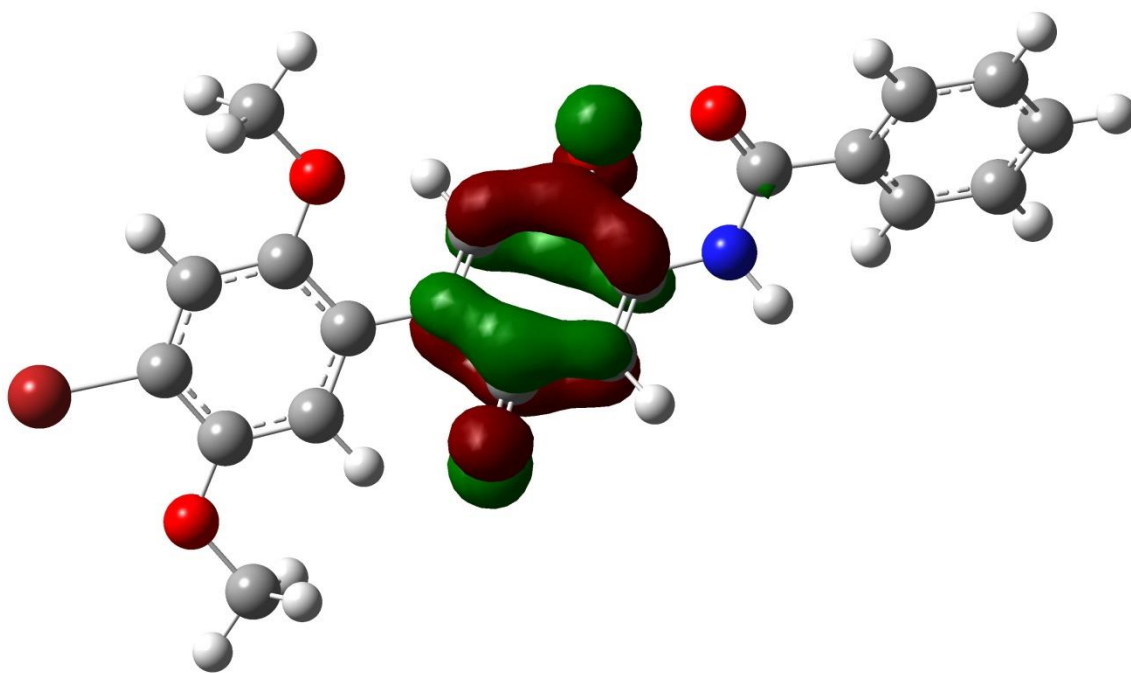
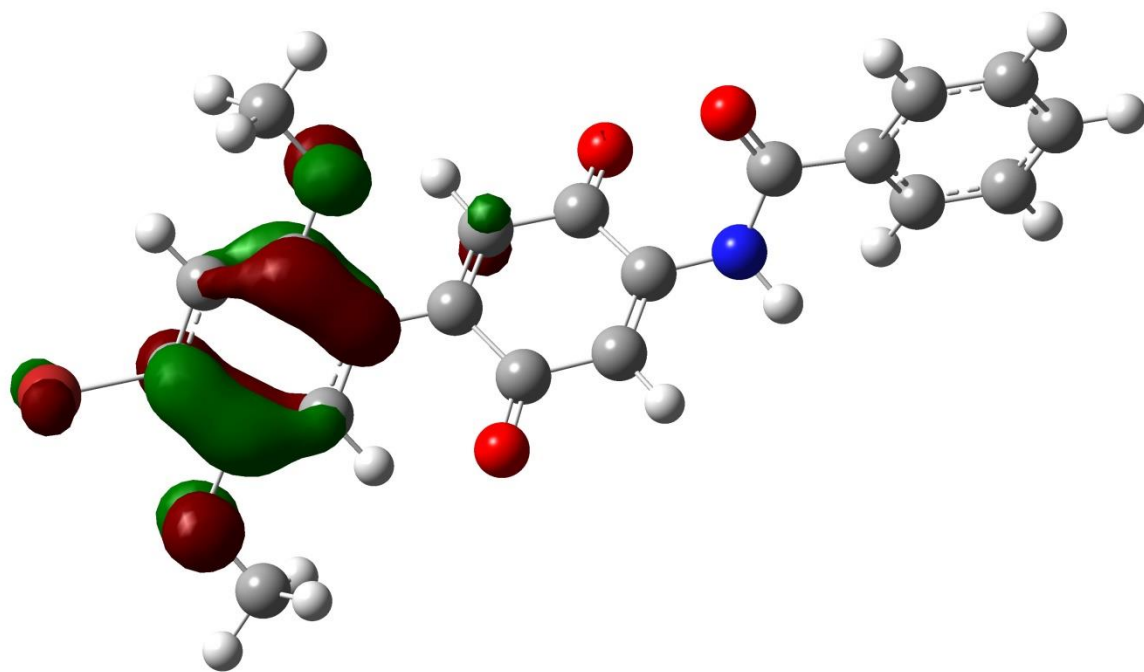
HOMO (top) and LUMO (bottom) of BrHBQNC



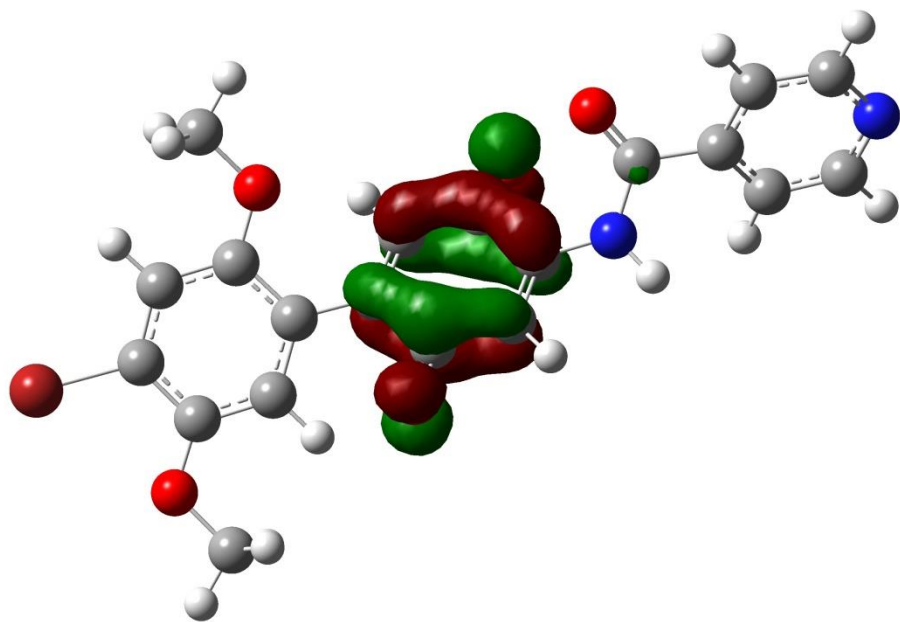
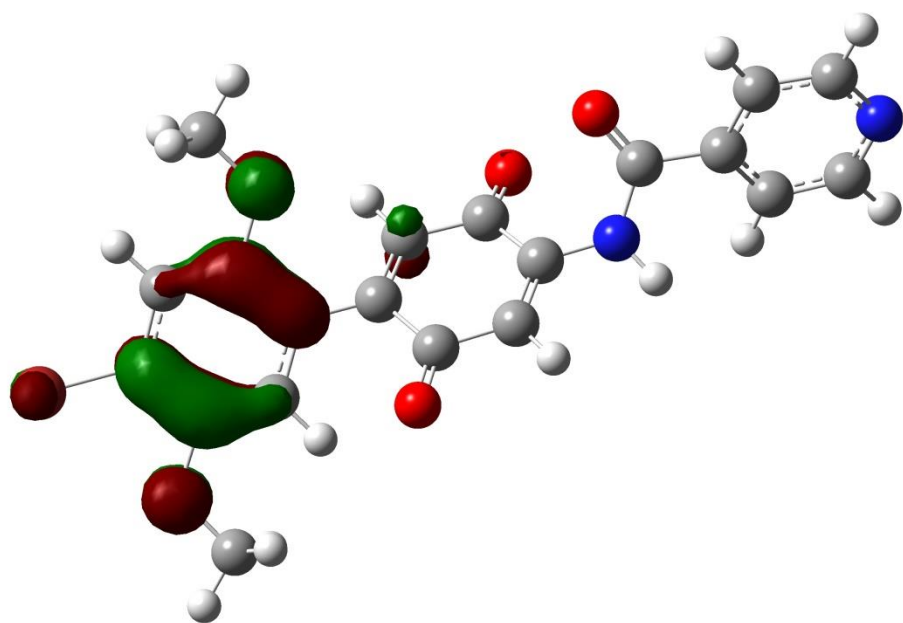
HOMO (top) and LUMO (bottom) of BrHBQNH₂



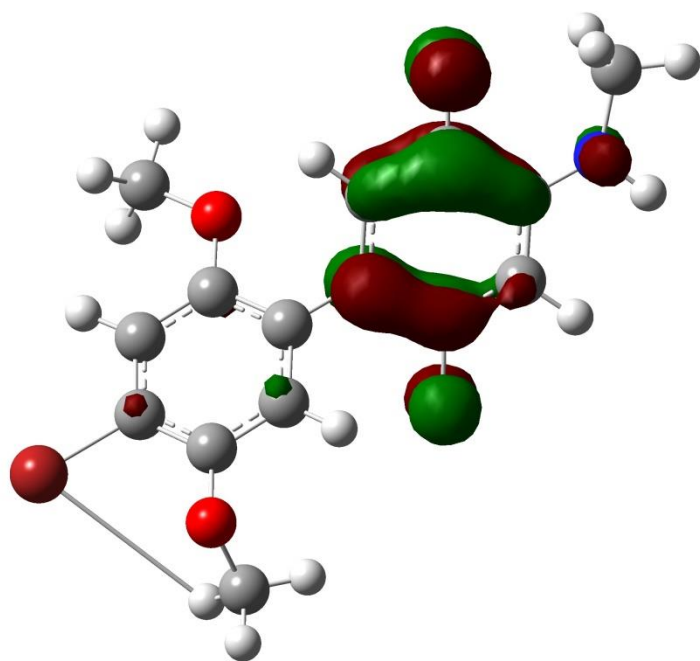
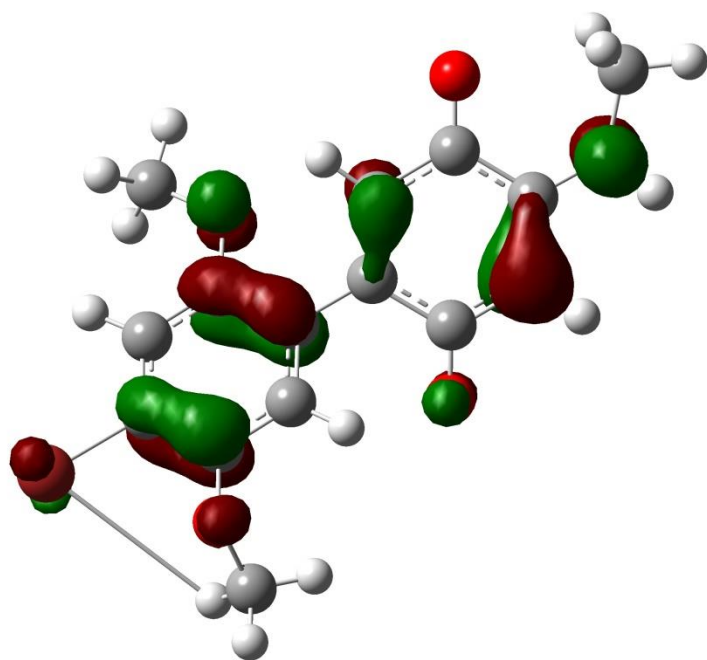
HOMO (top) and LUMO (bottom) of BrHBQNC(=O)H



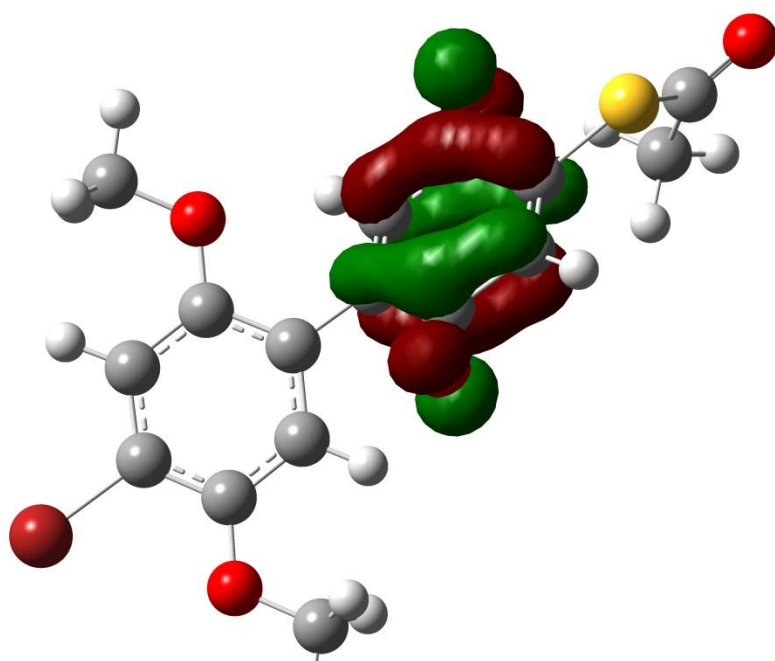
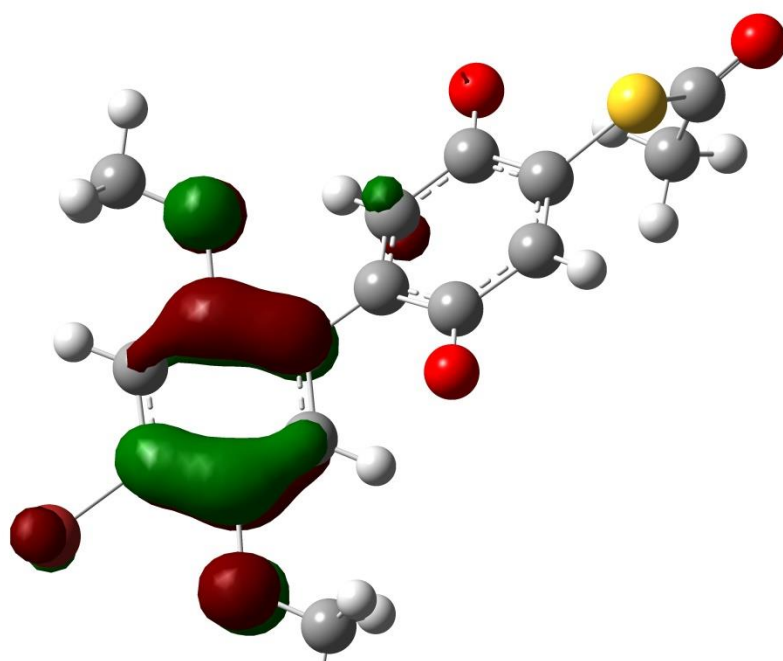
HOMO (top) and LUMO (bottom) of BrHBQNHC(=O)Ph



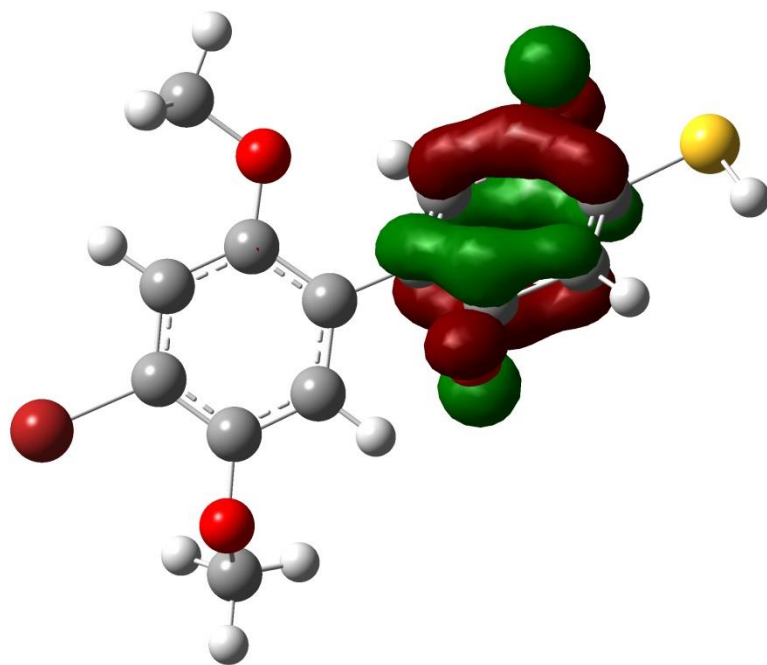
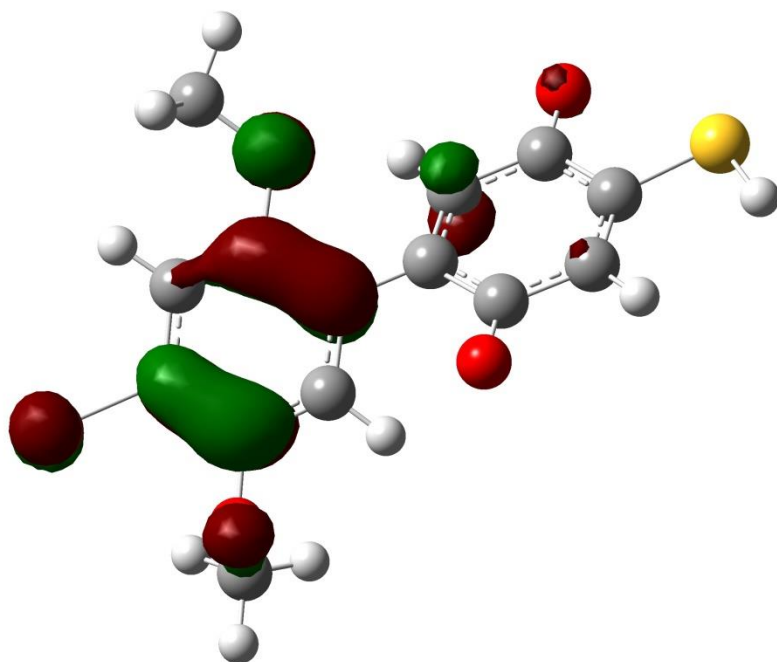
HOMO (top) and LUMO (bottom) of BrHBQNHC(=O)Py



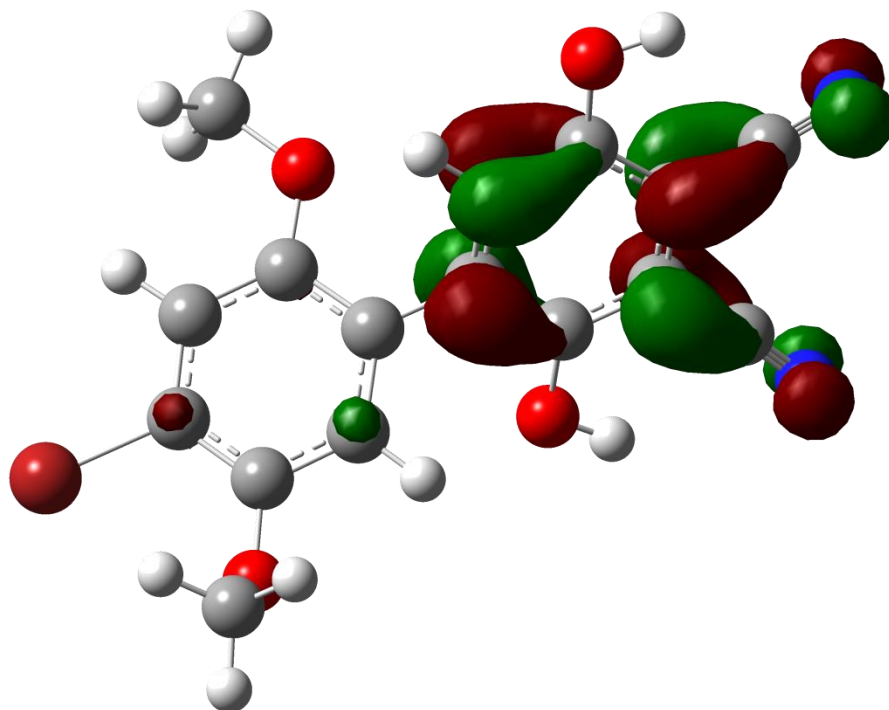
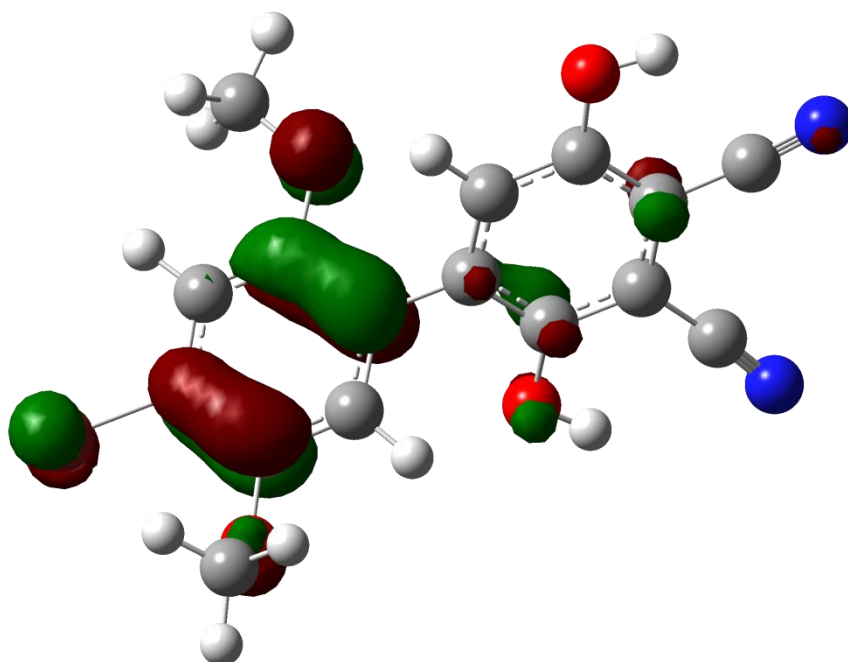
HOMO (top) and LUMO (bottom) of BrHBQNHMe



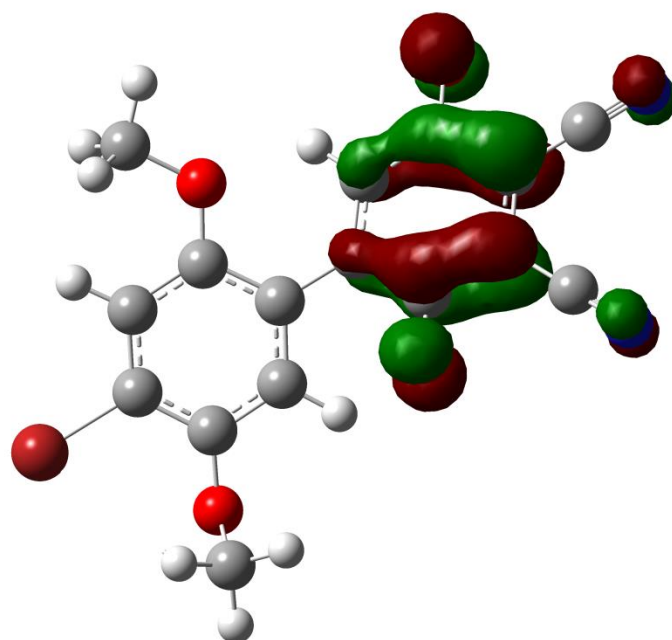
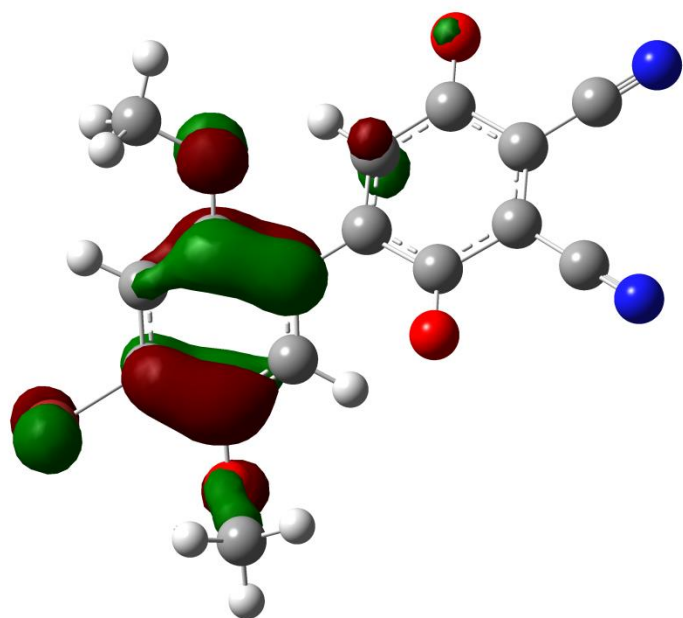
HOMO (top) and LUMO (bottom) of BrHBQSAc



HOMO (top) and LUMO (bottom) of BrHBQSH



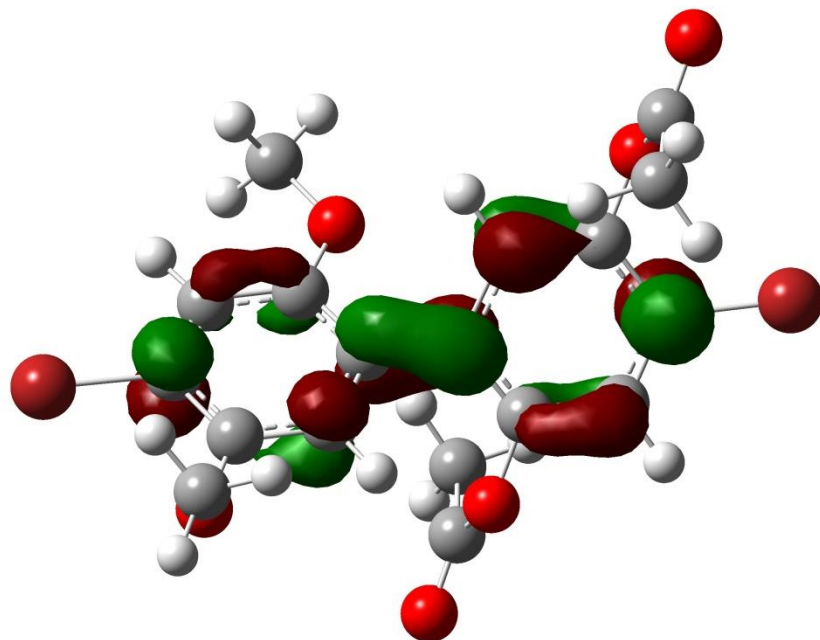
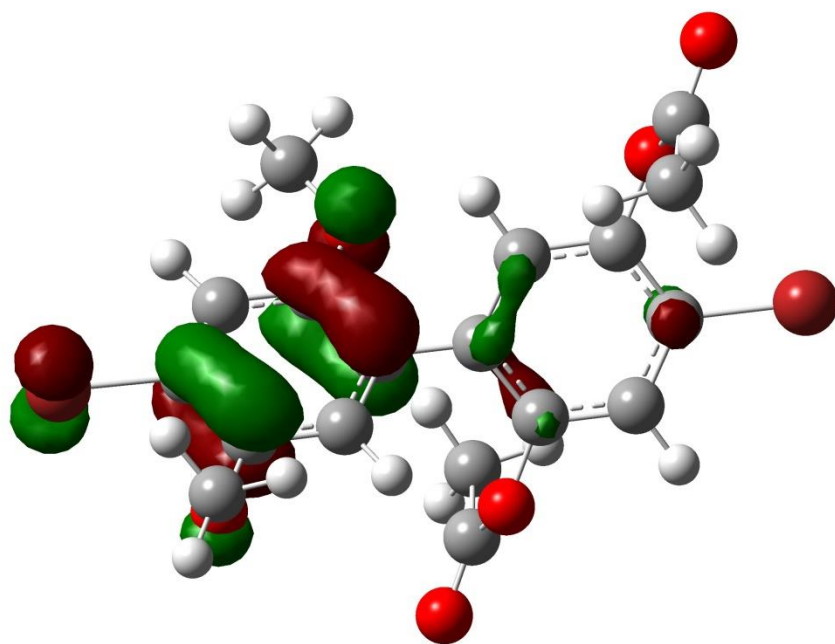
HOMO (top) and LUMO (bottom) of $\text{BrHBQH}_2(\text{CN})_2$



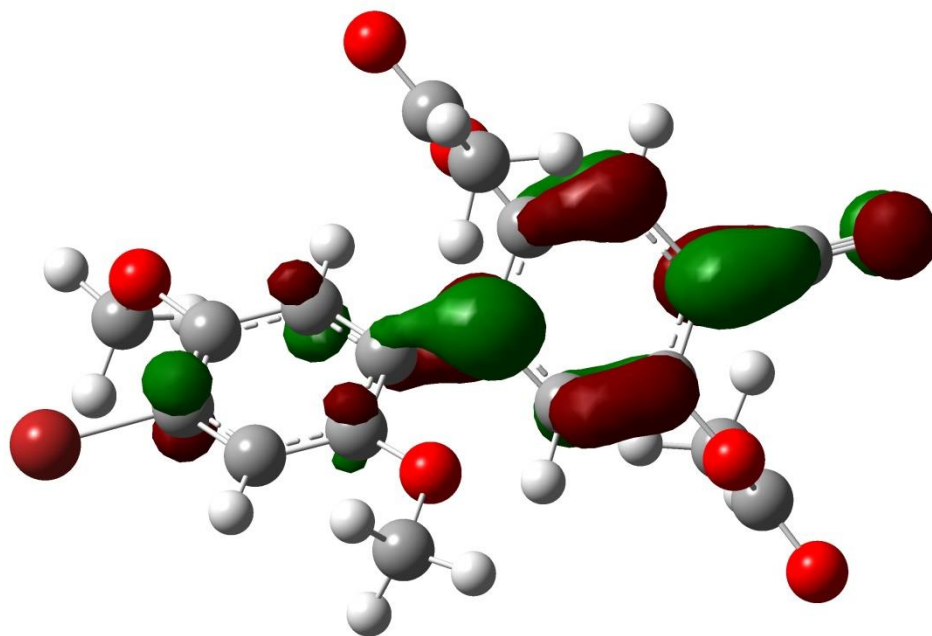
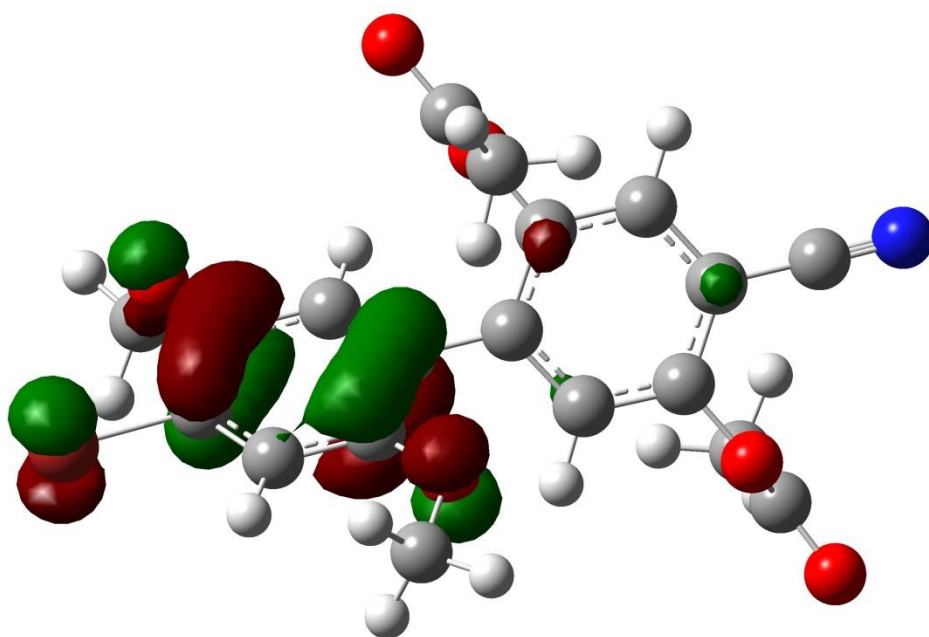
HOMO (top) and LUMO (bottom) of BrHBQ(CN)₂

APPENDIX B

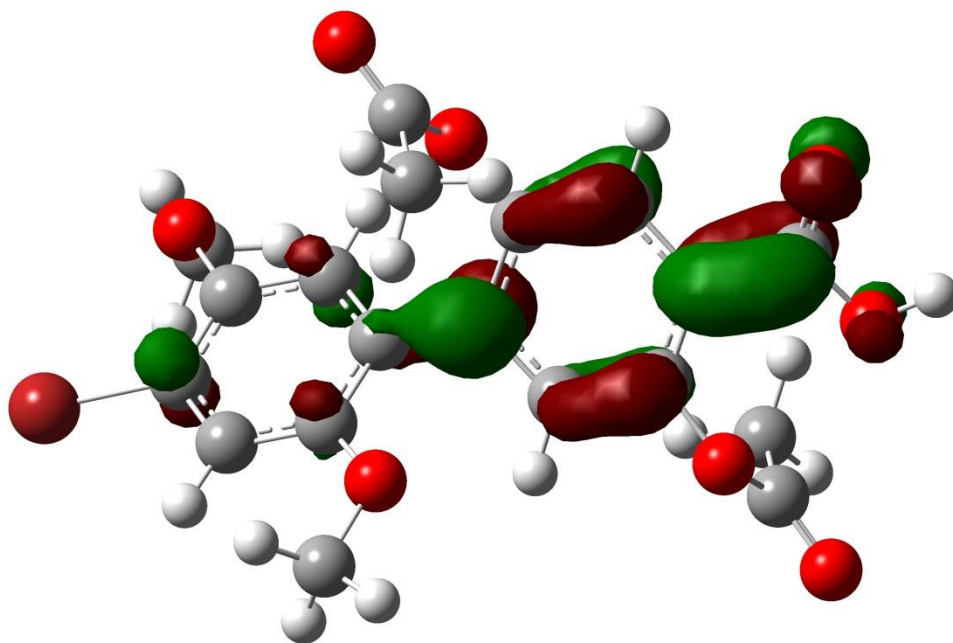
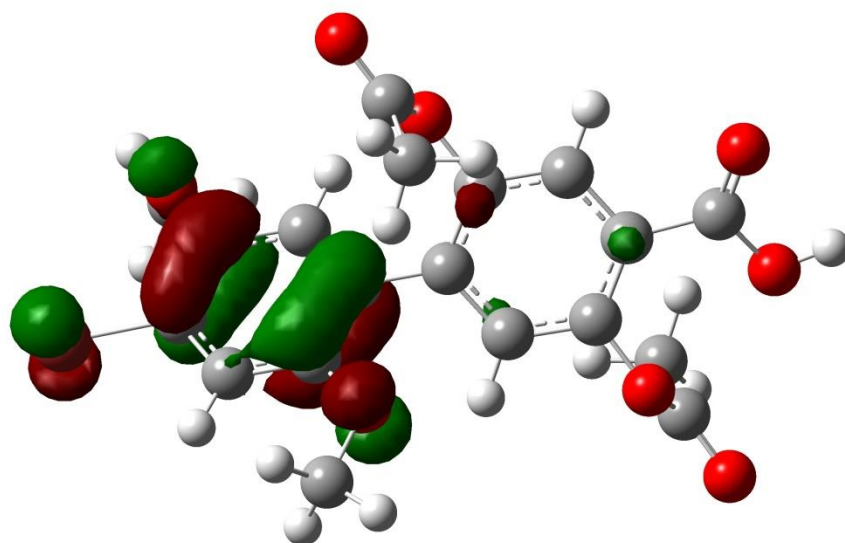
HBQAc₂ FMO Visualizations



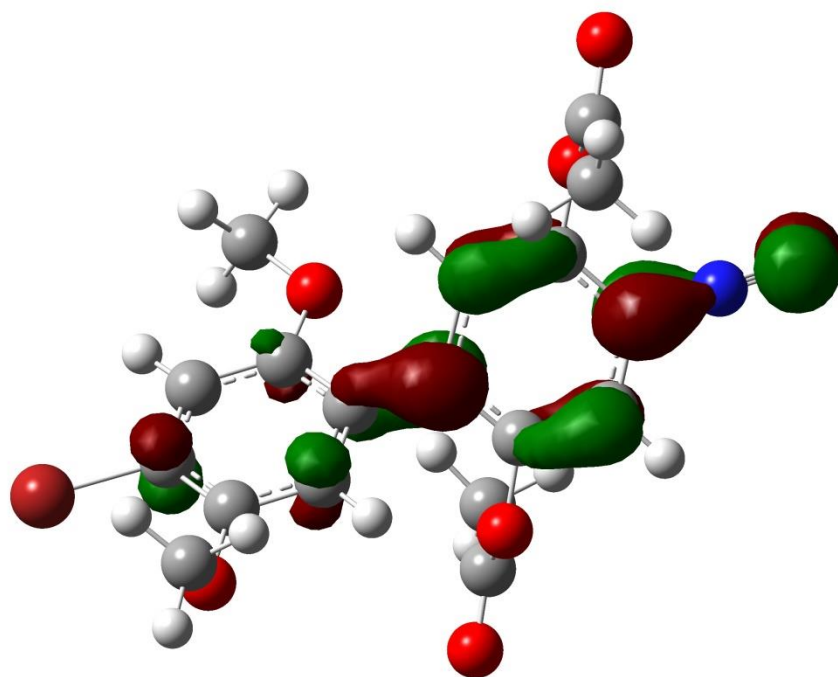
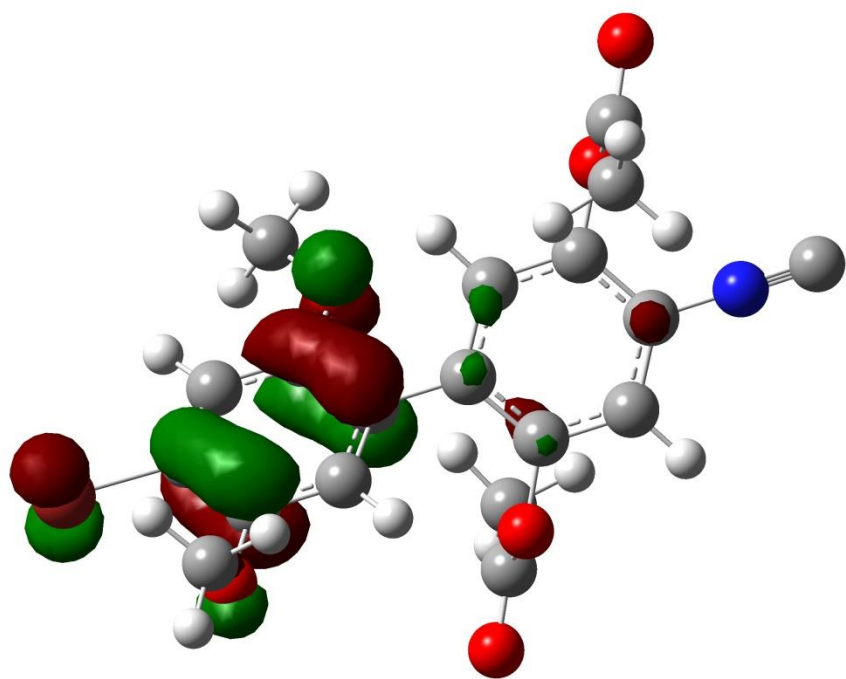
HOMO (top) and LUMO (bottom) of BrHBQAc₂Br



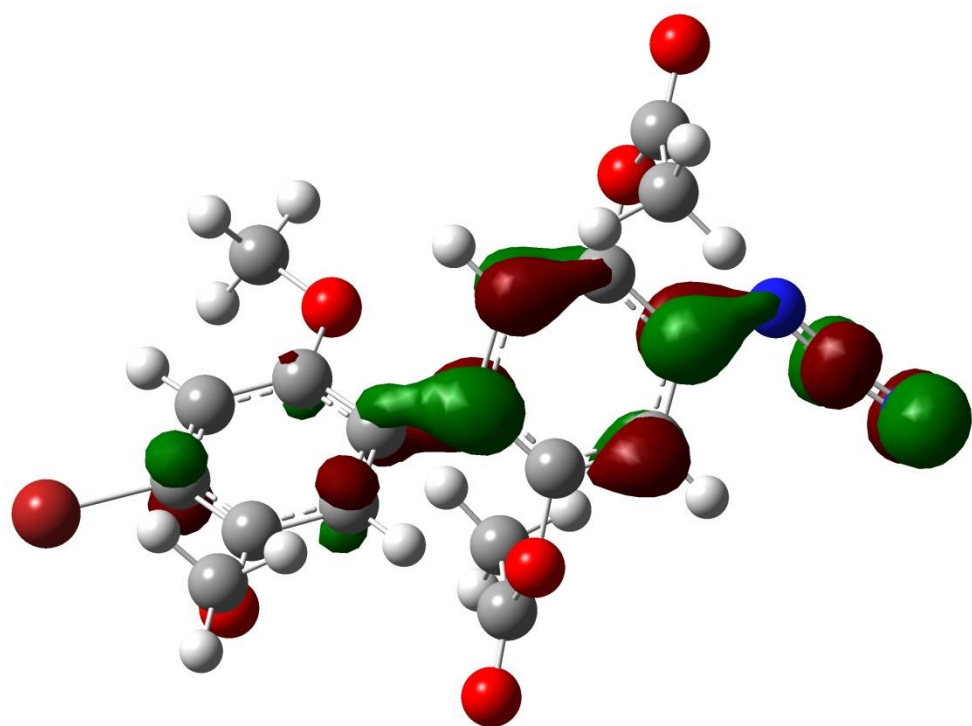
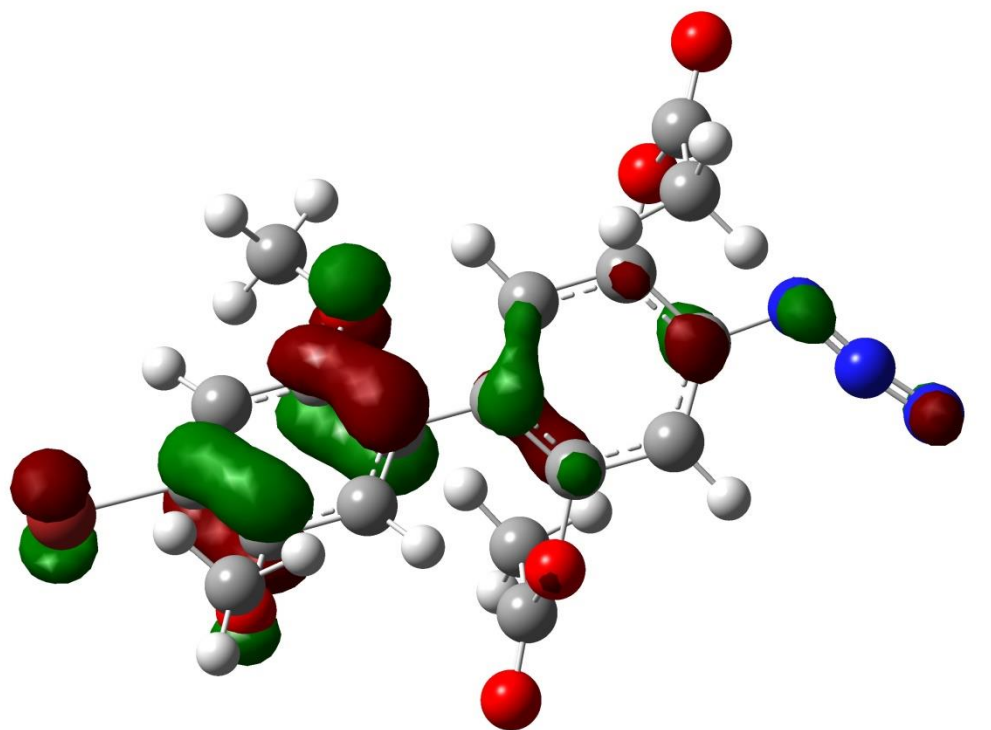
HOMO (top) and LUMO (bottom) of BrHBQAc₂CN



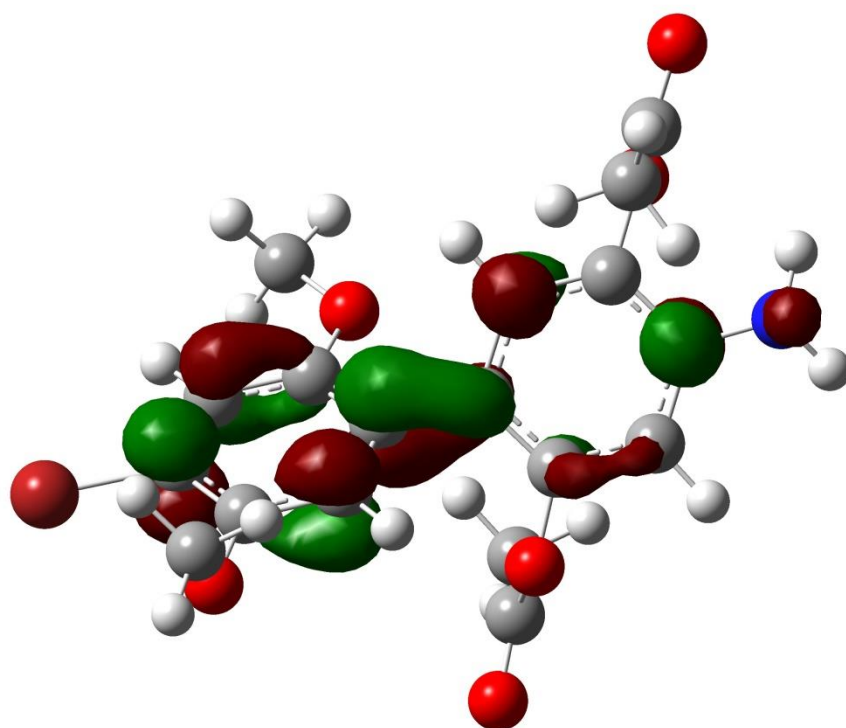
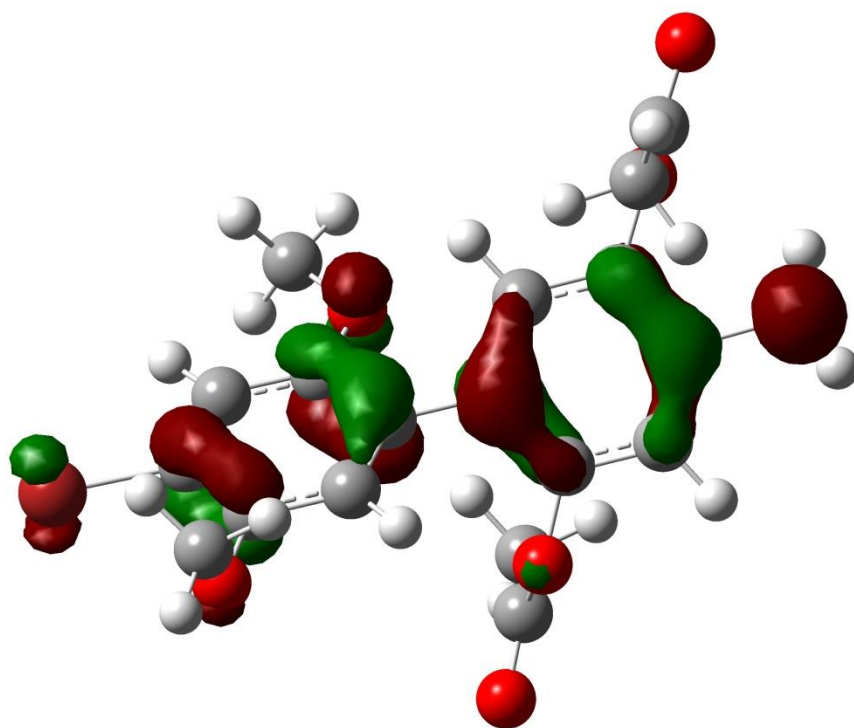
HOMO (top) and LUMO (bottom) of BrHBQAc₂COOH



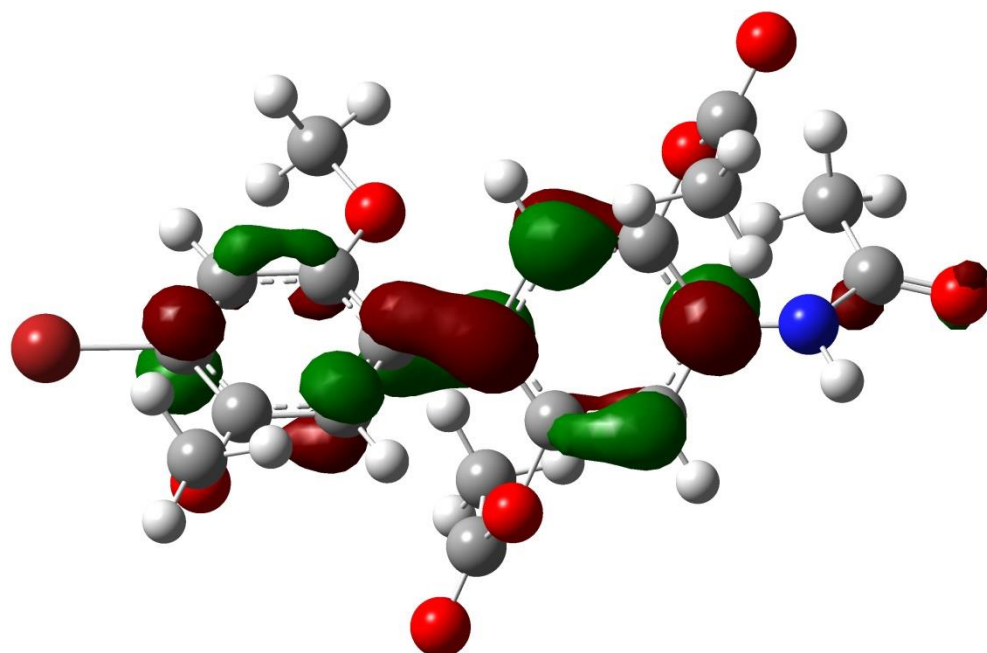
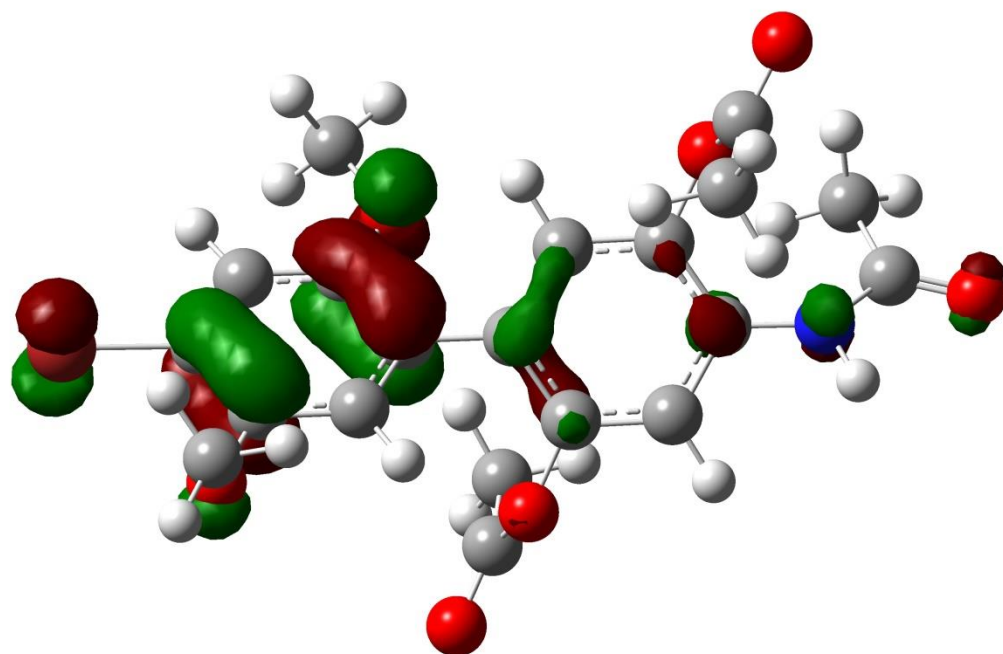
HOMO (top) and LUMO (bottom) of BrHBQAc₂NC



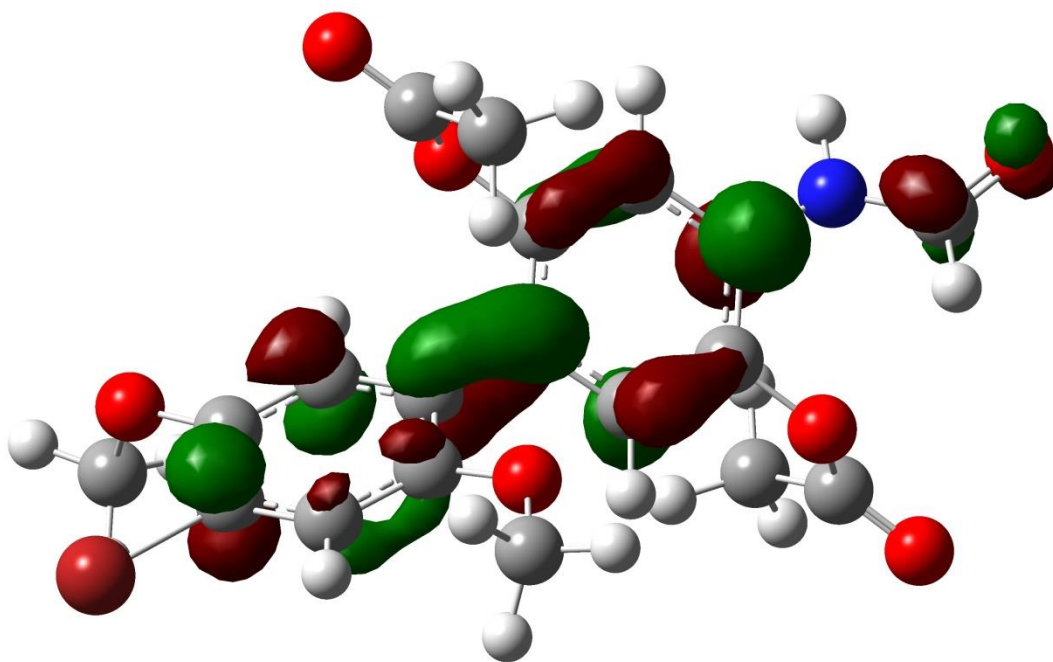
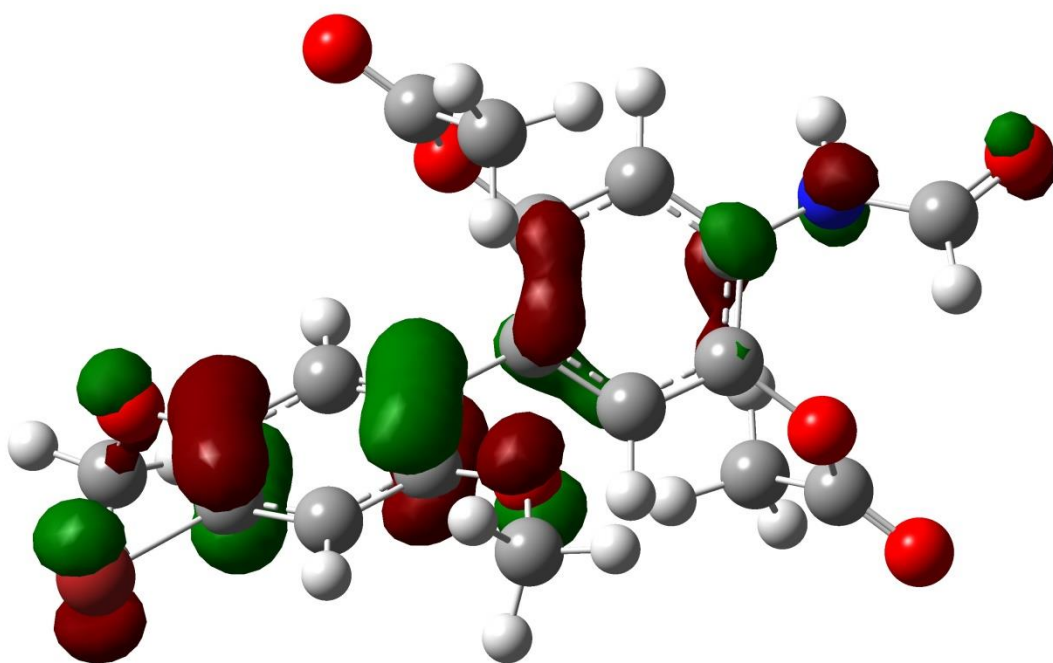
HOMO (top) and LUMO (bottom) of BrHBQAc₂N₃



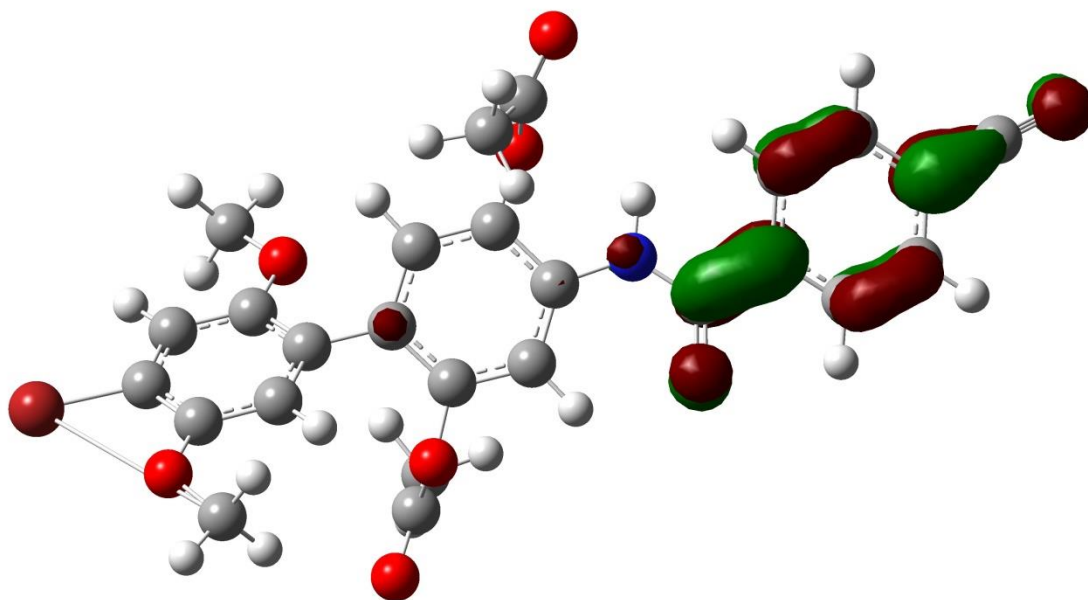
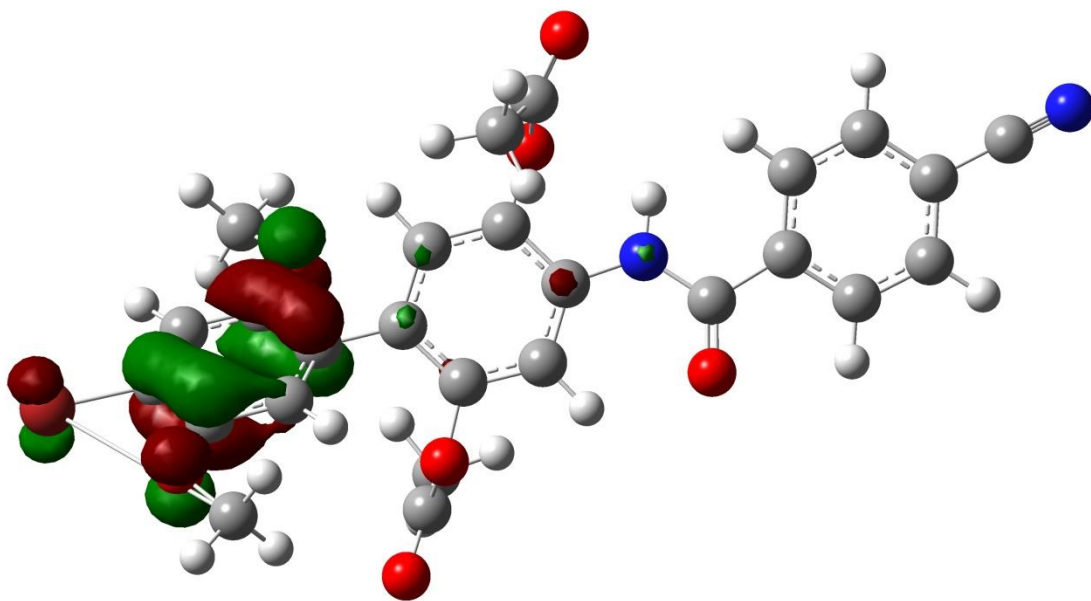
HOMO (top) and LUMO (bottom) of BrHBQAc₂NH₂



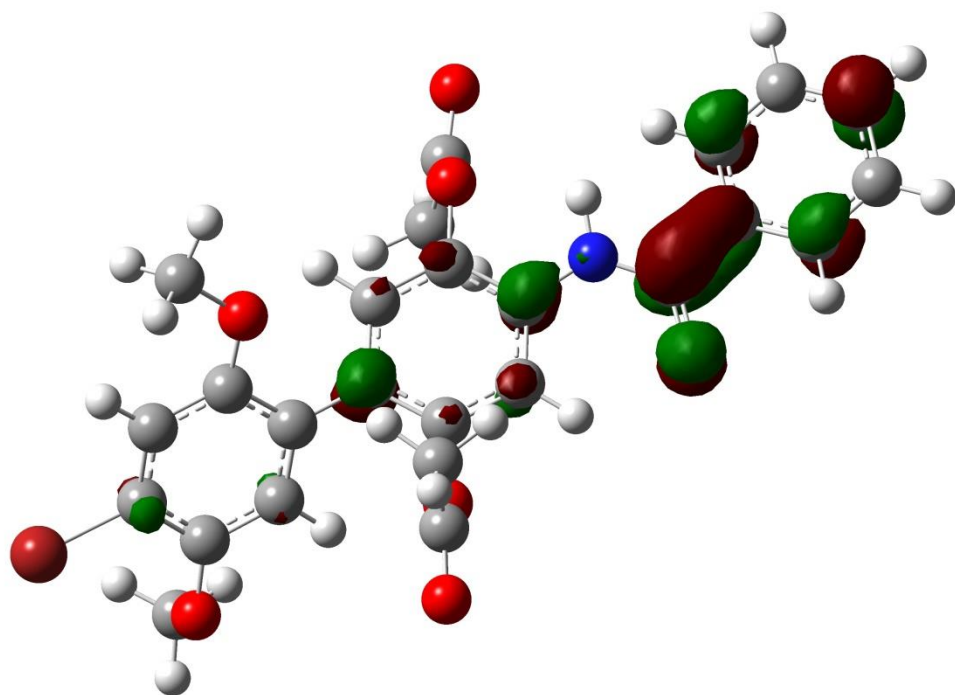
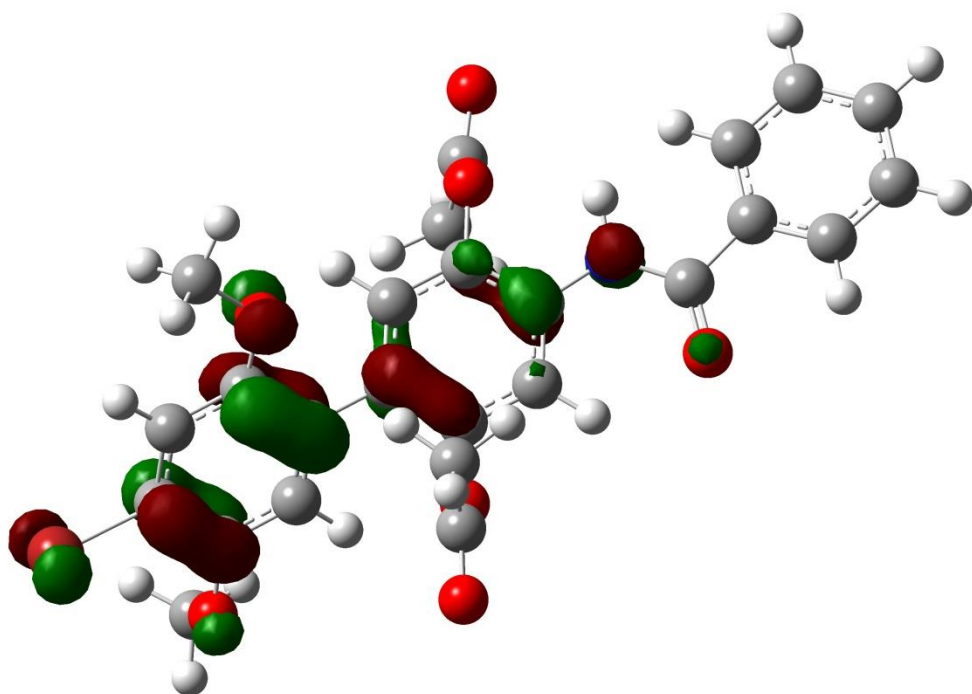
HOMO (top) and LUMO (bottom) of BrHBQAc₂NHAc



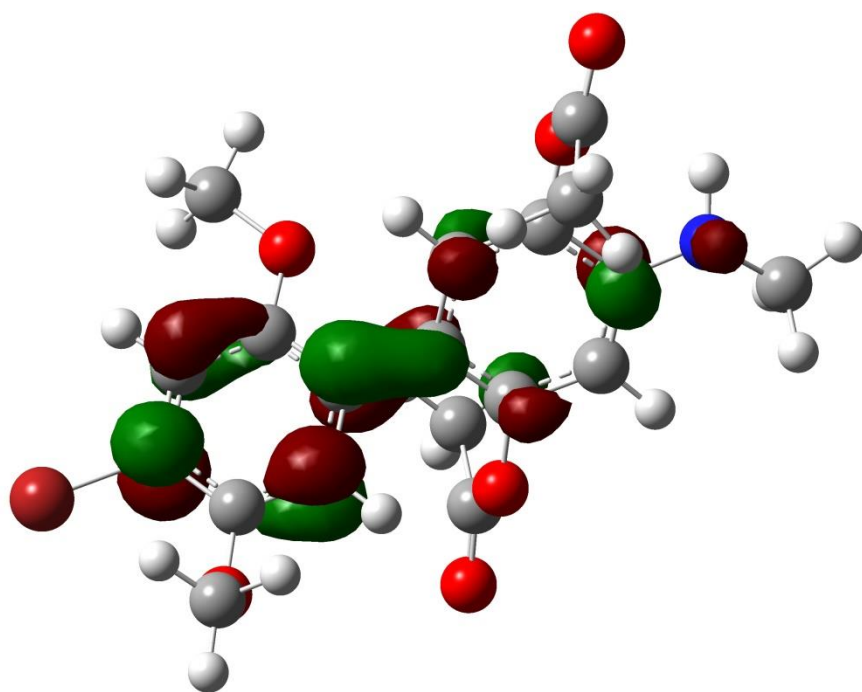
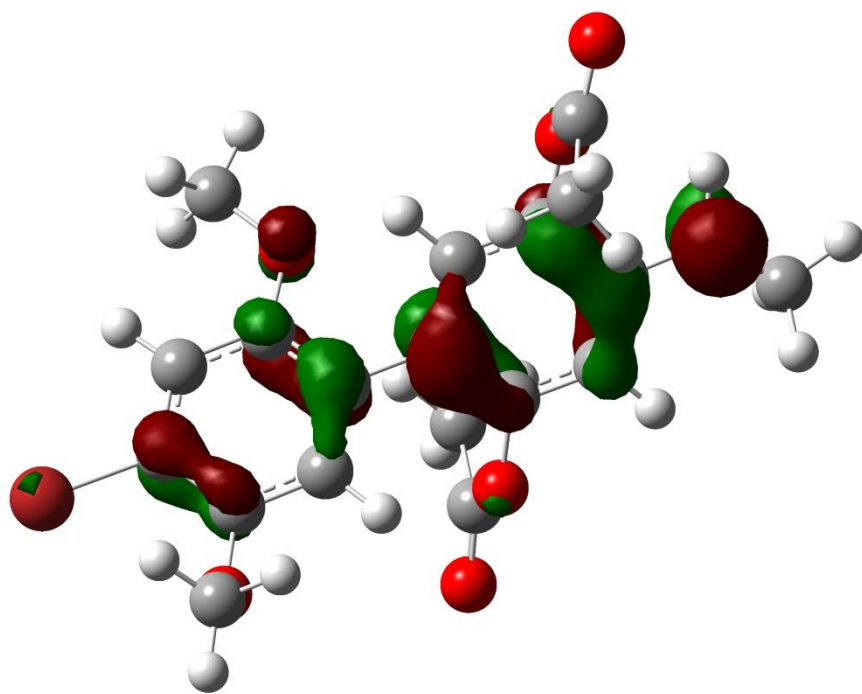
HOMO (top) and LUMO (bottom) of BrHBQAc₂NHC(=O)H



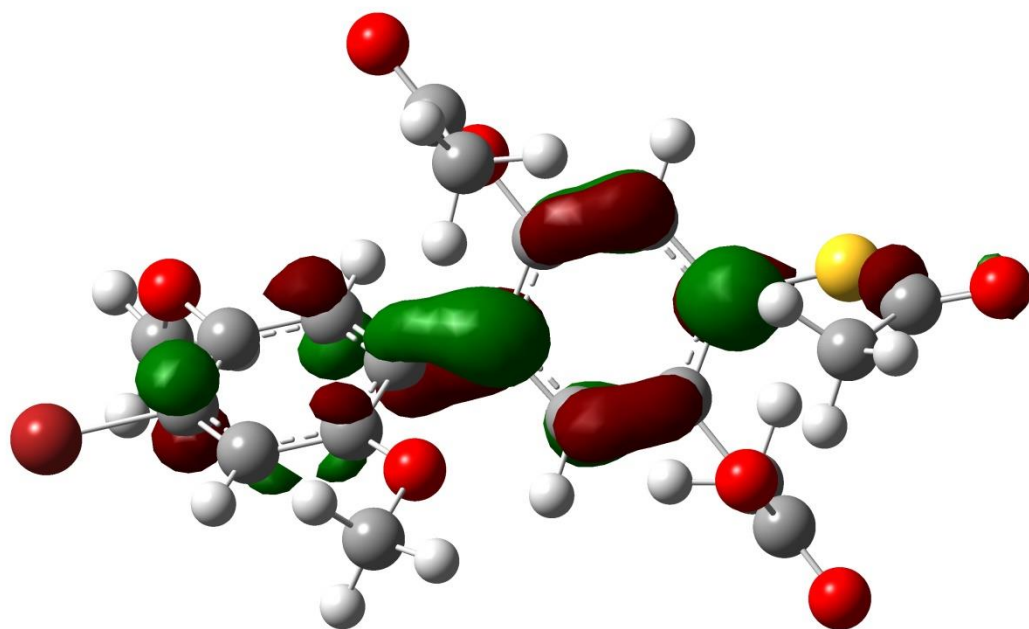
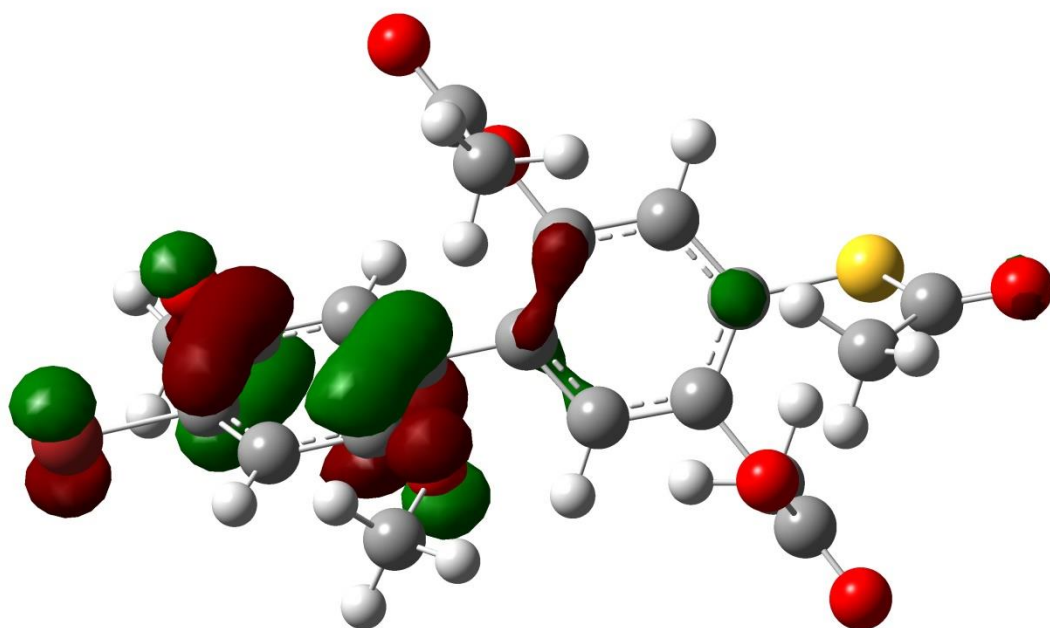
HOMO (top) and LUMO (bottom) of BrHBQAc₂NHC(=O)PhCN



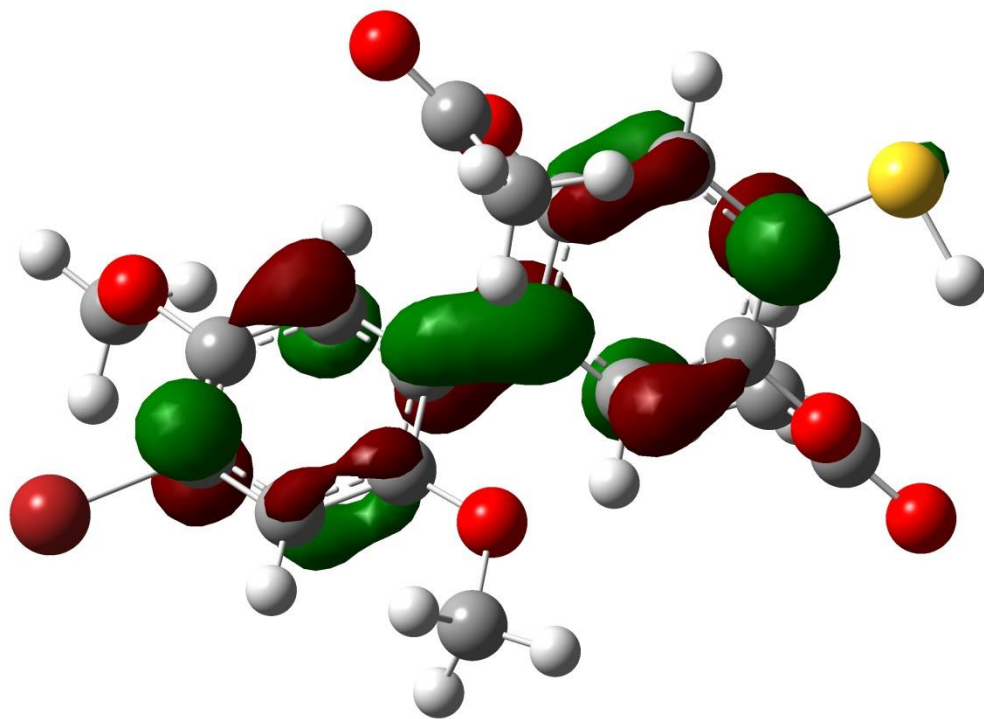
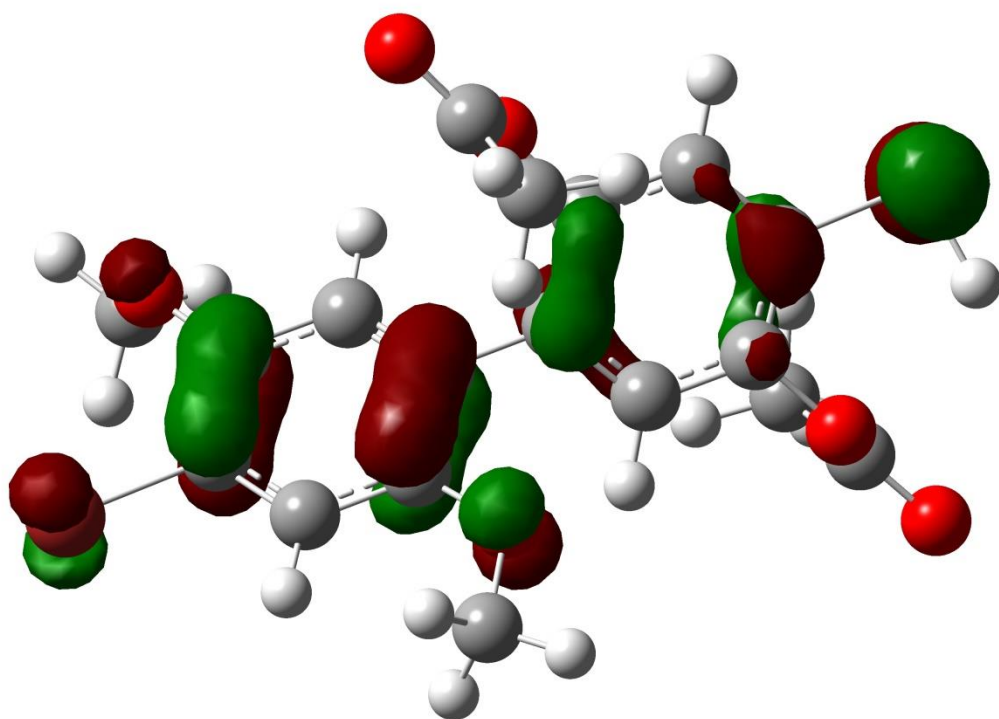
HOMO (top) and LUMO (bottom) of BrHBQAc₂NHC(=O)Ph



HOMO (top) and LUMO (bottom) of BrHBQAc₂NHMe



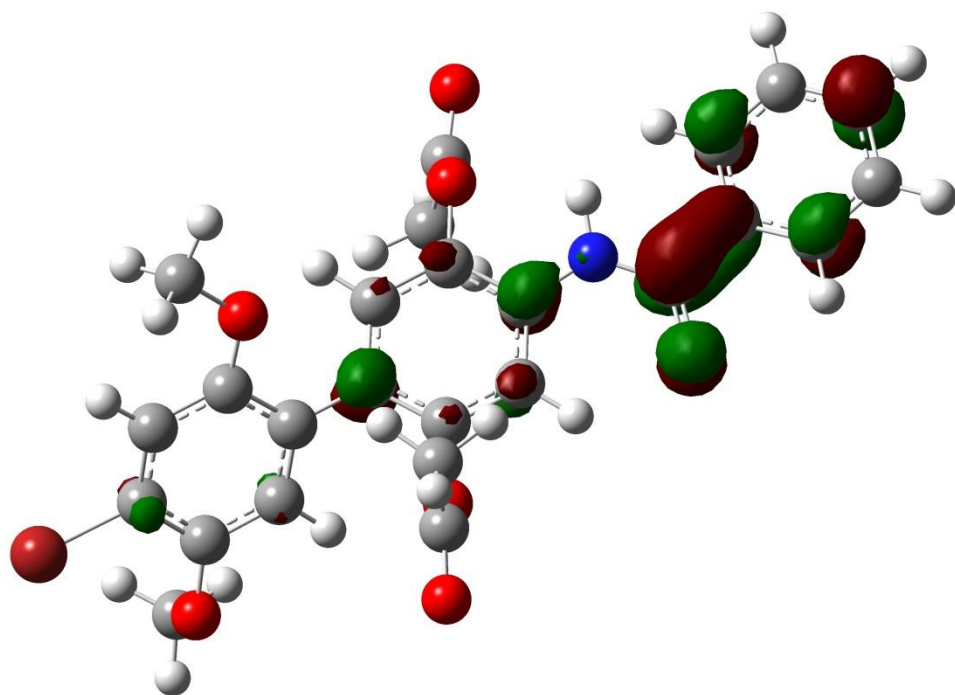
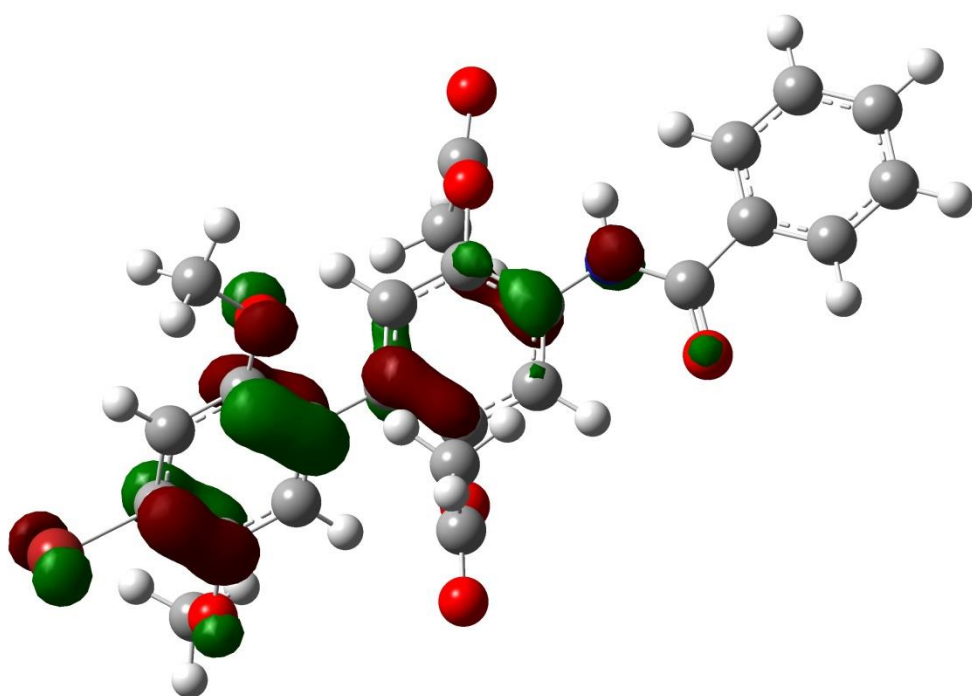
HOMO (top) and LUMO (bottom) of BrHBQAc₂SAc



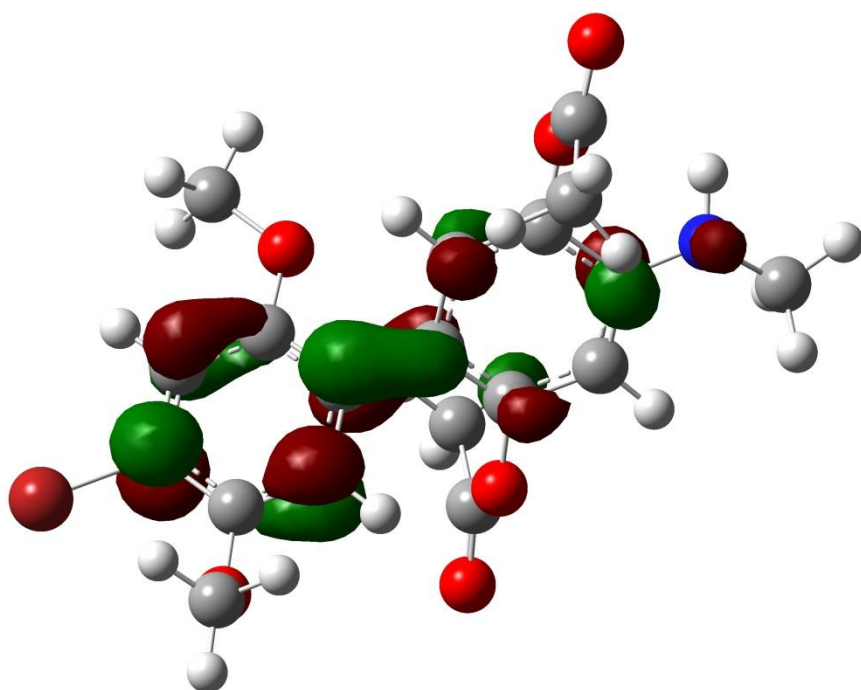
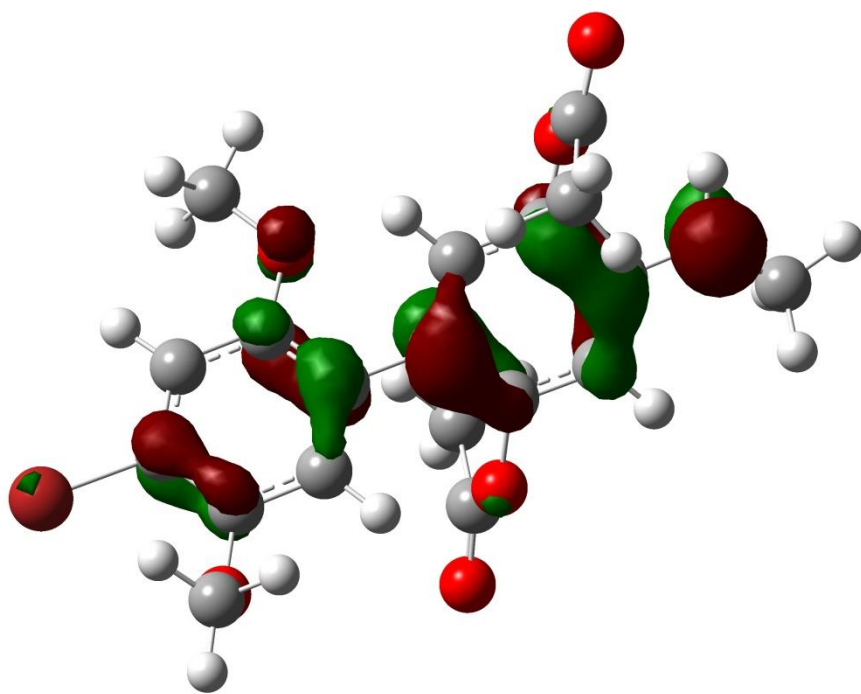
HOMO (top) and LUMO (bottom) of BrHBQAc₂SH

APPENDIX C

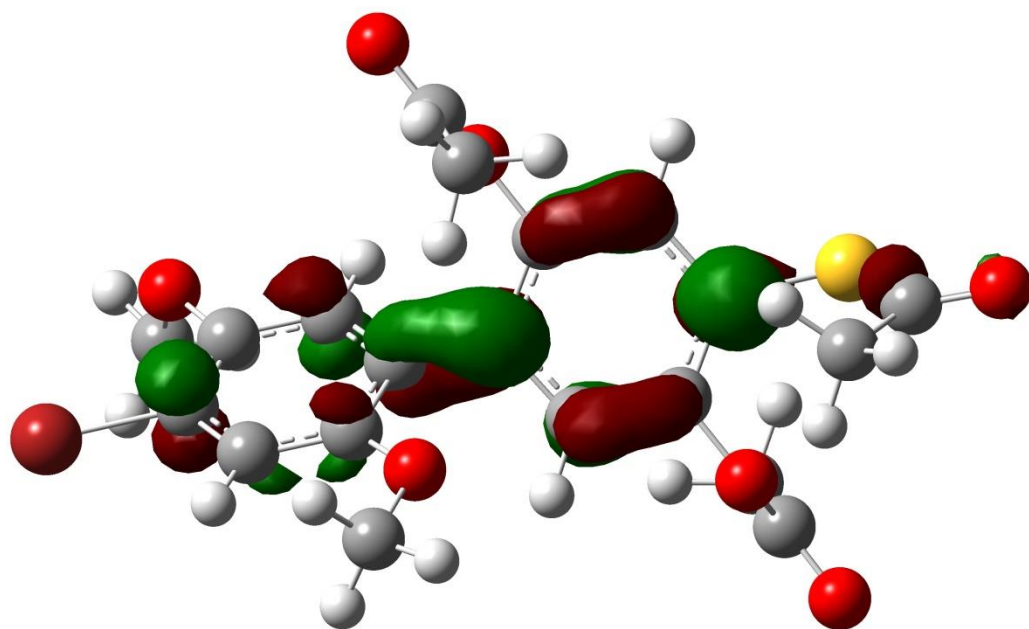
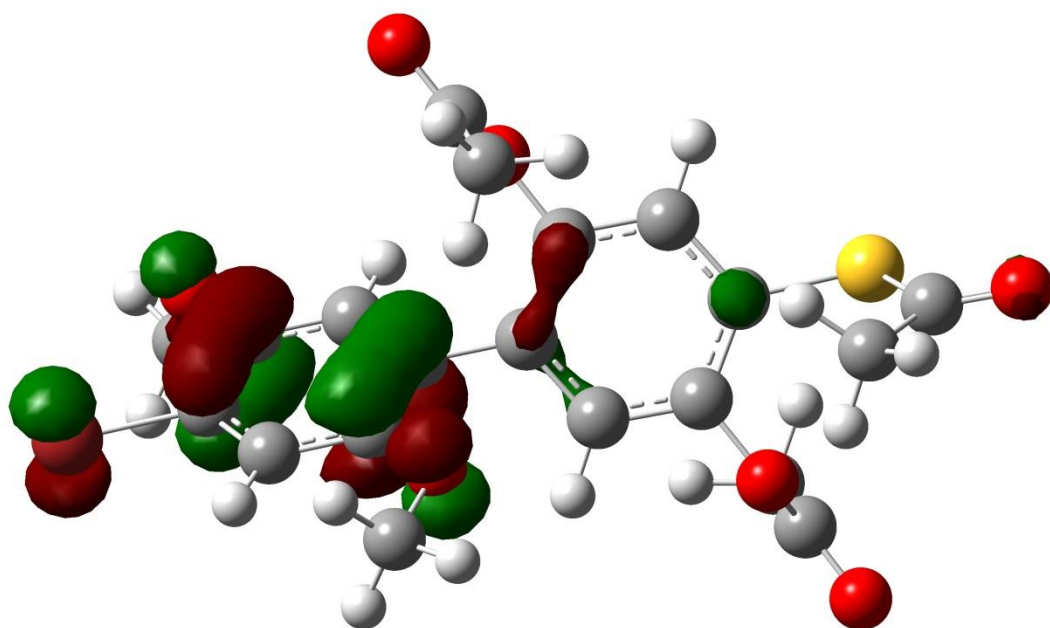
TCNQ- and DCNQI-functionalized HBQ FMO Visualizations



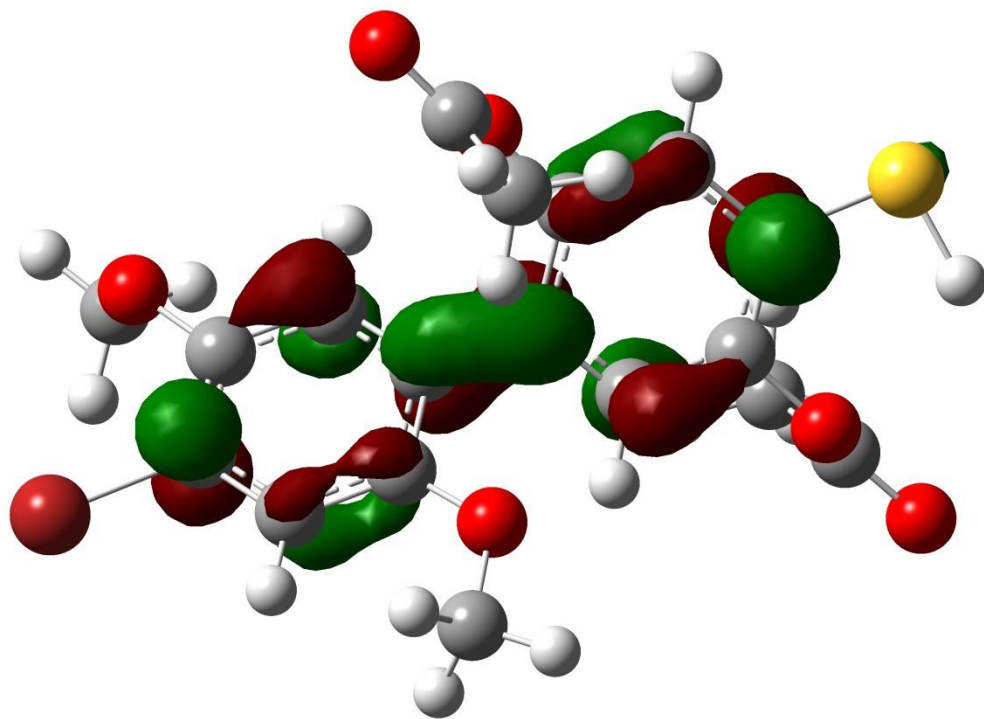
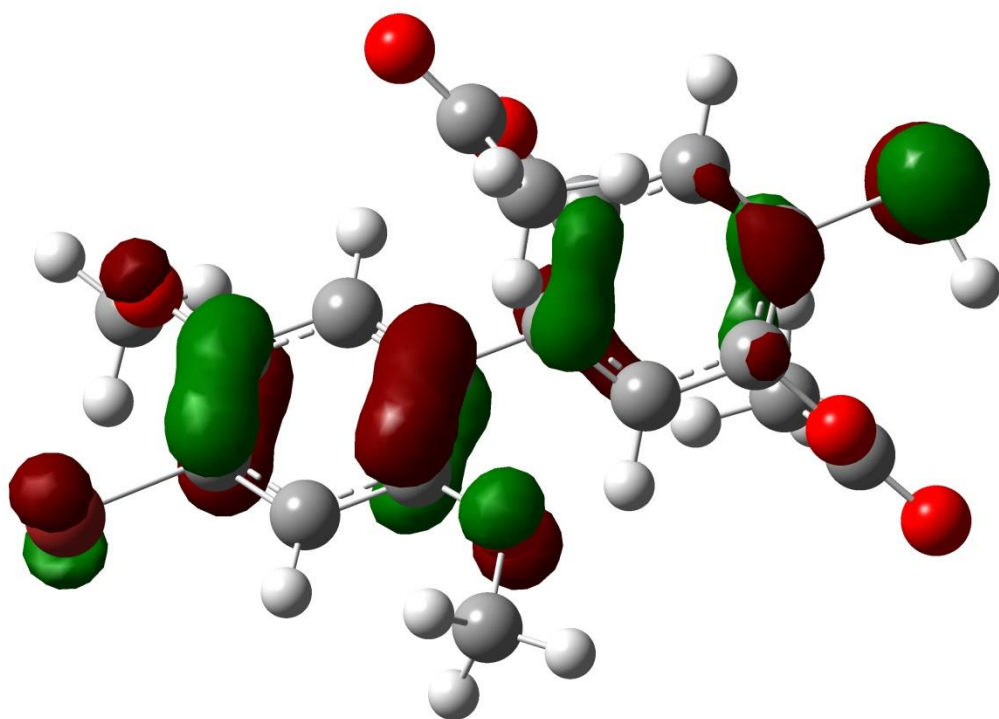
HOMO (top) and LUMO (bottom) of BrHBQAc₂NHC(=O)Ph



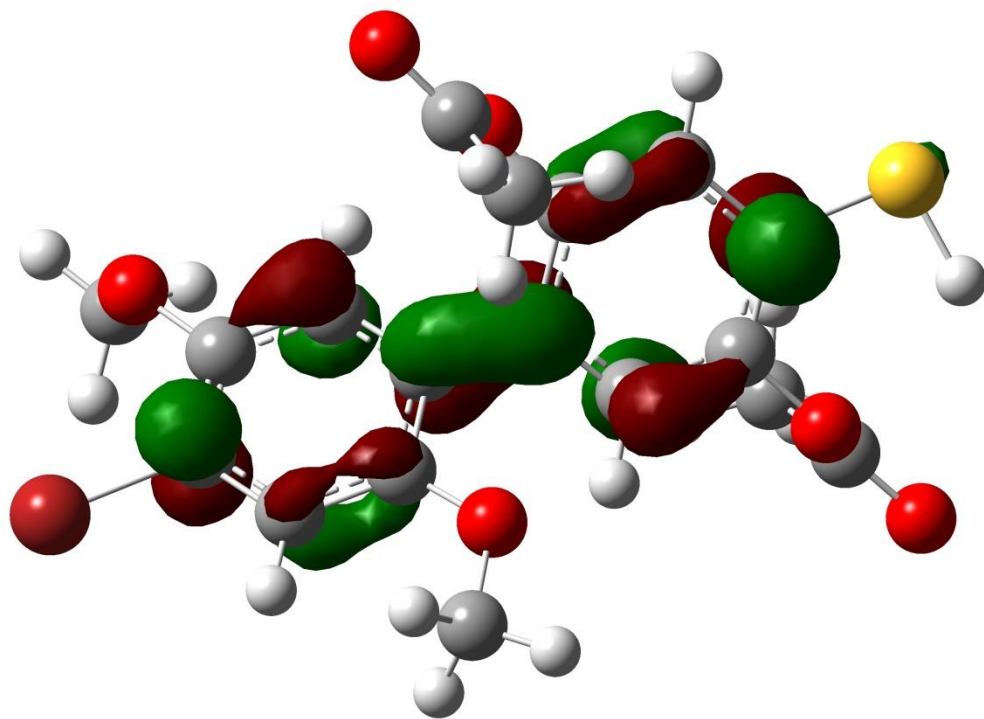
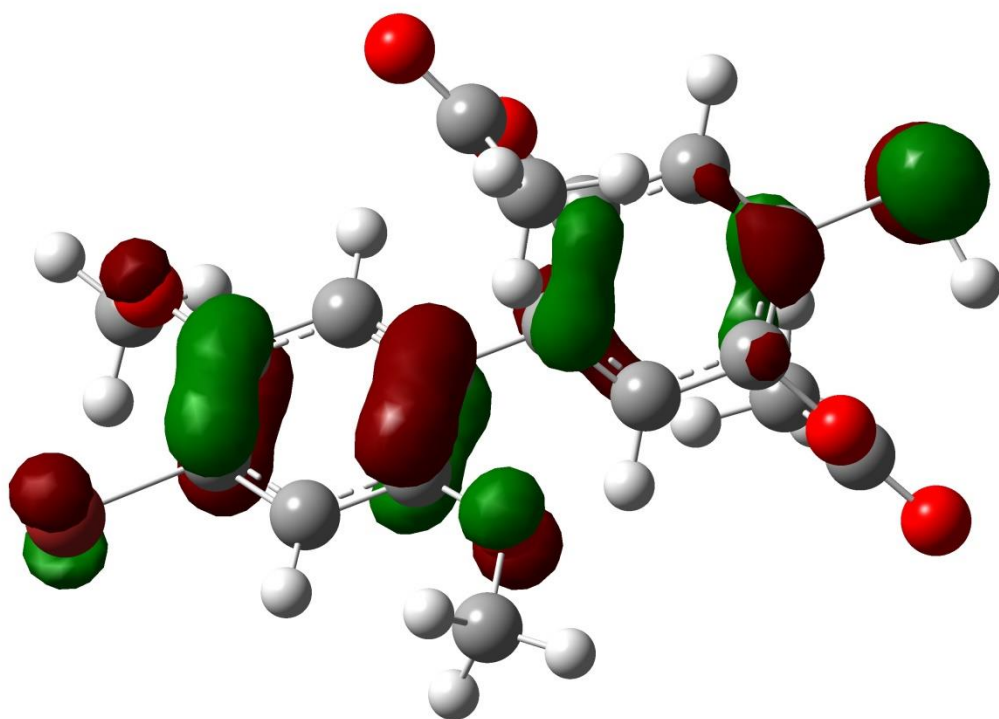
HOMO (top) and LUMO (bottom) of BrHBQAc₂NHMe



HOMO (top) and LUMO (bottom) of BrHBQAc₂SAc



HOMO (top) and LUMO (bottom) of BrHBQAc₂SH



HOMO (top) and LUMO (bottom) of BrHBQAc₂SH

APPENDIX D
COPYRIGHT NOTICES

Copyrighted figures are property of their respective owners and are reproduced here for noncommercial educational purposes. Some notices for permissions are currently pending. Original publications are cited where relevant and copyright owners are credited.

Permission for Figure 1.1, Page 6:

The screenshot shows the RightsLink website interface. At the top left is the Copyright Clearance Center logo. To its right is the RightsLink logo. Further right are navigation buttons for Home, Create Account, and Help. On the far right is a Live Chat icon. Below the navigation is a search bar with a LOGIN button. A search result is displayed, showing a request for permission to reuse content from an IEEE publication. The request details include the title, author, publication, and publisher. A login box is also visible, providing instructions for users who are already logged in or want to learn more.

Copyright Clearance Center RightsLink® Home Create Account Help Live Chat

IEEE Requesting permission to reuse content from an IEEE publication

Title: Cramming more components onto integrated circuits, Reprinted from Electronics, volume 38, number 8, April 19, 1965, pp.114 ff.

Author: Gordon E. Moore

Publication: Solid-State Circuits Newsletter, IEEE

Publisher: IEEE

Date: Sept. 2006

Copyright © 2006, IEEE

LOGIN

If you're a copyright.com user, you can login to RightsLink using your copyright.com credentials. Already a RightsLink user or want to [learn more?](#)

Thesis / Dissertation Reuse

The IEEE does not require individuals working on a thesis to obtain a formal reuse license, however, you may print out this statement to be used as a permission grant:

Requirements to be followed when using any portion (e.g., figure, graph, table, or textual material) of an IEEE copyrighted paper in a thesis:

- 1) In the case of textual material (e.g., using short quotes or referring to the work within these papers) users must give full credit to the original source (author, paper, publication) followed by the IEEE copyright line © 2011 IEEE.
- 2) In the case of illustrations or tabular material, we require that the copyright line © [Year of original publication] IEEE appear prominently with each reprinted figure and/or table.
- 3) If a substantial portion of the original paper is to be used, and if you are not the senior author, also obtain the senior author's approval.

Requirements to be followed when using an entire IEEE copyrighted paper in a thesis:

- 1) The following IEEE copyright/ credit notice should be placed prominently in the references: © [year of original publication] IEEE. Reprinted, with permission, from [author names, paper title, IEEE publication title, and month/year of publication]
- 2) Only the accepted version of an IEEE copyrighted paper can be used when posting the paper or your thesis on-line.
- 3) In placing the thesis on the author's university website, please display the following message in a prominent place on the website: In reference to IEEE copyrighted material which is used with permission in this thesis, the IEEE does not endorse any of [university/educational entity's name goes here]'s products or services. Internal or personal use of this material is permitted. If interested in reprinting/republishing IEEE copyrighted material for advertising or promotional purposes or for creating new collective works for resale or redistribution, please go to http://www.ieee.org/publications_standards/publications/rights/rights_link.html to learn how to obtain a License from RightsLink.

If applicable, University Microfilms and/or ProQuest Library, or the Archives of Canada may supply single copies of the dissertation.

BACK **CLOSE WINDOW**

Copyright © 2016 Copyright Clearance Center, Inc. All Rights Reserved. [Privacy statement](#). [Terms and Conditions](#).
Comments? We would like to hear from you. E-mail us at customercare@copyright.com

Permission request for Figure 1.9, Page 24:

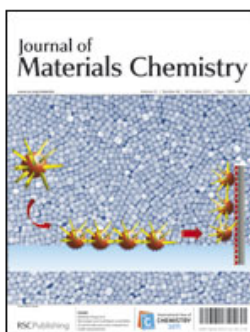


RightsLink®

Home

Account Info

Help



Title: Unimolecular electronics
Author: Robert M. Metzger
Publication: Journal of Materials Chemistry
Publisher: Royal Society of Chemistry
Date: Jun 23, 2008
Copyright © 2008, Royal Society of Chemistry

Logged in as:
Joseph Meany

LOGOUT

Order Completed

Thank you for your order.

This Agreement between Joseph E Meany ("You") and Royal Society of Chemistry ("Royal Society of Chemistry") consists of your license details and the terms and conditions provided by Royal Society of Chemistry and Copyright Clearance Center.

Your confirmation email will contain your order number for future reference.

[Get the printable license.](#)

License Number	3900321126084
License date	Jul 01, 2016
Licensed Content Publisher	Royal Society of Chemistry
Licensed Content Publication	Journal of Materials Chemistry
Licensed Content Title	Unimolecular electronics
Licensed Content Author	Robert M. Metzger
Licensed Content Date	Jun 23, 2008
Licensed Content Volume	18
Licensed Content Issue	37
Type of Use	Thesis/Dissertation
Requestor type	academic/educational
Portion	figures/tables/images
Number of figures/tables/images	1
Distribution quantity	100
Format	print and electronic
Will you be translating?	no
Order reference number	
Title of the thesis/dissertation	HEMIBIQUINONES: THE THEORY, SYNTHESIS, AND EXPERIMENTAL VALIDATION OF AN ASYMMETRIC D-A BIPHENYL SYSTEM
Expected completion date	Jul 2016
Estimated size	290
Requestor Location	Joseph E Meany 250 Hackberry Lane

Permission Request for Figure 1.10, Page 30:



RightsLink®

Home

Account Info

Help



Title: Molecular rectifiers
Author: Arieh Aviram, Mark A. Ratner
Publication: Chemical Physics Letters
Publisher: Elsevier
Date: 15 November 1974

Copyright © 1974 North-Holland Publishing Company.
Published by Elsevier B.V. All rights reserved.

Logged in as:
Joseph Meany

LOGOUT

Review Order

Please review the order details and the associated [terms and conditions](#).

No royalties will be charged for this reuse request although you are required to obtain a license and comply with the license terms and conditions. To obtain the license, click the Accept button below.

Licensed Content Publisher	Elsevier
Licensed Content Publication	Chemical Physics Letters
Licensed Content Title	Molecular rectifiers
Licensed Content Author	Arieh Aviram, Mark A. Ratner
Licensed Content Date	15 November 1974
Licensed Content Volume	29
Licensed Content Issue	2
Licensed Content Pages	7
Type of Use	reuse in a thesis/dissertation
Portion	figures/tables/illustrations
Number of figures/tables/illustrations	1
Format	both print and electronic
Are you the author of this Elsevier article?	No
Will you be translating?	No
Order reference number	
Original figure numbers	3
Title of your thesis/dissertation	HEMIBIQUINONES: THE THEORY, SYNTHESIS, AND EXPERIMENTAL VALIDATION OF AN ASYMMETRIC D-A BIPHENYL SYSTEM
Expected completion date	Jul 2016
Estimated size (number of pages)	290
Elsevier VAT number	GB 494 6272 12
Requestor Location	Joseph E Meany 250 Hackberry Lane TUSCALOOSA, AL 35487 United States Attn: Joseph E Meany
Total	0.00 USD

[Edit Order Details](#)

Permission for Figure 1.11, Page 31:



RightsLink®

Home

Account
Info

Help



Title: Molecular Rectifiers: A New Design Based on Asymmetric Anchoring Moieties
Author: Colin Van Dyck, Mark A. Ratner
Publication: Nano Letters
Publisher: American Chemical Society
Date: Mar 1, 2015

Logged in as:
Joseph Meany

LOGOUT

Copyright © 2015, American Chemical Society

PERMISSION/LICENSE IS GRANTED FOR YOUR ORDER AT NO CHARGE

This type of permission/license, instead of the standard Terms & Conditions, is sent to you because no fee is being charged for your order. Please note the following:

- Permission is granted for your request in both print and electronic formats, and translations.
- If figures and/or tables were requested, they may be adapted or used in part.
- Please print this page for your records and send a copy of it to your publisher/graduate school.
- Appropriate credit for the requested material should be given as follows: "Reprinted (adapted) with permission from (COMPLETE REFERENCE CITATION). Copyright (YEAR) American Chemical Society." Insert appropriate information in place of the capitalized words.
- One-time permission is granted only for the use specified in your request. No additional uses are granted (such as derivative works or other editions). For any other uses, please submit a new request.

If credit is given to another source for the material you requested, permission must be obtained from that source.

BACK

CLOSE WINDOW

Copyright © 2016 Copyright Clearance Center, Inc. All Rights Reserved. [Privacy statement](#). [Terms and Conditions](#).
Comments? We would like to hear from you. E-mail us at customer@copyright.com

Permission for Figure 2.1, Page 39:



RightsLink®

Home Account Info Help



Title: Dependence of single-molecule junction conductance on molecular conformation
Author: Latha Venkataraman, Jennifer E. Klare, Colin Nuckolls, Mark S. Hybertsen and Michael L. Steigerwald

Logged in as:
Joseph Meany

LOGOUT

Publication: Nature
Publisher: Nature Publishing Group
Date: Aug 24, 2006

Copyright © 2006, Rights Managed by Nature Publishing Group

Order Completed

Thank you for your order.

This Agreement between Joseph E Meany ("You") and Nature Publishing Group ("Nature Publishing Group") consists of your license details and the terms and conditions provided by Nature Publishing Group and Copyright Clearance Center.

Your confirmation email will contain your order number for future reference.

[Get the printable license.](#)

License Number	3900340094882
License date	Jul 01, 2016
Licensed Content Publisher	Nature Publishing Group
Licensed Content Publication	Nature
Licensed Content Title	Dependence of single-molecule junction conductance on molecular conformation
Licensed Content Author	Latha Venkataraman, Jennifer E. Klare, Colin Nuckolls, Mark S. Hybertsen and Michael L. Steigerwald
Licensed Content Date	Aug 24, 2006
Licensed Content Volume	442
Licensed Content Issue	7105
Type of Use	reuse in a dissertation / thesis
Requestor type	academic/educational
Format	print and electronic
Portion	figures/tables/illustrations
Number of figures/tables/illustrations	2
High-res required	no
Figures	2, 3
Author of this NPG article	no
Your reference number	
Title of your thesis / dissertation	HEMIBIQUINONES: THE THEORY, SYNTHESIS, AND EXPERIMENTAL VALIDATION OF AN ASYMMETRIC D-A BIPHENYL SYSTEM
Expected completion date	Jul 2016
Estimated size (number of pages)	290
Requestor Location	Joseph E Meany 250 Hackberry Lane

Permission for Figure 2.2 (Left), Page 40:



RightsLink®

Home Account Info Help



Title: Dependence of single-molecule junction conductance on molecular conformation
Author: Latha Venkataraman, Jennifer E. Klare, Colin Nuckolls, Mark S. Hybertsen and Michael L. Steigerwald

Logged in as:
Joseph Meany

LOGOUT

Publication: Nature
Publisher: Nature Publishing Group
Date: Aug 24, 2006

Copyright © 2006, Rights Managed by Nature Publishing Group

Order Completed

Thank you for your order.

This Agreement between Joseph E Meany ("You") and Nature Publishing Group ("Nature Publishing Group") consists of your license details and the terms and conditions provided by Nature Publishing Group and Copyright Clearance Center.

Your confirmation email will contain your order number for future reference.

[Get the printable license.](#)

License Number	3900340094882
License date	Jul 01, 2016
Licensed Content Publisher	Nature Publishing Group
Licensed Content Publication	Nature
Licensed Content Title	Dependence of single-molecule junction conductance on molecular conformation
Licensed Content Author	Latha Venkataraman, Jennifer E. Klare, Colin Nuckolls, Mark S. Hybertsen and Michael L. Steigerwald
Licensed Content Date	Aug 24, 2006
Licensed Content Volume	442
Licensed Content Issue	7105
Type of Use	reuse in a dissertation / thesis
Requestor type	academic/educational
Format	print and electronic
Portion	figures/tables/illustrations
Number of figures/tables/illustrations	2
High-res required	no
Figures	2, 3
Author of this NPG article	no
Your reference number	
Title of your thesis / dissertation	HEMIBIQUINONES: THE THEORY, SYNTHESIS, AND EXPERIMENTAL VALIDATION OF AN ASYMMETRIC D-A BIPHENYL SYSTEM
Expected completion date	Jul 2016
Estimated size (number of pages)	290
Requestor Location	Joseph E Meany 250 Hackberry Lane

Permission for Figure 2.2 (Middle), Page 40:



RightsLink®

Home

Create Account

Help



Title: Influence of Conformation on Conductance of Biphenyl-Dithiol Single-Molecule Contacts

Author: Artem Mishchenko, David Vonlanthen, Velimir Meded, et al

Publication: Nano Letters

Publisher: American Chemical Society

Date: Jan 1, 2010

Copyright © 2010, American Chemical Society

LOGIN
If you're a [copyright.com](#) user, you can login to RightsLink using your [copyright.com](#) credentials. Already a [RightsLink](#) user or want to [learn more?](#)

PERMISSION/LICENSE IS GRANTED FOR YOUR ORDER AT NO CHARGE

This type of permission/license, instead of the standard Terms & Conditions, is sent to you because no fee is being charged for your order. Please note the following:

- Permission is granted for your request in both print and electronic formats, and translations.
- If figures and/or tables were requested, they may be adapted or used in part.
- Please print this page for your records and send a copy of it to your publisher/graduate school.
- Appropriate credit for the requested material should be given as follows: "Reprinted (adapted) with permission from (COMPLETE REFERENCE CITATION). Copyright (YEAR) American Chemical Society." Insert appropriate information in place of the capitalized words.
- One-time permission is granted only for the use specified in your request. No additional uses are granted (such as derivative works or other editions). For any other uses, please submit a new request.

If credit is given to another source for the material you requested, permission must be obtained from that source.

BACK

CLOSE WINDOW

Copyright © 2016 [Copyright Clearance Center, Inc.](#) All Rights Reserved. [Privacy statement.](#) [Terms and Conditions.](#) Comments? We would like to hear from you. E-mail us at customer@copyright.com

Permission for Figure 2.2 (Right), Page 40:



RightsLink®

Home

Create Account

Help



ACS Publications
Most Trusted. Most Cited. Most Read.

Title: Single-Molecule Junctions Based on Nitrile-Terminated Biphenyls: A Promising New Anchoring Group
Author: Artem Mishchenko, Linda A. Zotti, David Vonlanthen, et al
Publication: Journal of the American Chemical Society
Publisher: American Chemical Society
Date: Jan 1, 2011
Copyright © 2011, American Chemical Society

LOGIN

If you're a [copyright.com](#) user, you can login to RightsLink using your [copyright.com](#) credentials. Already a [RightsLink user](#) or want to [learn more?](#)

PERMISSION/LICENSE IS GRANTED FOR YOUR ORDER AT NO CHARGE

This type of permission/license, instead of the standard Terms & Conditions, is sent to you because no fee is being charged for your order. Please note the following:

- Permission is granted for your request in both print and electronic formats, and translations.
- If figures and/or tables were requested, they may be adapted or used in part.
- Please print this page for your records and send a copy of it to your publisher/graduate school.
- Appropriate credit for the requested material should be given as follows: "Reprinted (adapted) with permission from (COMPLETE REFERENCE CITATION). Copyright (YEAR) American Chemical Society." Insert appropriate information in place of the capitalized words.
- One-time permission is granted only for the use specified in your request. No additional uses are granted (such as derivative works or other editions). For any other uses, please submit a new request.

If credit is given to another source for the material you requested, permission must be obtained from that source.

BACK

CLOSE WINDOW

Copyright © 2016 [Copyright Clearance Center, Inc.](#) All Rights Reserved. [Privacy statement](#). [Terms and Conditions](#).
Comments? We would like to hear from you. E-mail us at customercare@copyright.com

Permission for Figure 2.3, Page 47:



RightsLink®

Home

Account Info

Help



ACS Publications
Most Trusted. Most Cited. Most Read.

Title: Molecular Rectifiers: A New Design Based on Asymmetric Anchoring Moieties
Author: Colin Van Dyck, Mark A. Ratner
Publication: Nano Letters
Publisher: American Chemical Society
Date: Mar 1, 2015

Copyright © 2015, American Chemical Society

Logged in as:
Joseph Meany

LOGOUT

PERMISSION/LICENSE IS GRANTED FOR YOUR ORDER AT NO CHARGE

This type of permission/license, instead of the standard Terms & Conditions, is sent to you because no fee is being charged for your order. Please note the following:

- Permission is granted for your request in both print and electronic formats, and translations.
- If figures and/or tables were requested, they may be adapted or used in part.
- Please print this page for your records and send a copy of it to your publisher/graduate school.
- Appropriate credit for the requested material should be given as follows: "Reprinted (adapted) with permission from (COMPLETE REFERENCE CITATION). Copyright (YEAR) American Chemical Society." Insert appropriate information in place of the capitalized words.
- One-time permission is granted only for the use specified in your request. No additional uses are granted (such as derivative works or other editions). For any other uses, please submit a new request.

If credit is given to another source for the material you requested, permission must be obtained from that source.

BACK

CLOSE WINDOW

Copyright © 2016 Copyright Clearance Center, Inc. All Rights Reserved. [Privacy statement](#). [Terms and Conditions](#).
Comments? We would like to hear from you. E-mail us at customer@copyright.com

Permission for Figure 2.4, Page 48:



RightsLink®

Home

Account Info

Help



Title: Molecular Rectifiers: A New Design Based on Asymmetric Anchoring Moieties
Author: Colin Van Dyck, Mark A. Ratner
Publication: Nano Letters
Publisher: American Chemical Society
Date: Mar 1, 2015

Logged in as:
Joseph Meany

LOGOUT

Copyright © 2015, American Chemical Society

PERMISSION/LICENSE IS GRANTED FOR YOUR ORDER AT NO CHARGE

This type of permission/license, instead of the standard Terms & Conditions, is sent to you because no fee is being charged for your order. Please note the following:

- Permission is granted for your request in both print and electronic formats, and translations.
- If figures and/or tables were requested, they may be adapted or used in part.
- Please print this page for your records and send a copy of it to your publisher/graduate school.
- Appropriate credit for the requested material should be given as follows: "Reprinted (adapted) with permission from (COMPLETE REFERENCE CITATION). Copyright (YEAR) American Chemical Society." Insert appropriate information in place of the capitalized words.
- One-time permission is granted only for the use specified in your request. No additional uses are granted (such as derivative works or other editions). For any other uses, please submit a new request.

If credit is given to another source for the material you requested, permission must be obtained from that source.

BACK

CLOSE WINDOW

Copyright © 2016 Copyright Clearance Center, Inc. All Rights Reserved. [Privacy statement](#). [Terms and Conditions](#).
Comments? We would like to hear from you. E-mail us at customer@copyright.com